SINGLE AND TWO-PHASE FLOWS IN DUCTS AND STIRRED REACTORS

JAMSHID MALEKMOHAMMADI NOURI

B.Sc

Thesis submitted for the degree of

Doctor of Philosophy

in the the University of London

and for the

Diploma of Membership of the Imperial College

Imperial College of Science and Technology

Department of Mechanical Engineering

January 1988

To my family and above all my parents
as a mere fruit of their sacrifices

ABSTRACT

Measurements of the velocity characteristics of small and large particles have been made by laser-Doppler velocimetry in a fully developed pipe flow and around a disc baffle with 50% blockage in a descending vertical pipe. The mean velocities showed that the length of the recirculation region downstream of the baffle in single-phase flow, as represented by the small particles, was 2.15 times the baffle diameter. Spherical Diakon particles of 272, 310 and 665 μm mean diameter were used as a dispersed phase, and an amplitude discrimination method was used to measure their velocities. To allow the penetration of the laser beam for particle velocity measurements at higher particle concentrations, a technique was developed in which the refractive index of the particles was matched to that of the carrying fluid. The two-phase results showed that the particle mean velocity profiles became more uniform and the particle turbulence velocities smaller than those of the single-phase flow. The particle mean velocity in the pipe flow decreased with concentration and the apparant slip velocity decreased with Reynolds number. The length of the recirculation region was shorter than in single-phase flow by about 11% and 24% for particle concentrations of 4% and 8% respectively. The particle mean velocities were little affected by particle size but the turbulent levels were lower with the larger particles.

Similar measurements in single-phase and two-phase flows have also been made in a baffled stirred reactor vessel driven by a six-blade disc impeller. Flow visualisation was used to provide qualitative information and, together with single-phase mean flow velocity measurements, showed the presence of ring vortices above and below the impeller and that the flow entering the impeller stream region was mainly from below the impeller causing the inclination of the jet stream. The flow was strongly three-dimensional with large regions having tangential velocities in a direction opposite to that of the impeller rotation. The turbulence results showed that the turbulence was nearly isotropic in the impeller stream whereas it was anisotropic in the bulk flow, and the turbulence kinetic energy in the impeller stream was higher than in the bulk flow by an order of magnitude. Parametric results revealed that the mean and rms velocities scaled with impeller rotational

ABSTRACT

speed everywhere in the stirred vessel and that the size of the impeller had no effect on mean flow and turbulence levels in the impeller stream, but the mean and tubulence velocities of the bulk flow increased with impeller size for the same Reynolds number. Spherical Diakon and glass particles were used as the dipersed phase in the stirred vessel and the two-phase flow results showed the presence of strong particle concentration gradients along the height of the vessel and considerable particle settling as the impeller speed was reduced. Particle mean velocities showed that the particles lagged behind the fluid at the impeller tip, and in the bulk flow they either lagged behind or led the fluid depending on local flow direction. The particle turbulence levels were smaller, by up to 15%, than single-phase levels.

ACKNOWLEDGEMENTS

My most sincere gratitude goes to my supervisor Prof. J. H. Whitelaw whose continuous interest and support made this study possible. This thesis, though its imperfections are mine, owes a great deal to his valuable advice and constructive criticism, for which I am greatly in debted.

I am obliged to Dr. M. Yianneskies, for his time and knowledge generously given, and benefitted from the discussions we have had over the years.

I have also benefitted from my association with all my colleagues, particulary Dr. A. Bicen, Mr. F. de Pinho, Mr. R. Hockey, Dr. L. Khezzar, Mr. S. Polities, Dr. J. Rojhs, Dr. A. M. K. P. Taylor and Dr. C. Vafidis.

I wish to express my deepest gratitude to my true friends and colleagues A. Bolour-Froushan, S. Etemad, A. Ghobadian, M. Moussavi, K. Servat-Djoo, and B.S. Tabrizi who shared my disappointments and successes over these years.

I am grateful to Messrs. B. Crew, J. Laker, A. Raper, A. Smith, D Syman, P. Trowell and O. Vis for their help with the design and construction of the experimental apparatus.

I am grateful to Imperial Chemical Industries (ICI) and Unilever for financial support provided for this work. Special thanks are due to Mr. D. A. Hines, Dr. K. Looney and Dr. J. C. Middleton.

CONTENTS

CONTENTS

CONTENTS

LIST OF TABLES

LIST OF FIGURES

LIST OF FIGURES

LIST OF FIGURES

LIST OF FIGURES

LIST OF FIGURES

LIST OF FIGURES

LIST OF FIGURES

LIST OF FIGURES

LIST OF FIGURES

LIST OF FIGURES

NOMENCIATURE

Latin characters

A_p	Cross-section area of measuring volume.
a	Distance from measuring volume to collecting lens.
b	Distance from collecting lens to photomultiplier pinhole.
b_o	Diameter of laser beam at laser output.
b_s	Diameter of laser beam at measuring volume.
b_x	Diameter of measuring volume at e^{-2} intensity.
b_y	Length of measuring volume at e^{-2} intensity.
C	Impeller clearance.
C_d	Drage coefficient.
C_l	Local particle concentration.
$C_{l,max}$	Local maximum particle concentration.
C_m	Volumetric percentage of tetraline in the mixture.
C_v	Volumetric particle concentration.
C_μ	Constant in effective viscosity hypothesis (0.09).
D	Impeller diameter.
D_b	Disc baffle diameter.
D_e	Jet exit diameter.
D_f	Depth of flow field.
D_p	Pipe diameter.
d	Impeller disc diameter.
d_f	Fringe spacing in measuring volume.
d_p	Particle mean diameter.
$e_{r\theta}$	Shear strain rate $[(\partial\overline{W}/\partial r - \overline{W}/r) + \partial\overline{V}/r.\partial\theta]$.
f_D	Doppler frequency.
f_τ	Counter clock frequency.
f_1	Focal length of lens L_1.
f_2	Focal length of lens L_2.

NOMENCIATURE

f_3	Focal length of lens L_3.
g	Specific gravity constant (9.81 m/s^2).
H	Height of liquid in the stirred vessel.
h	Impeller blade width.
$I_{m,l}$	a.c. component of scatter light intensity from small particles.
$I_{m,p}$	a.c. component of scatter light intensity from large particles.
$I_{p,l}$	d.c. component of scatter light intensity from small particles.
$I_{p,p}$	d.c. component of scatter light intensity from large particles.
K_d	Discharge coefficient.
k	Turbulence kinetic energy.
L	Impeller blade length.
M	Magnification of scatter light.
N	Impeller rotational speed.
N_{fr}	Number of fringes in measuring volume.
N_p	Power number.
N_{ph}	Number of validated Doppler cycles.
$\dot{N}$	Rate of Doppler-burst arravial.
n	Refractive index.
P	Power input.
Q	Mass flow rate.
Q_a	Axial mass flow rate into the impeller.
Q_{ap}	Axial mass flow rate in the pipe.
Q_d	Radial discharge mass flow rate.
Q_i	Induced mass flow rate into the impeller stream.
Q_{in}	Total axial mass flow rate into the impeller from above and below.
Q_r	Radial mass flow rate at impeller tip.
R	Pipe and impeller radius.
Re	Reynolds number.

NOMENCIATURE

R_e	Jet exit radius.
R_t	Radial location as close as possible to the tip of the impeller.
R^*	Normalised radial distance (r/R).
r	Radial distance.
S	Slip factor.
T	Cylindrical vessel diameter.
T_r	Induce torque.
$\overline{U}$, $\overline{V}$, $\overline{W}$	Ensemble-averaged single-phase mean velocity components.
$\overline{U}_c$	Centerline single-phase axial mean velocity.
$\overline{U}_f$, $\overline{V}_f$, $\overline{W}_f$	Ensemble-averaged liquid-phase mean velocity components.
$\overline{U}_p$, $\overline{V}_p$, $\overline{W}_p$	Ensemble-averaged solid-phase mean velocity components.
$\overline{U}_{pc}$	Centerline solid-phase axial mean velocity.
$\overline{U}_s$, $\overline{V}_s$, $\overline{W}_s$	Apparant velocity components.
u', v', w'	Ensemble-averaged single-phase turbulence velocity fluctuations.
u'_c	Centerline single-phase axial turbulence velocity fluctuation.
u'_f, v'_f, w'_f	Ensemble-averaged liquid-phase turbulence velocity fluctuations.
u'_p, v'_p, w'_p	Ensemble-averaged solid-phase turbulence velocity fluctuations.
u'_{pc}	Centerline solid-phase axial turbulence velocity fluctuation.
V_b	Pipe bulk velocity.
V_{gs}	Laminar particle terminal velocity.
V_{gt}	Turbulence particle terminal velocity.
V_o	Pipe annular bulk velocity.
V_t	Impeller tip velocity.
$\overline{W}_{mean}$	Tangential mean velocity over the width of the impeller.
Z	Axial distance.
Z, r, θ	Cylindrical polar coordinate.
Z_c	Constant of confidence limit.
Z^*	Normalised axial distance.

NOMENCIATURE

$Z_{(1/2)}$	Width of the radial jet stream at half maximum velocity.

Greek characters

β	Area blockage by the baffle in the pipe.
ε	Dissipation of turbulence kinetic energy.
ε_{ave}	Average dissipation of turbulence kinetic energy.
ε_r	Clock counting error.
ϕ	Half angle of laser beam intersection.
η	Mechanical efficiency.
λ	Light wavelength.
μ	Fluid dynamic viscosity.
ν	Fluid kinematic viscosity.
π	PIE constant ($\approx$3.14)
θ	Angular location with respect to baffle position.
ρ	Fluid density.
ρ_p	Particle density.
τ_f	Fluid response time.
τ_p	Particle response time.
Δn	Change in refractive index.

CHAPTER I

INTRODUCTION

1.1 Background and objectives

Stirred reactors are widely used in the chemical and food process industries and typically comprise a cylindrical vessel with baffles and an agitator. The mixing process that can be achieved can be either reactive or passive and operations include the mixing of miscible and immiscible liquids, suspension of solids in liquids, suspensions of liquid (droplet) in gas and dispersion of gas in liquid.

The design of a mixing vessel for a particular mixing operation involves consideration of process design, the impeller power characteristics and the mechanical design (Oldshue, 1983), each of which plays a major part in improvement in design and performance of the reactors. The process design requires understanding of fluid mechanics since the mixing process, in turbulent mixing with or without reaction, is accomplished by a combination of mechanisms such as bulk flow, eddy diffusion and molecular diffusion (Uhl and Gray, 1966). Proper selection of impeller type, size and speed and also the relationship between these parameters and others which affect mixing is equally important (Holland and Chapman, 1967) and detailed knowledge of the mean flow and turbulence characteristics is required to yield a desired production rate with specified product properties at minimum capital and operating cost.

Due to the complexity of the flow in stirred reactors, which is turbulent, recirculating and three-dimensional (Uhl and Gray, 1966 and Yianneskis et al, 1987), the above problem becomes more complicated when multiphase mixing processes are involved so that it is necessary to understand the behaviour of each phase. This calls for a combined experimental and theoretical research effort which faces the formidable task of probing and analysing such complex multiphase flows. The present investigation was arranged to provide some of the essential experimental information.

The flow of suspensions of particles can be influenced by turbulence, the Magnus

force, the virtual mass, particle crossing-trajectories (free-fall velocity), and particle inertia and particle-particle interaction. In a complex flow such as stirred reactor, where the single-phase flow structure is not well understood, it is particularly difficult to determine the effect of the suspended particles on the flow structure. Also, as will be shown in the next section, the velocity data available in two-phase flows is small and mainly restricted to pipe flows. Therefore it is desirable to acquire knowledge about the effects of the second-phase (e.g. particles) on the carrying-phase flow structure when the particles are suspended in simpler and better established flows than the stirred reactors, such as fully developed turbulent pipe flow (Laufer, 1954) and flow around an axisymmetric baffle (Taylor and Whitelaw, 1984 and Nouri et al, 1984).

Attempts to obtain single-phase velocity measurements in stirred reactors have been made as early as 1954 (Sachs and Rushton, 1954), but it was during the last decade that most of the investigations using laser-Doppler velocimetry were carried out (e.g. Reed et al, 1977 and Yianneskis et al, 1987). In two-phase flow, optical methods (laser-Doppler velocimetry in particular) were found to be the only reliable diagnostic technique for measuring the velocities of both phases (see table 1.2). Computer models, on the other hand, took advantage of the latest developments in computers to describe the three-dimensional flow field in stirred reactors for both single (Bolour-Froushan, 1986) and two-phase (Looney et al, 1985) flows. Parallel developments of experimental and theoretical research are therefore of great importance since the latter depends on the former for the provision of boundary conditions and for the validation of the predictions against data.

Although there have been many experimental investigations with single-phase flow measurements in stirred vessels in the last years and these have produced a large amount of information and some useful conclusions, the results are restricted to limited regions in the vessel and they are far short of describing the overall flow characteristics and its three-dimensionality. As will be shown in the following section, little work has been

CHAPTER I

done to show the effects of impeller rotational speed, size and clearance on the flow field in stirred vessel in order to establish some scaling rules. In two-phase flows in stirred vessels, no measured velocity data have been reported to date and most two-phase flow investigations (see table 1.2) have been concerned with gas-solid flows in simple geometries such as pipe and jet flows. The complexity of the two-phase flow processes limits the ability of the experimental methods; for example the presence of the dispersed-phase results in damage or contamination of measurement probes, and suggests that laser-Doppler velocimetry should be used. However, with optical methods the blockage of the beams and the scattered light limit the velocity measurements to dilute flows.

These considerations have provided the motivation for the present thesis which contributes to understanding of single and two-phase flows in stirred vessels and of the two-phase flow in ducts, by describing the velocity field measurements in these flows. The experimental approach is that of detailed laser-Doppler velocimetry measurements in the ducts and stirred vessels. A refractive-index-matching technique was developed to use it in conjunction with laser-Doppler velocimetry to allow the measurement of the solid-phase velocities at higher particle concentrations. The results were obtained in sufficient detail to allow their use as input conditions and as a testing ground for calculations which have been carried out in parallel with this work.

The reminder of this chapter has been prepared in three sections which are concerned with a survey of previous work, the present contribution and an outline of the thesis.

1.2 Survey of previous work

This section reviews the literature on experimental and calculation studies of single-phase flows in stirred vessels and two-phase flows in different flow configurations particularly in duct flows. Also, a survey on the refractive-index-matching technique is

given. The review is presented in this section in order to provide the background for formulating the aims and purposes of the present contribution.

1.2.1 Experiments

Single-phase flow in ducts

Single-phase fully-developed turbulent pipe flows and flows around axisymmetric disc baffles have been studied extensively by a number of investigators and are well established in terms of velocity measurements and calculations. They are used here to study particle motion in two-dimensional flows which are simpler than those of stirred vessels (three-dimensional) and to improve understanding of particle behaviour so as to provide a fundation for explaning the effects of particle in more complex flows.

Detailed mean and rms velocity measurements are presented and discussed in pipes (Laufer, 1954) and around axisymetric disc baffles (Taylor and Whitelaw, 1984 and Nouri et al, 1984) and a comprehensive survey of experiments and calculations of duct flows has been given by Taylor (1981). The velocity measurements presented in section 2.4 have therefore been made partly to compare with the results of previous investigations and to provide confidence in the flow arrangements, and also to provide detailed results for comparison with the solid-phase measurements presented in section 2.5.

Single-phase flow in stirred vessels

The most relevent experimental investigations are listed in table 1.1 and consist mainly of:

(1) flow visualisation to obtain qualitative information;

(2) photographic, hot-wire and hot-film anemometry, and laser-Doppler velocimetry measurements to describe the mean and turbulence flow field.

The flow visualisations of Reed et al (1977) and Yianneskis et al (1987) made use of sheets of laser light to obtain photographs of bubble and particle motion in axial and

transeverse planes in stirred vessels and are comprehensive and useful: they show the presence of a strongly three-dimensional vortical mean flow in turbine stirred vessels. The results of Yianneskis et al demonstrate that a radial jet emanates from the impeller and divides upon impingement upon the vessel wall into two thin axial wall jets above and below the impeller to form the two main ring vortices. They also found that the stream jet is inclined at an angle which increases with decrease in impeller clearance, and that the flow in the transverse (r-θ) planes are weaker than in axial (r-Z) planes.

The first measurements of mean velocities in the impeller stream were reported by Sachs and Rushton (1954) who used a photographic technique and estimated velocities by measuring the length of the streak. Cutter (1966) used the same technique to measure three mean and rms velocity components. The photographic technique provides qualitative information, but is less suitable for quantitative measurements. Hot-wire and hot-film anemometry have also been used to measure mean and turbulence flow field in stirred vessels (e.g. Cooper and Wolf, 1968; Mujumdar et al, 1970; Nishikawa et al, 1976 and Costes and Couderc, 1982) and the continuous output signal of the anemometer with its high frequency response allows the measurement of turbulence characteristics. However, reliable quantitative information can only be obtained in limited locations in the impeller stream, due to the highly three-dimensional vortical nature of the flow (see e.g. Bowers, 1965) and the lack of directional sensitivity of the probes.

Laser-Doppler velocimetry is preferred because of its unobtrusive nature and its ability to resolve the direction of the flow and was used here for the measurement of velocity in stirred vessels. Early velocity measurements of the flow in a stirred vessel using laser-Doppler velocimetry were made by Reed et al (1977) and were followed by the other investigators listed in table 1.1. Reed et al used a frequency tracker to process the Doppler signals which prohibited accurate measurements of regions of high turbulence intensity (e.g. close to the impeller blades), due to the dropout limitations of the instrument. Yianneskis et al (1987) used a frequency counter and obtained the most detailed, to-date,

velocity measurements in stirred vessel.

The flow in the impeller region between the blades of a disc turbine impeller is dominated by pair of roll vortices behind each blade, as shown schematically in figure 1.2. There is one vortex above and one below the disc plane and they rotate in an direction opposite to that of the impeller: the vortices extend into the impeller stream as trailing vortices. Mujumdar et al (1970) first deduced the presence of the trailing vortices from the distinct peaks corresponding to the blade passage frequency in the one-dimensional energy spectrum of turbulence . These peaks disappeared further away from the impeller where the vortices decay rapidly. Van't Riet and Smith (1975) and Günkel and Weber (1975) investigated the structure of the trailing vortices in detail. In the former investigation a rotating camera and a pitot tube were used to visualise and measure the flow structure and the results showed that the axis of the vortices is vertical near the blade and becomes horizontal in the impeller stream. The position of the axis was found to be independent of Reynolds number. Günkel and Weber (1975) used a hot-wire anemometer mounted on the impeller and deduced the existance of a second pair of vortices in front of the blades. This pair of vortices was not detected by any other investigators.

The most comprehensive description of the trailing vortices was reported by Popiolek et al (1984) who used laser-Doppler velocimetry and synchronised the velocity measurements with the rotation of the impeller and obtained ensemble-averages over an interval of one degree rotation of the impeller. They showed that the periodic component of the flow, termed "Pseudo turbulence" by van't Riet and Smith (1975), persists up to 1.5 times the impeller width from the impeller tip, which is in agreement with the findings of van der Molen and van Maanen (1978).

A comprehensive assessment of the effect of the definition of the turbulence quantities in the impeller stream has been given by Bolour-Froushan (1986). When time-averages are obtained, the stationary probes measure over 360 °, i.e. over the whole cycle of rotation, and provide the sum of turbulence and a periodic component, whereas

probes moving with the impeller or ensemble averages over some angles of impeller rotation measure only the turbulence signals. The method of measuring turbulence quantities also affects the estimates of the dissipation length scale and the rate of energy dissipation since they are related to turbulence characteristics (e.g. u', v', w' and k). In order to remove the effect of periodicity, Mujumder et al (1970) suggested that the peaks in the energy spectra corresponding to the passage frequency of the impeller should be filtered. However, van't Riet and Smith (1975) showed that this filtering is not enough since the trailing vortices themselves contribute to the energy spectra. The technique used by Popiolek et al (1984) offers the best solution and involved ensemble averages over one degree of impeller rotation only.

Apart from the investigations mentioned above, the majority of investigations of stirred vessels have regarded the flow as steady and averaged over the whole impeller rotation to obtain the velocity characteristics which are presented below. This type of data is useful and are commonly used in the design of mixers (Uhl and Gray, 1966 and Oldshue, 1983), and also to comply with current numerical technique requirements (Bolour-Froushan, 1986). In the present investigation this type of the averaging (over 360 °) was used to measure the velocities in the stirred vessels for reasons which will be discussed further in chapter III.

The first velocity measurements in the impeller stream were reported by Sachs and Rushton (1954) who showed that the axial profiles of radial velocity flattened with increasing radial distance, a result which has been confirmed by all subsequent investigations. Cooper and Wolf (1968) showed that the radial velocities in the impeller stream were independent of impeller rotational speed. The impeller stream was found to be slightly inclined (Reed et al, 1977 and Yianneskis et al, 1987) and the inclination increased with decreasing impeller clearance (Yianneskis et al, 1987). A useful parameter for the characterization of the impeller stream mean flow is the radial mass flow rate (pumping capacity) in that region. Sachs and Rushton (1954) showed that the impeller flow rate is

independent of rotational speed and increases with radial distance up to r=D where it starts to decrease: the maximum value is approximately twice the discharge flow rate at the impeller tip, Q_d. The same trend was found by Cooper and Wolf (1968) but, in their impeller geometry, the maximum radial flow rate was 1.8 Q_d.

The impeller stream is a region of highly turbulent flow, and this has been confirmed by all the investigators listed in table 1.1. In the vicinity of the impeller, the axial prifiles of v' and w' are flatter than the corresponding mean velocity profiles, Yianneskis et al (1987), and the maximum turbulence kinetic energy at the impeller tip is about 0.17 V_t^2. Some of the investigators suggested that the turbulence in the impeller stream is anisotropic, while van der Molen and van Maanen (1978) and van Doorn (1982) found that the turbulence is near-isotropic. Ito et al (1975) measured all three components of the turbulent shear stress in the impeller stream and showed that $\overline{vw}$ is much larger than the two other components and Yianneskis et al (1987) showed that $\overline{vw}$ changes sign at the tip of the impeller blade.

The rate of dissipation of the kinetic energy of turbulence, ε, is not a directly measureable quantity, because ε is manifested by local generation of thermal energy and since the temperature changes are much too small. However, ε can be estimated as described below from the measurements of mean and rms velocities, energy spectra and cross-correlation terms, but the accumulated error can be relatively high. Cutter (1966) used Batchelor's (1953) proposed relationship for ε:

$$\varepsilon = [\, 3\ A\ (u')^3 / 2\ L] \qquad (1.1)$$

where L is the integral scale and A is a constant. Cutter integrated (1.1) over the impeller stream assuming homogeneous turbulence and found that 50% of the energy is dissipated in the impeller stream, 20% within the impeller and the remainding 30% in the bulk of the flow. Van Doorn (1982), Patterson and Wu (1985) and Laufhütte and Mersmann (1985)

used approaches similar to Cutter to determine ε. The first two investigators showed that the axial profiles of ε / N^3D^2 at the tip of the impeller have a peak at the middle of the impeller disc of about 35 and 12 respectively. Laüfhütte and Mersmann (1985) showed that at the impeller tip the periodicity can increase ε by about 2.5 times and van Doorn (1982) suggested that the errors in his estimation can be as high as 65%. Yianneskis et al (1987) used the effective viscosity hypothesis to estimate ε as

$$\varepsilon = C_\mu (k^2 / -\overline{vw})[e_{r\theta}] \qquad (1.2)$$

where C_μ=0.09 and $e_{r\theta}$ is the shear strain rate and they also found a peak at the centre of the impeller blade of about 27 m^2/s^3 or 22.5 N^3D^2. The uncertainties associated with this estimation are high and of the order of 0.3 ε.

Mean flow measurements in the bulk of the flow have been reported by a number of investigators including Aiba (1958), Günkel and Weber (1975), Nagata (1975) and Weetman and Salzman (1980). However their results were mainly in a single axial plane, and do not describe the three-dimensional features of the flow adequately. The first detailed measurements in the bulk flow were carried out by Reed et al (1977), but their presentation of the results make interpretation difficult. Yianneskis et al (1987) presented the most detailed measurements of the flow in a standard configuration vessel in four axial planes and showed the presence of the main ring vortices above and below the impeller. They found that the flow in the vessel was highly vortical and three-dimensional, that there were regions of flow below the impeller that rotated in an opposite direction to that of the impeller rotation and that the axial profiles were near-uniform except close to the wall of the vessel. The presence of the baffles results in a reduction of the swirl velocity which is compensated by an increase in the axial and radial velocities (Nagata, 1975). Reed et al (1977) and Yianneskis et al (1987) showed that there is a helical vortex behind each baffle.

Information on the turbulence in the bulk of the flow is far from complete, mainly

because not much data has been obtained in this region and the locations of the available data are too sparse for adequate judgement of the trends. Yianneskis et al (1987) found the variation of turbulence levels of u', v' and w' to be from 0.07 to 0.16 V_t and that the turbulence kinetic energy reached a maximum of $0.01V_t^2$, i.e. an order of magnitude smaller than in the impeller stream region. The Reynolds shear stresses (Nagata, 1975) decrease sharply and the turbulence becomes isotropic away from impeller stream. Nagata estimated ε from one-dimensional energy spectra and showed the region of high dissipation is in front of the baffle. The effect of the baffle was to suppress the turbulence levels in the vicinity of the vessel wall (Nagata, 1975). Günkel and Weber (1975) showed that 62% of the power input is dissipated in the bulk of the flow which is in contradiction with the finding of Cutter (1966) that only 30% of the power is dissipated in the bulk of the vessel.

Little experimental work has been done to determine the influences of the impeller rotational speed on the mean and turbulence flow field in order to establish scaling rules, and there is no detailed velocity information available on the effect of impeller size and clearance. Sachs and Rushton (1954) and Cooper and Wolf (1968) showed that the radial mean and mass flow rate in the impeller stream are independent of impeller speed and that the tip velocity can be used as the scaling factor and this has been verified by all the later investigators. These results are limited to the impeller stream region in the vessel and do not show the influence of the effect of speed on the overall flow pattern and in particular on the turbulence.

Two-phase flows in pipes and stirred vessels

Information on two-phase flow velocity measurements in stirred vessels and around baffles in a pipe is scarce, but the properties of suspension of solids or droplets in fluids have been examined for a variety of flow configurations mainly pipes and jet flows, and are summarised in table 1.2.

CHAPTER I

The presence of the dispersed-phase results in damage or contamination of measurement probes used for two-phase measurements and the application of non-obtrusive optical techniques for the measurement of the velocity characteristics is therefore advantageous. Laser-Doppler velocimetry has been employed successfully for the measurements of two-phase flows as shown in table 1.2, but the measurements of solid or droplet suspensions have been limited to dilute flows of concentrations below 1.5% (e.g. Lee and Durst, 1982 and Nouri et al 1984) and, in few exceptions, to around 5% (Zisselmar and Molerus, 1978). This limit is caused primarily by the blockage of the beams and of the light scattered by particles which attenuate the incident and scattered laser light. Light blockage can also introduce rms velocity errors of more than 10% as shown by Kliafas et al (1985).

Various methods have been suggested for the measurements of the velocities of fluid and solid-phase and are based mainly on electronic filtering and differentiation of a.c. and d.c. components of the Doppler signals (see for example Einav and Lee, 1973; Lee and Durst, 1982 and Tsuji amd Morikawa, 1984). The accuracy of amplitude discrimination is very good when the particles pass through the central portion of the measuring volume but there is a finite probability that the large particles (solid-phase) will pass through the outside edge of the measuring volume and hence the intensity of the Doppler signal produced may be below the preset threshold. In this case the signal of the large particles will be identified as originating from small ones (fluid-phase) and this "cross-talk" between the signals of the large and small particles (Durst, 1982), can be more severe especially when the difference in diameter of the small and large particles is small (Modarress et al, 1983). A possible way to eliminate this deficiency was suggested by Modaress et al (1983) and involves a two-colour laser-Doppler velocimeter to monitor the pedestal of the signals. Another method of discrimination which does not suffer the aforementioned problem was suggested by Durst and Zare (1975) and is based on the relationship between particle size and the phase shift which exists between Doppler signals

at different angles of observation. The method has been evaluated by Hardalupas (1986) who showed spherical particles are required to minimise errors.

As mentioned in previous section, the effects of turbulence, particle inertia and crossing trajectories, particle-to-particle interaction, Magnus force and virtual mass effects can influence the flow of suspension of particles. Previous investigations have been concerned with the determination of one or more of these effects in mostly gas-solid two-phase flows and particle-to-particle interaction is expected to be negligible for spherical particles with volumetric concentrations below 0.3% (Lumley, 1978). The effects of particle crossing trajectories and inertia on the dispersion of particles in turbulent flow was investigated by Wells and Stock (1983) who found that the inertia effect reduced the particle rms velocity for both 5 and 57 μm glass particles, and that the crossing trajectories effect can decrease the dispersion if the particle free-fall (terminal) velocity is larger than the fluid rms velocity. The presence of the solid particles may also alter the properties of the bulk flow and can affect properties of the fluid-phase. An increase in the particle volumetric concentration (C_v) is expected to cause an increase in pressure drop and friction factor (Cox and Mason, 1971 and Tsuji and Morikawa, 1982) and, the suspension may become non-Newtonian with high particle concentrations (Soo, 1967).

Soo et al (1964) observed that the mean velocity profile of the fluid-phase is unaltered by the presence of the solid particles for mass loadings up to 8.0, while Cox and Mason (1971) and Yianneskis and Whitelaw (1984) reported identical fluid and particle velocities for neutrally bouyant solids in low to moderate concentration. Tsuji and Morikawa (1982) found that 200 μm particles flattened both the fluid and the solid velocity profiles in dilute air-solid horizontal pipe flow and suppressed the turbulence of the fluid-phase, while 3 mm diameter particles increased the turbulence significantly, due to the wakes behind the particles. The flattening of the velocity profiles of both phases in horizontal and vertical pipe flows was confirmed by all the investigations cited. Birchenough and Mason (1976), Lee and Durst (1982) and Tsuji et al (1984) have

CHAPTER I

measured turbulent gas-solid upflow in vertical pipes for C_v up to 0.4% with laser-Doppler velocimetry and showed that the particle velocity decreases as C_v increases and that the particles lag behind the fluid. Modaress et al (1982, 1983) also used laser velocimetry to measure the downflow of a round particle-laden jet in a co-flowing stream and showed that the spread of the jet in two-phase is smaller than in single-phase flow resulting in a narrower jet.

Einav and Lee (1973) pointed out the importance of the near wall region in a liquid-solid suspension boundary layer channel flow and found that a particle-free zone existed in the vicinity of the wall. Lee and Durst (1982) showed that the thickness of this zone in upward-flowing gas-solid suspension is a function of particle size so that the thickness increases with particle diameter; they also suggested that this zone is much larger than the thickness of the viscous sublayer. The same authors showed that in a vertical upflow pipe, the particle velocities in the near wall region are larger than those of the fluid. This result was confirmed by Tsuji and Morikawa's (1982) experiments in a horizontal pipe and Tsuji et al's (1984) for a upward-flowing suspension vertical pipe. The latter investigation also showed that the radial distance from the wall over which the particle velocity is greater than that of the fluid, decreases with both C_v and d_p.

The first two-phase velocity measurements around axisymmetric baffles in a liquid-solid flow in a horizontal pipe were reported by Nouri et al (1984) and involved suspended particles which were almost neutrally buoyant. They found that for a particle concentration of 0.375% the particles followed the fluid motion behind a conical baffle of 25% area blockage, but the annular jet region behind a disc baffle of 50% area blockage was narrower with the particles lagging behind the fluid in the region around the centre of the annular jet. They also showed that the particle turbulence levels are smaller than in single-phase flow by about 3 to 38% depending on the location in the flow, and that the turbulence levels were further suppressed as C_v increased. Due to blockage of the beams by the suspended particles, Nouri et al's measurements were limited to volumetric

concentration below 1.5%.

refractive-index-matching technique

The range of applicability of optical techniques is limited by the separation which occurs when light is passed through solids or fluid of different refractive index as the experiment of Nouri et al (1984) showed. When local measurements are required, the location of measurement must be known or calculated for example by refractive index correction equations such as those of Bicen (1984). This may prove difficult where surface curvature is complex or where the light is required to cross a number of interfaces involving materials of different refractive index as in the case of transparent solid particles suspended in a fluid. The use of fluids and solid materials of identical refractive index helps to alleviate these problems as has been shown in the investigations listed in Table 1.3 which involved velocity measurements by laser-Doppler velocimetry in both single and two-phase flows.

With arcylic (Diakon) particles suspended in water, for example, the transmission of light is severely limited so that measurements become impossible if the volume concentration of 270 μm diameter particles exceed 1.5% with a 25 mm depth of field (Nouri et al, 1984). However, the maximum particle concentration through which beam penetration is possible in liquid-solid flows can be increased if the refractive indices of suspended particle material and of the carrier fluid are matched. Zisselmar and Molerus (1978) measured the fluid velocity in the presence of solid particles up to a volumetric concentration of 5.6% in a pipe, and showed the fluid turbulence levels are suppressed by up to 40% at C_v=5.6%. Yianneskis and Whitelaw (1984) made particle velocity measurements up to C_v=10% in a laminar liquid-solid suspension pipe flow and showed that the particle mean velocity profiles were identical to that of single-phase.

The rest of the investigators listed in table 1.3 employed refractive-index-matching to remove problems associated with the refraction of the laser

beams in order to measure single-phase flow mean and turbulence velocities in complex geometries. Elphick et al (1982) and Edwards and Dybbs (1984) used the technique and made single-phase velocity measurements in rod-bundles, and detailed mean and turbulence velocity measurements in a swirl chamber were made by Horvay and Leuckel (1984) with a mixture of tetraline (tetrahydronaphaline) and oil of turpentine.

1.2.2 Calculations

Early numerical modelling studies of the single-phase flow in stirred vessels were with laminar flow in the impeller stream. Sweeney and Patrick (1977) used a Cartesian co-ordinate representation of the geometry and solved the conservation equations in numerical form for the flow of a non-Newtonian fluid in the impeller region. Their predictions compared favourably with bubble flow visualisation photographs, but since they used the Cartesian representation, the effects of centrifugal and Coriolis forces set up by the rotation of the impeller were eliminated. Hiroaka et al (1978) adopted the same method to calculate the flow of a Newtonian fluid in the same region and claimed that the predicted velocity profiles accorded with experimental data.

The first model of single-phase turbulent flow in the whole stirred vessel was formulated by Harvey (1980) and Harvey and Greaves (1982) who solved the time-averaged Navier-Stokes equations for incompressible flow by assuming axial symmetry and using the k-ε turbulence model. The comparison of predicted results, in an air agitated standard configuration with C=T/2 clearance, with those reported by Günkel and Weber (1975) show qualitative agreement in the mean flow results in the impeller stream. Placek and Travlarides (1985) used a similar treatment and simulated the experiment of Günkel and Weber (1975) for water agitated in an open vessel. They used a three-equation model of turbulence in conjunction with the method of Gosman et al (1979) and the results show discrepancies of up to 50% from measured profiles.

Three-dimensional calculations of single-phase turbulent flows in baffled stirred

vessels have been attempted by Issa and Gosman (1981) who solved the time-averaged Navier-Stokes equations for single-phase flow with turbulence shear stresses obtained from the k-ε turbulence model; preliminary comparison of their results (single-phase) against the data of Cutter (1966) and Reed et al (1977) in the impeller stream showed reasonable agreement. Bolour-Froushan (1986) used the procedure of Issa and Gosman (1981) with the algorithm of Issa (1983) to produce fine grid solutions for the single-phase flow in a stirred vessel and confirmed quantitative agreement with the laser-Doppler velocimetry measurements reported by Yianneskis et al (1987), although with some smearing of the mean velocity gradients.

The complexity of the flow processes in stirred vessels and the presence of the solid particles provide difficulties for calculation methods and predictions of two-phase flow in stirred vessels are scarce. In general, there are two basic approaches to analysing the dispersed-phase (Durst et al, 1984), the Lagrangian approach is based on the trajectories of individual particles as in the methods of Shuen et al (1985), Watkins et al (1986) and Tabrizi (1988). The second approach is Eulerian with the dispersed-phase treated as a continum as in the studies of Pourahmadi and Humphrey (1983) and Looney et al (1985).

Owen (1969) estimated the rate of turbulence energy dissipation in a fluid containing small particles to be greater by ($1\pm \rho_p / \rho_f$) and the turbulence intensity smaller by $(1+ \rho_p / \rho_f)^{-0.5}$ than in a particle free fluid (single-phase). Choi and Chung (1983) calculated dilute gas two-phase flow in a pipe by considering the solid-phase to behave as a secondary fluid mixed with the primary fluid. Shuen et al (1985) and Shuen et al (1986) predicted two-phase flows in a particle-laden jet and in a diffusion flame respectively with results which were in reasonably good agreement with the experimental results reported by the same authors in a parallel study. Shih and Lumley (1986) introduced a set of second-order model equations for the motion of particles to evaluate the effects of particle inertia and the crossing trajectories and showed that the predicted results were in good

agreement with the experimental data of Wells and Stock (1983).

The first two-phase calculations in stirred vessels were attempted by Issa and Gosman (1981), and they were subsequently improved by Looney et al (1985) and Politis (1988), in a parallel study to the present work, by adding the drag terms for the particles and including the effect of void fraction on the carrying-phase. They compared their calculation results with the present experimetal results which are discussed in detail in section 3.4.

1.3 Present contribution

It is clear from the preceding section that detailed experimental information of the single and two-phase flows in stirred vessels and of the two-phase flows in ducts fall short of providing a clear picture of the effects of the distributed phase. It was also clear that laser-Doppler velocimetry is a suitable technique for the measurement of such flows within a limited range of uncertainties. The work presented in this thesis is intended to address the problems described above by obtaining laser-Doppler velocity measurements and to propose and use a method of measuring at high concentration, the particular objective being:

1. To develop refractive-index-matching in conjunction with laser-Doppler velocimetry and use it to measure the mean and rms velocities of both phases in liquid-solid flows with high particle volumetric concentration.

2. To obtain detailed measurements of mean and rms velocity of single and two-phase flows in a pipe and around an axisymmetric disc baffle in order to provide useful information on particle behaviour in two-dimensional turbulent high shear flow.

3. To provide detailed single-phase values of mean and turbulent velocity in stirred vessels of various configurations and to quantify the effects of influential parameters such as impeller rotational speed, size and clearance.

4. To obtain measurements of mean and rms particle velocities in two-phase flow

in stirred vessels and to quantify the effects of particle size, density and volumetric concentration on mean flow and the turbulence characteristics.

The experimental data should be in sufficient detail to use as input and boundary conditions for calculation methods and aid their assessment and improvement.

1.4 Thesis outline

The remainder of this thesis has been prepared in three chapters. The following chapter describes the work conducted on the flow in ducts and includes a brief introduction, description of the flow configuration, the experimental technique, and the laser-Doppler velocimetry systems together with assessment of the uncertainties and errors incurred in the measurements. The developement of the refractive-index-matching technique is described and its advantages and disadvantages are discussed. The results of single and two-phase in pipes and baffle flows are then presented and discussed in turn, especially with respect to the particle motion and the effects of particle size. The chapter is closed with a summary of main findings.

Chapter three presents single and two-phase flow measurements obtained in stirred vessels with different impeller geometries and operating conditions. After a short introduction the flow configurations are described and since the measuring technique was virtually identical to that of chapter two, only the modifications and the flow visualisation technique are described and their relevant errors discussed. The results of the single and two-phase flows are then presented and discussed in sections 3.4 and 3.5 respectively. The single-phase results include the flow visualisation, the flow field velocity measurements and the parametric studies. In section 3.5, the particle motion results are present and discussed together with the effects of particle size, density and concentration. In the last part, the most important conclusions of the chapter are summarised.

The last chapter provides a summary of the main findings of this thesis and makes suggestions for further investigations.

Notation used in tables 1.1, 1.2 and 1.3

Cv	Volumetric concentration of particles.
E	Energy spectrum.
Kd	Coefficient of discharge
k	Turbulence kinetic energy.
Re	Reynolds number.
$\overline{U}$, $\overline{V}$, $\overline{W}$	Single-phase mean velocity components.
$\overline{Uf}$, $\overline{Vf}$, $\overline{Wf}$	Liquid-phase mean velocity components.
$\overline{Up}$	Solid-phase axial mean velocity.
u', v', w'	Single-phase rms velocity components.
u'f, v'f, w'f	Liquid-phase rms velocity components.
u'p	Single-phase mean velocity components.
$\overline{V}$ave	Average mean radial velocity.
Vg	Laminar terminal velocity.
Vgt	Turbulent terminal velocity.
$\overline{V}$max	Maximum radial velocity.
Vt	Impeller tip velocity.

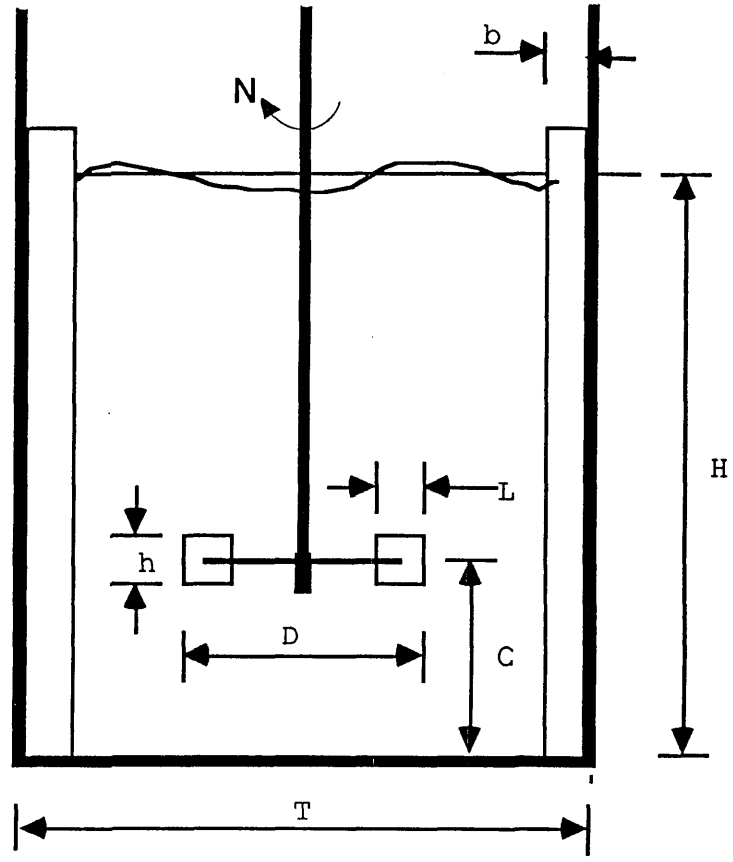

Fig 1.1 Schematic diagram of Rushton type stirred vessel.

TABLE 1.1 PREVIOUS EXPERIMENTAL INVESTIGATION OF THE FLOWS IN STIRRED VESSLS

Authors	Experimental Technique	Working Fluid and Geometry	Quantity Measured	Rotational Speed (rpm)	Main Findings
Sachs and Rushton 1954	Flow visualisation	Water T=292 mm & H=306 mm D = C = H / 4 D : h : L = 1 : 5 : 4 6-blade disc turbine 4 baffles; b = 25.4 mm	$\overline{V}$ and $\overline{W}$ in the impeller stream	100-200	1) $\overline{V}$ profiles flatten out with r and $\overline{V}ave/\overline{V}max$ is independent of impeller speed, but increases with r. 2) $\overline{V}$ and $\overline{W}$ change with respect to the angular position of the blade, so that their maxima are at 45 ¤ and 60 ¤ in front of the blade. 3) Radial mass flow is proportional to speed and increases with r. Total induced flow is the same as the discharge flow.
Aiba 1958	Radioisotope of Cobalt	Water and glycerine T=292 mm & H=279 mm 4 baffles; b = 33 mm	$\overline{U}$, $\overline{V}$ and $\overline{W}$ in the impeller stream and in the bulk flow.	20-150	1) Flow patterns are independent of impeller speed in turbulent flow region. 2) Flow patterns of viscous liquids are dependent on impeller rotational speed in laminar flow.
Cutter 1966	Flow visualisation	Water T = H = 306 mm D = T / 4 D : h : L = 1 : 5 : 4 6-blade disc turbine 4 baffles; b = T/10	$\overline{U}$, $\overline{V}$, $\overline{W}$ and corresponding rms velocities in the impeller stream.	200, 400 and 600	1) The ratio of mean velocity to tip velocity is a function of position in the vessel and the decay of $\overline{W}$ is faster than $\overline{V}$ in the impeller stream. 2) Mass flow increases with r to a maximum and then decreases. 3) The flow in the stirred vessel is far from homogeneous and the length scale of turbulence increases with r. 4) The estimation of energy dissipation gives 20% dissipation in the impeller, 50% in the impeller stream and 30% in the rest of the vessel.

TABLE 1.1 Continued

Authors	Experimental Technique	Working Fluid and Geometry	Quantity Measured	Rotational Speed (rpm)	Main Findings
Cooper and Wolf 1968	Hot - wire anemometry and 2-D and 3-D pitot tubes.	Water T=381 mm & H=508 mm D = 76.2 to 228.6 mm D : h : L = 1 : 5 : 4 6-blade disc turbine 4 baffles	$\overline{U}$, $\overline{V}$ and $\overline{W}$ in the impeller stream and in the bulk flow.	100 - 300	1) $\overline{V}/Vt$ is independent of impeller rotational speed and size in the impeller stream, for geometrically similar turbines and $\overline{W}$ profiles are flatter than $\overline{V}$. 2) Mass flow increases with r, and for 76 mm ≤ D ≤ 152 mm the discharge coefficient is; 0.73 < Kd < 0.89 for water and 0.62 < Kd < 0.77 for air 3) The axial profiles above and below the impeller are flat.
Mujumdar et al 1970	Hot - wire anemometry	Air T=381 mm & H=508 mm D =127 to 152.4 mm 6-blade disc turbine 4 baffles; b = T/10	$\overline{U}$, $\overline{V}$, $\overline{W}$ and corresponding rms velocities in the impeller stream.	600, 725 and 1100	1) Large periodic velocity components corresponding to the blade passage frequency exist at the impeller tip. 2) Uncorrected turbulence intensity, at the tip of the impeller, is much larger than the corrected one. 3) Macroscale is of order of impeller width; 4 - 13 mm. The dissipation scales (small eddies) are in range of 1 - 2 mm.
Nienow and Wisdom 1974	Flow visualisation	1) Water T = H = 290 mm D = 70-210 mm C = T/4 6-blade disc turbine 4 baffles; b = T/10 2) Model of one blade in a water tunnel at 45 ¤ to flow direction.	Observation	180, 420 and 600	1) Confirms the observation of van't Riet and Smith (1973) of the trailing vortices. 2) In the model test, there is a large volume of separation in front and behind the blade at low speed, indicating boundary layer flow, but at high speed there is only separated flow behind the blade and along its face.

TABLE 1.1 Continued

Authors	Experimental Technique	Working Fluid and Geometry	Quantity Measured	Rotational Speed (rpm)	Main Findings
Günkel and Weber 1975	Hot - wire anemometry probe, both fixed and rotating with the impeller	Air T = H = 457 & 914 mm D = C = T/2	$\overline{U}$, $\overline{V}$, $\overline{W}$ and corresponding rms velocities and the power spectra in and around of the impeller and in the bulk flow.	400 and 950	1) The results of the fixed probe were; (a) at tip $\overline{V}$=o.8 Vt, and mass flow increases with r to a maximum and then drops; (b) turbulence in the bulk flow is homogeneous & isotropic. 2) The rotating probe results show that; (a) there are 2 pairs of roll vortices one in front and one behind each blade; (b) $\overline{V}$ changes from 0.25Vt in front of the blade to 1.1Vt behind it; (c) turbulence intensities are between 4% and 16%.
Ito et al 1975	Platinum sphere and electrode probe	An aqueous solution T = 312 mm D = T/3 D : h : L = 1 : 5 : 4 6-blade disc turbine 4 baffles; b = T/10	$\overline{U}$, $\overline{V}$, $\overline{W}$ and corresponding rms velocities and the power spectra in the impeller stream	60, 90 and 120	1) The flow in the impeller stream can not be regarded as homogeneous isotropic flow. 2) One-point double correlation results show that $\overline{vw}$ values are much higher than $\overline{uv}$ and $\overline{uw}$ by an order of magnitude.
van't Riet and Smith 1975	Photographic and pitot tube. Both were rotating with the stirrer	Water T = H = 120 and 440 mm D = C = T/2.5 D : h : L = 1 : 5 : 4 6-blade disc turbine 4 baffles; b = T/10	$\overline{U}$, $\overline{V}$, $\overline{W}$ and pressure in the trailing vortices.	1.0 - 175	1) Vortex axis is independent of Reynolds number, but the angular and circumferential velocities and pressure are are dependent on Re and can be scaled with it. 2) Circumferential velocity increases with the vortex radius to a maximum and then drops. 3) Cavitation starts at low pressure and is dispersed by turbulence 4) Shear rate is about 10 times more than those given in the literature.

TABLE 1.1 Continued

Authors	Experimental Technique	Working Fluid and Geometry	Quantity Measured	Rotational Speed (rpm)	Main Findings
Nishikawa et al 1976	Hot - wire anemometry	Water T=H=150, 300 & 600 mm D = T/2 D : h : L = 1 : 5 : 4 6-blade disc turbine 4 baffles; b = T/10	Energy spectra (E) of u' and v' in the impeller stream and in the bulk flow.	30 to 320	1) The turbulence in the impeller stream deviates from both isotropy and homogeneity at low wavenumber, but it is isotropic in other regions. 2) The ratio of E / length-scale and E/ u' are independent of location, speed and apparatus size.
Reed et al 1977	Laser-Doppler velocimetry, using a frequency tracker processor	Water T = 192 mm D = C = T/3 D : h : L = 1 : 5 : 4 6-blade disc turbine 4 baffles; b = T/10	$\overline{U}$, $\overline{V}$, $\overline{W}$ and corresponding rms velocities in the impeller stream and in the bulk flow.	100	1) The influence of the baffles is not limited to the flow immediately around it. 2) The order of local turbulence intensities is about 100% in the impeller stream, and about several hundred percent around the baffles.
van Molen and Maanen 1978	Laser-Doppler velocimetry, using a frequency tracker processor	Water T=H=120, 290 & 900 mm D = T/3 and C = T/2 D : h : L = 1 : 5 : 4 6-blade disc turbine 4 baffles; b = T/10	$\overline{U}$, $\overline{V}$, $\overline{W}$ and corresponding rms velocities and the power spectra in the impeller stream.	78, 168 & 300 for T=900, 290 and 120 mm respectively	1) $\overline{V}/Vt$ is a function of r for all vessel sizes and the impeller jet is a two-dimensional at 45 ¤ to the impeller plane. 2) Random turbulence is isotropic in the impeller stream and the energy in the smaller eddies is proportional to $\sqrt{T}$. 3) The trailing vortices are dominant up to 1.5 times the impeller radius and the turbulence intensity increases with r up to 2r/D.
Weetman and Salzman 1980	Laser-Doppler velocimetry, two colour system, and strain gauge	Water T= 1220 mm D = C = T/3 6-blade disc turbine 4 baffles; b = T/12	$\overline{U}$, $\overline{V}$ and torque in the impeller stream and in the bulk flow.	----	1) Results show the flow patterns differ significantly when different type of impellers were used. 2) Side flow has a substantially large effect on radial flow impeller and increases the bending load.

TABLE 1.1 Continued

Authors	Experimental Technique	Working Fluid and Geometry	Quantity Measured	Rotational Speed (rpm)	Main Findings
Costes and Couderc 1982	Hot-flim anemometer with limearized output	Water T = 399, 444 and 630 mm D = T/3 and C = T/2 D : h : L = 1 : 5 : 4 6-blade disc turbine 4 baffles; b = T/10	$\overline{U}$, $\overline{V}$, $\overline{W}$ and corresponding rms velocities at impeller tip.	75- 200	1) $\overline{V}$ and $\overline{W}$ velocities are independent of impeller rotational speed and of the vessel size. 2) The coefficient of discharge is 0.97, and is proportional to impeller speed and vessel size. The mechanical efficiency was calculated to be 0.16.
Revill 1982	A survey on pumping capacit y of disc turbine — agitators.				1) The coefficient of discharge is recommended in the range of Kd = 0.75 ± 0.15 for 0.2 < D/T < 0.5 and 0.3 < C/T < 0.5.
Van Doorn 1982	Laser-Doppler velocimetry, using a frequency tracker processor	Water T= H = 266 mm D = 93 mm D : h : L = 1 : 5 : 4 6-blade disc turbine 4 baffles; b = T/9	$\overline{U}$, $\overline{V}$, $\overline{W}$ and corresponding rms velocities in the impeller stream.	100, 200 and 300	1) $\overline{V}$ and $\overline{W}$ decrease with r, but $\overline{W}$ decays faster and that the mass flow increases with r. 2) Local turbulence levels in the impeller stream are high and turbulence is near-isotropic. 3) Dissipation of k is maximum at the blade centre and estimated values from $\overline{W}$ component are higher than that of $\overline{V}$. The errors in estimation are about 65%.
Popiolek et al 1984	Laser-Doppler velocimetry, using a frequency counter processor	Water T = H = 294 mm D = C = T/3 D : h : L = 1 : 5 : 4 6-blade disc turbine 4 baffles; b = T/10	Gated measurements over one degree of impeller rotation of $\overline{U}$, $\overline{V}$, $\overline{W}$ and corresponding rms velocities in and around the impeller.	300	1) Trailing vortices were always present up to 20° behind each blade and they are subjected to erratic motion. The velocities in the vortices were of the order of 0.25 of the tip velocity. 2) Rms velocities measured over 360° of the revolution can be over-estimated by up to 400%. The turbulence is anisotropic, and k=0.19 Vt.

TABLE 1.1 Continued

Authors	Experimental Technique	Working Fluid and Geometry	Quantity Measured	Rotational Speed (rpm)	Main Findings
Keller 1985	Three beams two component laser-Doppler velocimetry using a frequency counter processor	Water T = H = 300 mm D = C = T/3 D : h : L = 1 : 5 : 4 6-blade disc turbine 4 baffles; b = T/10	$\overline{U}$, $\overline{V}$, $\overline{W}$ and corresponding rms velocities in the impeller stream.	100 to 600	1) The $\overline{V}$ velocity profiles are parabolic with maxima at the centre, and that there is no difference between the velocity profiles of baffled and unbaffled vessel. 2) $\overline{V}$ and $\overline{W}$ are approximately independent of impeller speed 3) The coefficient of discharge was calculated for different speeds to be in the range of 0.9-1.02 with an average value of 0.95.
Laufhütte and Mersmann 1985	Laser-Doppler velocimetry	Water T = H = 190 mm D = T/3 D : h : L = 1 : 5 : 4 6-blade disc turbine 4 baffle; b = T/10	u', v' and estimation of dissipation	450	1) The effect of periodicity on turbulence exists up to 1.8 times the impeller radius. 2) The turbulence intensity due to the periodic component is about 1.5 times less than that measured. 3) The estimated values of dissipation in the impeller stream are higer by up to two orders of magnitude than in the bulk flow.
Patterson and Wu 1985	Laser-Doppler velocimetry	Water T = H = 270 mm D = T/3 and C = T/2 D : h : L = 1 : 5 : 4 6-blade disc turbine 4 baffles; b = T/10	$\overline{V}$, $\overline{W}$ and corresponding rms velocities, and estimation of dissipation in the impeller stream.	100-300	1) $\overline{W}$ values are much smaller than $\overline{V}$ by 200%. 2) The turbulence intensity measurements were corrected by 10%, to take into account the effect of periodicity. 3) The distribution of dissipation show a peak at the centre of the impeller blade which is higher by an order of magnitude than the values outside the jet stream.

TABLE 1.1 Continued

Authors	Experimental Technique	Working Fluid and Geometry	Quantity Measured	Rotational Speed (rpm)	Main Findings
Plion et al 1985	Laser-Doppler velocimetry	Water T = H = 445 mm D = T/2.33 and C = T/3 3-blade propeller of pitch of 130 mm.	$\overline{U}$, $\overline{V}$, $\overline{W}$ and corresponding rms velocities in the impeller stream and in the bulk flow	200	1) Kd = 0.19 for the propeller in unbaffled vessel and increased to 0.45 in baffled one. 2) The velocity distribution in an unbaffled vessel is mainly tangential which is turned to a more axial flow near the propeller in a baffled vessel. The turbulence in a baffled vessel is more homogeneous than in an unbaffled one.
Armstrong and Ruszkowjki 1986	Laser-Doppler velocimetry using a frequency counter processor	Water Three type of the impeller were used, Rushton turbine, 45 ¤ pitched turbine and marine propeller.	$\overline{U}$, $\overline{V}$ and $\overline{W}$ around the impeller.	150 to 720	1) The coefficients of discharge were: $0.73 < Kd < 0.80$ for a Rushton turbine $Kd = 0.90$ for a 45 ¤ pitched blade turbine and $Kd = 0.41$ for a marine propeller 2) Flow generated for 45 ¤ turbine has much higher degree of swirl than that of marine propeller.
Yianneskis et al 1987	Laser-Doppler velocimetry using a frequency counter processor	Water T = H = 294 mm D = C = T/3 D : h : L = 1 : 5 : 4 6-blade disc turbine 4 baffles; b = T/10	$\overline{U}$, $\overline{V}$, $\overline{W}$ and corresponding rms velocities in the impeller stream and in the bulk flow.	300	1) The power number obtained from torque measurement was about 4.8±0.1. 2) Flow above and below the impeller was not entirely symmetric and there was a complicated vortical flow structure in the lower ring vortex. 3) Impeller jet is inclined at about 3.5 ¤ and 7.5 ¤ with C=T/2 and C=T/4 respectively. 4) In the impeller region the k values are greater by an order of magnitude than those in the lower ring vortex, and that the turbulence in anisotropic.

TABLE 1.2 PREVIOUS EXPERIMENTAL INVESTIGATION OF TWO-PHASE FLOWS

Authors	Experimental technique	Flow configuration and material of both phases	Quantity measured	Concentration	Main findings
Kay and Boardman 1962	Measurement of time between two fixed location of marked particles	Solid suspension in still liquid (parafine- glass beads) in a cylindrical tube. Particles of 850 μm mean dia.	Particle free fall velocity	Up to 20% by volume	1) $\overline{U}p \approx Vg$ up to Cv = 0.05%, and at 0.5 < Cv < 0.3% viscous interaction occurs and Up >Vg. 2) $\overline{U}p$ to Cv=3%, particle velocity increases further indicating formation of cluster. Above 3% settling occurs and particle velocity decreases with Cv.
Soo et al 1964	Fiber optics for concentration and electric ball probe for mass flow	Horizontal closed loop gas - solid (air-glass) turbulent pipe flow of 127 mm diameter. Particles of 55 μm mean dia.	Concentration, mass flow, $\overline{U}$, $\overline{U}f$ and $\overline{U}p$	Up to 1.4 kg solid suspension	1) Concentration decreases along the pipe diameter from the bottom to the top, while the mass flow decreases. 2) $\overline{U}p < \overline{U}$ in the core region but $\overline{U}p < \overline{U}$ in other regions. 3) $\overline{U}$ and $\overline{U}f$ profiles are similar and take the 1/7 power law shape within the measured range.
Hetsroni and Sokolov 1971	Constant temperature hot-wire anemometry	Horizontal gas-liquid (air-cotton oil droplets) turbulent jet of 25 mm exit dia. Droplets were injected via a constant tank supplier.	$\overline{U}f$ and u'f	Volumetric flow rate ratio of liquid to air were 2.16 to 3.08 x 10-6	1) The time average $\overline{U}f$ velocity profiles can be described as Gaussian and that the spread coefficient decreases with Cv. 2) Liquid-phase turbulence is suppressed, especially in the dissipation region, by about 30% at the centre and 50% in the outer region.
Kramer and Depew 1972	Optical cross-correlation	Upward gas-solid (air-glass) turbulent flow in a vertical pipe of 12.7 and 25.4 mm dia. Particles of 62 and 200 μm mean dia.	$\overline{U}f$ and $\overline{U}p$	Mass loading ratio up to 5	1) Liquid and particle velocity profiles flatten with Cv. 2) The slip velocity decreases with Cv and the rate of reduction is higher with 63 μm particles.

Table 1.2 continued

Authors	Experimental technique	Flow configuration and material of both phases	Quantity measured	Concentration	Main findings
Einav and Lee 1973	Observation	Liquid-solid boundary layer flow in channel. Particles of 30, 50 & 100 μm mean dia.		Up to 6% by volume	1) Migeration of particles away from the wall was observed in the boundary layer.
Birchenough and Mason 1976	Laser-Doppler velocimetry	Upward gas - solid (air - alumina powder) turbulent flow in a virtical pipe of 50 mm dia. Particle of 15 μm mean dia.	Particle velocity	Mass loadind of 0.226 to 1.44	1) Particle velocity decreases and the profiles become flatter with increasing Cv. 2) In the turbulent flow, particle velocities decrease as Reynolds number increases.
Okuda and Choi 1978	Double-flash photographic method	Gas- solid turbulent flow in air nozzels for different type of the particles 1) Polystyrene of 324 to 1095 μm mean dia; 2) glass beads of 775 μm mean dia and copper beads of 545 μm dia.	Particle velocity	------	1) Particle velocity decreases as the size and the density of the particle increases. 2) Particle velocity calculated from frictionless adiabatic flow in covergent- divergent nozzel was in good agreement with measured one.
Theofanous and Sullivan 1982	Laser-Doppler velocimetry	Upward liquid-gas (water-nitrogen) turbulent flow in pipe of 57 mm diameter.	$\overline{U}$, $\overline{U}f$ and the corresponding rms velocities.	Void-fraction of 3.7 to 9.3 x10-5	1) $\overline{U}$ and $\overline{U}f$ profiles are similar up to 3/4 of the pipe radius, but close to the wall $\overline{U}f$ is greater than $\overline{U}$ 2) u'f and v'f are considerably larger than u' and v' respectively due to the presence of the wake behind the bubbles. 3) u'f increases with void-fraction

Table 1.2 continued

Authors	Experimental technique	Flow configuration and material of both phases	Quantity measured	Concentration	Main findings
Lee and Durst 1982	Laser-Doppler velocimetry with amplitude discrimination technique	Upward gas-solid (air-glass) turbulent flow in pipe of 21 mm dia. Particles of 100 to 800 μm mean dia.	$\bar{U}$, $\bar{U}f$, $\bar{U}p$ and corresponding rms velocities	Volumetric concentration up to 0.12%	1) $\bar{U}f$ and $\bar{U}p$ profiles become flatter with increasing the particle size. 2) The particles lag behind the fluid in most of the region except close to the wall where they lead. 3) The slip velocity increases with particle size. There is a free-particle region close to the wall which increases with particle size. 4) u'f is always smaller than u', but u'p is smaller close to the wall and larger in the central regions than u', and that u'f is higher than u'p by a factor of 2.
Modarress et al 1982	Two-colour laser-Doppler velocimetry	Downward gas-solid (air-glass) turbulent flow in a jet of 20 mm exit dia. Particles of 50 and 200 μm mean dia.	$\bar{U}$, $\bar{U}f$, $\bar{U}p$ and correspondig rms velocities	Mass loading ratio of 0.64 equivalent to 0.025% by volume	1) In general, $\bar{U}p < \bar{U}f < \bar{U}$ and that the particles are spread mainly in the core of the jet. The slip velocity of 200 μm particles is larger than of 50 μm. 2) The spread of the air jet in two-phase flow is smaller than that of single-phase one resulting in narrower jet. 3) The air turbulence intensities in two-phase flow are smaller by 10% than the single-phase levels.
Tridimas et al 1982	Laser-Doppler velocimetry	Upward gas-solid (air-glass) turbulent flow in pipes of 22, 25.8 and 31.4 mm dia. Particles of 40 to1000 μm mean dia.	$\bar{U}$, $\bar{U}f$, $\bar{U}p$ and correspondig rms velocities		1) Both $\bar{U}f$ and $\bar{U}p$ are smaller than $\bar{U}$, and the $\bar{U}$ profiles were flatter than $\bar{U}f$ ones. 2) u'f of 200 μm particles were smaller than u'.

Table 1.2 continued

Authors	Experimental technique	Flow configuration and material of both phases	Quantity measured	Concentration	Main findings
Tsuji and Morikawa 1982	Laser-Doppler velocimetry with amplitude discrimination technique	Horizontal gas-solid (air - pellets) turbulent flow in a pipe of 30.5 mm dia. Particles of 200 and 3400 μm mean dia.	$\overline{U}$, $\overline{U}f$, $\overline{U}p$ and correspondig rms velocities	Mass loading ratio of 6.4 equivalent to 0.8% by volume	1) $\overline{U}f$ profiles show asymmerty with the peak above the centreline, and the peak moves upwards with Cv. 2) $\overline{U}p$ profiles are flatter than $\overline{U}f$ so that particles lag behind the fluid in central region and lead close to the wall. 3) u'f is much smaller than u' for 200 μm particles.
Modarress et al 1983	Two-component laser-Doppler velocimetry	Downward gas-solid (air-glass) turbulent flow in a jet of 20 mm exit dia. Particles of 50 μm mean dia.	$\overline{U}$, $\overline{U}f$, $\overline{U}p$ and correspondig rms velocities	Mass loading ratio up to 0.9 equivalent to 0.04% by volume	1) $\overline{U}p > \overline{U}f > \overline{U}$, and $\overline{U}p$ and $\overline{U}f$ increas with Cv. 2) The jet narrows as Cv increases. Also an increase in Cv results in a reduction of the turbulence shear stress. 3) u'p is higher than u' by about 40% at exit, but further downstream u'p< u'f< u' and u'f and u'p are further reduced as Cv increases.
Wells and Stock 1983	Hot-wire anemometry for single-phase and laser-Doppller velocimetry for two-phase flow	Horizontal gas-solid (air-glass) turbulent flow in wind tunnel of 355 mm sides and 2.2 m long. Particles of 5 and 57μm mean dia.	$\overline{U}$, $\overline{U}f$, $\overline{U}p$ and correspondig rms velocities	----	1) When Vgt < u'f then the effect of crossing-trajectories on particle dispersion is negligible; atVgt ≈ u'f the dispersion is reduced by 10% and when Vgt> u'f the dispersion reduces further. 2) The effect of particle inertia is to reduce u'p, so that for 57 μm particles the suppresion is about 30% while for 5 μm particles there is no suppresion.

Table 1.2 continued

Authors	Experimental technique	Flow configuration and material of both phases	Quantity measured	Concentration	Main findings
Nouri et al 1984	Laser-Doppler velocimetry	Horizontal liquid - solid (water - arcylic beads) turbulent flow around axisymmetric disc of, 50% blockage and cone of 25% in a pipe. Diakon particles of 270 μm mean dia.	$\overline{U}$, $\overline{U}p$ and the corresponding rms velocities	Up to 1.5% by volume	1) Particle mean velocity profiles and the single-phase profile are identical for the cone baffle, but with disc baffle the particle profiles are flatter, especially in recirculation zone. 2) The annular jet behind the disc baffle of the two-phase flow is narrower than in single-phase flow. 3) u'p is smaller than u' and u'p is further reduced as the particle concentration increases
Tsuji et al 1984	Laser-Doppler velocimetry with amplitude discrimination technique	Upward gas - solid (air - plastic particles) turbulent flow in a vertical pipe of 30.5 mm dia. Polystyrene particles of 200, 500, 1000 and 3000 μm dia.	$\overline{U}$, $\overline{U}f$, $\overline{U}p$ and correspondig rms velocities	Mass loading ratio up to 5 equivalent to 0.6% by volume	1) $\overline{U}f$ profiles exibite a concave shape at the centre with $\overline{U}f > \overline{U}$ and the $\overline{U}f$ and $\overline{U}p$ profiles are flatter than $\overline{U}$ profile. 2) The slip velocity increases with particle size, but decreases with Cv. 3) u'f increases as Cv increases, and that u'f < u' everywhere for 200 μm particles but u'f> u' for 3.0 mm particles.
Shuen et al 1985	Laser-Doppler velocimetry	Downward particle - laden turbulent flow in an air jet of 10.9 mm exit dia. Particle of 79, 119 & 207 μm mean dia.	$\overline{U}$, $\overline{U}f$, $\overline{U}p$ and the corresponding rms velocities	Mass loading ratio up to 0.66.	1) The rate of decay of centerline particle velocity reduces with an increase in both particle size and concentration. 2) The centreline particle turbulence kinetic energy is considerably reduced with particle size, but increases with Cv.
Tsuji et al 1985	Timing the flight of the particles	Flight of a sphere ball of 5 mm diameter on an inclined flat plate	Translation and angular velocity and the rang of the flight of the ball.	----	1) The comparison of measurements of the range of flight with calculation show the lift coefficient is (o.4±0.1)L where L is nondimentional angular velocity. This result is valid for 550 < Re < 1600 & L < 0.7.

Table 1.2 continued

Authors	Experimental technique	Flow configuration and material of both phases	Quantity measured	Concentration	Main findings
Shuen et al 1986	Laser Doppler velocimetry	Burner gas - liquid (air - liquid methanol) with exit diameter of 5 mm. Droplet size of 105 & 180 μm mean dia.	$\overline{U}$, $\overline{Up}$ and the corresponding rms velocities	----	1) Centreline droplet velocities of larger size are lower than the smaller size, up to 60 diameter downstream of the exit, and then are higher. 2) Normalised droplet profiles of both sizes are identical and higher than the single-phase profile. 3) u'p and v'p are smaller than u' and that they increase with droplet size.

TABLE 1.3 PREVIOUS INVESTIGATION OF REFRACTIVE-INDEX-MATCHING TECHNIQUE

Authors	Flow configuration	Material of solid	Fluid	Matching temp. (°C)	Main findings
Zisselmar and Molerus 1978	Liquid-solid flow in a horizontal pipe of 50 mm diameter.	Glass beads of 53 μm mean dia. as suspended particles and glass as solid boundary	Methylbenzoate	≈ 25	1) $\overline{U}$, $\overline{Uf}$ and the corresponding rms velocities were made by laser-Doppler velocimetry. 2) The turbulence was suppressed in the presence of particles by 12 to 40%, for particle concentration of 1.7 to 5.6% respectively.
Durst et al 1979	Single-phase flow in a horizontal pipe of 50 mm inside diameter.	Solid boundaries made of glass	Light fuel oil+30% by volume of Palatinol C.	26	1) Single-phase velocities were measured in the vicinity of the wall.
Elphick et al 1982	Single-phase flow in rod bundles in a model heat exchanger	Pyrex rods of 12.7 mm diameter.	A mixture of Xylene + 44% by volume of Varsol	20	1) The instantaneous velocities in the flow between the rods were measured by eliminating beam refraction at the interface boundaries.
Yianneskis and Whitelaw 1984	Liquid-solid flow in a horizontal pipe of 25.4 mm diameter	Diakon (Plexiglass) particles of 270 μm mean diameter	Di-butyl phthalate	25	1) $\overline{U}$, $\overline{Up}$ and the corresponding rms velocities were made by LDA up to particle concentration of 10%. 2) Particle velocities were identical to those of single-phase.
Horvay and Leuckel 1984	Single-phase flow in a swirl chamber for three different geometries	Swirl chambers made of Plexiglass.	Tetraline + 40% by weight of the oil of turpentine	25	1) LDA measurements were carried out inside the swirl chamber by eliminating beam refraction at the interface boundaries.
Edwards and Dybbs 1984	Single-phase flow in porous-media, rod-bundlesand inside and above a uniformly distributed roughness in boundary layer plate	Pyrex glass for porous media and the rod-bundles. Glass beads of 3 mm diameter were used for roughness.	Sohio MDI 57 oil plus 28.6% by weight of mineral seal oil, and Dow Corning 550 plus 48% by weight of Dow Corning 556.	23 and 28.1	1) Single-phase velocities were measured in three complex flow geometries using refractive index matching to reduce the refraction at the fulid / solid boundaries.

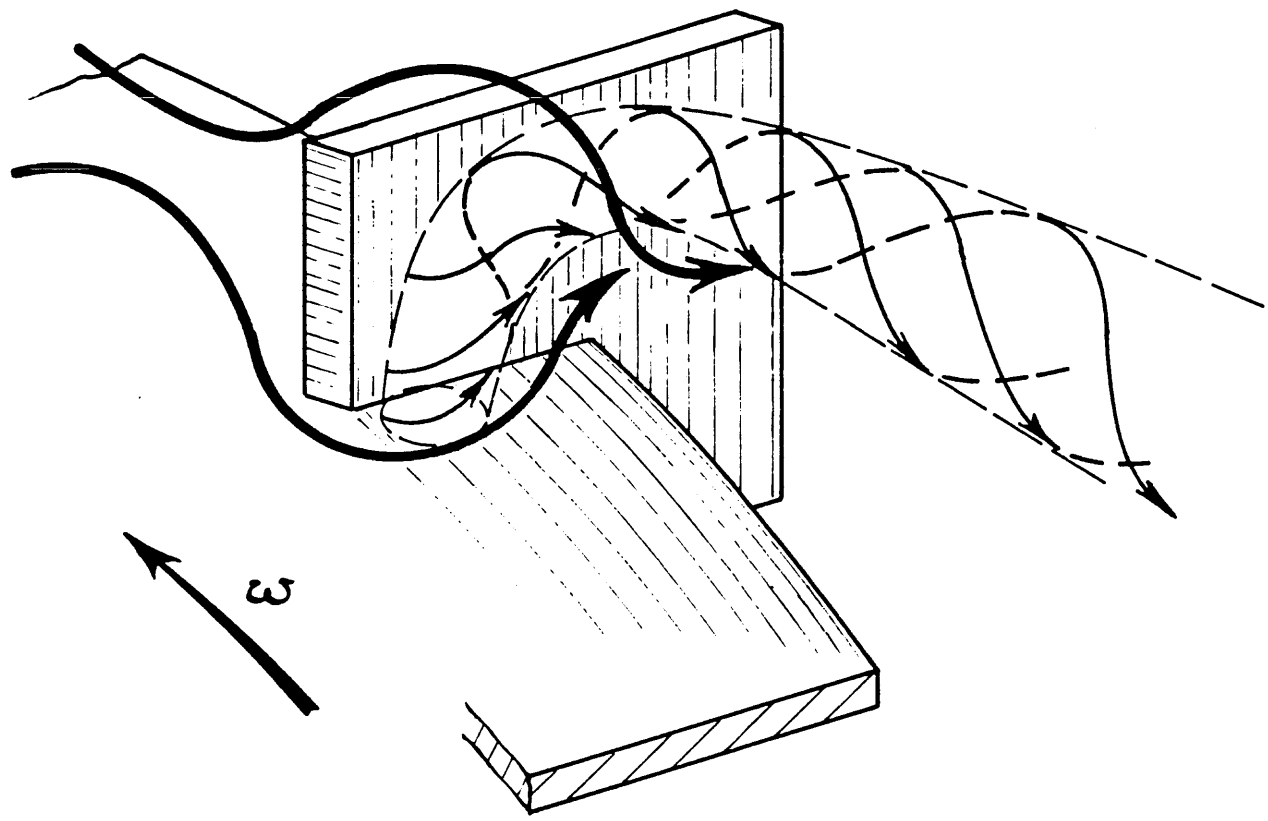

Fig 1.2 Three-dimensional schematic representation of trailing vortex, Popiolek et al (1984).

CHAPTER II

SINGLE AND TWO-PHASE FLOWS IN DUCTS

2.1 Introduction

This chapter describes experimental investigations of single and two-phase flows in a pipe and around an axisymmetric disc baffle with 50% area blockage placed in a vertical pipe. Laser-Doppler velocimetry was employed to measure the mean and turbulence velocity characteristics. A refractive-index-matching technique was developed to enable the measurement the velocities of suspended particles at high particle concentrations.

The following section gives details of the flow configurations. The laser-Doppler velocimetry and refractive-index-matching techniques are described in section 2.3 together with estimates of the errors and uncertainties incurred in the measurements. Sections 2.4 and 2.5 present and discuss the results of the single and two-phase flows respectively in the pipe and around the baffle. Finally, a summary of main findings is given in section 2.6.

2.2 Flow Configurations.

The measurements presented in sections 2.4 and 2.5 of this chapter were made in a vertical pipe of 25.4 mm diameter (D_p) and around a disc baffle placed centrally in the pipe. A schematic diagram of the closed circuit pipe rig is shown on figure 2.1. The working pipe section was manufactured from a square cross-sectioned block of acrylic plastic (Perspex) with external surfaces made flat to minimize the effect of refraction of the laser beams at the air/Perspex interface. The transparent test section was placed 45 pipe diameters downstream of a constant head tank, and the mean flow in the test section can be considered to be fully-developed (e.g. see Schlichting, 1955). The fluid was circulated by a centrifugal pump and the supply and discharge tanks were constructed so as to prevent settling of particles. The baffle is similar to that of Taylor and Whitelaw (1984) and Nouri et al (1984), and the forebody shape of the baffle was a disc of 45 degrees inclined angle

CHAPTER II

with 50% area blockage. The baffle geometry together with the co-ordinate system adopted and the location at which the measurements were taken are illustrated in figure 2.2 (a), and figure 2.2 (b) shows the photograph of the test section with the baffle placed in the pipe. The baffle was positioned centrally by four radial pylons abutting on a sting upstream of the baffle. The pylons were plates of streamlined shape, 10.4 mm long, 1.5 mm thick, and 6.35 mm wide, and were placed 40 mm upstream face of the baffle disc plane.

The working fluids were water and a mixture of oil of turpentine and 31.8% by volume tetraline (tetrahydronaphthalene). This mixture was chosen as its refractive index is identical to that of Diakon particles (1.489) at a temperature of 25.2 °C. The reasons for selecting the turpentine and tetraline mixture are given in detail in subsection 2.3.2. There were sufficient micron-size contaminant particles, which were suitable for use as scattering centres, suspended in both fluids so that seeding of the flow was not necessary.The flow conditions for the water and mixture pipe flow and mixture baffle flow are summarised in table 2.1 bleow.

The mass flow rates listed in table 2.1, were obtained by integrating the profiles of the axial mean velocity using equation (2.1). The integration was carried out using linear interpolation between the measured velocity values.

$$Q_{ap} = 2\pi \rho \int_0^R \overline{U}.\, r.\, dr \qquad (2.1)$$

The bulk velocity was calculated from the relation $Q_{ap}=\pi\rho V_b D_p^2/4$. The annular bulk velocity at the trailing edge of the baffle can be obtained either from expression like $V_\sigma=V_b/(1-\beta)$ where β is the area blockage presented by the baffle, or by integrating the axial profile of mean velocity at the trailing edge of the baffle. The values given in the table 2.1 were obtained from the former expression; values calculated using the second method were similar to within 1.5%. The Reynolds numbers are based on the bulk velocity and the pipe diameter (i.e. $Re=V_bD / \nu$ where ν is the kinematic viscosity of the fluid). Also, the

values of the ν given in table 2.1 for the mixture was measured by a viscometer and results are presented in sub-section 2.3.2. The flows of water in the pipe, of mixture in the pipe, and of mixture in the baffled pipe are hereafter referred to as case 1, case 2, and case 3 respectively.

Table 2.1 Flow conditions

	pipe flow-water case 1	pipe flow-mixture case 2	baffled flow-mixture case 3
Density, ρ, (kg/m^3)	1000	894	894
Kinematic viscosity, ν, (m^2/s x 10^{-6})	1.0	1.63	1.63
Bulk velocity, V_b, (m/s)	2.33	2.45	1.89
Annular bulk velocity, V_o, (m/s)	----	----	3.78
Reynolds number, Re	59,200	38,200	29,500
Mass flow rate, Q_{ap}, (kg/s)	1.18	1.11	0.85

Spherical acrylic plastic (Diakon) particles were used as the dispersed-phase. Diakon and Perspex are the trade names for the particles and sheet/block forms respectively of polymethylmethacrylate acrylic plastic. The density of the particles, ρ_p, was 1180 kg/m^3. The particle size range used in the case 1 and case 2 flows was 100-500 μm, with a mean diameter, d_p, of 272 μm (manufacturer's specification). In the flow of case 3, particles were sieved in order to reduce the size range and the mean value was obtained from a sample of 500 particles whose size were measured under a microscope. The size range of 240-400 and 590-730 μm with mean diameters of 310 and 665 μm respectively

were used in case 3 flow. A useful parameter to characterise particle inertial effects is the particle response time which is defined (Wells and Stock, 1983) as

$$\tau_p = (d_p)^2 \{[2\rho_p / (\rho-1)] / (36 \nu)\} \quad (2.2)$$

Since the fluid density (ρ) is much greater than unity the above equation can be written as

$$\tau_p = (d_p)^2 \rho_p / (18 \mu) \quad (2.3)$$

where μ is the dynamic viscosity of the fluid. A corresponding characteristic response time for the flows (τ_f) can be defined in terms of the pipe diameter and bulk velocity ($\tau_f = D_p/V_b$) in the flows of cases 1 and 2, and of the baffle diameter and annular bulk velocity ($\tau_f = D_b/V_o$) in case 3. The terminal velocities of the particles in the Stokes law region and in the turbulent region, based on drag and gravity considerations, are estimated from the expressions (e.g see Kay and Nedderman, 1985).

$$V_{gs} = (d_p)^2 (\rho_p-\rho) g / (18 \mu) \quad (2.4)$$

and

$$V_{gt} = \{\sqrt{[4 (d_p) (\rho_p-\rho) g / (3 \rho C_d)]} \} \quad (2.5)$$

where g is the gravitational acceleration and C_d is the drag coefficient taken as 0.44 in this case (the reasons for the selection of this C_d value are given in detail in section 2.5). Estimates of characteristic response times and terminal velocities of the particles in each flow are given in table 2.2 and it can be expected that the particles will follow the fluid flow faithfully, except for the particles of 665 μm diameter in case 3, as their response time is about four times higher than that of the flow.

The optical quality of the particles was examined using a microscope and the observations made are described in subsection 2.3.2.

CHAPTER II

Table 2.2 Particle characteristic parameters

	Flow investigated			
	case 1	case 2	case 3	
Flow response time, τ_f, (ms)	11	10	4.7	4.7
Particle mean diameter, (μm)	272	272	310	665
Particle response time, τ_p, (ms)	5	3.3	4.5	20
Time scale ratio, (τ_p / τ_f)	0.45	0.33	0.96	4.2
Particle terminal velocity, V_{gs}, (mm/s)	7.3	7.9	10.0	47
Particle terminal velocity, V_{gt}, (mm/s)	40	51	54.0	80

2.3 Measurement Techniques and Procedures

2.3.1 Laser-Doppler velocimetry

The principles and techniques of laser-Doppler velocimetry, hereafter referred to as LDV, are well documented in a number of texts as, for example, those of Durst, Melling and Whitelaw (1976), Drain (1980) and Adrian (1983) and so only the main features of the technique and of the present system in particular are discussed here. The use of the LDV is preferred because of its linear response to single velocity components and since direct velocity measurements can be made without introducing probe disturbances to the flow.

The amplitude of LDV signals depends on the laser power and on the properties of the photomultiplier (PM) used in the detection optics. Furthermore, the amplitude and modulation depth of LDV signals depend on the size of the scattering particles (Farmer, 1972 and Robinson and Chu, 1975), the optical properties of the particle material (Stümke

and Umhauer, 1978), the size and the location of the receiving aperture (Robinson and Chu, 1975), the wavelength of the laser radiation, and the angle between the two incident light beams. These parameters were kept constant throughout the experiments, except for the size of the scattering particles.

When a particle crosses the beam intersection volume in a fringe-type (dual-beam) anemometer, the laser light is scattered because of diffraction, reflection, and refraction of the light beams. As the size of the particles increases, diffraction becomes progressively negligible in comparison to geometrical scatter (Van de Hulst, 1957 and Hodkinson and Greenleaves, 1963), and signal strength increases considerably so that the scattered light intensity is proportional to the sixth power of the particle diameter (Durst, 1982). Two particle sizes were used in the present studies, the first were the micron-size contaminant particles which follow the fluid motion and were used to measure the single-phase velocity characteristics, and will be referred to as small particles. The second type of the particles were the transparent plastic particles with diameters in the region of 100-800 μm; these particles constituted the dispersed (solid)-phase and are referred to as large particles. Such small and large particles result in signals, at the output of the photomultiplier, like those shown in figure 2.3 where $I_{p,l}$ and $I_{p,p}$ are the pedestal (d.c.) components of the scattered light intensity of the small and large particles signals respectively and $I_{m,l}$ and $I_{m,p}$ are the corresponding a.c. component modulations. It is possible by means of amplitude discrimination to differentiate therefore the small particles from the large ones to measure the particle velocities and to link each velocity with a particle size range since $I_{p,p} >> I_{p,l}$ and $I_{m,p} > I_{m,l}$. But this possibility can only be realised to a limited extend since a small error in recognition can lead to a large error in one of the two probability density distributions, as shown by Kliafas (1985).

It is possible, however, to detect the large particle signals (high intensity) by reducing the photomultiplier sensitivity or by reducing the amount of light incident upon the photomultiplier cathode by means of an adjustable aperture (iris) diaphragm (Robinson and Chu, 1975) to a level low enough so that no signals will be detected from the small

particles. In this way the velocity of the large particles can be measured without error. For the liquid-phase measurements a technique was examined and is described in detail in subsection 2.3.2, in which the scatter from the large particles may be eliminated to allow the measurements of the small particles in the presence of the large ones and to permit the measurement of the velocity of the large particles through dense suspensions of solids.

LDV Optical System

The LDV was operated in the dual-beam (fringe) forward- scatter mode. The optical arrangements are shown on figure 2.5. A 5 mW helium-neon laser was used and the laser beam was focused by a plano-convex lens (L_1) onto a rotating radial diffraction grating (Technisch Physische Dienst, type H), where it was diffracted into the zero-order and pairs of higher order beams. The rotation of the diffraction grating provided a frequency shift between the diffracted beams. The two first order beams, in which approximately 60% of the power of the incident beam was transmitted,were collimated by a plano-convex lens (L_2) and then focussed by a second plano-convex imaging lens (L_3) to form the measuring volume. The best uniformity of the fringe spacing (d_f) and the smallest size of the measuring volume occur when the two first order beams intersect at their waist. The measuring volume shape is then ellipsoidal with its dimensions defined at the e^{-2} level of intensity as described below.The minor and major axis diameter are:

$$b_x = b_s / \cos(\phi) \tag{2.6}$$

$$b_y = n\, b_s / \sin(\phi) \tag{2.7}$$

where $b_S = 4 \lambda f_2 f_3 / (\pi b_o f_2)$, n is the refractive index of the fluid medium, and ϕ is the half angle of the intersection beams. The fringe spacing (d_f), the number of fringes (N_{fr}), and the magnification (M), are given by:

$$d_f = \lambda / 2 \sin(\phi) \qquad (2.8)$$

$$N_{fr} = b_x / d_f \qquad (2.9)$$

$$M = b / a \qquad (2.10)$$

On the collecting side of the optical system, the two first order beams were blocked by a mask and the light scattered by the particles from the measuring volume was then focused onto a pinhole, located in front of a photomultiplier (EMI 9815). The collecting lens (L_4) was equipped with an iris so that the amount of scattered light incident on the photomultiplier could be controlled. The main features of the optical arrangement are shown on table 2.3. The equation relating the Doppler frequency to the velocity of the large particles tends towards the universal equation of LDV for single-phase (small particle) measurements when the ratio of the distance of the measuring volume from the photomultiplier to the particle radius is large and the beam crossing angle is small (Durst and Zare, 1975). This was so in the present work; as for example for the 665 μm diameter particles, this ratio was of the order of 1000.

The mean and rms velocities of the small particles (single-phase) for all flow cases were measured first with the iris fully open. Then the photomultiplier voltage was reduced and the iris was partially closed so that no signals corresponding to the small particles were detected by the photomultiplier. The Diakon particles were then inserted into the the flow and the signals generated were detected and the corresponding mean and rms velocities were measured. In the flows of cases 2 and 3, where refractive-index-matching was employed, the light was scattered from the air-inclusions inside the large particles. The maximum particle volumetric concentration (C_v defined as the ratio of volume of particles to the volume of fluid) through which the velocity measurements were possible, were 0.75, 14.0 and 8.0 percent for cases 1, 2, and 3 respectively.

CHAPTER II

Table 2.3 Characteristics of the optical system

Laser power, mW	5.0
Laser wavelength, (λ), nm	632.8
Laser beam diameter at laser output, (b_o), mm	0.65
Laser beam diameter at the measuring volume, (b_s), mm	0.50
Focal length of lens L_1, (f_1), mm	60.0
Focal length of lens L_2, (f_2), mm	300.0
Focal length of lens L_3, (f_3), mm	200.0
Collecting optics magnification, (M)	2.25
Half-angle of beam intersection in air, (ϕ), degrees	8.85
Intersection volume diameter at e^{-2} intensity, (b_x), μm	50.0
Intersection volume length at e^{-2} intensity, (b_y), μm	433.0
Fringe separation (line-pair spacing), (d_f), μm	2.045
Number of stationary fringes in measuring volume, (N_{fr})	25
Frequency-to-velocity transfer constant, ms^{-1}/ MHz	2.045
Diffraction grating:	
Number of line pairs	16384
Spacing of the line pairs, μm	6.0
Long term stability, percent	0.1
Short term stability, percent	0.2
Frequency shift, MHz	$\pm$2.5

The transmitting and receiving sections of the LDV optical system were mounted on a traversing mechanism that could be translated in three orthogonal directions to scan

the whole flow field. The effects of the refraction of the laser beams at the curved optical boundaries were taken into account in the calculation of the measuring volume locations, and the necessary corrections were applied.

LDV signal processing system

A purpose-built frequency counter (described by Founti and Laker, 1981) was used for all measurements presented in this chapter. The signal output of the photomultiplier was amplified and band-pass filtered in the range of 0.5 to 20 MHz (Harwell signal conditioner model 91-2151-216) to remove the signal pedestals and high frequency noise; a second filter unit with fine high-pass filter adjustment (Krohn-Hite, model 3200) was occasionally used in series with the Harwell instrument.

The conditioned signal was fed to an oscilloscope (HP 180A) for display and to the input of the frequency counter. The frequency of a Doppler signal was measured by timing of the duration of the signal burst over a specified number of cycles by a high frequency clock. The measurements reported here were made using 16 cycles of each burst. Two threshold levels were used in the counter to discriminate the Doppler burst signals from the noise, and the signal timing would then be activated only if the signal amplitude exceeded both levels. An additional validation was imposed by comparing the frequency registered from the signal during 8 cycles, to that measured over the total number of cycles (16) and if the difference exceeded a preset value (0.19% of the measured frequency) then the measurement was rejected. This was done to reduce the possibility of measuring noisy Doppler bursts (Heitor et al 1984). A schematic diagram of the processing system is shown in figure 2.4.

The frequency counter was interfaced to a microprocessor (APPLE IIe) where the binary-coded decimal values generated by the counter were processed to yield decimal frequency values. The individual Doppler frequencies were processed to yield ensemble-averaged mean and rms velocities which in steady flow correspond to time averaged quantities. The data processing software could be used as filter to reject any

obviously erroneous data . Care was taken when such filtering was applied, so that the useful information was not rejected. In the present work the data rejected had a difference in frequency of an order of magnitude lower or higher than the majority of the data and the number of the samples rejected did not exceed 0.6% of the total sample size.

2.3.2 Refractive-index-matching technique

It was mentioned above that the amplitude discrimination technique can be used to observe large particles and it may be possible with an interferometric technique such as that of Durst and Zare (1975) to identify particles without error. However, the ability to measure in the presence of the large particles which block the laser beams and the light scattered from the measuring volume depends on the particle concentration, C_v, the difference between the liquid and solid refractive indices, Δn, the depth of field through which the beams have to travel in the flow, D_f, and the ratio of the particle diameter, d_p, to that of the laser beam. The smaller Δn, d_p, and D_f are the larger the concentration through which the beams can penetrate. In order to overcome these limitations and maximise the value of C_v for which measurements could be made, a technique based on matching the refractive indices of the carrier liquid to that of the dispersed particles was used and is presented in detail in this section .

In principle, by matching the refractive indices of continuous and discontinuous phases, the scatter at the solid/liquid interfaces can be eliminated and the light scattered from the solid particles at the laser wavelength is eliminated. The liquid-phase velocities can then be measured from the signals originating from the non-matched micron-size contaminant particles in the presence of the large particles. Subsequently, the large particle velocities can be measured by inserting a small number of unmatched large particles and identified by using the amplitude discrimination technique and thus the measurements of both phases can be performed at high particle concentrations. In order to develop the technique and to examine to what extent the above objectives could be achieved, a number of experiments were carried out.

CHAPTER II

First a working fluid with suitable properties was chosen. A mixture of tetraline and oil of turpentine, as suggested by Horvay and Leuckel (1984), was found suitable because its kinematic viscosity is close to that of water so that turbulent flow can be achieved easily. Also, the refractive index of the turpentine is below that of the acrylic plastic at a temperature of about 25°C and that of tetraline is higher so that the refractive index of the mixture can be easily made the same as that of acrylic plastic at near-ambient temperatures by varying its composition. Also the toxicity of both liquids is acceptably low. However, tetraline is a half organic liquid and would attack the acrylic materials especially when they are under stress; this was overcome by annealing all acrylic parts of the test section and the particles at 95 °C for 24 hours in order to releave the hidden stresses.

The procedure of annealing of acrylic materials was to heat the acrylic block in a temperature controlled oven to 95 °C at a rate of about 10 - 12 °C per hour. Once the annealing temperature has been reached, the block was maintained at the temperature for 24 hours, and then cooled at the same rate as it was heated, until the oven temperature was ambient. A list of important properties of tetraline and turpentine are provided in table 2.4 below.

Table 2.4 Properties of tetraline and turpentine at 20°C

	Tetraline	Oil of turpentine
Density, (kg/m^3)	967-970	855-868
Kinematic viscosity, ($m^2/s \times 10^{-6}$)	2.2	1.6
Refractive index	1.546	1.467-1.470

CHAPTER II

Properties of fluid and solid

Two types of measurement were carried out to determine the refractive index characteristics of the mixture. In the first, a Perspex rod of 12.7 mm diameter was placed in a temperature controlled bath containing 5 liters of the mixture of tetraline and turpentine with volumetric composition (C_m) of tetraline of around 31%. The change in composition was achieved using a graduated container of an accuracy of 0.001 liters which gives an accuracy of better than 0.02% in C_m. The temperature of the mixture was varied until a laser beam passed through the mixture and the edge of the rod without deflection. The deflection was measured on a graticule placed at a distance 3 m from the rod and zero deflection was found to correspond to C_m=31.65% at 25 °C: at the same temperature, C_m=31.6% and 31.7% led to deflection of 0.5 mm. With zero deflection of the laser beam, the outline of rod could be seen by at a close distance due to the difference in wavelength of the laser and white light. The second type of the measurement made use of a refractometer (Bellingham and Stanley, model ABBE 60) and, as in the measurement described above, the temperature of the liquid was controlled to within ±0.02 °C. Figure 2.6 quantifies the influence of temperature on the refractive index of two concentrations of tetraline for sodium light (λ=589.6 nm) and also allows comparison with results for the Helium-Neon laser light (λ=632.8 nm). The variations of the refractive indices of Diakon and Perspex are also shown on figure 2.6 and intersect those of the two liquid mixtures at temperatures which can conveniently be arranged in the flow equipment. The variation of refractive index is shown as a function of mixture composition and for five different temperatures on figure 2.7. The variation of the refractive index is proportional to the mixture composition and the constant of proportionality is the same for all five temperatures measured, $\partial n/\partial C_m = 7.92 \times 10^{-4}$. Near the operational temperature (25 °C), the refractive index of the mixture varies from 1.4870 at 30% volume concentration of tetraline to 1.4951 at 40% volume concentration of tetraline.

The kinematic viscosity of three mixtures of tetraline and turpentine, with C_m=30, 31.65 and 40%, was measured as a function of temperature with a standard viscometer

(B.S. 188) whose accuracy was evaluated by measuring the viscosity of distilled water at 20.0 °C and 25.0 °C and shown to be accurate within 0.2%. The results are shown on figure 2.8 and, within the measured range, take the form of straight lines. The variation of kinematic viscisity with C_m is also shown to be nearly linear and at 25 °C has a slope of 3.7×10^{-3} m^2/ s: the corresponding slopes at 22 °C and 27 °C are 4.53 and 3.38×10^{-3} m^2/ s respectively.

The quality of the particles was examined by visual inspection under a microscope. The sphericity of the particles was observed to be better than around 80% and surface irregularities were very small. Inspection of particles when immersed in a liquid of similar refractive index revealed the presence of inclusions (air bubbles, voids, etc.). The size of these inclusions was around 0.2-0.5 of the particle diameter and about 15% of the particles had such inclusions. It was evident that the air / vapour trapped in the inclusions would limit the extent to which refractive-index-matching would render the particle transparent to laser light. As a consequence, measurements of the liquid-phase velocities in two-phase flow could not be made in the presence of these unmatched voids and only the velocity of the large particles could be measured, since the Doppler signals produced by these inclusions have amplitudes much larger than those obtained from small contaminant particles because the difference in indices of air and the mixture is high, i.e. $\Delta n \approx 0.49$. In addition, the degree of the transparency that can be achieved was restricted by the presence of these inclusions and the maximum particle concentration through which measurements could be made was limited.

Particle arrival rate

Measurements of the rate of particle arrival through the measuring volume of the LDV were undertaken to assess the maximum particle concentration with which useful velocity measurements could be obtained. They were carried out with the velocimeter described in subsection 2.3.1. The Doppler bursts were counted by this arrangement with a digital counter (TSA 663612) controlled by the trigger output of an oscilloscope

(HP-180A), so as to count each Doppler signal once only and to operate with a preset discrimination level. The particles and the mixture were contained within a temperature controlled tank with sides 178x178x203 mm and fabricated from clear Perspex. The particle concentration, the photomultiplier voltage and the mixture temperature were variables and the results are presented on figure 2.9 to 2.12.

The variations of the rate of arrival of Doppler bursts with temperature and photomultiplier voltage are shown on figure 2.9. In the absence of Diakon particles the signals are due to the small particles present in the liquid. The data rate for the liquid alone is shown as a dotted line on the three figures and is zero with the 900V photomultiplier voltage, figure 2.9 (a). At temperatures displaced from that at which the refractive indices of particles and mixture are matched at 21.21 °C, the larger concentration of particles that can be detected by photomultiplier has the effect of reducing the data rate in the measuring volume as a consequence of beam attenuation: where the matching is most effective, the data rate corresponding to the inclusions in the particles alone reaches a maximum of around 0.18 and 0.3 for C_v=0.2 and 0.5% respectively at the 900V photomultiplier voltage. The ratio of these data rates does not correspond to that of the two particle concentrations because of the attenuation of light by air bubbles in particles away from the measuring volume. An increase in the photomultiplier voltage increases the data rate partly because the number of particles observed increases due to the increased number of voids observed, but also because some of the small particles in the liquid are also observed. With the present arrangement, it is not possible to distinguish the small particles from the large ones but, with the photomultiplier voltage suitably depressed or with the light intensity incident on the photomultiplier sufficiently reduced by means of a variable aperture (iris) placed in the scattered light path, only the air bubbles in the larger particles are detected and measurement of the particle velocity characteristics is possible with the concentration of 0.5%. The results of figure 2.10 show that this concentration can readily be extended to 1.4%.

Similar results were obtained with different concentrations of tetraline and

turpentine and are shown on figure 2.11 and 2.12. The same conclusions are supported by these data and, in addition, it is evident from figure 2.12 that the maximum particle concentration can be extended to around 2.0% before the data rate falls due to the light attenuation by the higher concentrations of voids. The results of figures 2.9 and 2.11 also show a small displacement from matching temperature results in a large reduction of the data rate, which is more evident with higher particle concentration, for the resons metioned above: a change of 0.03 °C from the matching temperature causes a reduction of the data rate of up to 10%. This implys that a good control of the temperature, with stability of better than ±0.03 °C, is required in order to make accurate velocity measurements at high particle concentration.

The refractive-index-matching technique was used to measure solid-liquid flows in a vertical pipe and in a stirred reactor vessel with diameters of 25.4 mm and 294 mm respectively and the maximum particle volumetric concentrations for which velocity measurements could be obtained were 14% and 2.5% for the pipe and stirred vessel respectively. For higher concentrations, the Doppler signal-to-noise ratio was unacceptably low. The corresponding maximum concentrations of particles for the same flow of particles suspended in water, were 0.75% for pipe and 0.02% for the stirred vessel, i.e. an increase in the particle concentration of about 20 and 125 times can be achieved in the pipe and in the vessel respectively when the matching technique is used.

The refractive-index-matching technique is also very useful in eliminating laser beam refraction at the transparent test section surfaces, such as the pipe wall and stirred vessel walls, baffles and impeller. A further test was therefore carried out to explore the accuracy and to assess any limitations of this technique when it is used for single-phase flow measurements in a complex geometry (such as flows between impeller blades, in curved bends, rod bundles, porous media, etc.). The arrangement shown schematically on figure 2.13 was set up, in which a series of rod bundles was arranged so that both laser beams passed through the edges of the three rod bundles. This rod bundle was chosen as it is far more severe test of the technique than can be expected in the stirred vessel and pipe

test sections. Axial velocities of an air jet of 10 mm exit diameter (D_e) were then measured at different axial locations with and without the obstruction of the laser by the rod bundles. The reference radial (i.e. zero position) location was fixed when the rod bundles were not in the path of the beams and was not changed throughout the experiment. The results of the mean and the rms axial velocity measurements are presented in figure 2.14. The profiles are identical for both cases implying no displacement of the measuring volume when the beams pass through the rods and thus no correction for the position is necessary. Also the quality of the signals (signal-to-noise ratio and the visibility) was the same in both cases. The results imply that the uniformity of the fringe pattern and spacing was unchanged when the beams go through such a series of severely curved surfaces. The technique is therefore a useful tool for both two-phase and single-phase (complex geometry) flows. The present technique has been adopted for use in complex geometries, for example the flows in the inlet ports of diesel engines as reported by Yianneskis et al (1987).

2.3.3 Error sources and measurement uncertainties

The main sources of errors and uncertainties involved in the present study are Doppler broadening, bias effects, statistical error and positional error. A brief analysis of their effect on the measurements is given below.

Doppler broadening

Broadening of the Doppler frequency spectrum can occur mainly because of mean velocity gradient, and the small scale fluctuations within the measuring volume. Finite transit-time broadening effects are significant in systems with a frequency domain processor such as a tracker, but not with counters as used in present study. Full accounts of these error sources are given by Durst et al (1976) and so only estimates of the errors for the anemometer used are given.

Velocity gradient broadening occurs when a finite size measuring volume is placed along a steep velocity gradient and results in broadening and sometimes skewing of the

probability distribution. The error in the mean and rms velocities can be estimated according to procedure described by Melling (1975) as

$$\text{Error in mean velocity} \approx 0.5\,(d_y / 4)^2\,(\partial^2 \overline{U} / \partial y^2) + \text{---} \qquad (2.11)$$

and

$$\text{Error in rms velocity} \approx (d_y / 4)^2\,(\partial \overline{U} / \partial y)^2 + \text{---} \qquad (2.12)$$

Thus the error in both mean and rms depends on the measuring volume size and on the local velocity gradient. In the present study such errors were minimized by reducing the size of the measuring volume and the maximum errors in the rms velocity, i.e. in the regions of the steepest non-linear gradient, were calculated to be about 0.3% and 3.0% of the bulk velocity for the pipe and baffled pipe flows respectively. The corresponding errors in the mean velocity were about $10^{-4}\,V_b$ and $7 \times 10^{-4}\,V_b$.

The broadening due to the small scale velocity fluctuation in the measuring volume is discussed extensively by George and Lumley (1973) and is significant when the size of the eddies is small compared with the measuring volume size. An accurate estimation of this effect is difficult, but it was suggested by Melling (1975) that the magnitude of this error can be expected to be comparable to that due to velocity gradient broadening.

Bias effect

Velocity bias effects can be significant in turbulent flow measurements when the velocity histograms in LDV systems are constructed using ensemble-averaging of data obtained from individual-realisations. The biasing is towards the higher end of the velocity range, since the average number of particles crossing the measuring volume is higher during the period when the velocity is fast, and vice versa (McLaughlin and Tiederman, 1973). A one-directional correction for biasing effects was suggested by McLaughlin and Tiederman and showed that the errors are negligible for turbulence intensities up to 15%, but for turbulence intensities around 40% an error of about 10% in the mean velocity could

be expected. Dimotakis (1976) suggested that the ensemble-averaging should be made by weighting the frequency measurement with the time of residence of the particles in the measuring volume. Durao et al (1980) showed that the time interval between the particles is shorter at higher velocities and introduces a bias towards the higher velocities, but the errors estimated were much less than those observed by McLaughlin and Tiederman. They also suggested that if the sampling time is larger than the particle arrival time then the velocity bias would be minimized. Comparison of the suggestion of Dimotakis and Durao et al was reported by Vafidis (1986) who showed that the maximum difference in mean and rms velocities were 2% and 5% respectively in regions of high turbulence intensity. Similar errors can be expected to be present in this study. Furthermore, Durao and Whitelaw (1978) showed that an opposite bias effect to that of McLaughlin and Tiederman may occur due to photodetector integration and the use of finite discrimination levels: these effects tend to reduce the signal visibility as the velocity increases and to reduce the overall bias effect.

The use of a band-pass filter can be another source of velocity bias in highly turbulent flow if the measured Doppler frequency lies outside the bandwidth of the filter. The bias can go towards either side of the velocity range depending on relative position of velocity probability distribution to the filter characteristics curves. In the present study a band-pass filter (Harwell model 91-2151-216) with frequency range from 0.5 to 20 MHz was used. The Doppler frequency encountered in all the flow cases was well within the filter range and the setting of low and high pass filter was checked at each measurement point in all flows.

Counting ambiguity and statistical errors

All frequency counting systems suffer an inherent error of ±1 clock count ambiguity. The relative timing error is given by Durst et al (1976) as

$$\varepsilon_r = f_D / (f_\tau . N_{ph}) \qquad (2.13)$$

where f_D is the Doppler frequency, f_τ is the clock frequency which is 100MHz for the present counter, and N_{ph} is the number of cycles of zero crossing, which is 16 cycles for the present system. In the range of Doppler frequencies encountered in this study the maximum frequencies were of the order of 5 MHz which gives a maximum counting error of about 3.125 kHz. This error corresponds to a negligible error in velocity of about 0.006 m/s or around 0.3% of the bulk velocities of the flows considered in this chapter.

Statistical errors can be introduced due to the finite sampling size on both mean and rms velocities and can be estimated within a cetain confidence level according to Yanta (1973) as

$$\text{Error in mean velocity} = Z_c \, (N_s)^{-0.5} \, (u' / \bar{U}) \qquad (2.14)$$

and

$$\text{Error in rms velocity} = Z_c \, (2 N_s)^{-0.5} \qquad (2.15)$$

where Z_c =1.98 and 2.58 for 95 and 99% confidence levels, and N_s is the number of samples. The error in the mean depends on the turbulence intensity and, in the present study, typical sample sizes taken were 3000 and 2000 for single and solid-phase respectively so that the corresponding errors in rms velocity are 2.5 and 3.2% for 95% confidence. The uncertainty in mean velocity for turbulence intensities of 5% and 65% are 0.2 and 3.0% respectively for 95% confidence.

The uncertainty of the positioning of the measuring volume in the flow stems from imperfections in the traversing mechanism of the optical system. The accuracy of the compound traversing tables was 0.025 mm. The error in locating the measuring volume at two adjacent points separated by 1.0 mm is thus ±2.5%.

The long term stability of the grating rotation was (manufacturer's specification) 0.1% and the rms variation (short term stability) was 0.2% at a rotational speed of 3360 rpm: the variation was monitored by positioning the measuring volume on the wall of the test section and the above stability was confirmed. This small variation of the grating speed

has negligible effect on the velocities measured.

With the errors discussed above, the overall uncertainty of the present flow measurements was estimated to be less than 2% and 5% in the mean and the rms velocities respectively. The maximum uncertainties are expected to be 5% and 10% in the mean and the rms velocities repectively, in regions of steep and non-linear velocity gradients and of high turbulence intensity.

2.4 Single-phase flow results and discussion

As mentioned in chapter I, many studies of single-phase duct flow, with and without bluff bodies, have been carried out and include those of Laufer (1954), Taylor and Whitelaw (1984) and Nouri et al (1984). The primary aim of the present duct flow investigations was to acquire understanding of the behaviour of suspended particles in such flows and to compare them with the single-phase flow characteristics which are presented and discussed in detail in section 2.5.

The single-phase measurements are presented to; (a) compare the present and previous investigation results in order to provide confidence in the flow arrangements and (b) produce single-phase data in sufficient detail to facilitate the comparison of the single and two-phase results. In this section axial mean and rms velocities of the small particles (single-phase flow) are reported and are normalized by the bulk velocity (V_b) unless stated otherwise. The results are presented under two headings, for the pipe flow and for the confined baffled pipe flow.

2.4.1 Pipe flow

The axial mean and rms velocities at different axial locations for the water pipe flow are shown in figure 2.15. The mean velocity profiles, figure 2.15 (a), are identical at both locations, implying that fully-developed flow was achieved. Mass continuity was found to be satisfactory at both locations to within 3%. The axial turbulence levels of figure 2.15 (b) indicate identical profiles with a minimum value of $0.056V_b$ at the axis of

the pipe and increase with increasing radius to a value of $0.12V_b$ in the vicinity of the wall. The same results are presented in figure 2.16 for the mixture pipe flow and show similar features to those of the water flow with the profiles of both the mean and the rms velocities at the two different axial locations being identical.

The symmetry of the mean and rms velocity profiles across the pipe cross-section is demonstrated by the results of figure 2.17. The degree of symmetry of the profiles is very good with an error within the positioning uncertainty of the measuring volume. There are differences of up to 5% in the water and mixture flow profiles so that the water flow mean velocity profile is more developed than that of the mixture. These differences are partly due to the change in Reynolds number and partly due to experimental scatter.

Comparison with the pipe flow results of Laufer (1954) and Tsuji et al (1984) is allowed by figure 2.18. The mixture flow results are in good agreement with Laufer's results for similar Reynolds numbers (note that the Reynolds number given in figure 2.18 are based on centre line velocity rather than bulk velocity) but the water flow mean velocity profile is flatter than that of Laufer partly due to the higher Reynolds number and partly due to experimental scatter. Differences between the present rms profiles and those of Tsuji et al are less than 0.5% of V_b, within experimental error.

2.4.2 Baffled flow

Measurements were made to ensure the symmetry of the flow over the whole pipe cross-section at $Z/D_b=0.75$ and the results are shown in figure 2.19. It can be seen that the asymmetries in the mean (figure 2.19(a)) and in the rms (figure 2.19(b)) velocity profiles are very small and within the errors of positioning the measuring volume. A further check was made by calculating the mass flow rate from the mean velocity profiles on either side of the axis of symmetry of the pipe, and gave values of 0.865 and 0.83 kg/s, a difference of 4%. The consistency of the results was also checked by comparing the calculated mass flow rates at different axial locations: the mass flows at Z/D_b= 0.0, 0.75 and 3.0 were 0.865, 0.84 and 0.843 kg/s respectively which shows differences of about 3%.

CHAPTER II

Considering the error in the numerical integration carried out to obtain mass flow rates, the agreement is very good.

The streamwise mean velocities upstream, at the trailing edge and downstream of the baffle are presented in figure 2.20 (a)-(d) with the axial location denoted as Z/D_b, i.e. expressed in baffle diameter from the trailing edge of the baffle. The results at Z/D_b=-0.142, figure 2.20 (a) show that there is a small recirculating region bounded between the sting and the upstream face of the baffle with a maximum reverse velocity of about $0.35V_b$. Away from this region the velocity increases rapidly towards the wall and, in the annular jet around the baffle, the velocity profile is more uniform with an average value of $1.5V_b$. The profile at the trailing edge of the baffle is near uniform with a maximum velocity of $2.15V_b$ located close to the tip of the baffle. The velocities decrease from this value to $1.9V_b$ in the vicinity of the wall. The results downstream of the baffle show the presence of an annular jet near the wall, a recirculating zone behind the baffle and a recovery region further downstrean. The annular jet (figure 2.20 (b)-(d)) accelerates from Z/D_b=0.0 to 0.75 and then decelerates. In the region from Z/D_b=2.15 onwards (figure 2.20 (d)), the mean velocity profile recovers rapidly so that the flow accelerates in the central region of the pipe, with corresponding deceleration near the wall region.The profiles tend to fully-developed profile further downstream, such as those shown in figures 2.15 (a) and 2.16 (a).

The length of the recirculation zone was obtained from figure 2.21 (a), where the centre line axial mean velocities are plotted as a function of axial location, to be $2.15D_b$. The maximum negative velocity is $1.25V_b$ at Z/D_b=1.0. The mass in the recirculation region at this axial location was calculated to be 0.154 kg/s, which is about 18% of the total mass flow through the pipe. Figure 2.21(b) presents the positions of zero axial velocity downstream of the baffle, and the locus of these values can be regarded as the variation of the width of the recirculation region with axial distance along the pipe. The recirculation region width varies from a maximum of 0.6 r/R at Z/D_b=0.25 to 0.51 r/R at Z/D_b=1.0 and 0.2 r/R at Z/D_b=1.91.

CHAPTER II

The distributions of the axial rms velocities measured around the baffle are shown in figure 2.22. The turbulence levels in the annular jet upstream of the baffle at Z/D_b=-.142 (figure 2.22 (a)) are about one fourth of those near the upstream face of the baffle where u' reaches a local maximum value of $0.35V_b$. The turbulence levels along the annular jet at the trailing edge (Z/D_b=0.0) are nearly uniform, with magnitude around $0.10V_b$. The results downstream of the baffle indicate that the recirculation zone is a region of intense generation of turbulence, which is subsequently dissipated further downstream in the recovery region. This large turbulence intensity exists over the whole length of the recirculation region beyond which the turbulence levels decay rapidly. The maximum turbulence level at each axial location in figure 2.22 (b)-(c) lies on the steep mean velocity gradient in the region $0.6 < r/R < 0.8$ with magnitudes in all cases of $0.7\text{-}0.75V_b$. The rms velocity profile in the recovery region, figure 2.22 (d), show more uniform profile than those in the recirculation region and that the profiles get more uniform with increasing Z/D_b.

The axial mean and rms velocity distributions downstream of the baffle are presented in contour form in figure 2.23, where the pattern of the mean flow can be seen clearly with three distinct regions the annular jet, recirculation zone and the recovery region. The contours of turbulence intensity show that the turbulence levels in the region of the steep velocity gradient at the edge of the annular jet have been reduced by about 50% from Z/D_b=0.3 to 3.0 and that on the axis of the pipe the intensity remains almost the same (about $0.3V_b$) at all axial locations within the recirculation zone and thereafter decreases with axial distance downstrem.

The results are in very good agreement with those obtained by Taylor and Whitelaw (1984) and Nouri et al (1984) in horizontal flows past identical baffles as compared by figures 2.24 and 2.25. The probability density functions of the velocity measurements were close to Gaussian except in the regions of the steep gradients at the edges of the annular jet where the distributions were skewed, which is typical of flow regions with strong gradients of turbulent intensity. This effect is discussed further in

subsection 2.5.2 in relation to the two-phase flow.

The result presented in the last two sub-sections showed the main features of the flow in the pipe and around the axisymmetric disc baffle and establish them for the subsequent measurements in two-phase flows presented in next section.

2.5 Two-phase flow results and discussion

The results of the large particle mean and rms velocities in the two-phase flows in the pipe and in the baffled pipe are presented in this section together with some of the single-phase results which are shown for comparison. The particle velocities have been normalized with the bulk velocity obtained from the single-phase flow measurements

.

2.5.1 Pipe flow

The particle mean velocities measured in the flow of water in the pipe with particle volumetric concentrations (C_v) of up to 0.75% are shown in figure 2.26. The particle velocities are consistently larger than the single-phase fluid velocities ($\overline{U}$), but there is no discernable trend or variation of the particle velocity ($\overline{U}_p$) with concentration. It is useful to consider an apparent slip velocity defined as $\overline{U}_s=\overline{U}_p - \overline{U}$, but the interpretation of the $\overline{U}_s$ must be made with care as the true slip velocity is the difference between $\overline{U}_p$ and the liquid velocity ($\overline{U}_f$) in the presence of the particles, and $\overline{U}_f$ may be different from $\overline{U}$, that is the fluid velocity may vary in the presence of the particles. With the present arrangement, measurements of $\overline{U}_f$ cannot be made as explained in subsection 2.3.3. The magnitude of $\overline{U}_s$ is on average 65 mm/s in the water flow, i.e. $0.025V_b$.

The mean velocity results obtained with the refractive-index matched mixture and suspensions of particles with C_v=2-14%, i.e. with up to a twentyfold increase in the concentration of the particles show, figure 2.27, that the particle velocity profile changes shape with particle concentration. At the lowest particle concentration, the $\overline{U}_p$ profile has a pronounced peak on the axis in comparison to the single-phase results. The particle velocity profiles become flatter and more similar in shape to that of single-phase flow as

the concentration is increased. The flattening of the profile with increase in concentration is in agreement with all previous investigations cited such as those of Tsuji and Morikawa (1982) and Tsuji et al (1984). The peak in the particle velocity profile (in comparison to the single-phase result) has been attributed to the radial migration of the particles towards the tube wall for spheres more dense than the fluid in a downflow, while in upflow of denser spheres the profile becomes blunter (Cox and Mason, 1971); as a result the effective viscosity of the suspension in the present flow is greater near the wall (Maude, 1960, for example, has suggested that $\mu = \mu_o / (1-2.5\ C_v)$ for laminar flow and $C_v < 28\%$, i.e. μ increases with C_v) and the near-axis velocities are larger. Shih and Lumley (1986) reached a similar conclusion for particles located far from the centre of a two-phase mixing layer: the local density was lower than that near the mixing layer and particles were travelling faster than average. Here $\overline{U}_S$ varies from 165 mm/s near axis to 70 mm/s near the wall for C_v=2%; the apparent slip velocities decrease as C_v increases and the corresponding values for C_v=8% are 102 and 35 mm/s respectively and for 12%, 46 and 7 mm/s.

The terminal velocity of the particles due to drag and gravity forces was calculated (see section 2.2) to be about 8 mm/s for a laminar (Stokes) flow of a single particle in an infinite medium of mixture fluid. The measured apparent slip velocities are considerably larger, partly because of the non-uniform velocity and concentration gradients present in the flow which imply that particle-to-particle and wall interaction effects are important. In addition, the assumption of laminar flow around the spherical particle in the above estimation is incorrect as the particle rms velocities (u'_p) are in the range of 100-300 mm/s with an average of about 200 mm/s: Wells and Stock (1983) have shown that turbulence strongly influences the particle motion for u'_p greater than the terminal velocity. The corresponding terminal velocity estimated from drag and gravity force considerations for turbulent flow (using a value of C_d=0.44) is 50 mm/s, which is more appropriate. But the results show that the effect of the suspension is to reduce the drag on individual particles even further. A similar conclusion may be reached from inspection of the results of Lee and Durst (1982) and Tsuji et al (1984): the drag coefficient for a particle in suspension is

almost always lower than that of a single particle in a laminar flow and, as a result, the terminal velocities are larger in a suspension flow (Lee, 1985). By comparison with the results of other investigations, e.g. Tsuji et al, it can be expected that the true slip velocities (i.e. $\overline{U}_p - \overline{U}_f$) will be smaller than $\overline{U}_s$ and closer to the estimated terminal velocities for turbulent flow.

The decrease in $\overline{U}_p$ with increasing C_v is in agreement with well-established empirical relationships that state in general the slip velocity is proportional to $(1-C_v)^{1.325}$ and with the result of Birchenough and Mason (1976) and Tsuji et al (1984), which showed that the particle velocities decrease with increasing mass loading of the solids. Tsuji et al have stated that $\overline{U}_p$ increased with C_v, but their results show the opposite effect and their conclusion was based on velocity magnitudes which were not normalized by the same value. The value of $\overline{U}_s$ also decreases with C_v in present results; Tsuji et al found that $\overline{U}_p-\overline{U}_f$ decreased whereas $\overline{U}_s$ increased with mass loading in upflow and Birchenough and Mason's findings are in agreement with the latter result. In conjunction with the present results, it can be concluded that in both upflow and downflow of particles denser than the fluid, an increase in concentration results in a decrease in particle velocities and therefore the $\overline{U}_s$ velocities will be larger or smaller respectively, as gravity acts in opposite senses. This effect has been also quantified and discussed in subsection 3.5.2 where both upflow and downflow were present in the stirred reactor vessel.

The difference in $\overline{U}_s$ velocities measured in water and in the mixture are in agreement with the Reynolds number effect on the relative velocity shown by Birchenough and Mason (1976); in that investigation the $\overline{U}_s$ velocities in upflow increased by a factor of 1.7 as Re increased by a factor of 1.4, and similarly in the present results the average apparent slip velocity (for C_v=0.75 and 2%) decreases by a factor of 1.8 as Re increases by a factor of 1.5 from 39,650 in the mixture flow to 59,200 in the water flow. This result indicates that the importance of particle inertia increases with Reynolds number, and the particle lag is more significant. Thus in upflow the particles lag increasingly more behind the fluid and $\overline{U}_s$ increases as Reynolds number increases, whereas in downflow the lead of

the particles over the fluid becomes progressively smaller as Re increases, i.e. $\overline{U}_s$ decreases. The same effect has been observed by Khezzar (1987): the particle velocities, at a fixed point in the unsteady flow behind projectile gun barrel in the flow, lag behind the fluid in the beginning of the cycle (high fluid velocity) and subsequently change sign later in the cycle and lead the fluid at the end of the cycle where the fluid velocity is lower than that of the begining of the cycle, by about 50%.

The particle velocity at any point along the pipe radius remains nearly uniform with increasing concentration for the water flow, i.e. for C_v up to 0.75%, with the exception of the near-wall region at r/R=0.9 and 0.95 where $\overline{U}_p$ increased. In higher concentrations in the mixture flow , the particle velocity at a point decreased with increasing concentration and the decrease near the axis was twice that in the near-wall region. This local variation in magnitude of $\overline{U}_s$ is associated with particle migration and the total increase in the viscosity and density of the suspension, as mentioned earlier. These effects are not as significant with the lower concentration and, as a result, the particle velocity profiles tend to be more uniform for C_v=0.1-0.75%.

The single-phase and particle streamwise rms velocity components are shown in figure 2.28 for water flow and in figure 2.29 for the mixture flow. Figure 2.28 shows that the fluctuating velocity of the particles is always smaller than that of the single-phase, by around 5% on the pipe axis and 13% near the wall. A similar trend is shown by the particle rms velocities measured in the mixture, with levels lower by about 10% in the central region near the axis (i.e. from r/R=0.0 to 0.4), and around 7% close to the wall. The levels at 0.8 of the pipe radius are similar to those of single-phase flow. The u'_p levels decrease with increasing concentration so that, for example at r/R=0.4, the levels for C_v=6% are 15% smaller than the single-phase value, whereas for 14% concentration they are about 30% smaller.

Tsuji et al (1984) also found that u'_p levels are smaller than the single-phase levels, for the flow of 200 μm particles in air, and that they decrease with increasing concentration. Owen (1969) calculated that the fluid rms levels decrease in comparison to

the single-phase levels due to the presence of particles by $[1+(\rho_p / \rho)]^{-0.5}$ and this suggests that the fluid rms velocity at the presence of the particles (u'_f) for the present flow with C_v=10% will be smaller than the single-phase levels (u') by about 6%. By comparison the measured u'_p levels were 7% smaller than the single-phase levels. Tsuji et al also found that $u_f \approx 0.6u'$ for 200 μm particles with C_v=0.3% and Zisselmar and Molerus (1978) reported that for liquid-solid flow in a horizontal pipe, the fluid rms levels were reduced by 12-40% in the presence of glass particles of 57 μm for volumetric concentrations of 1.7-5.6% respectively. The result that the values of u'_p are larger in the presence of smaller particles (e.g. 57 μm particles, Zisselmar and Molerus) than with larger ones (e.g. 200-300 μm particles, Tsuji et al. and present results) is in agreement with the results presented in the following section for 310 and 665 μm particles. The reduction of u'_p in comparison to u'_f has been attributed to the particle inertia, which is characterised by the particle responce time (Snyder and Lumley, 1971). Boothroyd (1967) found that turbulence of the carrier-phase is generated by the presence of the particles and suggested that the particles extract large scale turbulence energy from the mean flow: in the present case the turbulence acquired by the solids is lower than the single-phase levels.

2.5.2 Baffled flow

Symmetry of the particle mean and rms velocity profiles was checked with C_v=4.0% at two different axial locations (Z/D_b=0.75 and 3.0) and the results are shown on figure 2.30. It is evident that the asymmetries of the profiles at both axial locations are very small and within the errors of positioning the measuring volume.

The mean streamwise velocities for suspensions of 310 μm mean diameter particles and concentrations in the range of 1-8% in the mixture flow around the axisymmetric disc baffle are presented in figure 2.31. The results for two values of C_v (4.0 and 8.0%) are shown at each axial location except at Z/D_b=0.75 where mean velocity measurements for ten values of C_v are presented. The results for C_v=0.0 are those of single-phase and are presented for comparison.

CHAPTER II

The particle velocity profiles at the trailing edge of the baffle (figure 2.31 (a)) are flatter than the single-phase profile, and the same trend is evident in the profiles at all the subsequent axial locations (figure 2.31 (b)-(h)). The $\overline{U}_s$ velocities increase with concentration in the recirculation region and in the centre of the jet, and $\overline{U}_p$ decreases with concentration in the same flow regions, while the $\overline{U}_p$ velocities tend to be larger in the near-wall region. The annular particle jet profiles are more uniform and the spread of the jet is smaller than in single-phase: this reduced spread of the jet is in agreement with findings of Modarress et al (1982) for a round two-phase flow jet discharging into a co-flowing stream. The skewness of the probability density functions of the measured particle velocity distributions at the edges of the jet was smaller than the single-phase flow. As the skewness appears in the mean square turbulent vorticity equation as a factor of the rate of production of vorticity, the present results suggest that the turbulent vorticity of the particles is destroyed by viscous effects more rapidly than in single-phase flow: this result is in agreement with the particle turbulence results presented in this section, which are lower than the single-phase levels.

The differences in the $\overline{U}_p$ and $\overline{U}$ profiles become more pronounced as the particle concentration increases (figure 2.30 (c) and (d)), with $\overline{U}_p$ greater than the single-phase velocities near the wall for all concentrations, and smaller in the centre of the annular jet and recirculation regions. The maximum apparent slip velocity ($\overline{U}_s$) for the 4% concentration was located near the pipe axis and was 0.33, 0.47 and 0.19 m/s at Z/D=0.75, 1.407 and 3.0 respectively, while for C_v=8% the $\overline{U}_s$ on the axis were 0.56, 0.75 and 0.47 m/s at Z/D_b=0.75, 1.91 and 3.0 respectively. The same effects on the mean velocities can be seen over the whole pipe cross-section, figure 2.32 (a), where the particle velocity profiles at C_v=4.0 and 8.0% were compared with that of single-phase profile, with particles lag behind the fluid in the recirculation zone and in the central region of the annular jet, while leading the fluid in the region close to the walls. It is also clear that the particle rms velocities (figure 2.32 (b)) are smaller than those of single-phase velocities everywhere across the pipe section with greater reduction in particle turbulent levels close

to the walls. The effects of particles are discussed in more detail later in this section.

The variations of the single-phase and of the particle velocities along the pipe centreline are shown in figure 2.33 (a) with the change of sign of the particle velocities occuring nearer the baffle than for the single-phase flow, indicating that the particles leave the recirculation zone earlier. As there are strong acceleration and decelerations in the flow, especially in the recirculation region, particle inertia and virtual mass effects are more important than in the pipe flow and results indicate that the particles follow the fluid motion less faithfully (this was expected from particle time response considerations, i.e. the particle time response was higher by a factor of 5: see table 2.2) as concentration increases and the length of the recirculation region, in $\overline{U}_p$ terms, is shorter by 0.22 and $0.52D_b$ (3.9 and 9.3 mm) for the 4% and 8% concentrations respectively, than in single-phase flow where the recirculation length is $2.15D_b$ or 38.6 mm. Consequently, the recovery of the downstrean flow occurs earlier (figure 2.31 (f) to (h)). Hardalupas (1986) has found that few of the 40 μm glass particles in an annular gas-solid downflowing jet were entrained in the recirculation zone; in the present results the solid/liquid density ratio ($\rho_p / \rho = 1.32$) is much smaller and the particles enter the recirculation region but drop out due to gravity as they approach the low-velocity region near the stagnation point.

The particle rms velocities along the centreline (figure 2.33 (b)) are lower than the fluctuating levels of the single-phase flow in most Z-locations and the same in some other locations: in the axial location ranges of $0.0 < Z/D_b < 1.0$ and $2.0 < Z/D_b < 3.4$ the particle turbulence levels are lower by about 7 and 9% respectively, while in the axial locations of $1.0 < Z/D_b < 2.0$ they are similar and increases slightly with concentration. This increase may be a result of the particle-to-particle interaction. The change in u'_p, in general, is small along the centreline with increase in concentration, and this is in contrast to the relatively large changes in $\overline{U}_p$ observed with increasing C_v (figure 2.33(a)). This is a consequence of the near-uniform distribution of u' near the axis: as $\partial(u') / \partial Z \approx 0$, even large changes in $\overline{U}_p$ result in little or no change in u'_p.

The turbulence levels measured at the axial locations of figure 2.31 are shown in

figure 2.34 (a)-(h). For C_v=1.0% (figure 2.34 (c)) the u'_p levels are 5-10% lower than the single-phase ones near the axis and 20-30% lower close to the wall. The particle rms levels are further suppressed for C_v=2.0% and the corresponding values are 6-10% and 25-60%; for higher concentrations, C_v=3-8%, the percentage reductions are around 10% and 30-65% respectively. In the shear layer between the jet and the recirculation region, the particle rms levels are similar and sometimes higher, within 5-15% of the single-phase levels. In the recovery region downstream (Z/D_b=2.0 onwards) the u'_p levels are on average 20% lower. The results of Nouri et al (1984), for an identical baffle in a horizontal pipe, showed that the reductions in turbulence levels at C_v=0.375% were 4-13% and 4-17% near the axis and close to the wall respectively, which in comparison to the present results is slightly lower than for the case of C_v=1.0%.

The particle-to-particle interaction effects in the present flow are not expected to be uniform and may vary locally. The interaction is high in regions where there are local cross-stream flows, such as the flow at the trailing edge of the baffle, the flow near the axis upstream of the stagnation point (i.e. $1.0<Z/D_b<2.0$) and the flow in the shear layer between the annular jet and recirculation zone (i.e. $0.6<r/R<0.8$). The measured turbulence intensities in these regions show that the particle rms levels are higher than, or similar to, those of the single-phase levels so that, for example, the u'_p levels at the baffle tip (figure 2.34 (a)) are higher by about 17% than u' levels, in the shear layer (figure 2.34 (c)-(e)) are similar or sometimes up to 15% higher and on the axis they are similar. These turbulence levels, which are higher than those of the single-phase flow in above regions in comparisons to the levels in other regions where they are always lower than the single-phase, suggest the effect of particle-to-particle interaction is to increase the turbulence intensity of the particles.

The influence of the particle size on the mean and fluctuating particle velocities is shown in figure 2.35 by the results for Z/D_b=0.75 with particles of 310 and 665 μm mean diameters. Measurements at concentrations of 1 and 2% are shown: no measurements were possible with higher concentrations of large particles as they were damaged by the pump

impeller. The differences in the mean velocities are small, with the velocities of 665 μm particles a few percent smaller than those of the 310 μm particles, and the differences are more pronounced at higher concentration (figure 2.35 (b)). The results suggest that increase in particle size does not affect the mean flow as much as may have been expected because the response time of the 665 μm particles is about four times larger than that of the 310 μm particles.

The rms levels of the 665 μm particles (figure 2.35 (c) and (d)) are consistently smaller by about 10% in the reverse flow region and by up to 30% close to the wall, except on the axis and in the shear layer region where they are the same, due to the particle-to-particle interaction as explained before. Modarress et al (1982) have also found that the suppression of turbulence in a round jet was greater with 200 μm than with 50 μm particles. Lee and Durst (1982) suggested that the fluid rms levels increase in gas-solid upward flow when large (800 μm) particles are suspended in the flow, whereas 400 μm or smaller particles dampen the turbulence levels. Tsuji et al (1984) have confirmed the latter result and also showed that with intermediate particle size ranges (500 μm) turbulence is promoted at some locations whereas in others it is suppressed. In comparison with the latter gas-solid findings, the present data show that in liquid-solid flow, where the particles follow the fluid motion more faithfully, a similar increase in particle size from 310 to 665 μm results in a reduction of the particle fluctuating velocities.

2.6 Summary

The most important findings and conclusions of this chapter are summarised below

(1) A refractive-index-matching technique was developed to enable the measurement of particle velocities at dense volumetric concentration. Matching of the refractive indices of acrylic (Diakon) particles and mixtures of tetraline and turpentine can readily be achieved at convenient temperatures provided the temperature control is better

than around ± 0.03 ^{o}C. The viscosity of the mixture is similar to that of water so that turbulent flow with high Reynolds numbers can be reached.

(2) The presence of inclusion of gas inside the particles limit the extent of the velocity measurements so that only solid-phase velocities can be obtained in the presence of the particles; the gas-inclusions also limit the transparency of the flow that can be achieved when refractive-index-matching is employed. However the maximum particle concentration through which the particle velocity measurements were possible for a depth of flow field of 25.4 mm, was increased from 0.75% in water to 14% when the matching technique was applied.

(3) Single-phase mean velocity results in the baffled pipe flow showed that upstream of the baffle there is a small recirculating region bounded between the upstream face of the baffle and its sting, and that the length of the recirculating region downstream of the baffle is 2.15 times the baffle diameter (D_b).

(4) Single-phase turbulent results in the baffled pipe flow showed that the recirculation bubble is a region of intense turbulence generation with a maximum intensity in the shear layer of about 70% of the bulk velocity which is dissipated further downstream in the recovery region and reduces to about 30%.

(5) The two-phase results in the pipe flow show that the mean particle velocity decreases and the profiles of the particle velocity become more uniform as the particle concentration increases. The difference between the particle and the single-phase fluid velocities decreases with increasing Reynolds number.

(6) The mean particle velocity results in the baffled pipe flow allow the following conclusions.

(a) The length of the reciculation region of the flow of particles downstream of the baffle was shorter than the length in single-phase flow by 11% and 24% for particle concentrations of 4% and 8% respectively.

(b) The spread of the particle annular jet is less than that of single-phase flow.

(c) The particle mean velocity profiles in the recovery region are flatter than those

in single-phase flow, and they become more uniform as the particle concentration increases.

(7) The fluctuating velocities of the particles are, in general, smaller than those of single-phase ones in all flow cases, and they are reduced further with increasing the particle concentration.

(8) Measurements with 310 μm and with 665 μm particles in the baffled pipe flow with particle concentrations up to 2% showed that the particle mean velocities are little affected by particle size, whereas the fluctuating velocities were up to 30% lower with the larger particles.

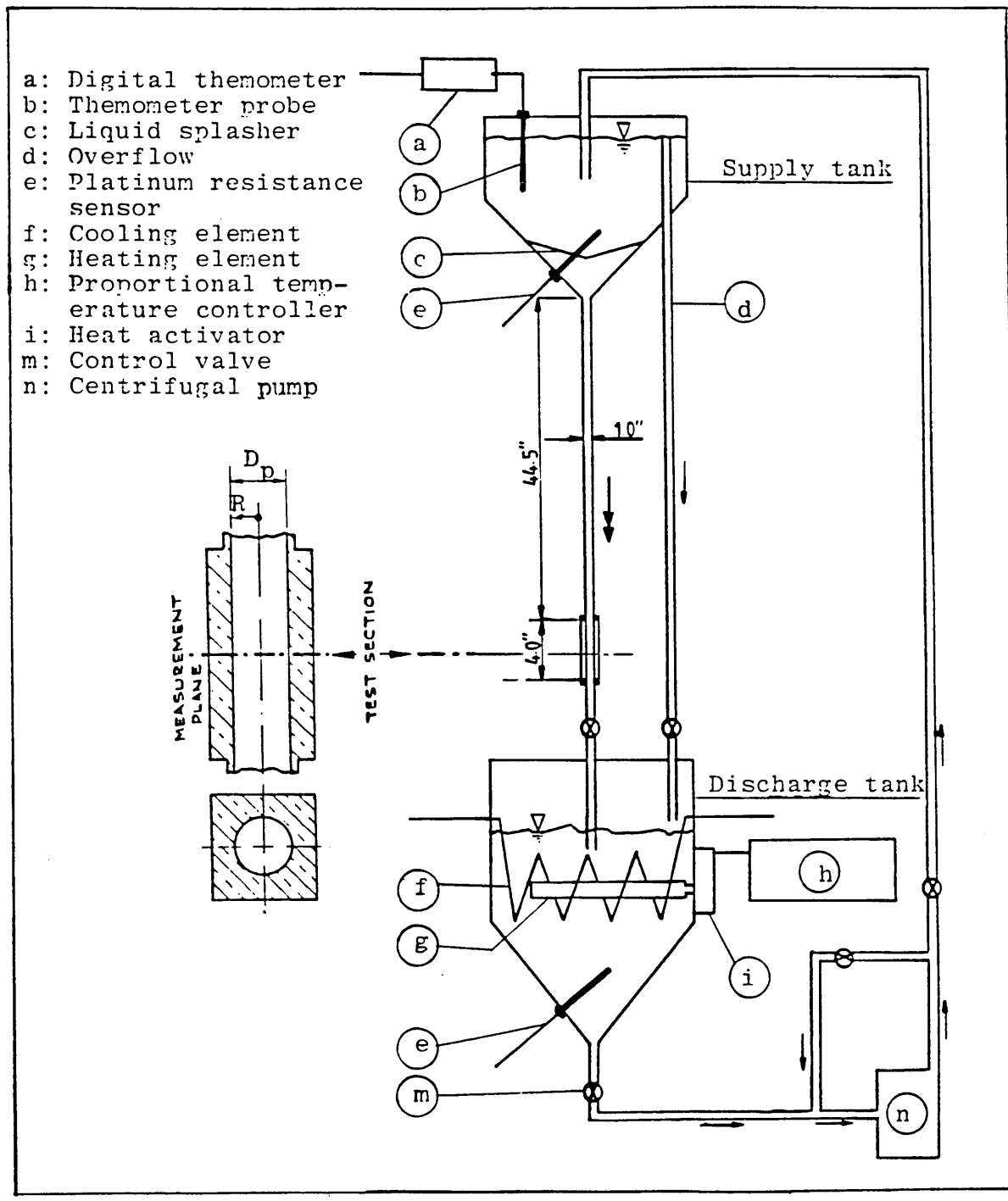

Fig 2.1 Close circuit of the pipe line system.

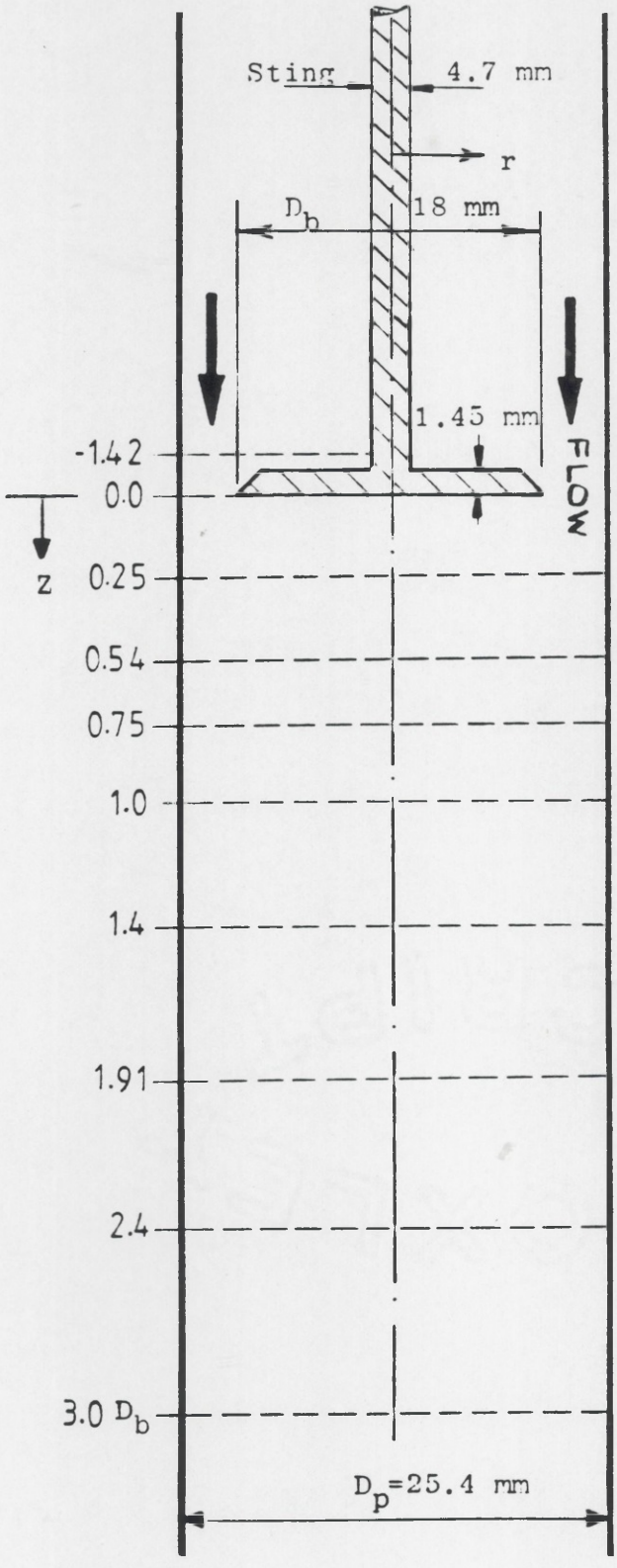

(a)

(b)

Fig 2.2 Flow configuration; (a) pipe and baffle geometry, (b) photograph of the test section.

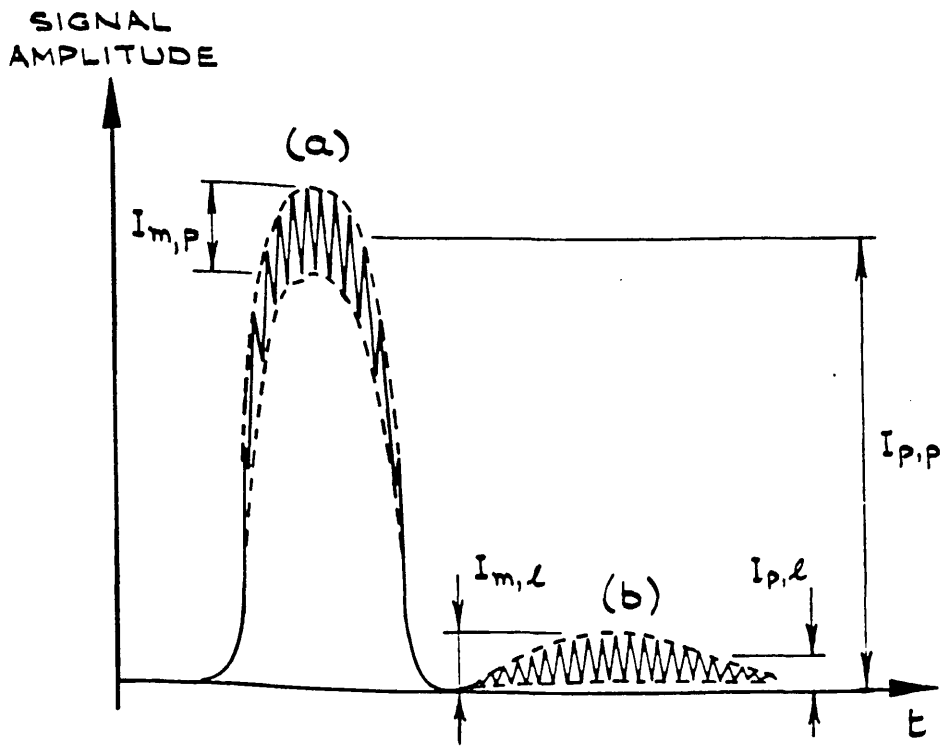

Fig 2.3 Characteristic Doppler signals from; (a) large particles, (b) small particles.

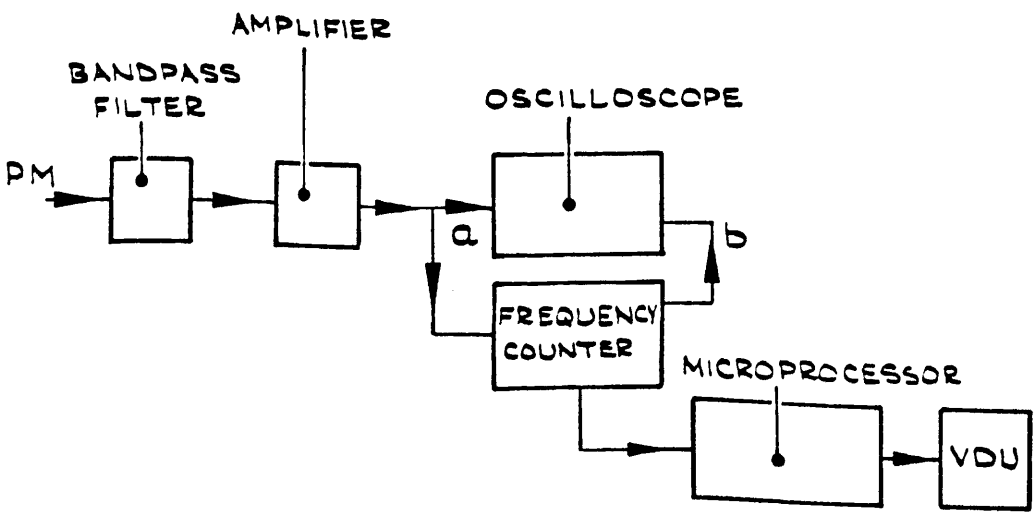

Fig 2.4 LDV signal processing system.

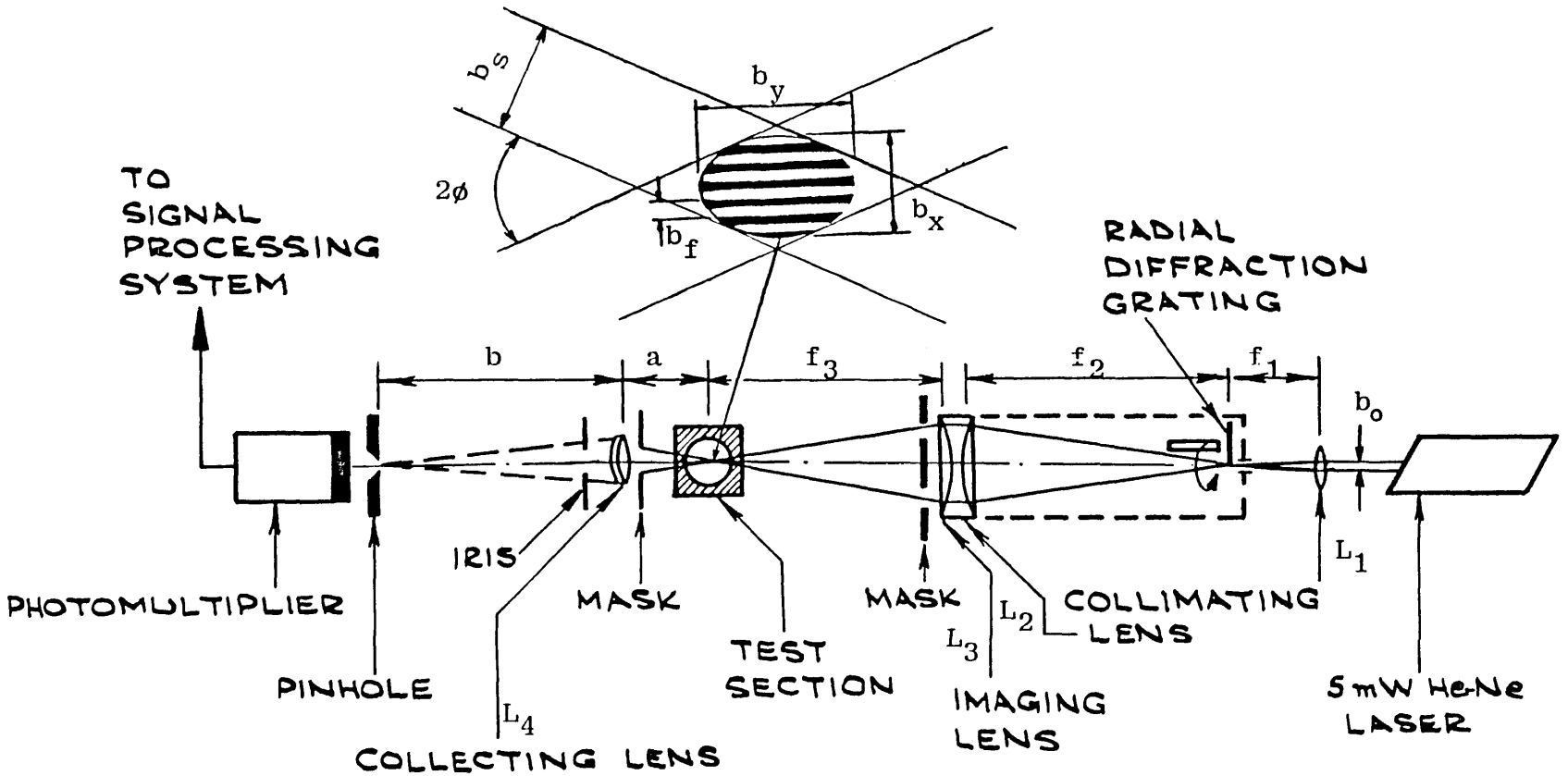

Fig 2.5 LDV optical system.

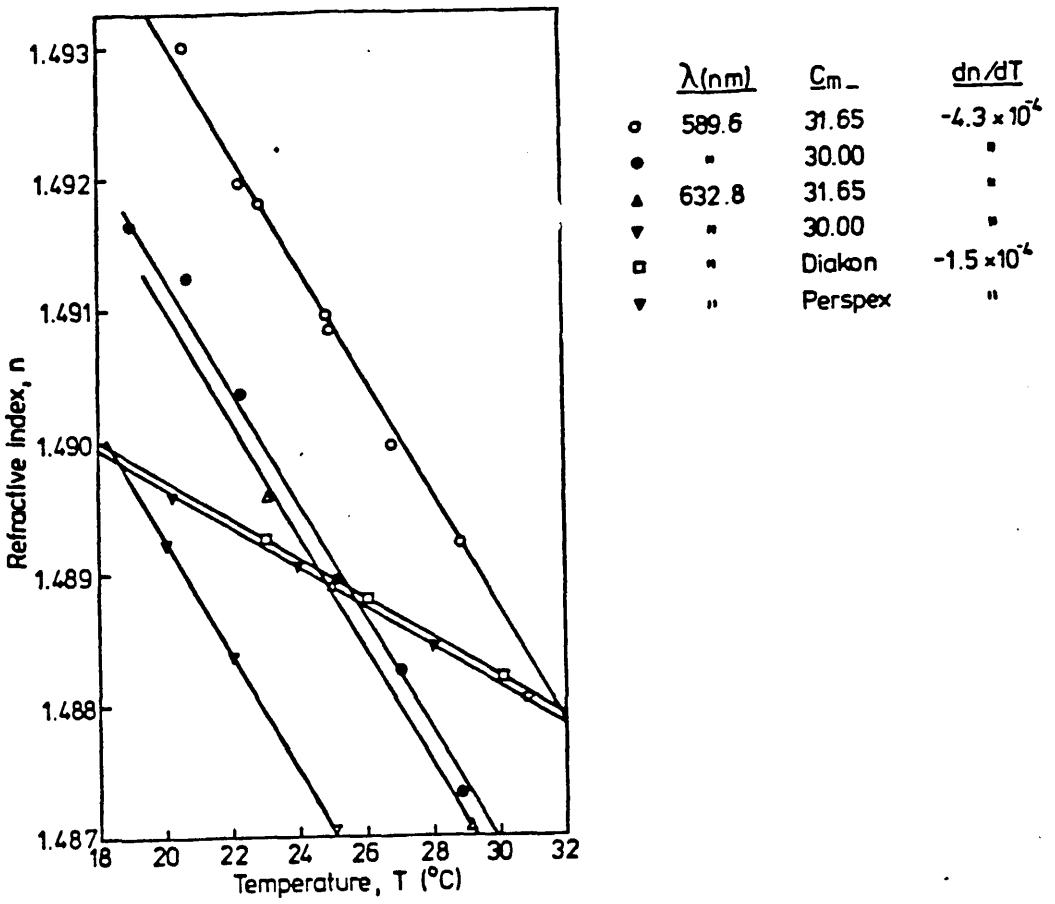

Fig 2.6 Variation of refractive index of mixture, Diakon, and perspex as a function of temperature and light wavelength.

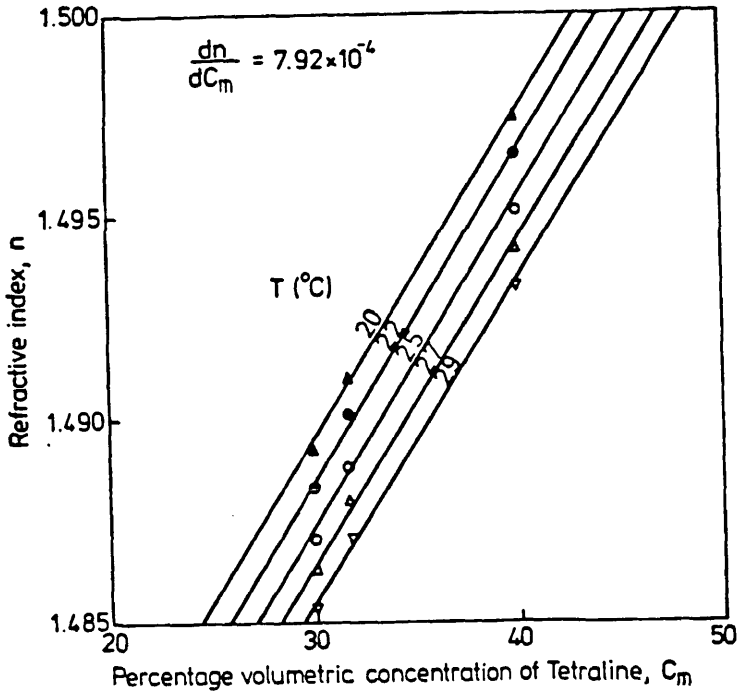

Fig 2.7 Variation of refractive index of mixture as a function of composition of tetraline (C_m) at different temperature.

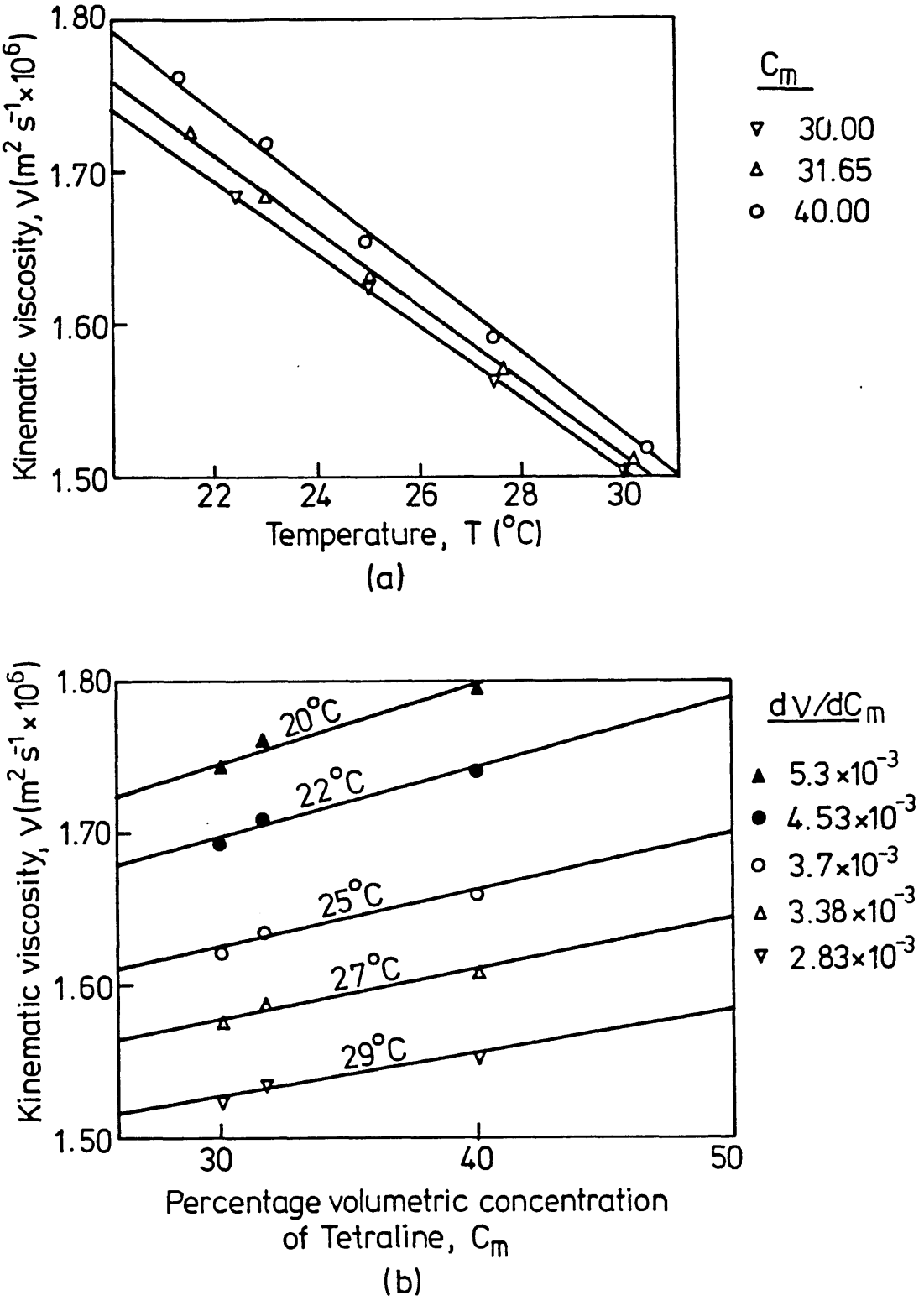

Fig 2.8 Variation of kinematic viscosity of the mixture as a function of (a) temperature and (b) composition of tetraline (C_m).

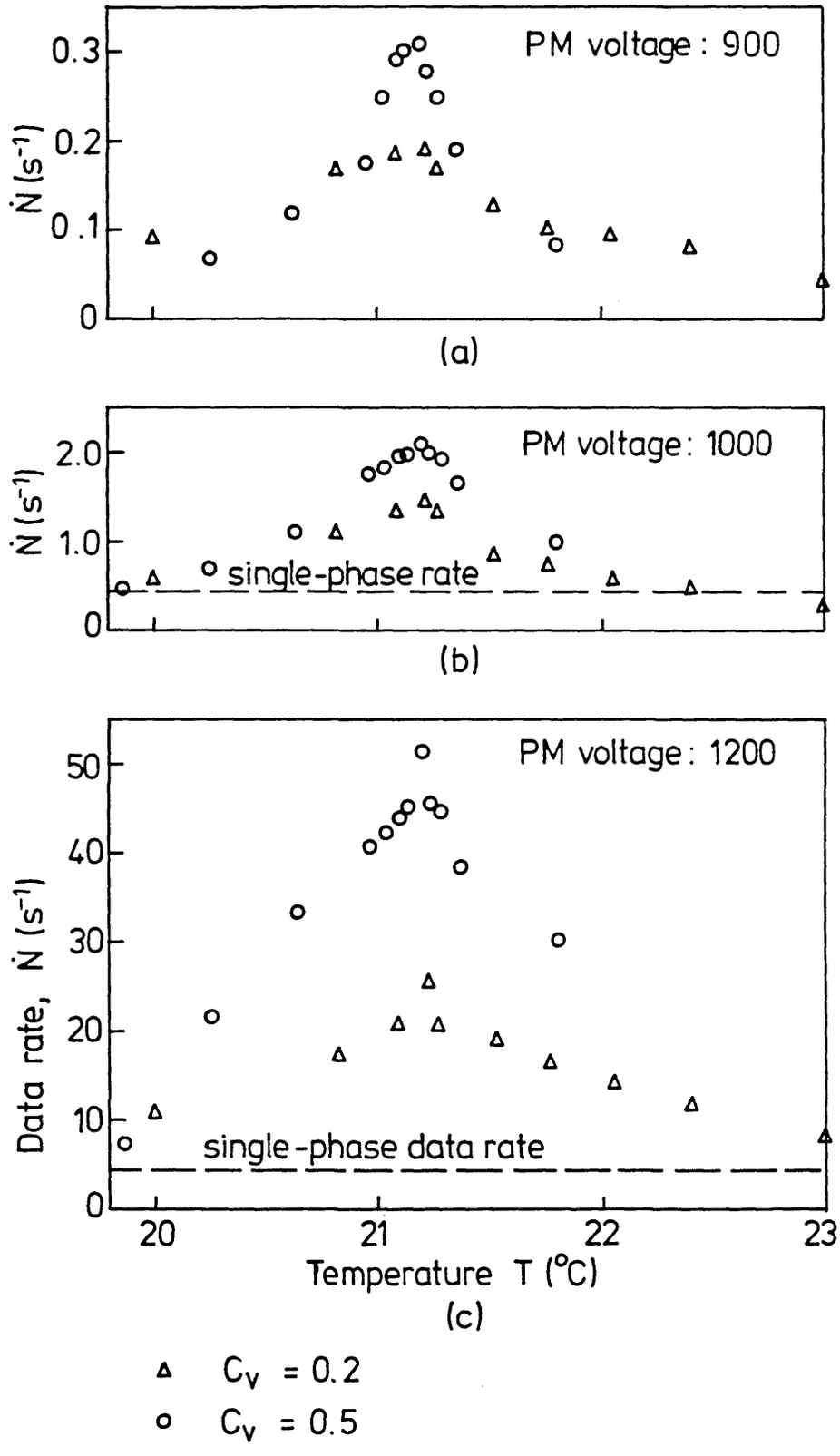

Fig 2.9 Number of Doppler bursts (data rate) as a function of temperature for C_m=30.5%.

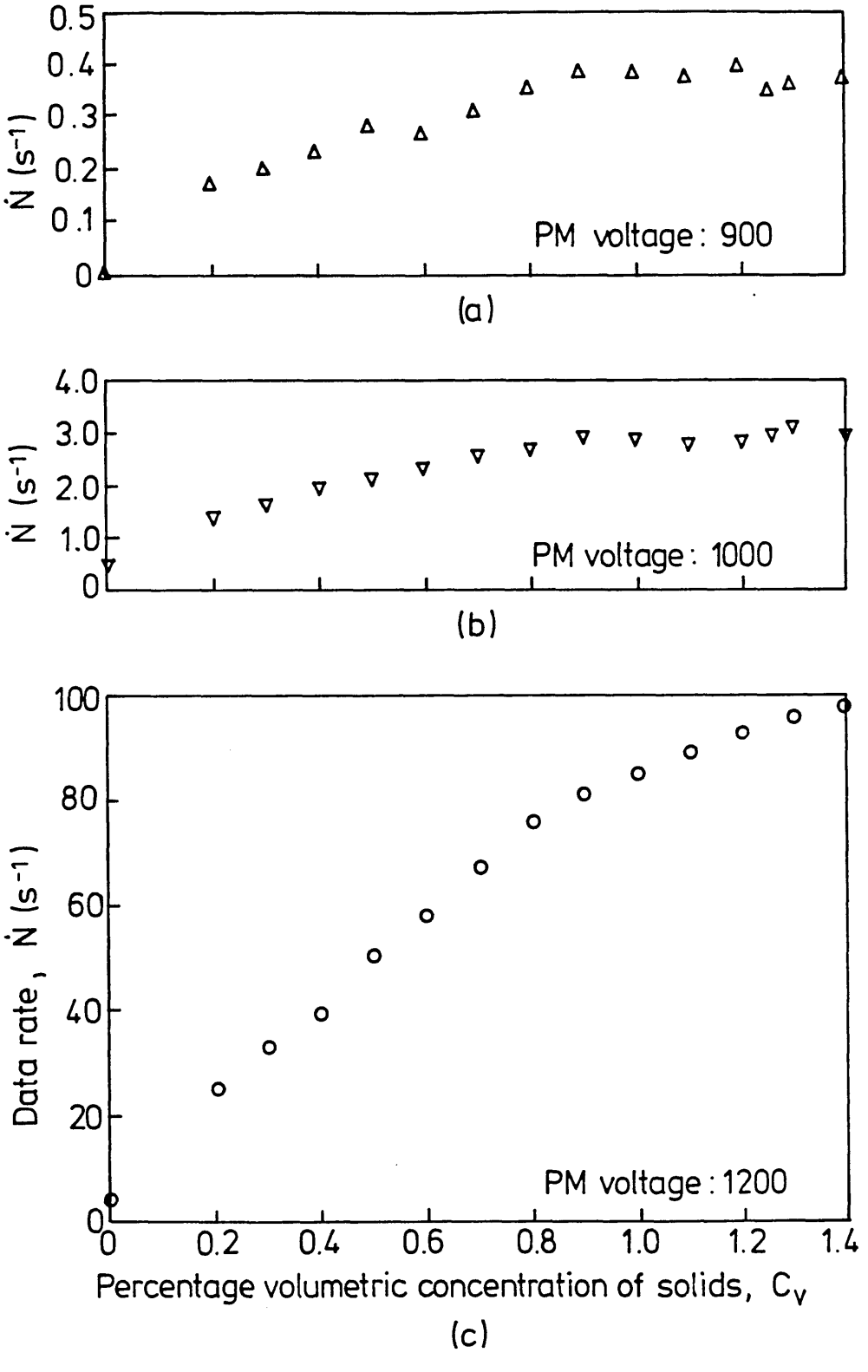

Fig 2.10 Data rate as a function of particle concentration (C_v) for C_m=30.5% at 21.21 °C.

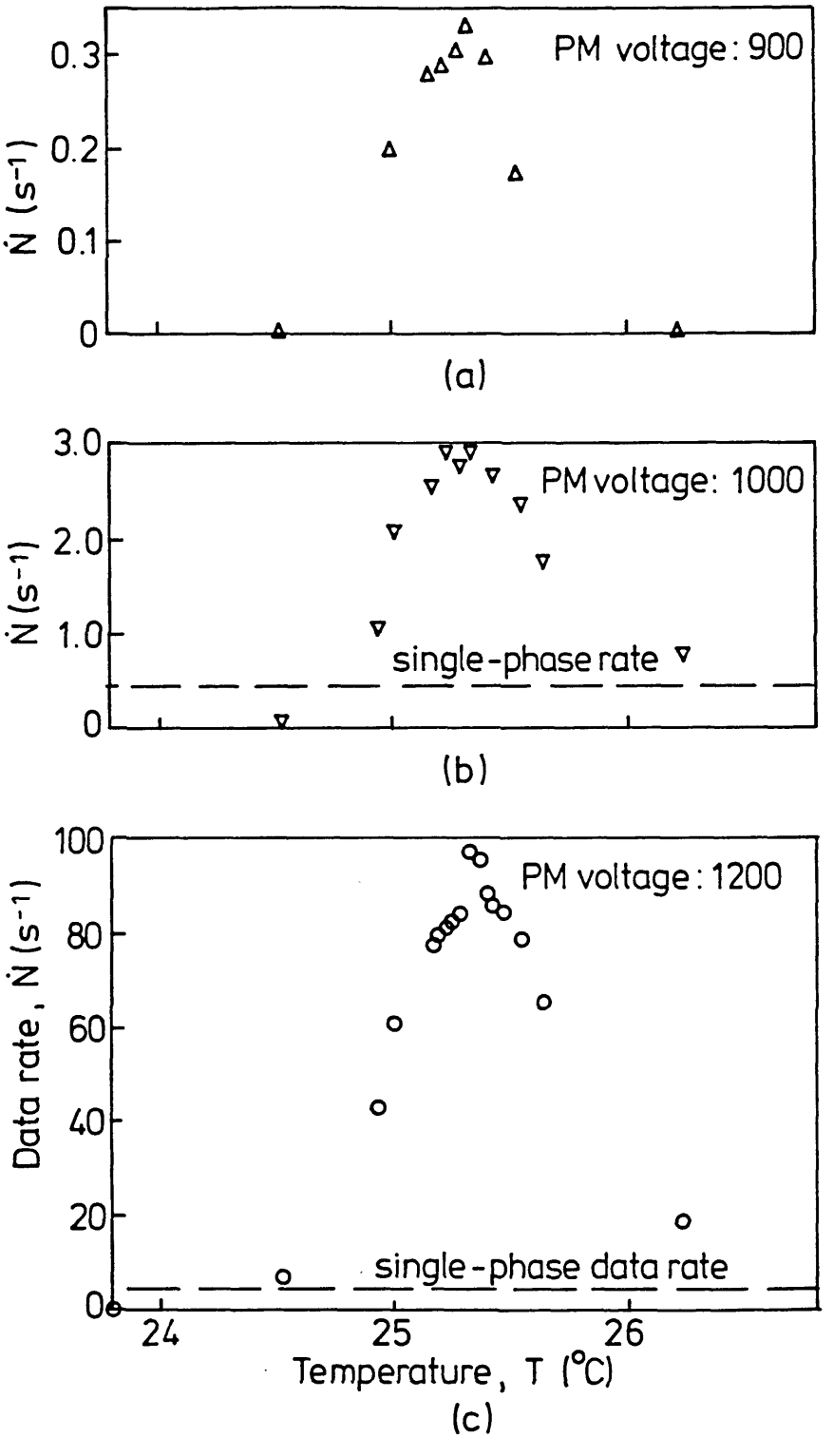

Fig 2.11 Data rate as a function of temperature for C_v=1.26% and C_m=32%.

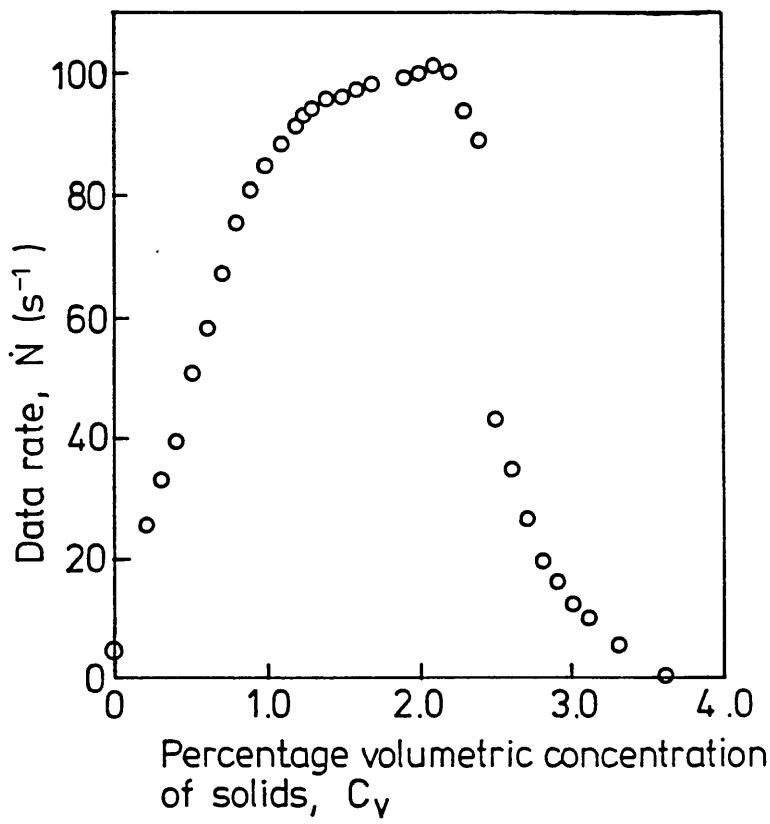

Fig 2.12 Data rate as a function of particle concentration for C_m=32.0% at 25.32 °C.

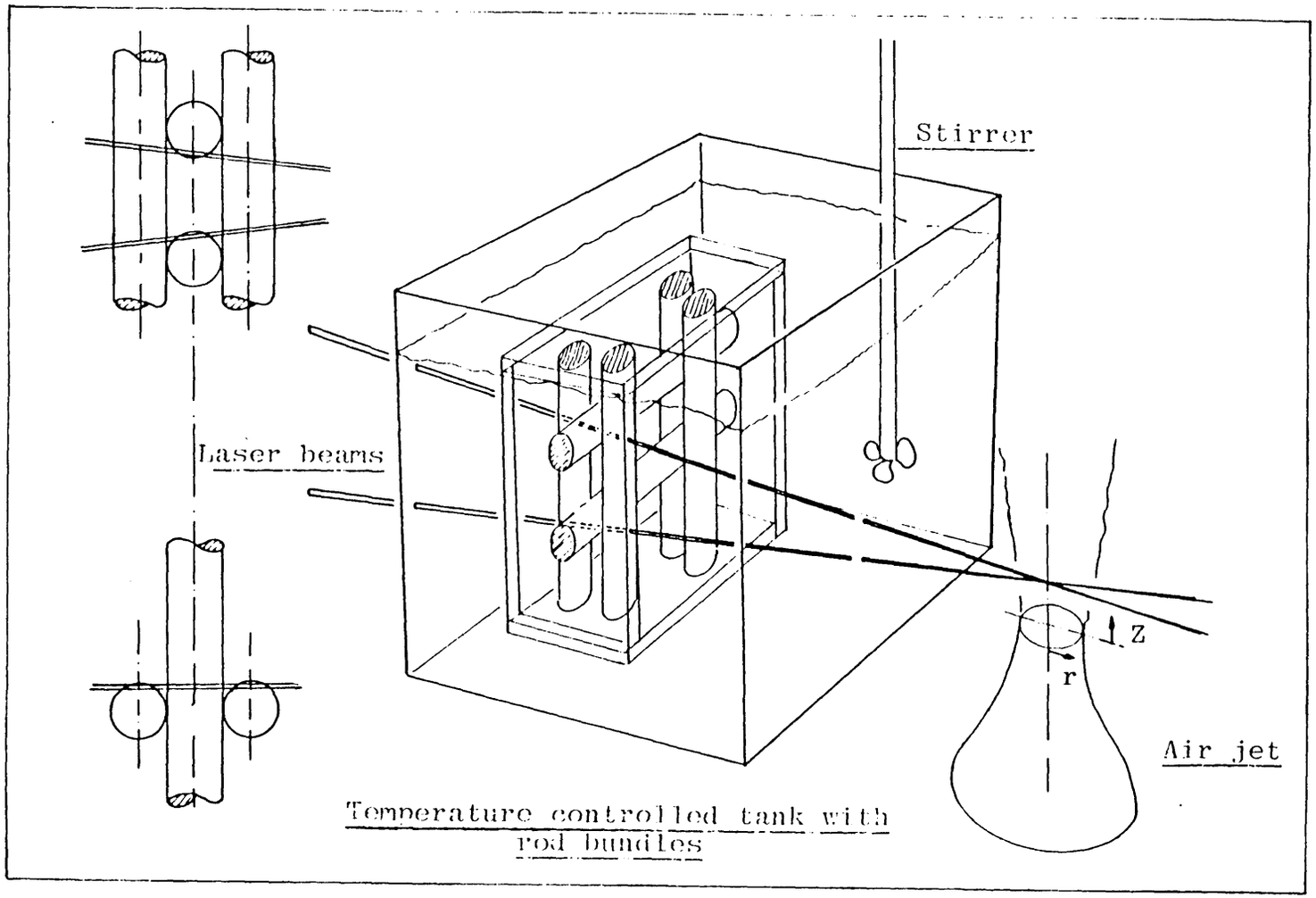

Fig 2.13 Schematic diagram of air jet and rod bundle arrangement.

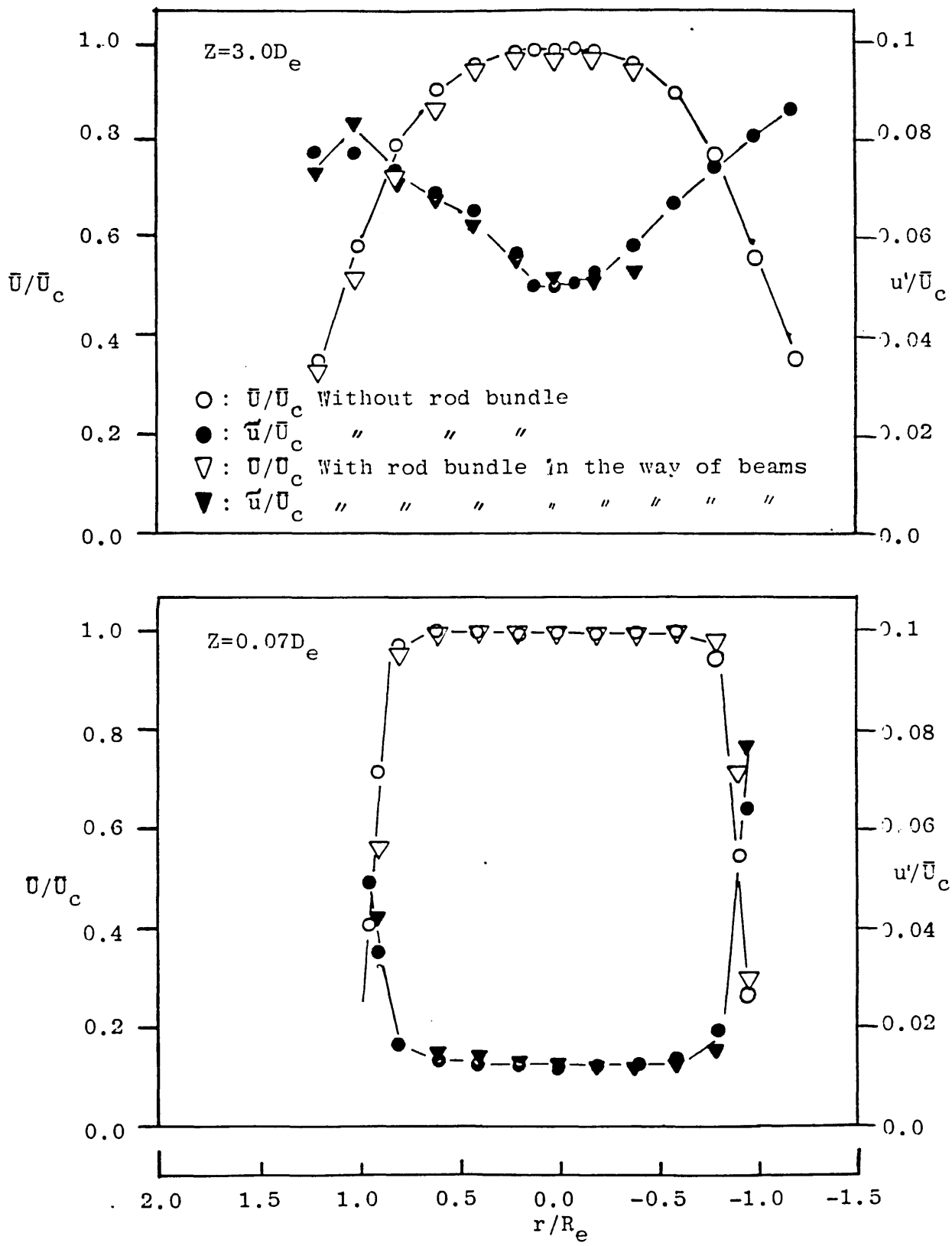

Fig 2.14 Radial distributions of axial mean and rms velocities at different axial locations; U_c=0.877 m/s.

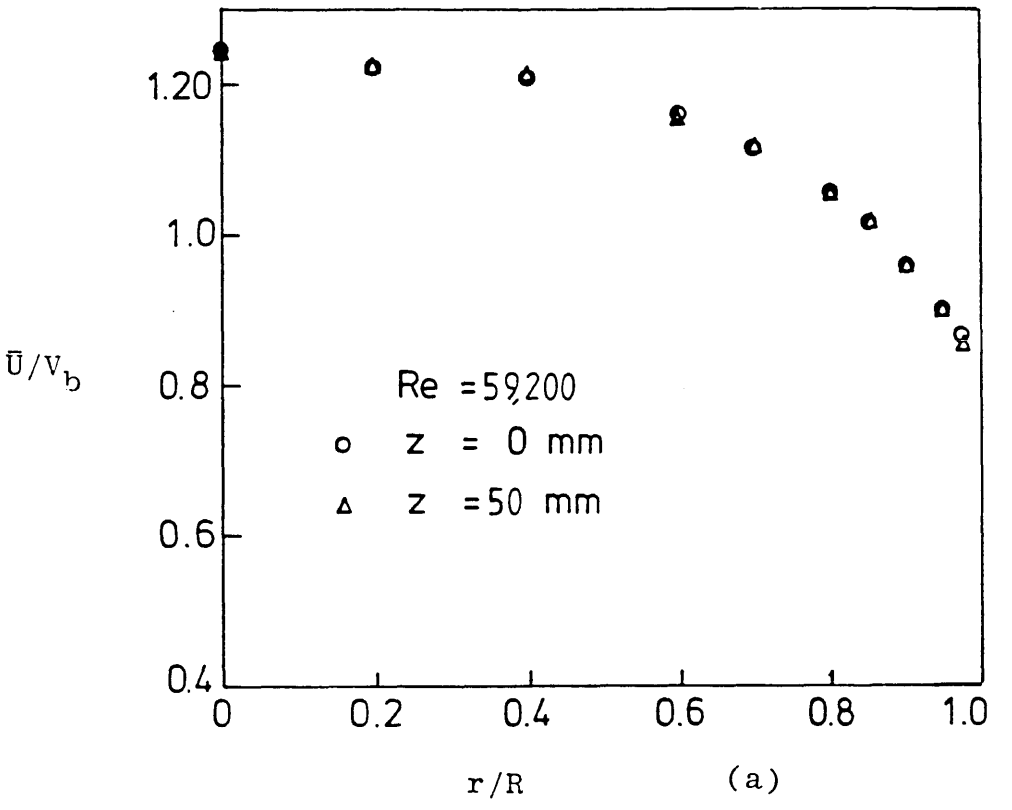

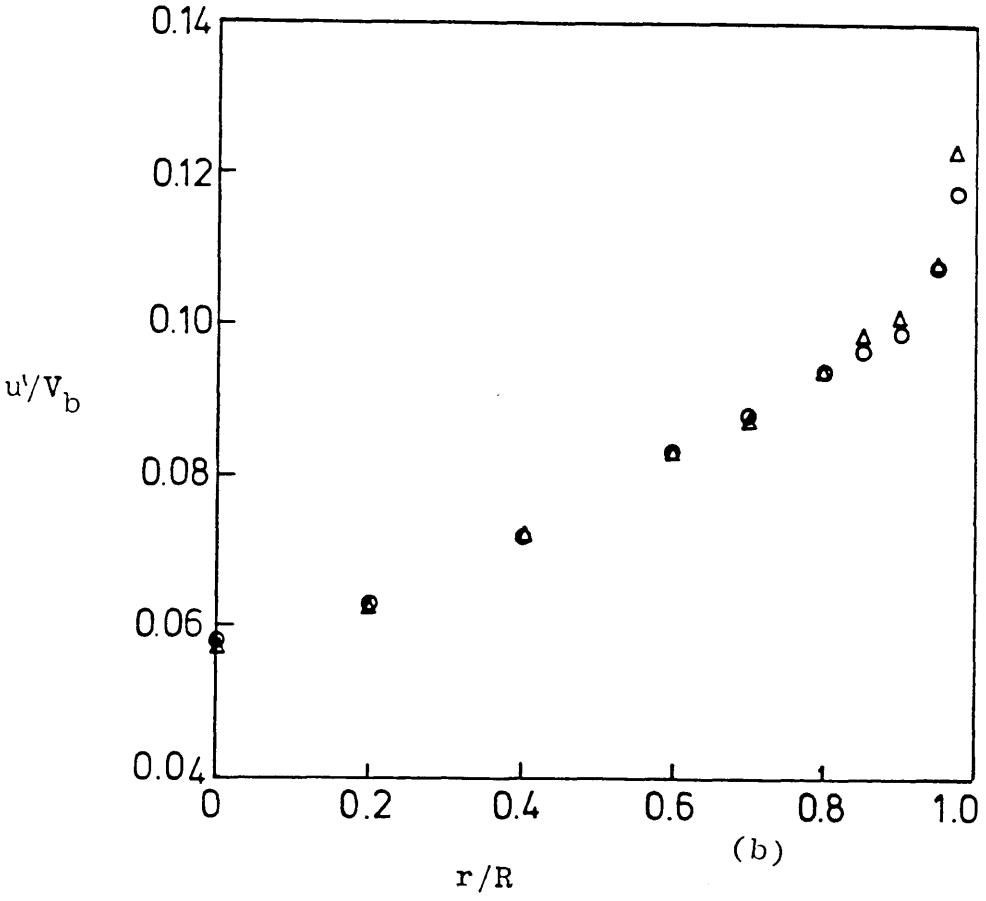

Fig 2.15 Water flow: Axial (a) mean and (b) rms velocities at different axial locations.

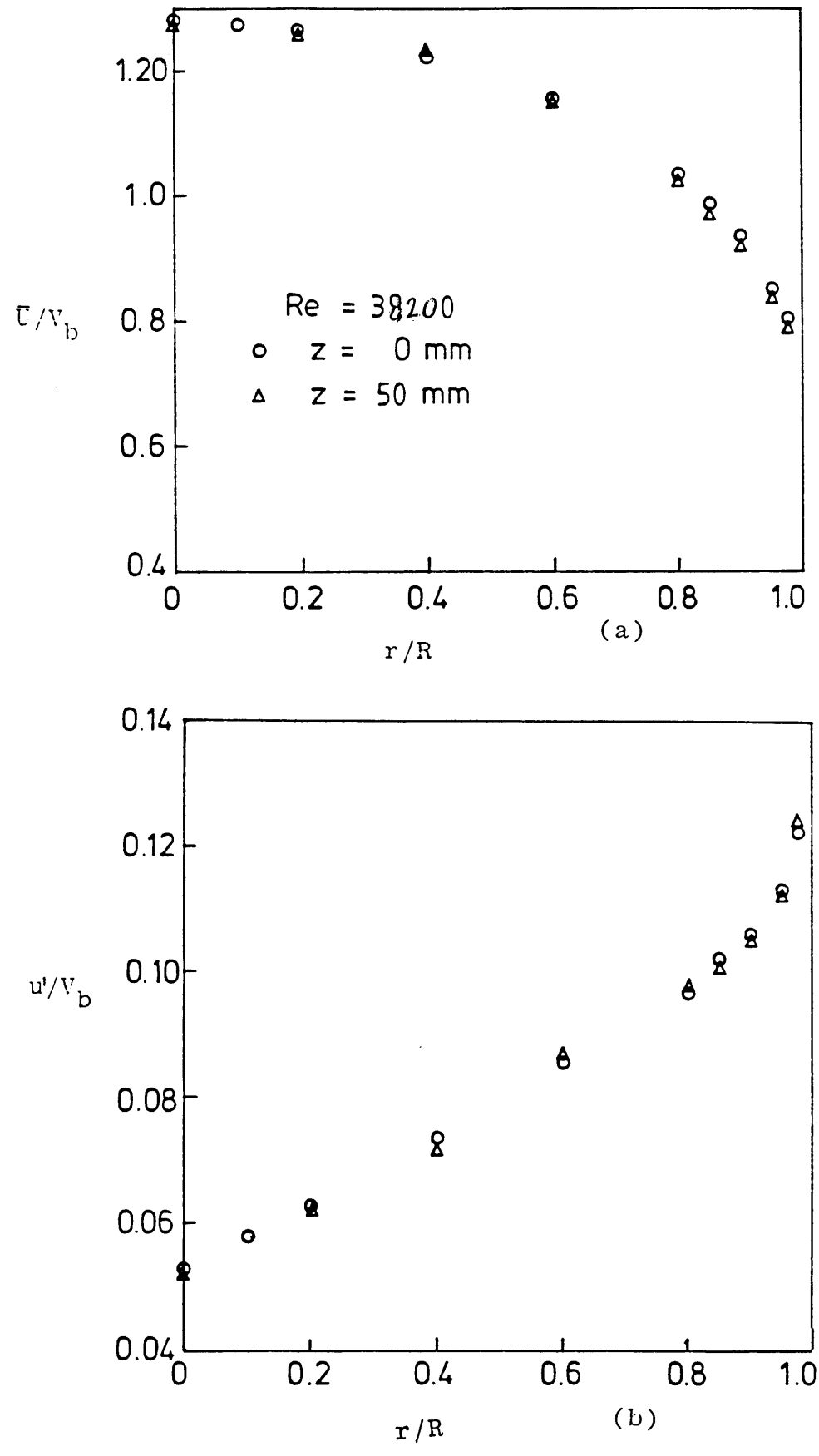

Fig 2.16 Mixture flow: Axial (a) mean and (b) rms velocities at different axial locations.

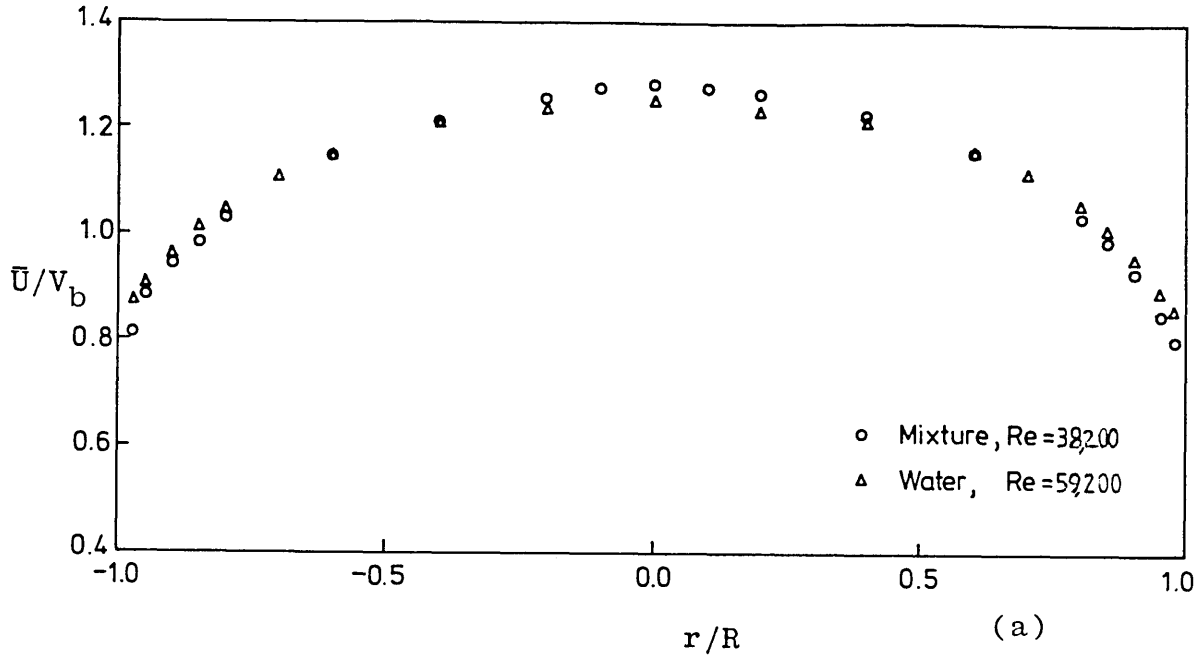

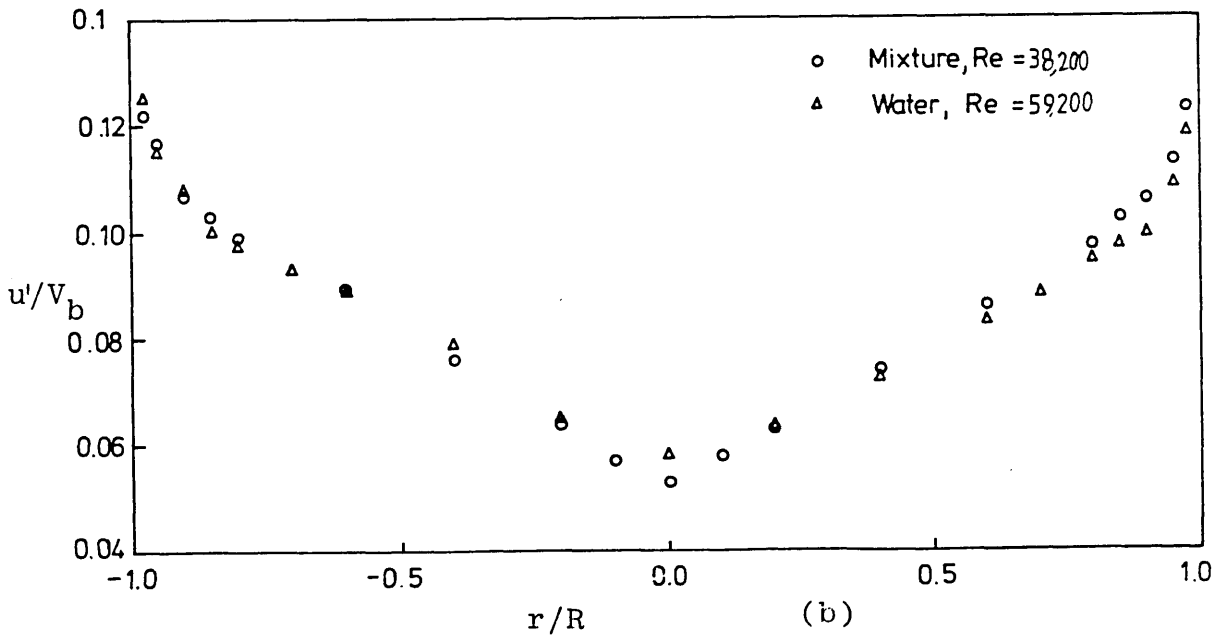

Fig 2.17 Comparison of water and mixture axial velocities; (a) mean, (b) rms.

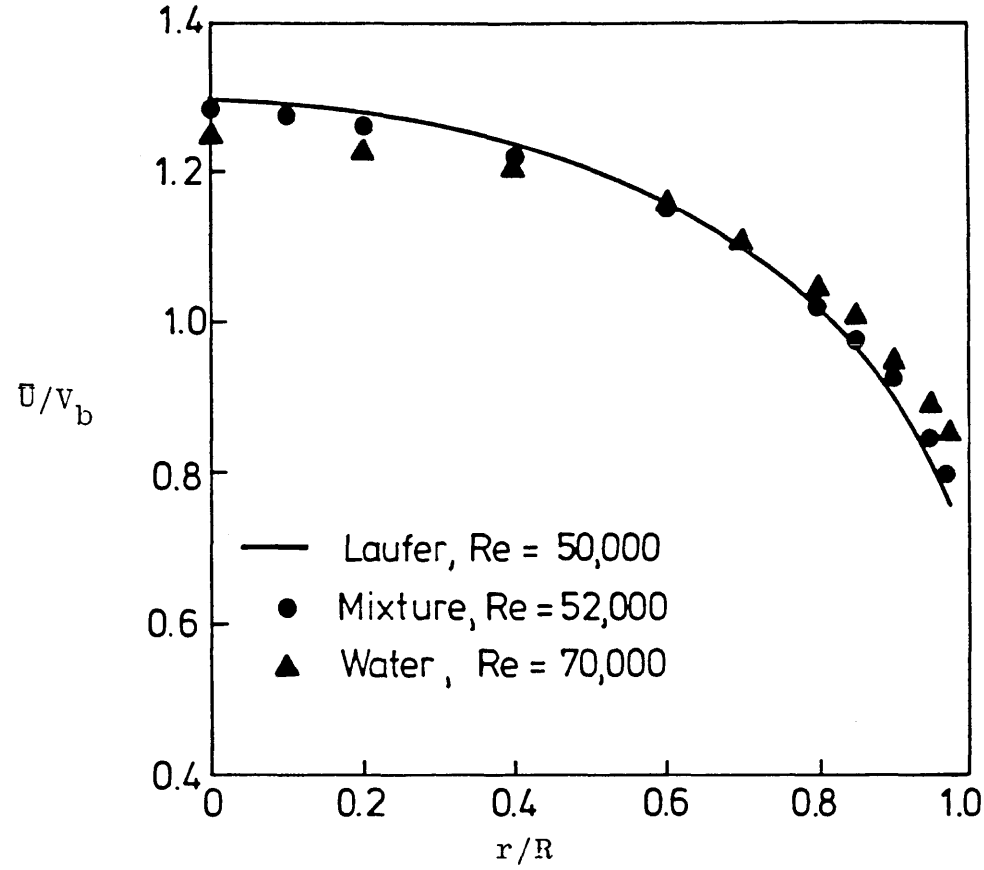

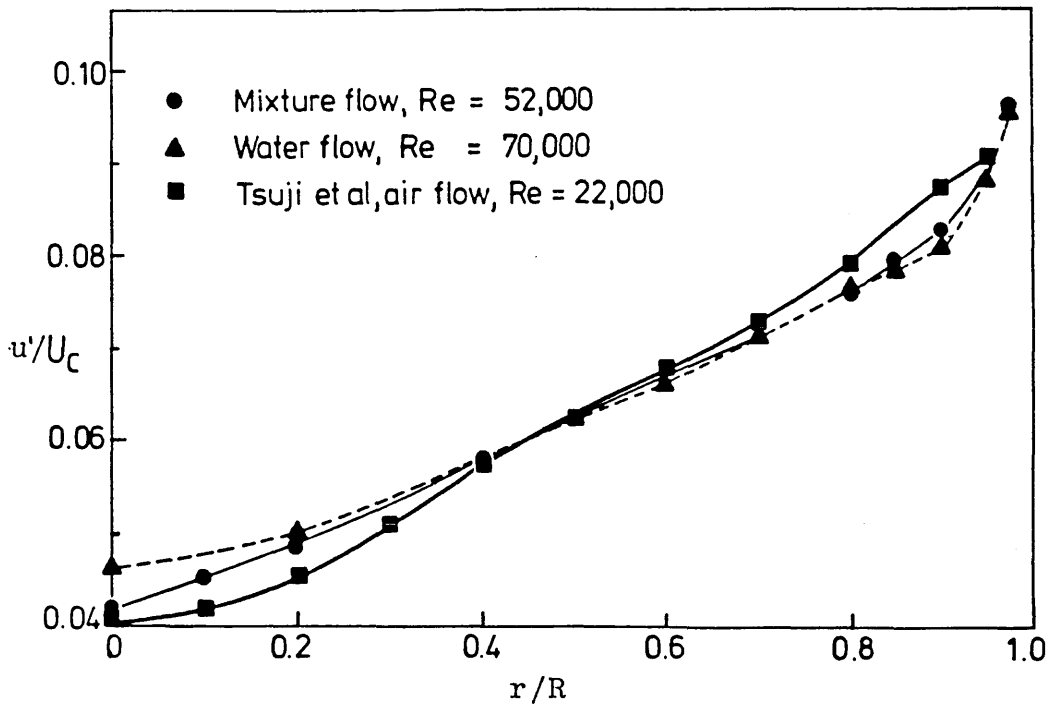

Fig 2.18 Comparison of present study and other investigators.

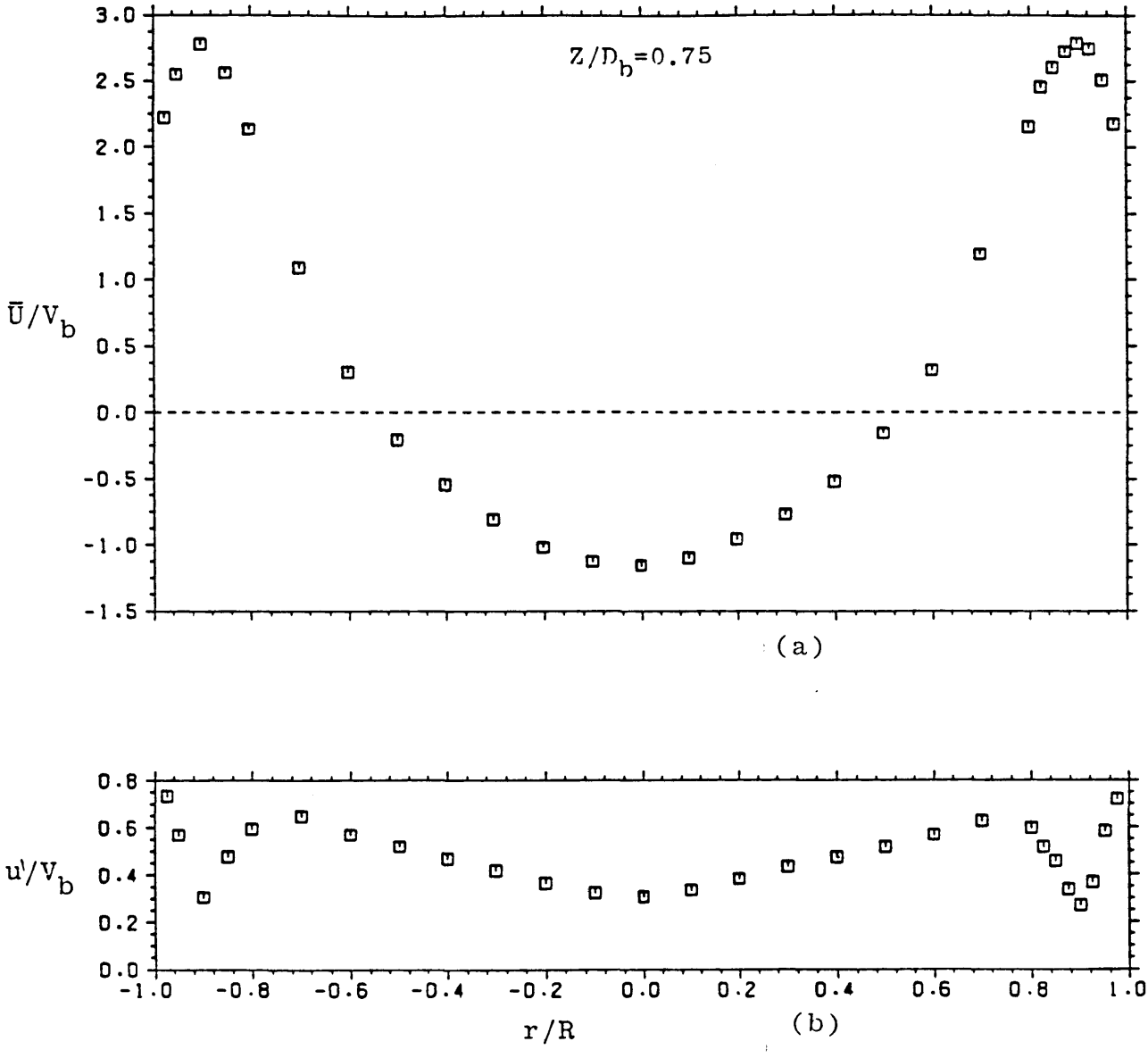

Fig 2.19 The symmetry of axial velocities downstream of baffle over the pipe cross section, V_b=1.89 m/s; (a) mean, (b) rms.

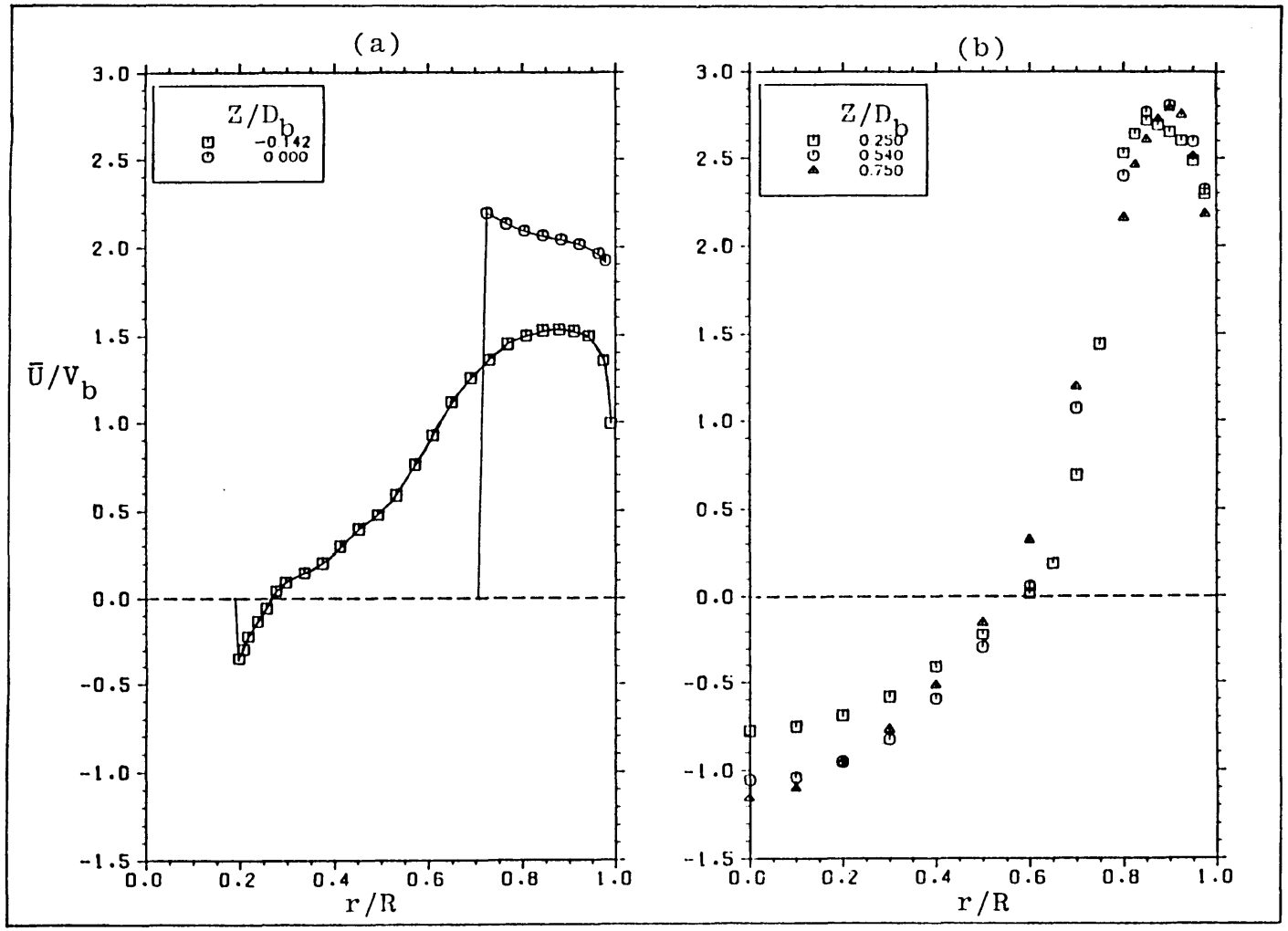

Fig 2.20 Axial mean velocity around the baffle.

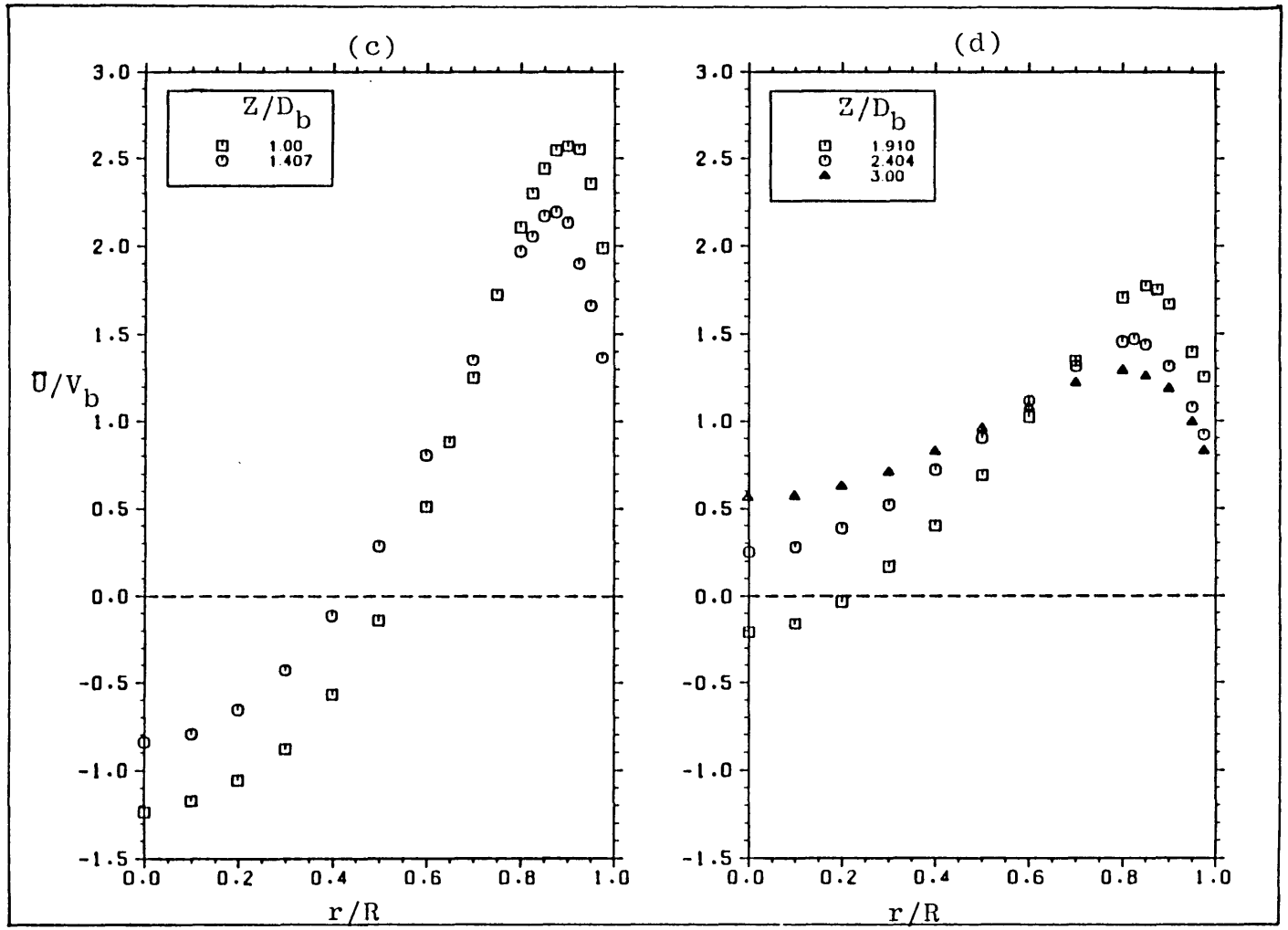

Fig 2.20 Continued.

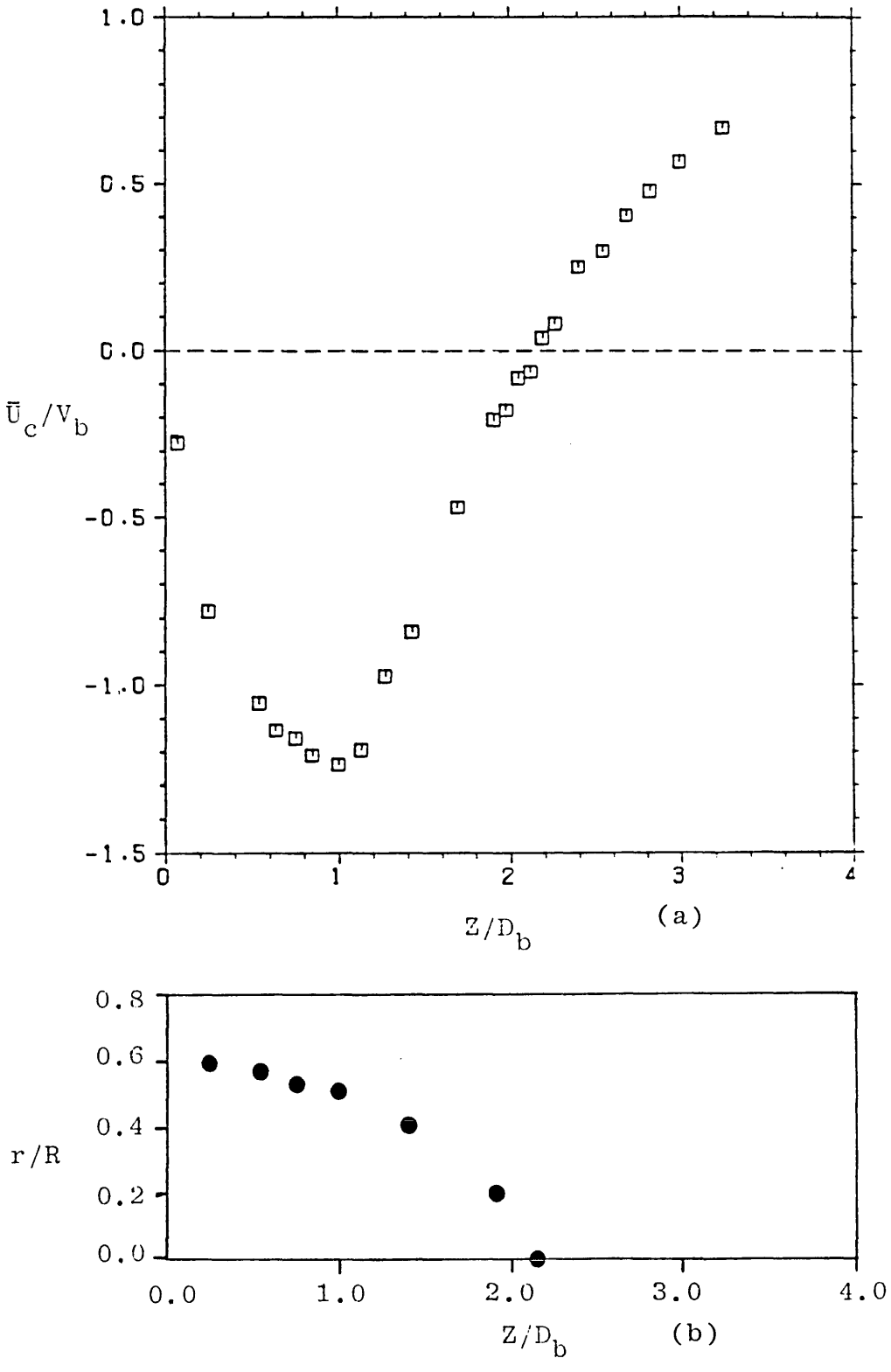

Fig 2.21 Variation of; (a) centreline mean velocity, (b) loci of zero axial mean velocity.

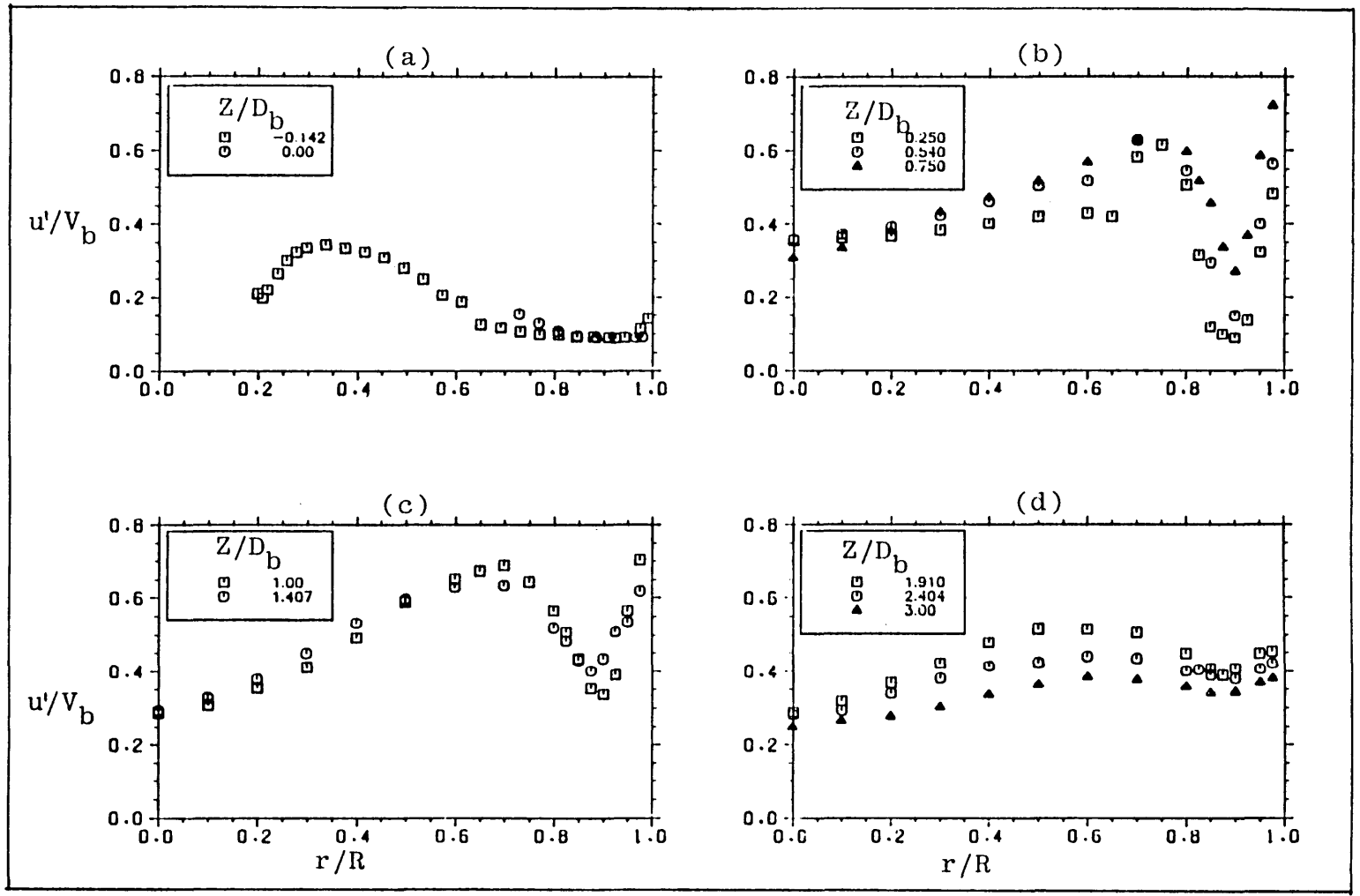

Fig 2.22 Axial rms velocity around the baffle.

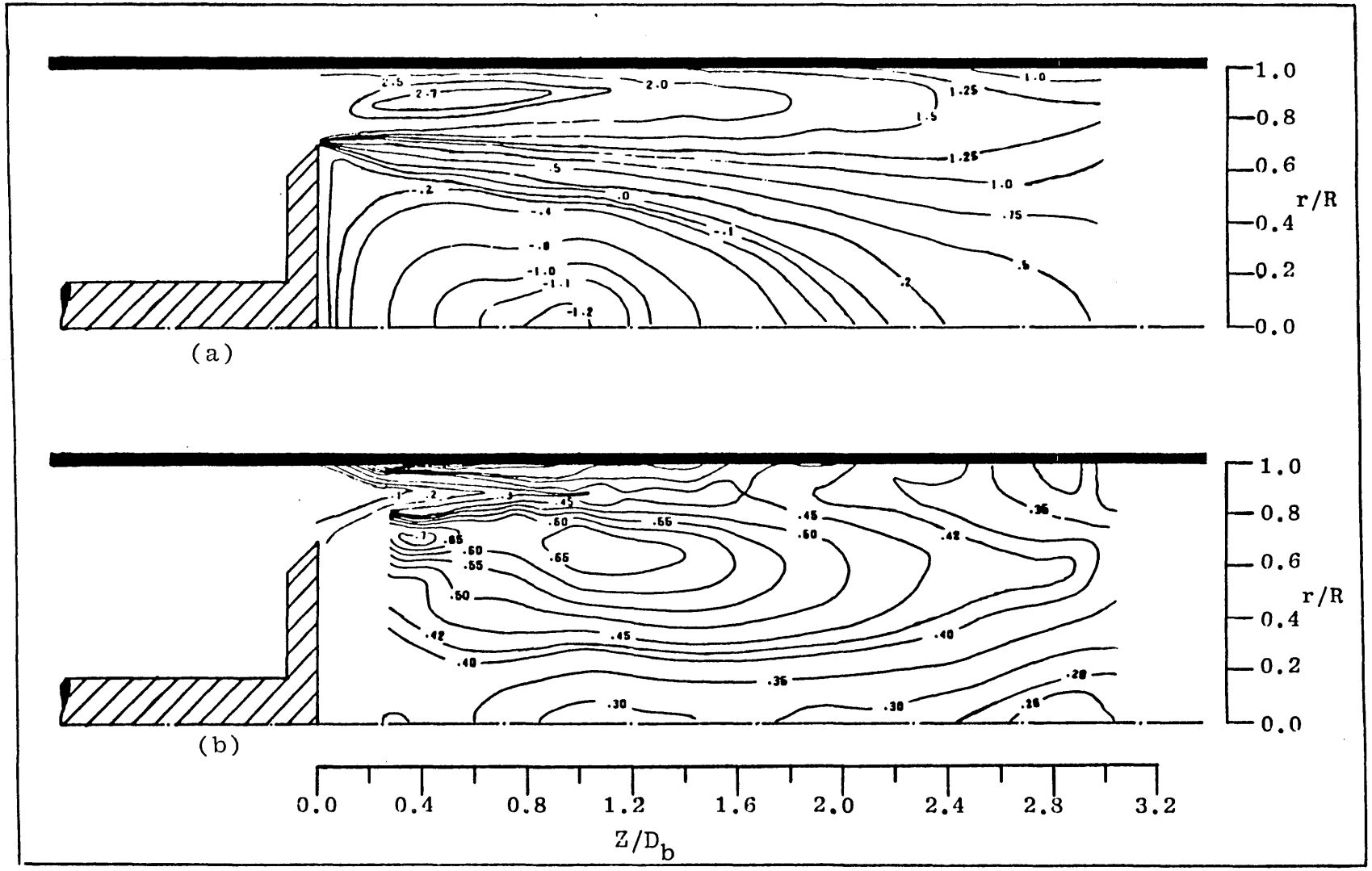

Fig 2.23 Contours of normalised axial mean (a) and rms (b) velocity distributions downstream of the baffle.

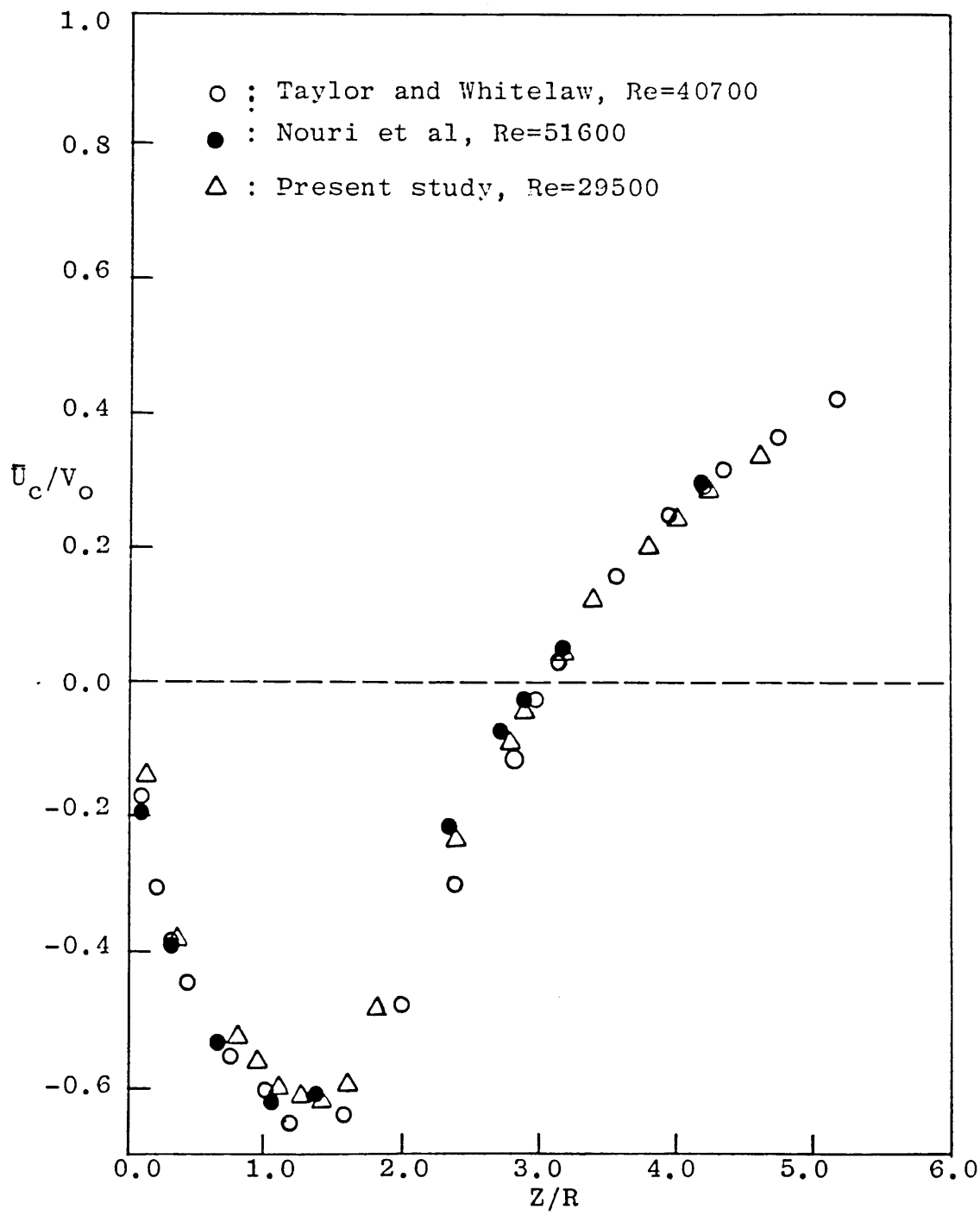

Fig 2.24 Comparison of centreline mean velocity profile of the present study and other investigators.

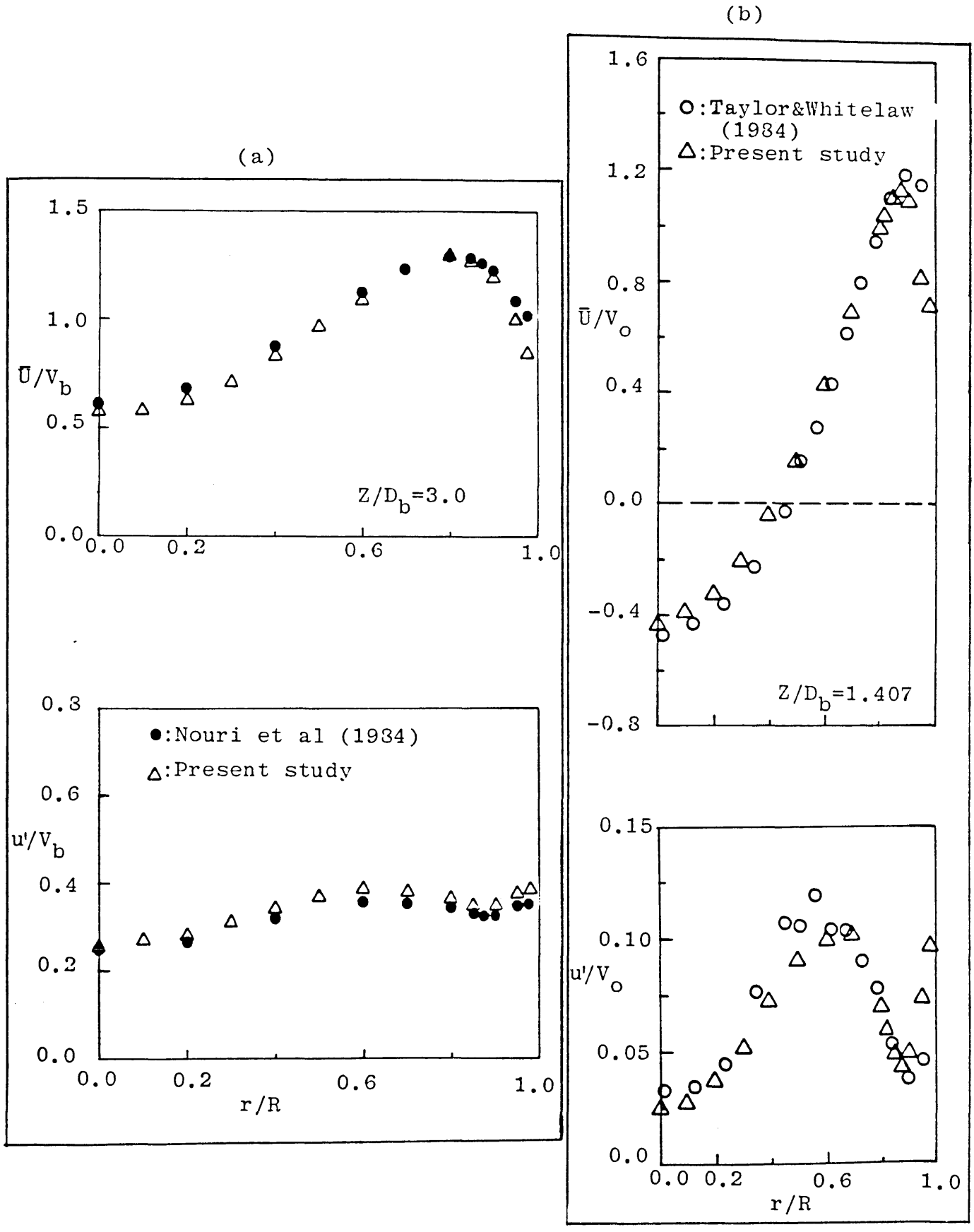

Fig 2.25 Comparison of mean and rms velocities of the present study and other investigators at different axial locations.

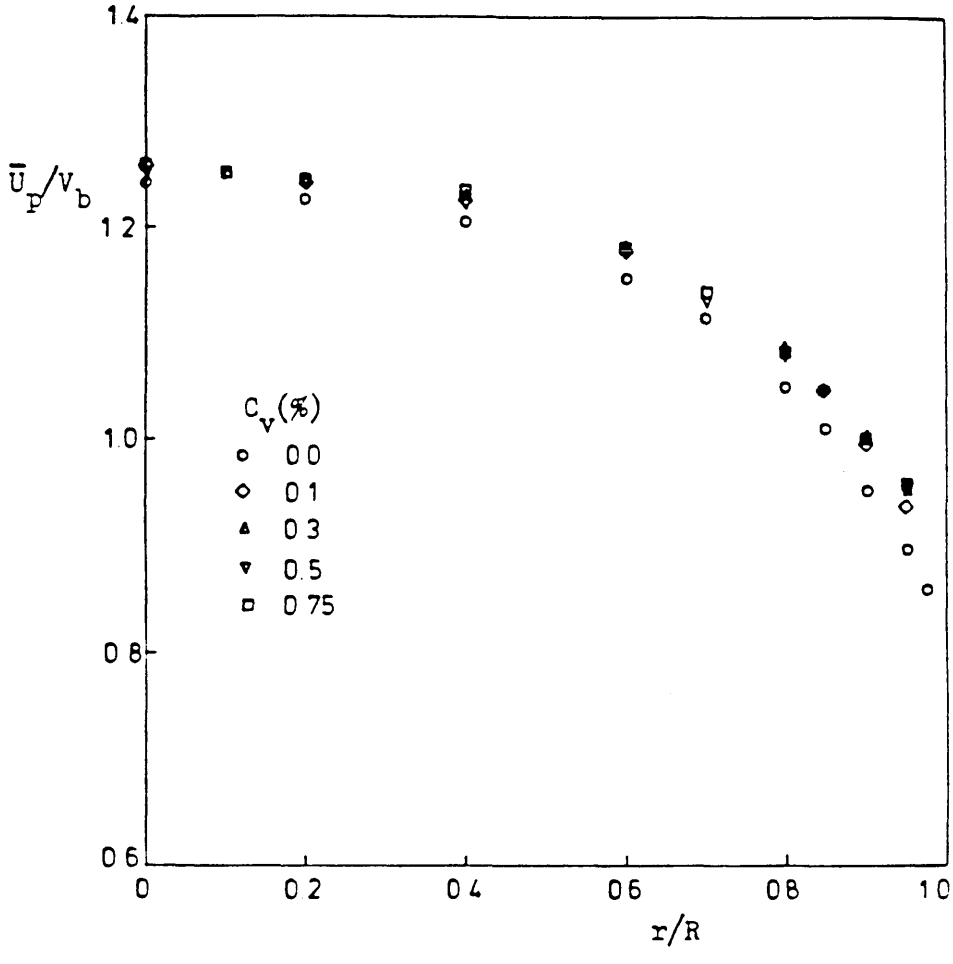

Fig 2.26 Water flow in the pipe: single-phase and particle axial mean velocities.

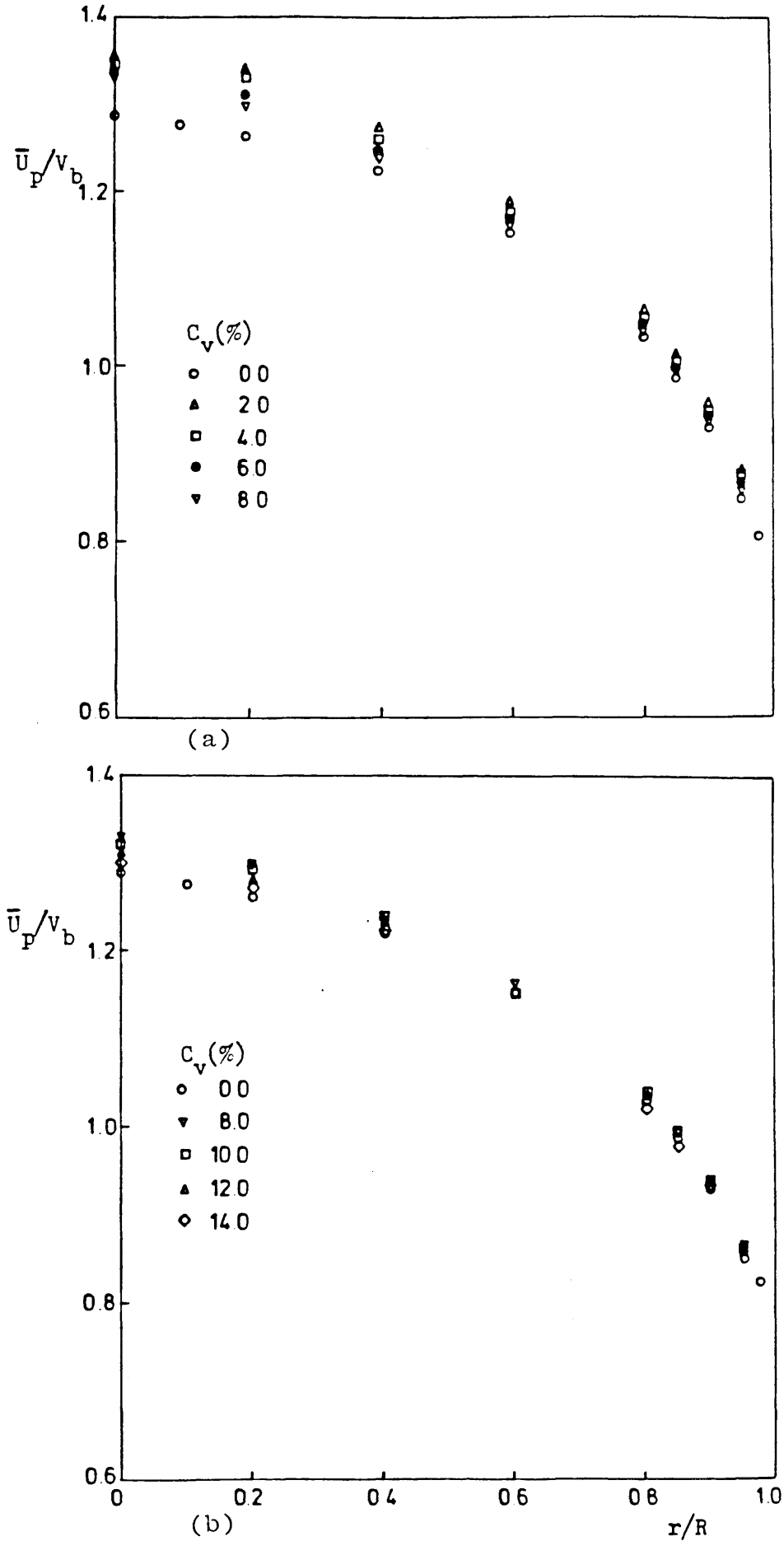

Fig 2.27 Turpentine / tetraline mixture flow in the pipe: single-phase and particle axial mean velocities.

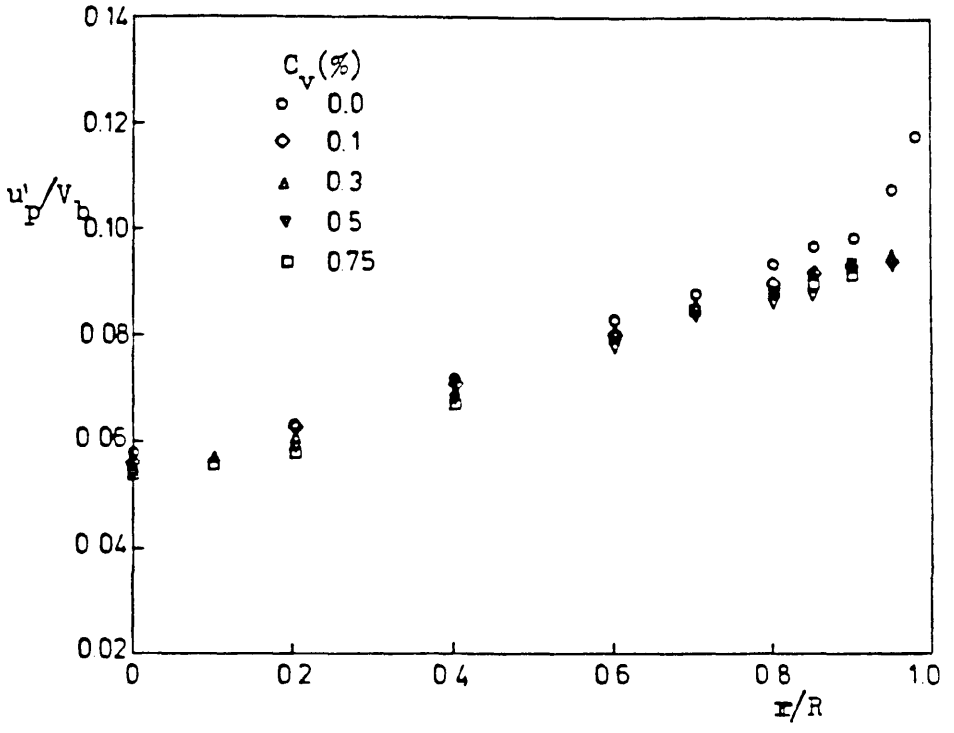

Fig 2.28 Water flow in the pipe: single-phase and particle axial rms velocities.

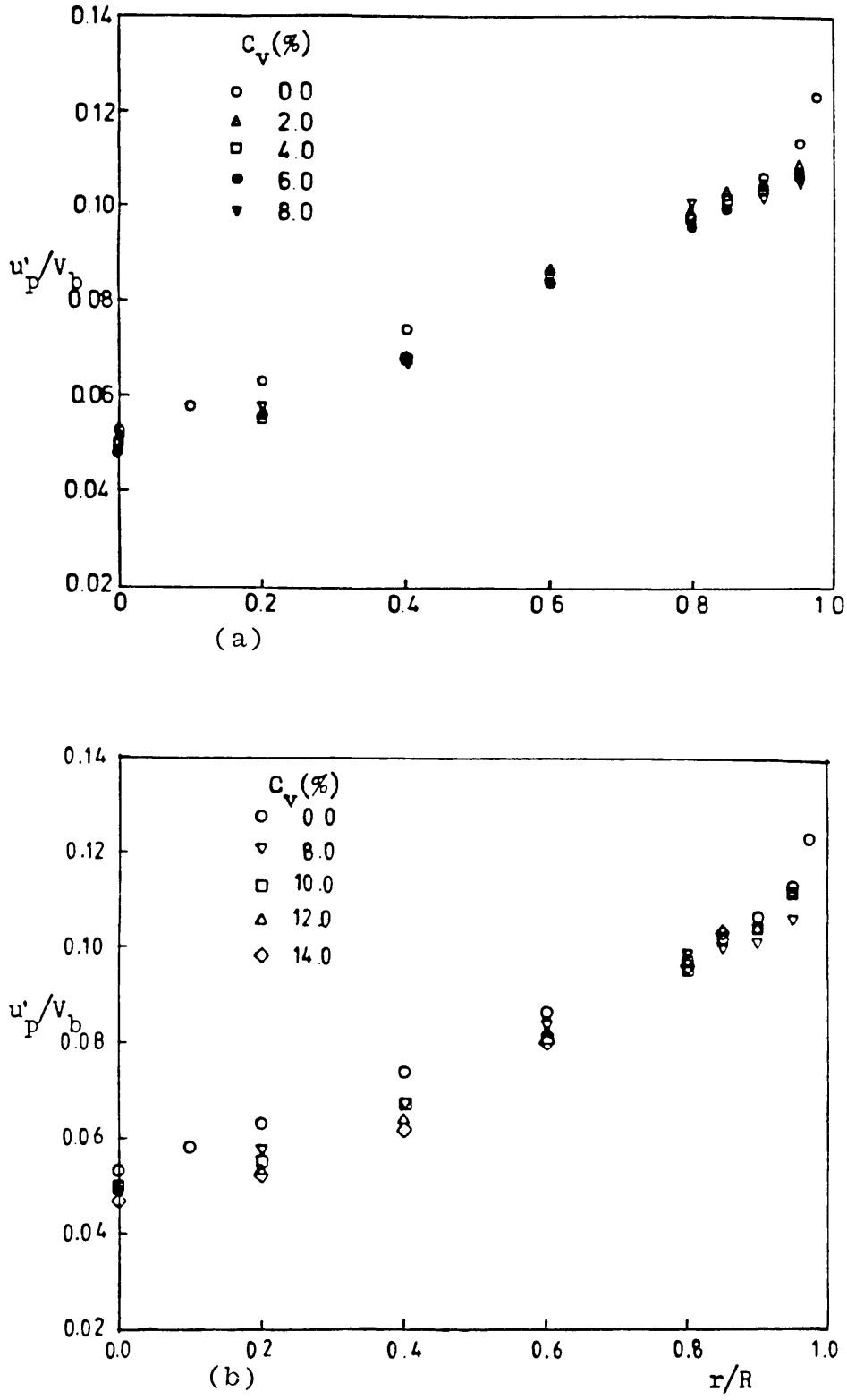

Fig 2.29 Turpentine / tetraline mixture flow in the pipe: single-phase and particle axial rms velocities.

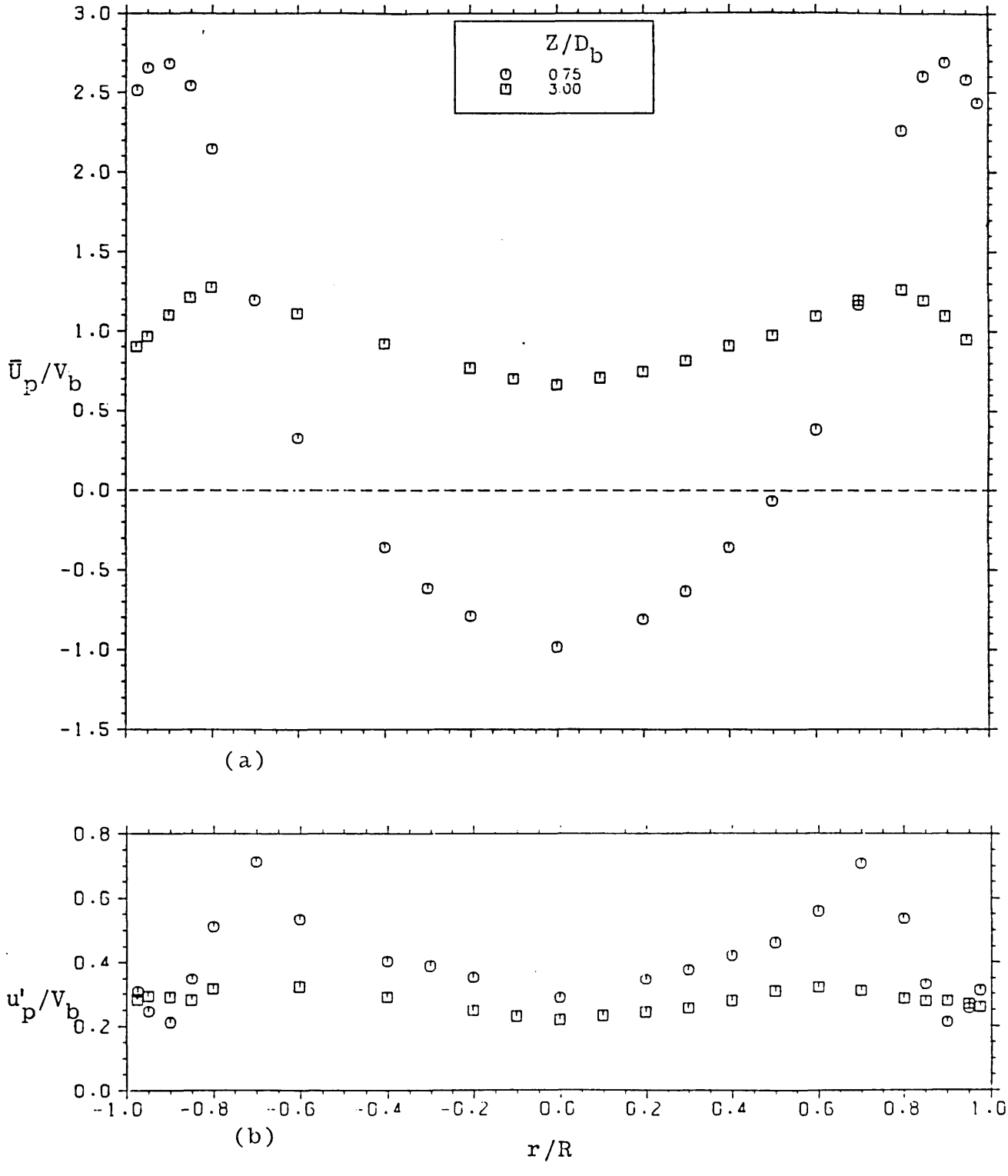

Fig 2.30 Symmetry of profile of mean (a) and rms (b) velocities across the pipe cross section for C_v=4.0% at different axial locations.

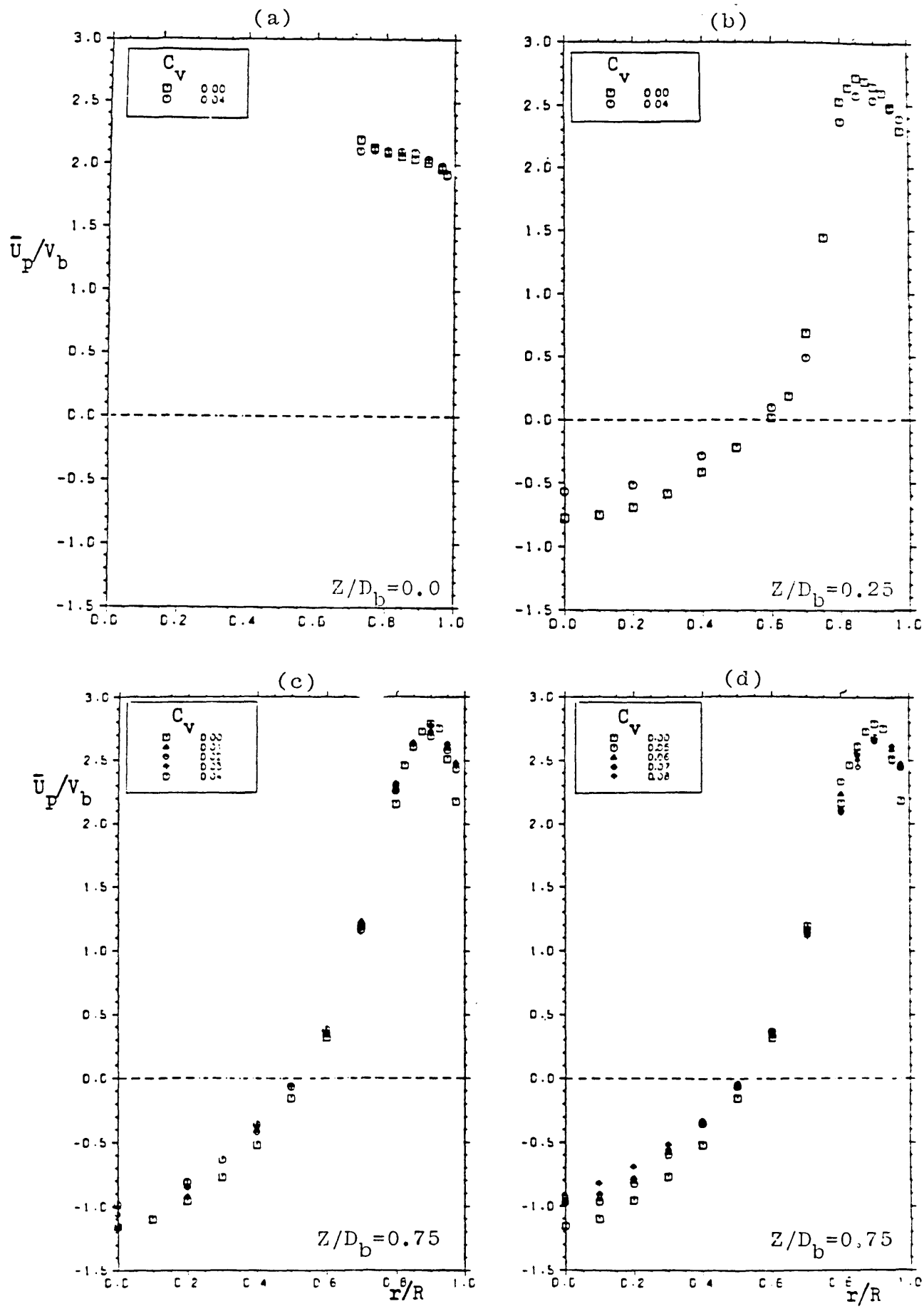

Fig 2.31 Mixture flow in baffled pipe: single-phase and particle axial mean velocities.

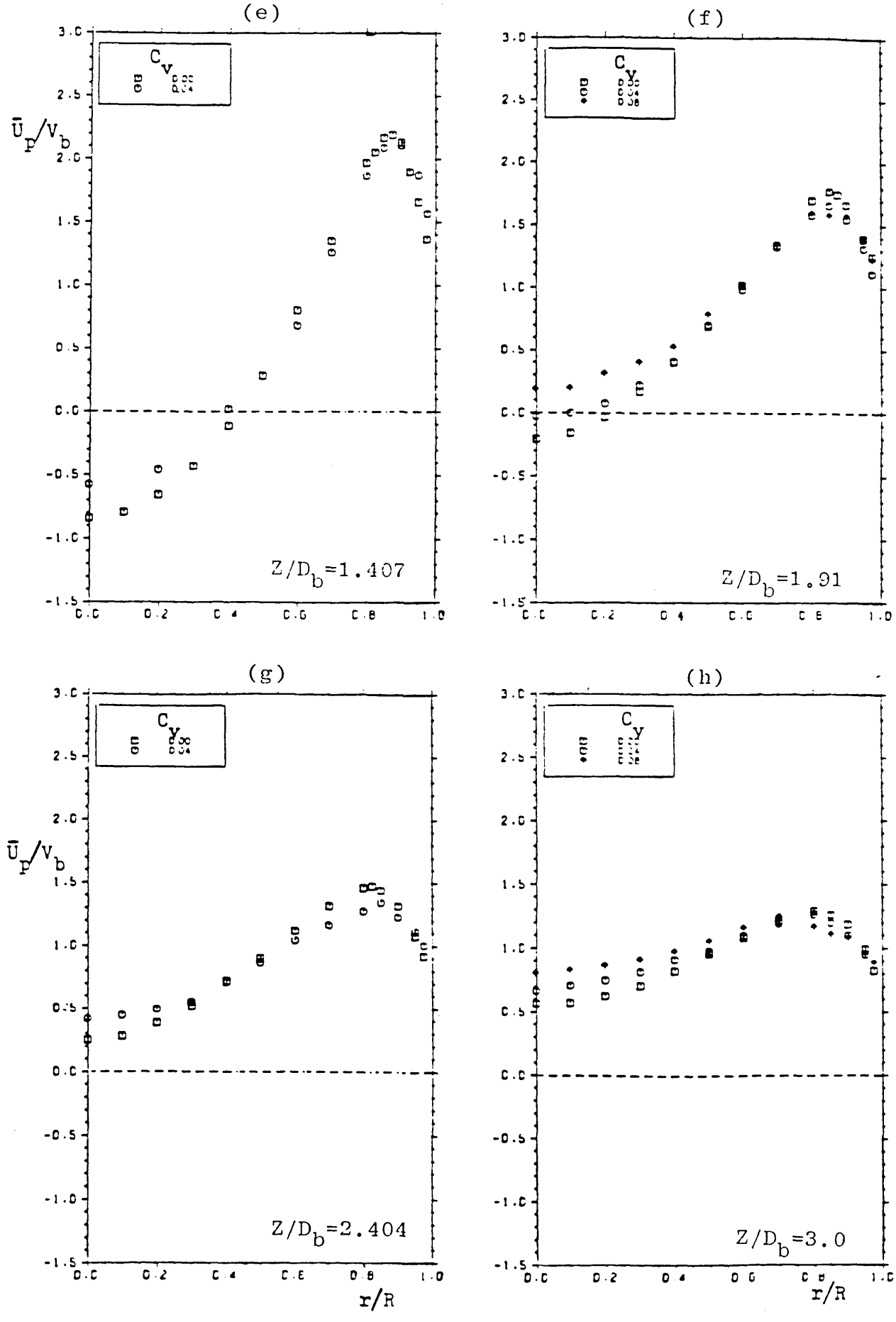

Fig 2.31 Continued.

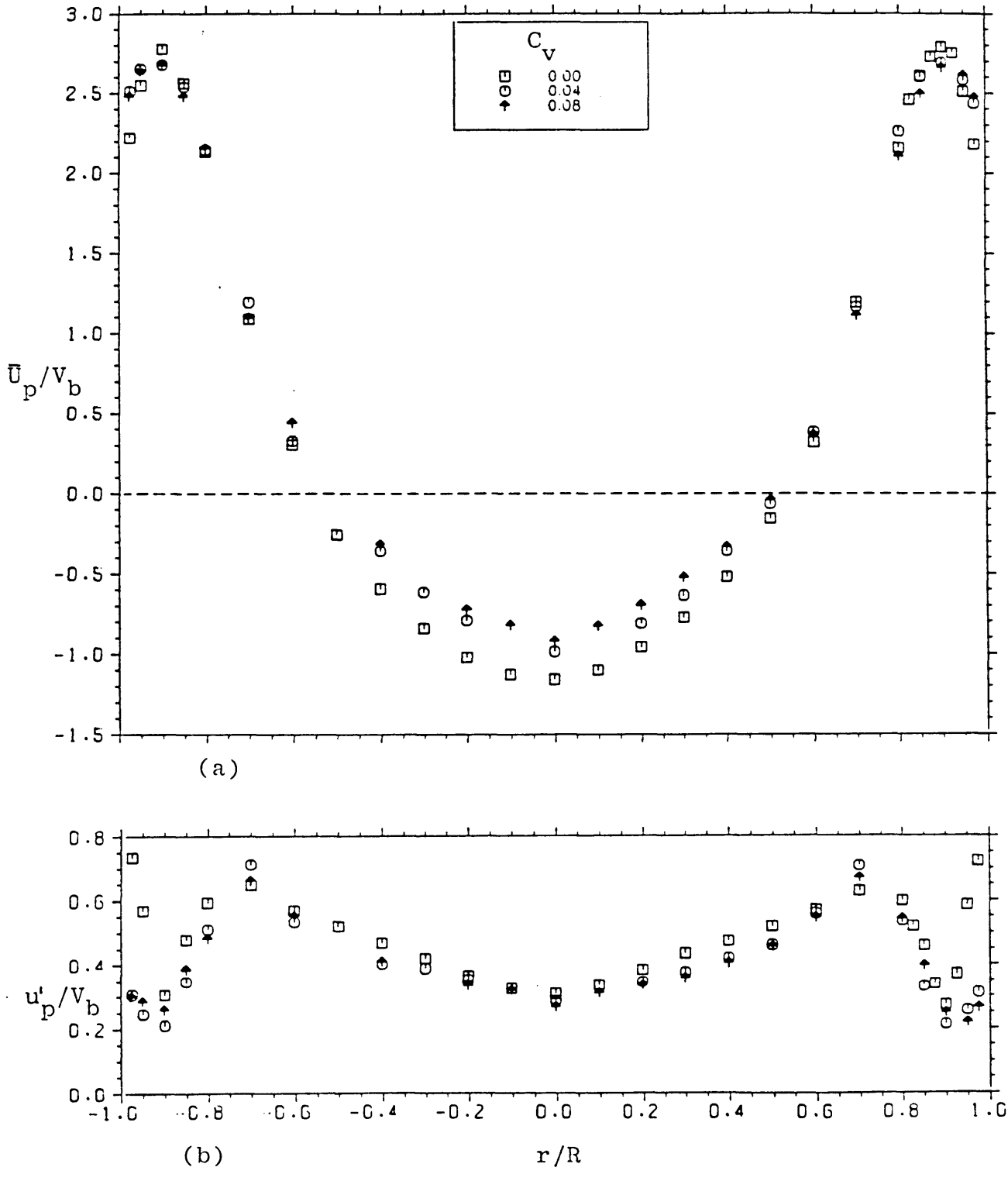

Fig 2.32 Comparison of the symmetry of single-phase and particle mean (a) and rms (b) velocity profiles at $Z / D_b = 0.75$.

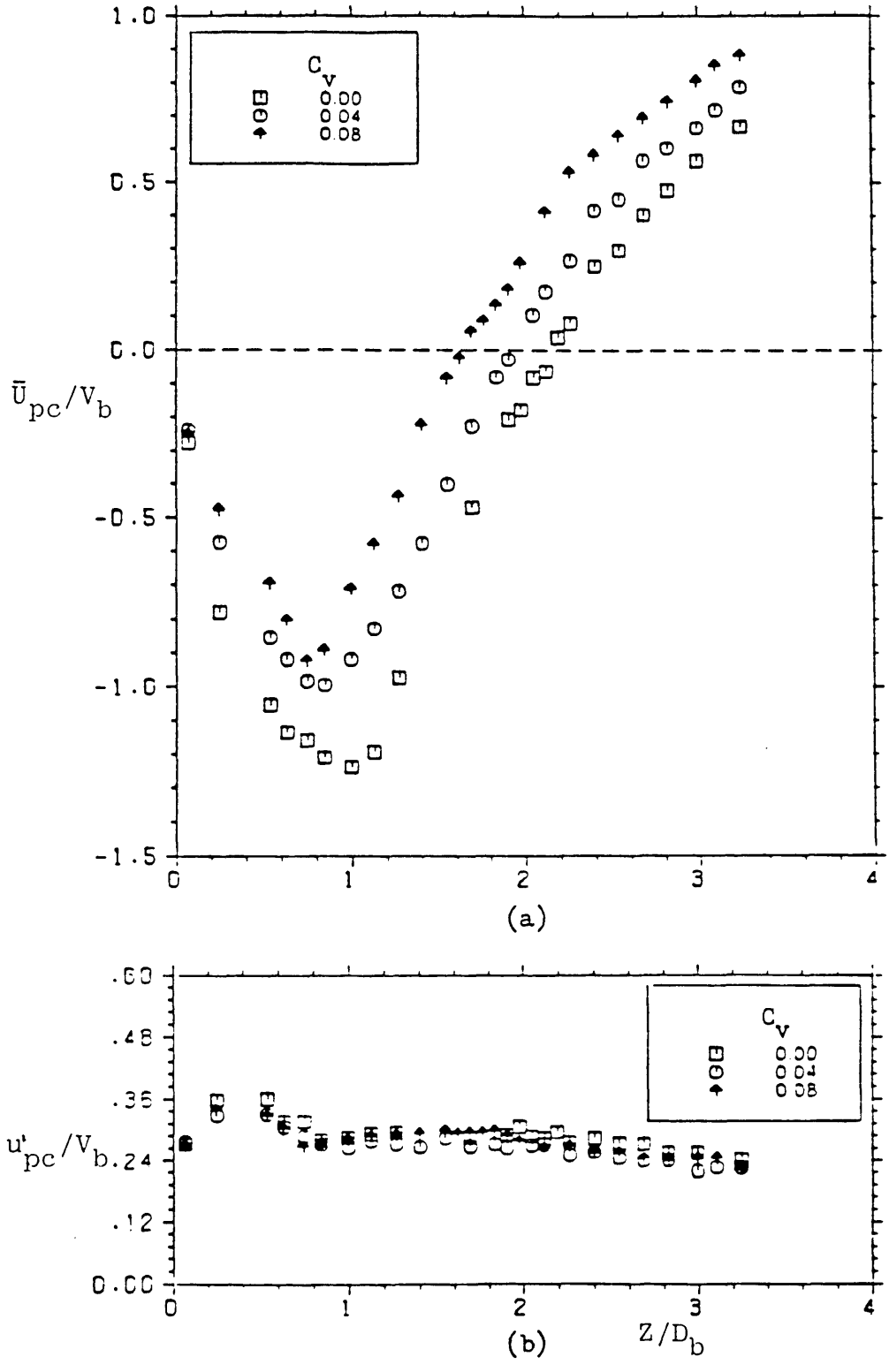

Fig 2.33 Centreline variation of single-phase and paticle axial mean (a) and rms (b) velocity components in the baffle flow.

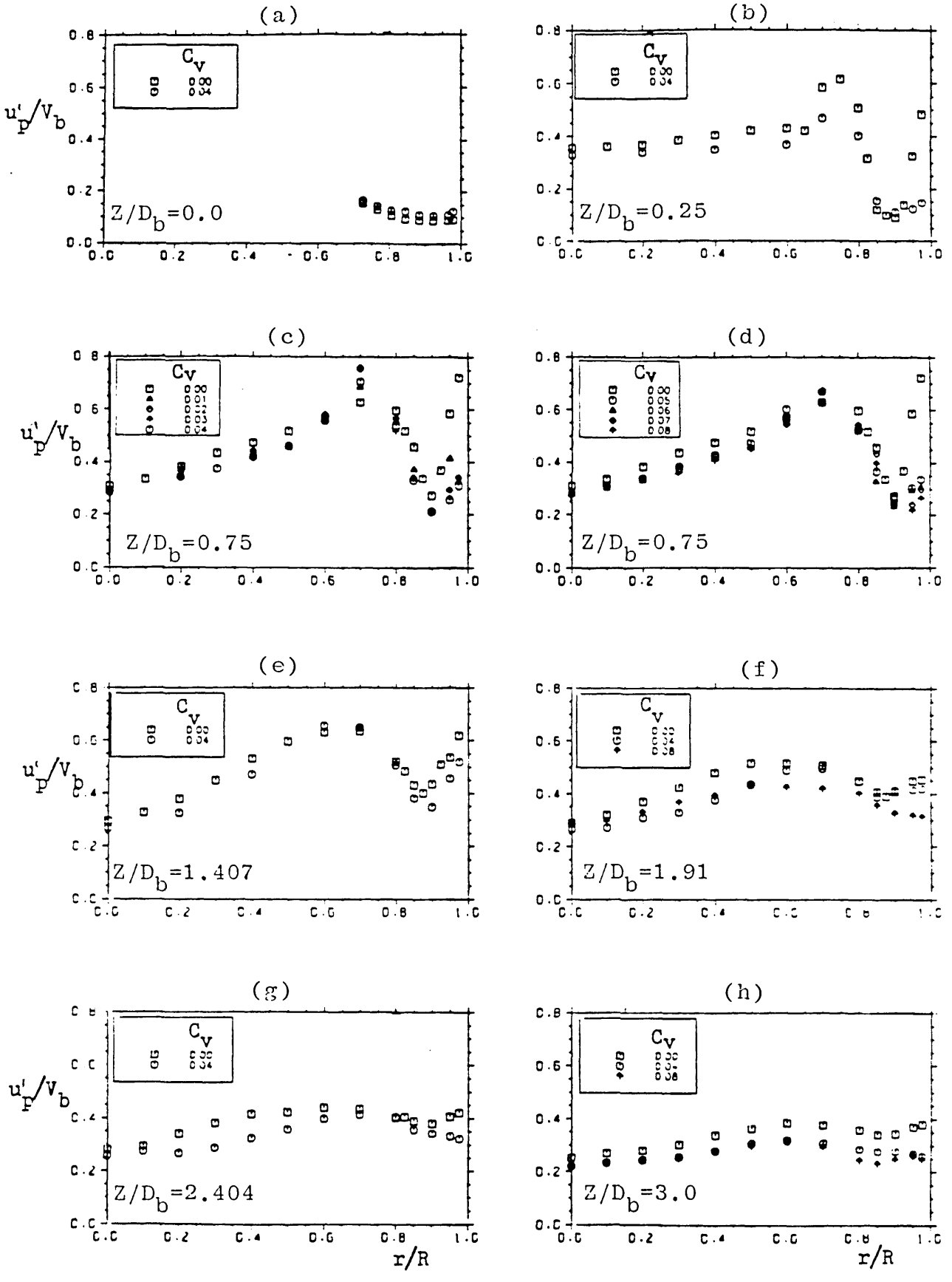

Fig 2.34 Mixture flow in baffled pipe: single-phase and particle axial rms velocities.

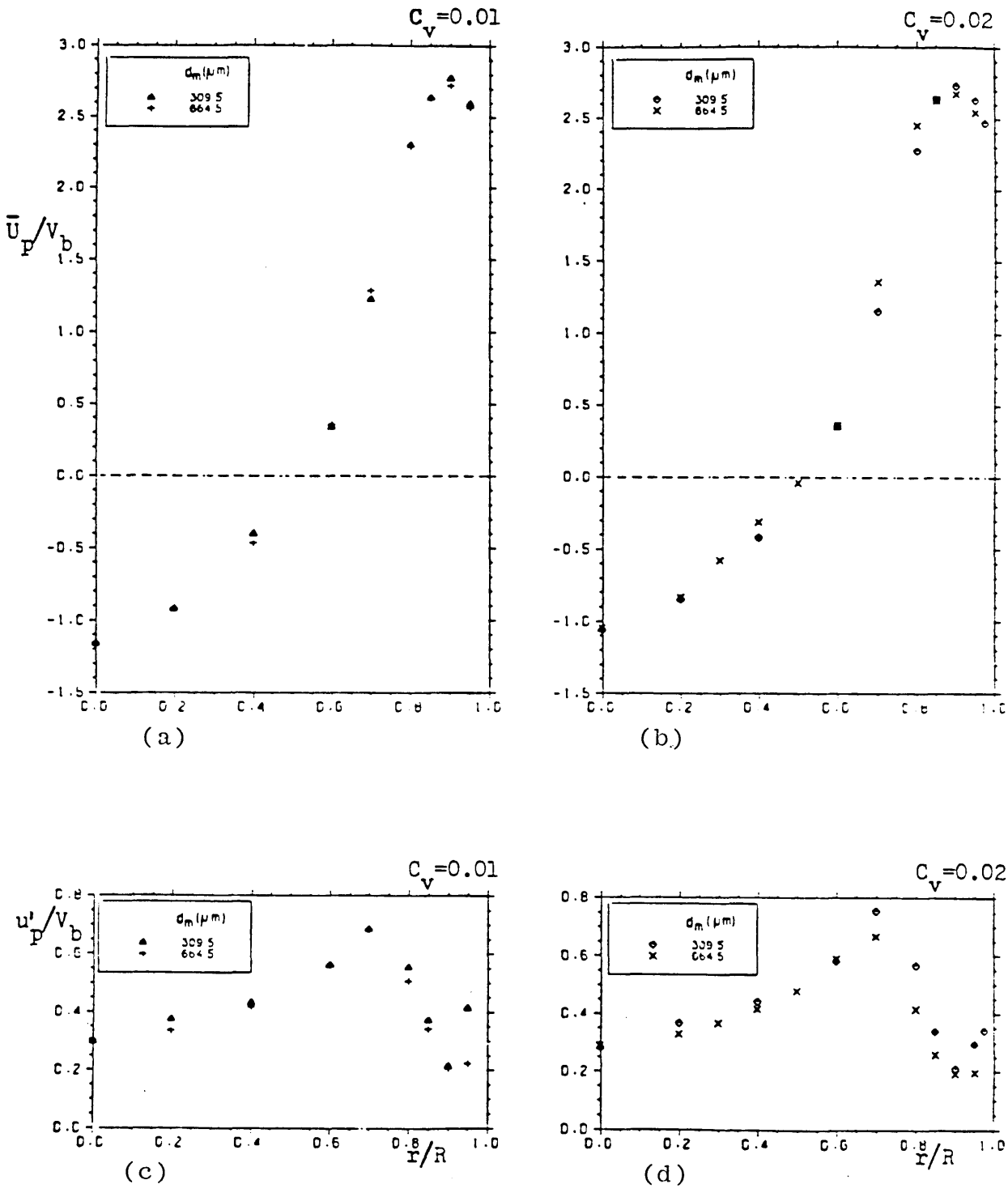

Fig 2.35 Baffled flow: Comparison of axial mean (a and b) and rms (c and d) particle velocities at $Z / D_b = 0.75$ with 310 and 665 μm paticles suspended in the flow.

CHAPTER III

SINGLE AND TWO-PHASE FLOWS IN STIRRED REACTORS

3.1 Introduction

Detailed experimental investigations of single and two-phase flows in a stirred vessel driven by a six-blade disc type impeller are described in this chapter. Laser-Doppler velocimetry was employed to measure the mean and rms velocity components of the single and two-phase flows and, in conjunction with a refractive-index-matching of fluid and particles, to allow the penetration of the laser beams at high particle concentrations for the velocity measurements of the solid-phase particles.

The following section gives details of the flow configurations. The techniques used for the velocity measurements presented in this chapter are similar to those of chapter II and so they are described only briefly in section 3.3 together with an approximation of the errors and uncertainties incurred. Sections 3.4 and 3.5 present the results and discussion of the single and two-phase flows respectively in the stirred vessel for different impeller geometries, rotational speed and two working fluids. Finally, a summary of main findings is given in section 3.6.

3.2 Flow configurations

The results presented in sections 3.4 and 3.5 were obtained in a stirred vessel of diameter T=294 mm with geometry shown in figure 3.1 together with the co-ordinate system adopted in the presentation and discussion of results. The vessel was made of clear cast acrylic (Perspex) and placed inside a rectangular box (trough), also made of Perspex, with either water or a mixture of turpentine/tetraline in the vessel and in the space between the flat surfaces of the trough and the vessel. In this way, the problems associated with refraction of the light beams over the curved surface were reduced, or eliminated in the case when the mixture was used. The baffle thickness was 3 mm and its width was a tenth of the vessel diameter. The geometry of the vessel was the same for both the water and mixture flows except for the baffle thickness which was changed, in the case of mixture

flow, from 3 mm to 4 mm to allow a Platinum resistance thermocouple probe (2 cm long and shielded in a stainless steel cylinder of 3 mm outside diameter) to be fixed on the baffle in order to monitor the temperature of the mixture inside the vessel without introducing disturbances to the flow.

The impeller dimensions are shown in figure 3.2. It comprised six blades spaced at 60 °. Three sizes of impeller were used as shown in the same figure, and the intermediate size (D = C = T/3) is referred to hereafter as the standard geometry. The thickness of the blades and of the impeller disc was 3 mm. The impeller shaft was 12.7 mm in diameter and was driven at speeds of up to 500 rpm by a motor-gear arrangement (Bodine Electric Co, model 179 with model 946 controller). A digital shaft encoder (Digitech Model DR-1034) allowed the rotational speed to be monitored with an accuracy of ± 0.2 rpm. The motor was fixed on a metal plate which was grooved to fit precisely on the Perspex walls of the trough. The cylindrical vessel was located centrally onto the bottom of the trough and a metal shift which protruded through a hole in the bottom of the trough, allowed the vessel to be turned.

Water and a mixture of oil of turpentine and 32.6% by volume tetraline were used as the working fluids. The former was used for most of the measurements presented in this chapter (i.e. for the single-phase and for the two-phase at low particle concentration), and the latter was used for some of the two-phase flow experiments to allow laser beam penetration at high particle concentrations. A temperature rise of the water of about 1 °C per hour was observed during the operation of the mixer and a heat-exchanger was provided in the form of eight brass pipes crossing the trough below the cylinderical vessel. A thermostatic valve (Danfoss AVTA15) was connected to the heat-exchanger water supply and the valve's sensor inserted into the space between the trough and the vessel. The valve control was set so that the water temperature in the vessel was at 20 °C with an accuracy of ±1 °C.

In order to match the refractive index of the mixture to that of the Diakon particles, it was necessary to control the fluid temperature to within ±0.03 °C. Direct temperature

control of the mixture inside the vessel was not possible since the heating and cooling elements would have disturbed the flow so water bath was constructed and the water temperature controlled to within 0.02°C by means of a proportional controller. The water was circulated via a pump through a heat-exchanger coil, made of 6.35 mm diameter copper tubing, and placed in the mixture located between the the rectangular trough and the vessel. Two paddles were placed between the trough and the vessel to stir the mixture in the trough and to increase heat exchanger performance. Approximately 30 minutes were required to raise the mixture temperature inside the vessel by 5 °C above ambient. The short-term temperature stability of the mixture temperature in the cylindrical vessel (up to 60 minutes) was within 0.04 °C and the long-term within 0.1 °C.

The two most important dimensionless groups charactrising the flow in the baffled stirred reactors are the Reynolds number (Re) and power number (N_p) defined as

$$Re = N D^2 / \nu \qquad (3.1)$$

and

$$N_p = P / \rho N^3 D^5 \qquad (3.2)$$

where N is the impeller rotational speed in revolutions per second, D is the impeller diameter and P is the power input to the fluid. As the Reynolds number is the ratio of inertial to viscous forces, the power number, N_p, represents the ratio of flow-producing pressure differences to the inertial forces and can be evaluated by measuring the torque induced, T_r, on the fluid by the rotation of the impeller with

$$T_r = P / 2 \pi N \qquad (3.3)$$

A complete range of torque measurements was made by Yianneskis et al (1987) for impeller speeds of 200 to 500 rpm (i.e. Reynolds numbers of 30,000 to 78,000) and nine impeller and clearance geometries. The maximum error in these torque measurements

was about 10% at the lower range of the impeller speed (Re=30,000) and the results were consistent with previous measurements, such as those of Ulh and Gray (1966). Therefore, in the present work values of N_p were obtained directly from the data of Yianneskis et al (1987) except at N=50 rpm (corresponding to Re=8,000 for D=T/3 impeller) where N_p was obtained by linear interpolation of the data. The flow conditions for the different impeller geometries for both the single and two-phase flows are listed in table 3.1.

Table 3.1 Flow conditions

	Single-phase			Two-phase		
	Water flow			Water flow		Mixture flow
Impeller diameter (D)	T/2	T/3	T/4	T/2	T/3	T/3
Impeller clearance (C)	T/3	T/3	T/2,T/3,T/4	T/4	T/3	T/4
Impeller speed (N), rpm	125	300	400	150	300	313
Impeller tip velocity (V_t), m/s	0.962	1.54	1.54	1.115	1.54	1.6
Reynolds number (Re), $x10^3$	45	48	36	54	48	32.5
Power number (N_p)	4.9	4.7	4.2	5.0	4.7	4.4
Flow response time (τ_f), ms	30	13	9.6	25	13	12

The impeller tip velocities of table 3.1 were calculated from the expression $V_t=\pi ND$ and the flow response time from the ratio of impeller width (h) to the impeller tip velocity (i.e. h / V_t). Peliminary measurements showed that air entrainment through the free surface took place at high impeller rotational speeds and, as a result, the measurements were limited to maximum speeds of 400, 300 and 130 rpm for D=T/4, T/3 and T/2 respectively at the maximum impeller clearance of C=T/2. Reduction in the clearance allowed a small increase of speed and the corresponding maximum speeds for C=T/4

(smallest clearance) were 420, 315 and 150 rpm. It was also noted that the free surface remained practically flat with no air entrainment up to about 0.35 of the maximum speed. Above this speed the whirlpool vortex on the surface became stronger and penetrated deeper into the flow as speed increased. At the above maximum speeds, the whirlpool penetrated down to 10 mm from the free surface and none or very few bubbles were present in the water.

Diakon and lead-glass particles of different sizes were used as the solid-phase in the low particle concentration two-phase flow experiments, and Diakon particles were used for the higher concentration two-phase flow experiments where the refractive index of the mixture was matched to that of the particles. The maximum particle concentration with which measurements were possible was 0.02% when the particles were suspended in water, and this was increased to 2.5% when the refractive-index-matching technique was employed. The properties of the fluids and of the particles are given in table 3.2, for water and for the mixture flows respectively. The terminal velocity for Stokes flow (V_{gs}) and for turbulent flow (V_{gt}) and the time response of the particles (τ_p) were calculated according to the procedure described in section 2.2.

CHAPTER III

Table 3.2 Fluid and particles properties

(I) Water flow at room temperature

Properties at 20 °C	Water	Diakon		Leadglass	
Density (ρ), kg / m^3	998	1180		2950	
Kinematic viscosity (ν), x10^{-6} m / s^2	1.02	-----		-----	
Refractive index (n), at λ=589.6 nm	1.334	1.490		1.60	
Particle size range, μm	-----	180-350	600-850	210-255	310-415
Particle mean diameter (d_p), μm	----	272	725	232.5	367.5
Particle terminal velocity, V_{gs}, (mm/s)	----	7.2	51.7	57.5	144
Particle terminal velocity, V_{gt}, (mm/s)	----	38	62	116	146
Particle response time (τ_p), ms	----	4.0	34	9.0	22.0

(II) Mixture flow at 28.5 °C

Properties at 28.5 °C	Mixture	Diakon
Volumetric percentage of tetraline (C_m)	32.6	----
Density (ρ), kg / m^3	894	1180
Kinematic viscosity (ν), x10^{-6} m / s^2	1.54	-----
Refractive index (n), at λ=632.8 nm	1.4884	1.4884
Particle size range, μm	----	590-730
Particle mean diameter (d_p), μm	----	665
Particle terminal velocity (V_{gs}), mm/s	----	50
Particle terminal velocity (V_{gt}), mm/s	----	76
Particle response time (τ_p), ms	----	21

CHAPTER III

Particle suspension

Due to the three-dimensional nature of the flow in the stirred vessel and the existence of near-stagnant flow regions in the vessel, it was necessary to establish the amount of particle settling that took place. This was carried out by visual observation of the particle suspension and of the quantity of particles setted at the bottom of the vessel.

Diakon particles of diameters up to 700 μm remained suspended in the flow with the standard impeller geometry (D = C =T/3) at the maximum operational speed (N =300 rpm), but for larger diameters they began to settle on the bottom of the vessel. The glass particle sedimentation in the same geometry and at the same speed was different, due to larger density, so that about 50% of the 232.5 μm diameter particles were suspended in the flow and the rest were deposited on the vessel bottom. With 367.5 μm diameter glass particles, only a small number remained suspended and the rate of arrival of Doppler signals was extremely slow. By changing the geometry to D=T/3 & C=T/4 for Diakon and D=T/2 & C=T/4 for lead-glass, more vigorous mixing was achieved near the bottom of the vessel and a large proportion of particles remained in suspension: the maximum impeller speed in the first case was 313 rpm with which more than 95% particles were suspended. The impeller speed for the second geometry had to be reduced to 150 rpm to ensure that no air bubbles were entrained into the flow and about 90% of the 232.5 μm diameter glass particles were suspended in the flow and at least 50% of the 367.5 μm glass particles. The results are presented in section 3.5 for the six two-phase flow cases listed in table 3.3.

Concentration gradients could be observed visually in the flow along the height of the vessel and were more prominent as the particle size increased and steeper with glass particles than with Diakon particles. A relative cocentration gradient along the height of the vessel was quantified for the Diakon particles and the result is presented in sub-section 3.5.2. The measurements with the first five cases in table 3.3 were made in water at low particles concentration (C_v=0.02%) and the last case with the mixture of turpentine and tetraline and particle volumetric concentrations of up to 2.5%. It is anticipated that the results of the first five cases are unaffected by the variation of concentration, as the particle

separations are large and particle-to-particle interactions should be negligible. These effects are expected to be more significant in the flow of case 6 where the average particle concentration was larger by a factor of 125 (i.e. C_v =2.5%).

Table 3.3 Two-phase flow configurations investigated

Case NO.	Particle material	d_p (μm)	D	C	N (rpm)	Temperature (°C)	C_v (%)
1	Diakon	272	T/3	T/3	300	20±1.0	0.02
2	Diakon	725	T/3	T/3	300	20±1.0	0.02
3	lead-glass	232.5	T/3	T/3	300	20±1.0	0.02
4	lead-glass	232.5	T/2	T/4	150	20±1.0	0.02
5	lead-glass	367.5	T/2	T/4	150	20±1.0	0.02
6	Diakon	665	T/3	T/4	313	28.5±0.02	0 to 2.5

3.3 Measurement methods

3.3.1 Laser-Doppler velocimetry

Laser-Doppler velocimetry was used for the single and two-phase velocity measurements of this chapter in a form similar to that described in sub-section 2.3.1. The focal length of the lens L_1 was changed from 60 mm to 150 mm which resulted in a larger measuring volume. The characteristics of the optical arrangement are given in table 3.4 and the optical and signal-processing systems are shown schematically in figures 3.3(a) and (b) respectively: figure 3.4 corresponds to the photographs of the optical system, the stirred vessel, and the signal processing system.

CHAPTER III

The data rate for the single-phase flow was typically about 100 Hz in the impeller stream reduced to about 60 Hz in the bulk flow, while the data rates in the two-phase situations were about 5 Hz except for case 5 above the impeller. In case 5, the data rate was about 7 samples per minute (i.e. ≈ 0.12 Hz) and the results are subject to errors as bubbles and contaminants can contribute to affect the solid-phase results; as a result, no measurements were taken with this particle size above the impeller.

Table 3.4 Characteristics of the optical system

Laser power, mW	5.0
Laser wavelength, (λ), nm	632.8
Laser beam diameter at laser output, (b_o), mm	0.65
Laser beam diameter at measuring volume, (b_s), mm	0.125
Focal length of lens L_1, (f_1), mm	150.0
Focal length of lens L_2, (f_2), mm	300.0
Focal length of lens L_3, (f_3), mm	200.0
Distance a, mm	250.0
Distance b, mm	450.0
Half-angle of beam intersection in air, (ϕ), degrees	8.9
Intersection volume diameter at e^{-2} intensity, (b_x), μm	125.0
Intersection volume length at e^{-2} intensity, (b_y), μm	1063.0
Fringe separation (line-pair spacing), (d_f), μm	2.045
Number of stationary fringes in measuring volume, (N_{fr})	61
Frequency-to-velocity transfer constant, ms^{-1}/ MHz	2.045
Frequency shift, MHz	±1.75

CHAPTER III

Averaging method

As mentioned in chapter I , there are two techniques for measuring the velocity characteristics in stirred vessels. One is to ensemble-average over a specified angular interval of impeller rotation, say one degree, which is known as "gated-measurement", and the second is to average over the whole 360 degree cycle of impeller rotation. These two types of averaging can be regarded as a moving or a stationary observer with respect to the impeller and therefore the results obtained from the two methods would be different, especially for turbulence quantities in the immediate vicinity of the impeller, due to the cyclic nature of the flow. Popiolek et al (1984) showed that the turbulence quantities were overstimated when 360°-averaging was used, due to the periodic passage of the impeller blades whereas 1°-averaging provides an ensemble average of the turbulent flow. The cyclic effect of the impeller blades is, however, important only in the vicinity of the impeller up to 1.5 and o.5 times the blade width (h) away from the impeller tip and above and below the impeller respectively (Van Reit and Smith, 1975 and Popiolek et al, 1984). Averages over 360 degrees are presented here since:

1. This type of information is commonly used in the design of mixing vessels (Uhl and Gray, 1966 and Oldshue, 1983): and parameters which characterise the impeller performance and efficiency (see equations 3.9 to 3.13) are calculated from this type of data.

2. It was clear from chapter I and table 1.1 that the majority of the investigations in stirred vessels were conducted using 360°-averaging and the present data can be compared with those of the earlier work.

3. The rate of arrival of Doppler signals in 1°-averaging is small, especially whem measuring between the blades, (Popiolek et al, 1984) and was expected to cause difficulties with particle velocity measurements. Data rate of the order of 5 samples per second were experienced with the Diakon particles when taken over 360° and support the decision and allowed measurements in an acceptable time interval.

CHAPTER III

4. In current numerical methods, the flow is considered to be a steady one and the effect of the periodicity is not included.

Beam orientation

The manner in which the various velocity components were measured is described below. The effects of refraction on the location of measuring volume and on the anemometer frequency-to-velocity transfer constant were calculated in an iterative manner with a computer program (Vafidis and Yianneskis, 1982) which estimated the apparent co-ordinates in water corresponding to those in air for each point in the desired measurement grid. The calculation allowed for the presence of the trough, the cylinder and the baffles in all the beam orientation. The calculations in the case of refractive-index-matching were required only to take account of the apparent depth due to the single change of refractive index at the air/trough interface since the vessel, the baffles and the impeller were optically uniform and the whole test section and the fluid can be considered as a rectangular box.

The axial velocity component, $\overline{U}$, in water flow was measured below the impeller with the beams placed in plane of the axis as shown on figure 3.5 (a), while around and above the impeller (and below the impeller in the $\theta = 45^{\circ}$ plane where the baffle was in the way of the beam) due to the presence of the impeller blades and shaft, it was measured with an off-axis arrangement as shown in figure 3.5 (b). The double-tip arrow on each figure indicates the direction of the traverse of the anemometer. In the mixture flow, $\overline{U}$ was measured above and below the impeller with the on-axis arrangement of figure 3.5 (a), and with the off-axis arrangement around the impeller. The last measurement station in the Z-direction was at Z=275 mm since the surface vortex interfered with the laser beams above this height. The radial component, $\overline{V}$, was measured in all planes in the manner shown in figure 3.6 (a) for both water and mixture flows.

The tangential component, $\overline{W}$, below the impeller in both water and mixture flow was measured on-axis as shown on figure 3.6 (b) but around and above the impeller, in

water flow, measurement was not possible because of the blockage of the light by the impeller shaft and blades. With the refractive-index-matching technique it was possible to measure the $\overline{W}$ component above and below the impeller with the on-axis arrangement, but this was not possible around the impeller because of the thread cut in the material which could not be made entirely transparent. Since no direct measurement of $\overline{W}$ were obtained around the impeller (and above it in water flow) measurements were obtained in two directions at ±45° to the radial direction of the axial plane θ as shown on figures 3.7 (a) and (b). From the measurements of $\overline{V}$, v', $\overline{V}_{45}$, v'_{45}, V_{-45} and v'_{-45}, the $\overline{W}$ and w' components and the cross-correlation $\overline{vw}$ can be obtained in the manner described by Melling and Whitelaw (1976) from the relationships:

$$\overline{W} = (\overline{V}_{45} - \overline{V}_{-45}) / (\sqrt{2}) \qquad (3.4)$$

$$w' = \{\sqrt{[(v'_{45})^2 + (v'_{-45})^2 + (v')^2]}\} \qquad (3.5)$$

and

$$\overline{vw} = [(v'_{45})^2 - (v'_{-45})^2] / 2 \qquad (3.6)$$

3.3.2 Refractive-index-matching technique

This technique was used to allow laser beam penetration and the measurement of particle velocities in two-phase flows with high particle concentrations. The technique has been described in detail in sub-section 2.3.2. An arrangement was made in order to control the temperature in the vessel which was explained in section 3.2. A visual demonstration of the refractive-index-matching is presented in photograph of Figure 3.8 which shows the stirred vessel and the mixture in it when their indices are matched at 28.5 °C. The laser beam orientation is for axial velocity measurements off-axis and the beams pass through the blades close to the tip of the impeller without any deflection.

As mentioned before in chapter II, the presence of gas-inclusions inside the

particles prevented the measurement of liquid-phase velocity in the presence of the suspended particles and limited the solid-phase velocity measurements to a maximum particle concentration of 2.5% by volume. This concentration is much higher than that when the particles were suspended in water (i.e. 0.02%). The results obtained using this technique are presented in sub-section 3.5.2.

3.3.3 Flow visualisation technique

Flow visualisation for both single and two-phase flows was carried out in the stirred vessel to obtain qualitative information of the flow patterns, to define flow regions of interest, and to determine the influence of the impeller size and clearance in the case of single-phase flow and of the particle concentration and impeller rotational speed on the sedimentation of particles in the two-phase flow. A sheet of laser light, 4 mm thick, was produced with a cylindrical lens placed in the path of a beam from an Argon-Ion laser (Spectra-Physics model 194) operating in the green mode at about 500 mW. Polysterene beads with a size range of 300-550 μm and a mean diameter of 430 μm were used as markers to scatter the laser light. A volumetric concentration of less than 0.01% was used, so that particle-to-particle interactions were negligible and the size of the particles was small enough so that they could follow the mean flow motion. In the two-phase flow case, inclusions of gas in the Diakon particles acted as scattering centres when the refractive indices of the particles were matched to that of the mixture. The photographs of the visualisation of both single and two-phase flows are presented and discussed in sub-sections 3.4.1 and 3.5.2 respectively.

3.3.4 Error sources and measurement uncertainties

Experimental errors and uncertainties may arise due to Doppler broadening, bias effects, statistical errors, and error in the positioning of the measuring volume, as discussed in sub-section 2.3.3. The change in the angle between the beams for different orientations, and the consequent change in the anemometer transfer constant, the variation

of impeller speed, and the oscillation of the impeller and the shaft are additional sources of errors and are considered in the following paragraphs.

The change in the frequency-to-velocity transfer constant due to the change of the angle between the beams in the fluid at different off-axis beam orientations was always less than 0.2% of the corresponding value for the beams crossing in air, except for some of $\overline{V}_{45}$ and $\overline{V}_{-45}$ component measurements where the change was about 0.8%, and corrections were applied to the measurements of these components.

The oscillation of the impeller and shaft was measured in air to be about 1.0 mm in amplitude and in water was visually observed to be of the same order: a test with a single laser beam passing through the vessel in grazing incidence on the blade tip indicated a movement of about 0.5 mm. Furthermore, it has been shown by Yianneskis et al (1987) that the impeller and shaft movement are not erratic. That is, the shaft axis prescribed the same path in each revolution. The short term variation in the impeller rotational speed did not normally exceed ±0.2 rpm (0.07% of the tip velocity, V_t, for a speed of 300 rpm) and the long-term ones was ±0.8 rpm (0.25%). The variation of the impeller speed was monitored regularly and correction was applied, by adjusting the motor controller. The fluctuations in impeller speed increased with decreasing the rotational speed so that the tip velocity varied by up to 0.4% at 50 rpm. In general, the variation of impeller speed have negligible effects on the velocities measured.

3.4 Single-phase flow results and discussion

The results of this section are presented under three headings: flow visualisation, velocity field measurements and parametric studies. The three components of the mean and rms velocities are normalized by the impeller tip velocity unless otherwise stated. In each of the following sub-section the mean velocity results are presented first, followed by the turbulence quantity results.

CHAPTER III

3.4.1 Flow visualisation

Flow visualisation was carried out as explained in sub-section 3.3.3 and sample photographs are shown in figures 3.9-3.13. The photographs are instantaneous pictures of the flow and should not be interpreted as mean flow patterns. Information about the impeller geometry and speed are given on the caption of each photograph.

Figure 3.9 shows photographs of the flow at $\theta=0^{\circ}$ and 42.5° in a r-Z plane. They show the presence of two main ring vortices above and below the impeller and that the circulation in the lower vortex is faster than that above the impeller since the streaklines are longer below the impeller. The shape of the upper ring vortex is less ordered and defined than the lower one due to the impeller clearance, as is discussed in more detail later in this section. The very short streaks around the impeller shaft indicate that the flow motion in those regions is mainly in the tangential direction. The flow patterns at the two r-Z planes of figures 3.9 (a) and (b) are similar. The impeller stream is inclined to the horizontal and is redirected into two thin wall jet regions along the vessel wall as a result of its impingement on the wall. A magnified picture of the impeller stream, figure 3.10, shows the jet stream inclination and indicates the location of the centre of the lower ring vortex: it represents an average of the fluid motion over 1.66 revolution / second of the impeller (i.e. N=100 r.p.m) and since the time exposure is 1 second, then the structure of the trailing vortex behind the blades cannot be observed.

The flow patterns in the r-θ plane can be seen in the photograph of figure 3.11 (a) at an axial location just below the impeller and indicate that the flow is mainly in the same direction as that of the impeller rotation except behind the baffle. The streaks are shorter than in the r-Z planes which suggests that the residence time of the particles within a r-θ plane is shorter than that in a r-Z plane and that the tangential velocity components away from the impeller stream are smaller than the axial and radial ones. The photograph of figure 3.11 (b) shows the flow near the free surface when a whirlpool is formed which moves with the bulk of the flow around the impeller shaft in the same direction as the shaft rotation, but the local vortical motion rotates in an opposite direction to that of the shaft.

The small spots (very short streaks) around the whirlpool extend to the upper face of the impeller and indicate a strong swirl motion with small radial and axial components. The presence of whirlpools could affect the structure of the upper ring vortex, but observation revealed that their formation was less frequent and also more random at the lower speeds than the photograph of figure 3.11 (b), and they were usually destroyed before completing one revolution.

The photographs of figure 3.12 show that the flow patterns are similar for the three impeller sizes and that the strength of the flow field seems to be dependent on the impeller size, as can be seen from the streaklines of the D=T/3 which are longer than those of D=T/4 impeller for the same impeller speed. It can also be seen that the free surface is more violent with D=T/3 than with D=T/4 for which the surface is almost flat and that the inclination of the impeller jet increases with impeller size. The effects of the impeller clearance are shown by the photographs of figure 3.13 for the D=T/4 diameter impeller and N=300 r.p.m. For C=T/2 (figure 3,13 (a)) the ring vortices above and below the impeller are almost symmetric about the impeller stream and the impeller stream is almost horizontal, without any inclination, in contrast to the C=T/3 and C=T/4 cases. It is also evident that the shape of the upper vortex, at C=T/2, is more ordered and well defined. As C increases, for C=T/3 and C=T/4, figures 3.13 (b) and (c), the impeller stream is inclined more away from the horizontal and the upper vortex becomes less ordered. Similar results on the effect of impeller size and clearance were obtained for the other geometries.

The flow visualisation results show that the flow consists of two ring vortices one above and one below the impeller stream with their centres located close to the impeller stream and the wall. A helical vortex was observed to exist behind each baffle, and the flow in these vortices rotated in an opposite direction to that of the impeller. The flow patterns seem to be similar in different r-Z planes and for different impeller sizes, but the impeller clearance clearly affects the direction of the impeller stream and the size of the ring vortices.

CHAPTER III

3.4.2 Mean velocity and turbulence quantity measurements

The results presented in this section are for three impeller geometries: D=C=T/3 (the standard configuration), D=T/3 and C=T/4, and D=T/2 and C=T/3. The working fluid with the first and third geometry was water, whereas a mixture of oil of turpentine and tetraline was used with the second impeller. The results include ensemble-averaged values, measured over 360° of the impeller rotation, of all three mean velocity components and the corresponding rms velocities. The kinetic energy of turbulence (k) is also presented. In the vicinity of the impeller, measurements of the vw cross-correlations were also made and were used together with the k values to obtain estimates of ε, the rate of dissipation of turbulence kinetic energy.

A measure of the accuracy of the measurements may be deduced from Table 3.5 which presents values of the axial mass flow into the impeller, from above and below, and the radial discharge into the impeller stream. These results were obtained by integrating axial and radial profiles of mean velocity in vertical (r-Z) planes using the expressions

$$Q_r = 2\,\pi\,\rho\,R_t \int_{Z_1}^{Z_2} \overline{V}\,.\,dZ \qquad (3.7)$$

and

$$Q_a = 2\,\pi\,\rho \int_{0}^{R_t} \overline{U}\,.\,r\,.\,dr \qquad (3.8)$$

where Z_1 and Z_2 are the axial locations at which the axial velocity profiles were measured and R_t is the radius at which the radial velocity profile was measured: the locations of Z_1, Z_2 and R_t were chosen to be as close to the impeller as possible, so that the measuring volume was located just off the edges of the blades. The differences between Q_r and Q_{in} are less than 6% and, considering the errors in the velocity measurements and interpolation errors, the agreement is excellent.

CHAPTER III

Table 3.5 Mass Balance Around the Impeller in Vertical Plane

Impeller diameter D	Impeller clearance C	Impeller speed N (rpm)	Radial discharge outflow, (Q_r) at the impeller tip (kg/s)	Total mass inflow (Q_{in}) from above and below the impeller (kg/s)	Q_r/Q_{in}
T/3	T/3	300	4.05	3.80	1.065
T/3	T/3	150	1.93	1.81	1.06
T/3	T/3	50	0.493	0.51	0.976
T/2	T/3	125	5.89	5.99	0.98
T/2	T/2	150	7.303	7.668	0.95

3.4.2.1 Flow characteristics of standard configuration (D=C=T/3)

This arrangement was operated with an impeller speed of 300 rpm corresponding to a Reynolds number of 48,000. The mean and rms velocity results are presented in figures 3.14-26 for a number of r-Z and r-θ planes and for the impeller stream region in the r-Z plane located half way between two adjacent baffles (i.e. $\theta = 0\ ^\circ$). The mean velocity vectors ($\sqrt{(\overline{U}^2 + \overline{V}^2)}$) in the r-Z planes of $\theta = 0\ ^\circ$ (or 90 °), 22.5 °, 45.0 ° and 67.5 ° are presented in figures 3.14 (a), (b), (c) and (d) respectively. The outline of the impeller, the shaft, the wall, the tip and the root of the baffle and the level of the free surface of the water are indicated on each graph. The measurement locations are also indicated by a cross situated in the middle of the vector.

The results in all θ planes show the presence of the impeller stream emanating from the impeller tip and two ring vortices on either side of the impeller stream. The lower

ring vortex is ordered and circular in shape, whereas the upper one is larger with smaller velocities and is almost egg-shaped. Detailed measurements below the impeller at $\theta=0$ ° show that the centre of the ring vortex is at $r\approx110$ mm or 1.12 D and Z=60 mm, and this position moves radially towards the axis of the vessel as the flow approaches the baffle so that, at $\theta= 22.5$ ° and 45 °, the radial locations of the centre are at $r\approx1.0$ D and 0.82 D respectively. After the baffle the vortex centre starts to move back again towards the wall and at $\theta= 67.5$ ° its radial position is at the same location as at $\theta=0$ °. A similar trend can be observed in the vortex above the impeller.

The jet region near the wall, which is a result of the impingement of the radial impeller jet, is wider at $\theta=22.5$ ° upstream of the baffle than at $\theta=67.5$ ° downstream of it. To quantify this in more detail, measurements were made with a fine grid of measurement points and these results are presented and discussed later in this section. The results at $\theta=22.5$ ° and 67.5 ° also show that the axial velocities upstream of the baffle are larger than those downstream of the baffle in the wall jet region due to the tangential flow upstream of the baffle being redirected vertically after it impinges on the baffle. The velocity vectors in the region near the axis of the vessel, both above and below the impeller, are mainly in the axial direction with very small radial components and the axial profiles are near-uniform as the flow accelerates towards the impeller from both the top and the bottom of the vessel. The shear rates, $\partial\overline{U}/\partial r$, are very small in that region with a maximum value of 4 s^{-1}. At the bottom and the top of the vessel (i.e. for $0< Z < 30$ mm and $260<Z<294$ mm) the motion is predominantly in the radial direction with maximum magnitudes of 0.18 V_t and 0.1 V_t respectively.

The flow in the impeller stream is mainly in the radial direction with a small axial component directing the flow upwards and causing the inclination of the impeller stream observed in the flow visualisation. This effect is more evident at $\theta=0$ ° where more data were taken and show the asymmetry of the impeller stream about the centreline plane of the impeller disc. The inclination is about 2-4 ° and is dependent on the impeller clearance, as is discussed in more detail in sub-section 3.4.3. Detailed measurements were also made in

the impeller stream to characterise the flow in that region and are presented and discussed later in this section.

Figure 3.15 shows the mean velocity vector ($\sqrt{(\overline{V}^2+ \overline{W}^2)}$) in r-θ planes at different axial locations and for one quarter of the vessel, from θ=0 ° to 90.0 °, with the baffle located at θ=45 ° and symmetry assumed. In locations where one or both components could not be measured due to optical access restrictions or severe refraction problems, a circular symbol is superimposed. At Z=5 mm (figure 3.15 (a) the flow is mainly in the radial direction towards the axis of the vessel with magnitudes of the order of 0.3 V_t. This strong radial motion is a result of the deflection of the wall jet at the bottom of the vessel. There is also a large area of counter-rotating circumferential motion (i.e. rotating in a direction opposite to that of the impeller rotation) at 56.5 °<θ < 90 ° and 0.°<θ < 22.5 °, and a purely circumferential motion is presented along the wall in a counter-rotating fashion. The former was first reported by Yianneskis et al (1987).

At Z=20 mm (figure 3.15 (b)) the flow pattern is similar to that at Z= 5 mm but with reduced radial velocities and a maximum of 0.23 V_t. The counter-rotating motion along the wall is reduced to near-zero, while the other one is still present in the same angular planes as in Z=5 mm but at radial locations of 50< r< 80 mm. Figure 3.15 (c) shows the flow pattern at Z=50 mm and that the velocities are further reduced to less than 0.1 V_t. The overall flow pattern is that of circumferential motion in the same direction as the impeller rotation, and the presence of the two vortices is evident, with one rotating anti-clockwise in the same sense as the impeller with its centre at θ≈75 ° and r≈85 mm and the other rotating clockwise behind the baffle with its centre at θ≈50 ° and r≈126 mm. The vortex behind the baffle seems to be destroyed at Z=5 and 20 mm which may be due to the radial velocity component, which is strong in comparison to the tangential velocity around the baffle, and stems from the deflection of the wall jet mentioned earlier.

At Z=70 mm (figure 3.15(d)) the flow patterns have changed significantly and the flow is predominantly in the radial direction but away from the axis towards the wall. The two vortices at Z=50 mm are still present at this axial plane but with reduced sizes and the

centre of the first one has moved to $\theta \approx 90$ ° and $r \approx 85$ mm. At the next axial station z=82.5 mm there is no evidence of this vortex (figure 3.15(e)) and the flow is mainly in the radial direction in the region of 22.5 ° < θ < 67.5 °, towards the wall. The baffle vortex is further reduced at 82.5 mm, both in size and strength, due to the proximity of the impeller and the associated uni-directional impeller stream flow in this axial station.

The results of figure 3.15 show that a vortex of helical nature exists in the r-θ planes and rotates in the same direction as the impeller in some planes and in the opposite direction in others. The flow direction near the impeller and near the bottom of the vessel is predominantly in the radial direction due to influence of the impeller stream and the deflected wall jet respectively. There are considerable regions of counter-rotating flow especially close to the bottom of the vessel around θ=0 ° and to obtain a better picture of the flow mechanism, detailed measurements of the $\overline{W}$ component were taken at θ=0 °, and are shown in figure 3.16.

The profiles of figure 3.16 (a), with positive values (directed upwards) indicates motion in the direction of the impeller rotation, show the near-uniform distribution of $\overline{W}$ along the raduis of the vessel and that $\partial\overline{W} / \partial r$ and $\partial\overline{W} / \partial Z$ are small with maxima of 2 and 3 s^{-1} respectively. They also show large areas of negative velocities (counter-rotating flow), especially close to the bottom of the vessel and these are also evident in contour form in figure 3.16 (b). There are two regions of counter-rotating flow, one at the corner of the vessel occupying an area of about 17x17 mm and the other a 90 mm wide region at the bottom of the vessel located at 30 < r <120 mm and extends towards the impeller until Z=80 mm. The maximum positive and negative $\overline{W}$ velocities were 0.17 and -0.1 m/s or $0.11V_t$ and $-0.065\ V_t$ respectively. The results of figure 3.15 confirm that flow patterns similar to those at θ=0 ° in figure 3.16, exist up to ± 22.5 ° aroundthe plane of θ=0 °.

The pressure gradients in the r-θ planes, due to the presence of the baffle, are responsible for this counter-rotational flow. The existence of regions with lower velocity components at θ=0 °, compared with θ=45 ° where the cross-section is smaller due to the presence of the baffle, are associated with higher local pressures. Therefore, pressure

decreases in the θ-direction from θ=0 ° to θ= 45 ° and then starts to increase again with θ up to θ=90 ° (i.e. an adverse pressure gradient exists). To counter-balance this pressure gradient, cross-flows are set up and if they are larger than the local $\overline{W}$ velocity, the fluid rotates in an opposite direction to that of the impeller. The possibility of this counter-rotation taking place is higher where the $\overline{W}$ velocity components are very small away from the impeller.

The radial distributions of the axial mean velocity are presented in figure 3.17 at different r-Z planes and show the presence of the ring vortices at θ=0.0° with near-uniform profiles above and below the impeller from the axis up to r=100 mm where $\partial\overline{U}/\partial r$ is small with maxima of 3.5 s^{-1}. In the wall jet region, r=100 to 147 mm, $\partial\overline{U}/\partial r$ is much larger than in the rest of the vessel with a maximum of 23 s^{-1} at Z=70 and 150 mm and $\partial\overline{U}/\partial Z$ is small everywhere with a maxima of 4 s^{-1} along the wall. The flows above and below the impeller, at the same axial distance from the centre of the impeller, are axially symmetric to within 10% . The flow accelerates slightly as it approaches the impeller from the top and the bottom and, in the wall jet, accelerates first up to Z=70 mm and subsequently decelerates as it approaches the bottom consistent with the decrease and increase of the width of the wall jet respectively. Similar features can been seen at θ=33.75 ° and 56.25 ° except for the width of the wall jet, which varies considerably with θ.

To investigate the change of the width in the wall jet and the detailed flow structure around the baffle, measurements of the axial and tangential components were taken at Z=70 mm and the results are presented in figure 3.18. In front of the baffle, figure 3.18 (a), the width of the wall jet increases as the baffle is approached to a maximum at θ=40 °, i.e. 5 ° in front of the baffles, and is greater by about 42% than at θ=0 °. The negative velocities in figure 3.18 (b) indicate that the flow direction is opposite to that of the impeller. The distributions of tangential velocity are near-uniform and decrease in magnitude as the baffle is approached, with near-zero magnitude at θ=40 °, indicating that the flow in front of the baffles is unidirectionally downwards (upwards above the

impeller).

The flow behind the baffle is more complex with a region of flow separation .The double peaks of the wall jet at θ=47.5 °, 50 ° and to some extent at θ=52.5 ° show the interaction of the main ring vortex with the region of separated flow (the helical vortex behind the baffle). This double peak feature was also reported by Yianneskis et al (1987) for the same flow geometry but at Z=50 mm. The tangential velocities behind the baffle show the circulation of the vortex at θ=47.5 ° and 52.5 ° with its centre at about half of the baffle width away from the wall and with a maximum negative velocity of about 0.14 V_t. Both the axial and tangential velocities at θ=56.25 ° show that the main ring vortex has re-attached and that the width of the wall jet has started to decrease as θ increases. It is also clear from the $\overline{W}$ velocity profiles that there is no recirculation at the point of re-attachment. Moreover, the length of the region of separated flow along the wall is about 29.0 mm, about the same as the baffle width (29.4 mm).

Detailed measurements were obtained in the impeller stream at θ=0 ° and are presented in figures 3.19-3.23. Figure 3.19 shows that the radial velocities from the impeller tip to the wall decrease with r, and the profiles become more uniform as the flow approaches the wall. The profiles have near-parabolic shapes and the locus of the peaks of the profiles moves upwards with r so that the radial jet is inclined from the impeller disc centreline by about 4.0 degrees. Figure 3.20(a) shows the decay of the axial shear rate, $\partial\overline{V}/\partial Z$, obtained as a function of radial position from the profiles of figure 3.19. The maximum values represent the steepest gradient in each profile and the average values were obtained from the best line fitted on the data. The results show that $\partial\overline{V}/\partial Z$ is very high in the vicinity of the impeller, about 155 s^{-1} and decays rapidly with r to r=85 mm where the shear rate is reduced by a factor of 5. They also show that the maximum $\partial\overline{V}/\partial Z$ is always higher than the average and that the difference reduces with r, as expected, since the radial profiles will become more uniform as r increases and thus the maximum and average estimates tend to the same value. The symmetry of the radial centreline velocity at different baffle locations can be seen in figure 3.20 (b) with similar mean and rms velocities

obtained at all locations, indicating that $\partial\overline{V}/\partial\theta$ is very small and, for all practical purposes, negligible.

Figure 3.21 shows that the tangential velocity profile close to the impeller tip has a similar trend and almost the same magnitude as that of $\overline{V}$-velocity (figure 3.19) except near the plane of the impeller disc (i.e. Z=95.5 to 103 mm) where the $\overline{W}$ velocities are near-unifom and higher. The maximum value of $\partial\overline{W}/\partial Z$ is 120 s^{-1} which is about 14% lower than $\partial\overline{V}/\partial Z$ at the same radial location. The axial distributions of axial mean velocities in the impeller stream are shown in figure 3.22 with positive velocities in the Z-direction directed away from the axis. The results show that the total induced axial flow into the impeller stream is from below the impeller, in accord with the inclination of the impeller stream jet. There are no steep gradients in the profiles and the axial velocities are much smaller than the radial and tangential ones, especially at the impeller tip. At r = 105.6 mm the axial velocities are very small everywhere along the impeller width, indicating the lack of inflow from either side of the impeller to the impeller stream flow and, at r = 120 mm, it can be seen that the flow has started to change direction. The effect of the impingement of the radial jet on the wall is evident from r =105 mm, i.e. 55 mm away from the impeller tip.

Important parameters in characterising the impeller performance and its efficiency are the pumping capacity, which can be expressed in terms of the radial flow rate (Q), the dischage flow (Q_d) and the induced flow into the impeller stream (Q_i), the coefficient of discharge (K_d), the slip factor (S) and the mechanical efficiency (η) and they are obtained from the following expressions.

The radial flow rate, Q, across the impeller width at any radial location is given by the equation:

$$Q = 2\pi\rho r \int_{-h/2}^{+h/2} \overline{V} \, . \, dZ \qquad (3.9)$$

where h is the height of the blades. The Q at the impeller tip (i.e. when r= R_t) is called the discharge flow and is denoted by Q_d. The induced flow rate at any radial location is given by:

$$Q_i = Q - Q_d \tag{3.10}$$

Also the discharge coefficient, the slip factor and the mechanical efficiency are defined respectively as:

$$K_d = Q_d / (\rho N D^3) \tag{3.11}$$

$$S = \overline{W}_{mean} / V_t \tag{3.12}$$

$$\eta = K_d / N_p \tag{3.13}$$

where $\overline{W}_{mean}$ is the average value of the $\overline{W}$ velocity (calculated from the $\overline{W}$ profile of figure 3.21in the present case). The results of figure 3.23 show these characteristics of the impeller stream. The decay of the radial centreline velocity, figure 3.23 (a), is slightly faster in the impeller region than away from it and the centreline velocity at the tip is about 0.78 V_t, reducing to 0.25 V_t at r =130 mm. Figure 3.23 (b) shows the spread of the radial jet, where $Z_{(1/2)}$ is the width of the jet calculated from the locations in the radial velocity profiles where the local magnitude was half of the maximum velocity for the whole profile. The jet width is very small in the vicinity of the impeller (up to 5 mm from it) and increases almost linearly with r from about 0.5 h to 1.8 h at r =130 mm. Figures 3.23 (c) and (d) show that the mass flow increases with r due to axial flow induced into the impeller stream up to r =105 mm, where the axial velocities are almost zero (figure 3.22), and then decreases; the maximum mass flow is 1.66 times more than the discharge flow and the total induced axial flow is about 40% of Q_d. The coefficient of discharge of the impeller was calculated to be 0.84 which is within the upper range recommended by Revill (1982)

but is smaller, by about 10%, than the value reported by Keller (1985). This difference is probably due to Keller's use of a closed-top vessel with no free surface and to the length of her measuring volume which was 2.8 times longer than that of the present work with consequent errors due to velocity gradient broadening. The slip factor and the mechanical efficiency were calculated to be 0.58 and 17.9% which are around 6% lower than the value of Keller but, considering the errors involved in calculating N_p from torque measurements (up to 10%) and also in K_d, the agreement is reasonable.

Turbulence quantities are presented and discussed below in two parts: first in the impeller stream and secondly in the bulk of the flow and as mentioned before, the results are ensemble-averaged over the whole cycle of impeller rotation (360°). Measurements of u', v' and w', and hence the turbulence kinetic energy, $k=\{[(u')^2+(v')^2+(w')^2] / 2\}$, were obtained in the impeller stream, in the main ring vortices and around the baffle. In the impeller stream, measurements of radial component and radial-tangential components (±45° to the local radial direction) were made to allow the determination of the $\overline{vw}$ cross-correlations as well as $\overline{W}$, v' and w'.

The distribution of the axial and radial rms velocities in the impeller stream show, figure 3.24 (a), that they are of similar magnitude except at the top and bottom edges of the impeller blade where the u' levels are higher by up to 10%.The results are in good agreement with those reported by Yianneskis et al (1987), but are smaller than those of Cutter (1966), who used an approximate photographic technique to obtain rms velocities. The variation of w' velocities at impeller tip, figure 3.24 (b), also show similar ditributions and magnitudes to those of u' and v' with maximum differences of about 10% and limited to a small area. It can be concluded that turbulence properties measured over the whole cycle, i.e. 360 ° averages in the impeller stream is near-isotropic: van der Molen and van Maanen (1978) and van Doorn (1982) reached the same conclusion, but results reported by Nagata (1975) and Nishikawa et al (1976) suggest that v' is twice as large as u' in the impeller stream. This difference may well be due to the different measuring technique, since obstrusive probes were used in both references.

CHAPTER III

The large turbulence levels in the vicinity of the impeller are due in part to the periodic nature of the flow and the measured level is the sum of the true turbulence levels plus the turbulence introduced by the passage of the impeller blades. Away from the impeller the turbulence levels decay almost linearly as shown in figure 3.24 (c): the level is reduced from 0.3 V_t at the impeller tip to 0.13 V_t at r=130 mm.

Figure 3.25 (a) shows that the axial distribution of the kinetic energy of the turbulence at the impeller tip has the same pattern as the rms velocity distributions with near-uniform magnitudes along the width of the impeller blades (i.e. 91 < Z < 106 mm) of about 0.34 $(m/s)^2$ or 0.145 V_t^2 and decrease beyond these points to about 0.02 V_t^2 at Z=83 and 113 mm. The results of k are in agreement with those of Yianneskis et al (1987) at the same radial location and in the same axial region (i.e. 91 < Z < 106 mm) with differences up to 8%. The average value of k at the impeller tip was 0.25 $(m/s)^2$ or 0.106 V_t^2.

The distribution of the $\overline{vw}$ cross-correlation at the impeller tip, figure 3.25 (b), shows near-symmetry about the plane of the impeller disc with a peak value at the centre of about 0.05 $(m/s)^2$. The $\overline{vw}$ levels drop sharply on either side of the centreline and change sign with maximum negative value of -0.01 and -0.013 $(m/s)^2$ at Z=90.5 and 105.5 mm respectively. The distribution pattern with the peak value at the centre is in agreement with that of Ito et al (1975) who showed that $\overline{uv}$ and $\overline{uw}$ components are smaller than $\overline{vw}$ by at least an order of magnitude, but they did not show the change of sign in the $\overline{vw}$ cross-correlations because the radial location of their results was at r=0.625 D, compared with 0.54 D in this case, and their profile was more developed. As shown later in this section, the $\overline{vw}$ profiles recover rapidly with radial distance and the average value of $\overline{vw}$ at the impeller tip was 0.0055 $(m/s)^2$ which correspond to a Reynolds shear stress ($-\rho\overline{vw}$) of 5.5 N/m^2 and is around 50 times larger than the corresponding maximum laminar stress. The Reynolds normal stresses (i.e. $-\rho u'^2$, $-\rho v'^2$ and $-\rho w'^2$) are twice as large as the shear stresses with maximum values of the order of 100 N/m^2 at the tip of the impeller.

The rate of turbulence kinetic energy dissipation, ε, is useful in turbulence

modeling and may be estimated from the expresion

$$\varepsilon = C_\mu [k^2 / (-\overline{vw})].[e_{r\theta}] \qquad (3.14)$$

Apart from the approximations of axial symmetry in the effective viscosity hypothesis and the value of C_μ (0.09), measurement uncertainties lead to an accumulation of experimental errors which mean that the uncertainty in ε is of the order of 30%.

Figure 3.25 (c) shows the distribution of ε determined from equation 3.14 and indicates large variations along the width of the impeller blade caused by the value of ε tends to infinity where $\overline{vw}$ tends to zero. At the centre (Z=98 mm), the value of ε reaches a minimum of 36 m^2/s^3 or 30 N^3D^2 and the profile assumes a concave shape around the centreline plane. The reason for this is that the variation of $\overline{vw}$ around the centre (i.e. 91<Z<106 mm) is very large (figure 3.25 (b)), whereas the variations of k (figure 3.25 (a)) and $e_{r\theta}$ (about 45 s^{-1} on average) are very small and since $\overline{vw}$ is maximum at the centre and ε is proportioal to $1/\overline{vw}$, a minimum value of ε is therefore expected at the centre. Away from the impeller stream (i.e. Z<85 mm and Z>110) ε is an order of magnitude smaller. An average value ε_{ave}=33 m^2/s^3 or 27.5 N^3D^2 can be estimated by taking average value of k, vw and $e_{r\theta}$ ($\approx$32 s^{-1}) from the profile in the impeller stream. It may be compared with the value obtained from the expression $\varepsilon_o=3.3(k_o)^{3/2}/ r_o$ (where k_o=0.1 $(V_t)^2$ and r_o is the radius of the impeller) suggested by Issa and Gosman (1981) which, for this impeller size and speed, is ε_o =7.9 m^2/s^3, i.e. 74% less than the experimental value.

The values of ε at the centre of the tip of the impeller blade (when normalised with N^3D^2) estimated by van Doorn (1982), Laufhütte and Mersmann (1985), Yianneskis et al (1987) and the present work were 35, 29, 22.5 and 30 respectively and the differences may be attributed to experimental uncertainty. The distributions of ε of the present work shows large variations along the width of the impeller, while those of van Doorn (1982) and Patterson and Wu (1985) showed that ε is maximum at the centre and decays gradually away from the centreline: this difference is due mainly to their use of equation 1.1.

CHAPTER III

The turbulece intensities in the bulk of the flow at $\theta=0^{\circ}$ are presented in figures 3.26-3.28 with contours of u' and v' above and below the impeller (figure 3.26) showing that the impeller stream is a region of high turbulence intensity compared to the bulk flow region where, in general, the variations of the turbulence intensities are small in both the r and Z directions with minimum and maximum levels of 0.07 and 0.15 m/s or 0.045 and 0.1 V_t respectively. In comparison, the u' levels below the impeller from r=0 to 50 mm are smaller than v' by a factor of 2 whereas they are higher by about 1.2 times in the wall regions (r=100-147 mm), but are similar in the central region (r=50-100 mm). Fig 3.27 shows the radial distribution of w' below the impeller in profile and contour form. The profiles are almost uniform in the r and Z directions and the magnitude of v' and w' are similar.

The distribution of k below the impeller is shown in figure 3.28. The profiles (figure 3.28 (a)) have again near-uniform distributions and k decreases with r up to r=65 mm and subsequently increases towards the wall. The minimum value is about 0.009 $(m/s)^2$ covering an area about one quarter of the plane as shown in figure 3.28 (b) and it increases to a maximum of 0.025 $(m/s)^2$ at the bottom close to the axis. In comparison to levels in the impeller stream, the k values in the main ring vortices are at least an order of magnitude smaller. Within the lower ring vortex, the k values are almost constant (0.018 $(m/s)^2$) in the wall region as the flow moves towards the bottom, but in the deflected jet along the bottom k decreases gradually from the wall (r=147 mm) up to r=60 mm where it increases again to the axis. The corresponding generation of turbulence is caused partly by the impingement of the radial jet at the bottom of the vessel around the axis and also by the change of sign in tangential flow direction close to the axis. From the bottom of the vessel to the impeller k decreases as the flow approaches the impeller along the axis of the vessel.

The effect of the baffle on the turbulence levels is shown in figure 3.29 with u' and w' profiles near-uniform at around 0.09 V_t in front of the baffle in the wall region. Behind the baffle, the u' and w' turbulence levels increase by about 30% and 20% up to $\theta=52.5^{\circ}$ (i.e. 7.5° upstream of the baffle) and from r=120 to 130 mm. This is the shear

region between the wall jet and the separated flow (see the double peak region in figure 3.18 (a)). The turbulence results in the bulk of the flow are in good agreement with those reported by Yianneskis et al (1987) both in magnitude and in distribution.

3.4.2.2 Flow characteristics with the D=T/3 and C=T/4 configuration

Velocity measurements were obtained at $\theta=0^\circ$ and at a rotational speed of 313 rpm corresponding to a Reynolds number of 32,500. A mixture of oil of turpentine and 32.6% by volume tetraline was used as the working liquid which had a refractive index identical to that of the acrylic test section material (n=1.489) at 28.5 °C. The refractive-index-matching technique made it possible to measure axial and tangential velocity components on-axis above the impeller which was not possible in the water flow case because of the refraction caused by the impeller shaft.

Figure 3.30 shows that the axial mean velocity at the impeller stream is much smaller than the radial and tangential components, especially at the impeller tip where they differ by a factor of 5. The axial velocity values show that the entrainment into the impeller region originates from below the impeller. The $\overline{W}$ velocity profile at the impeller tip is less steep and has larger magnitude than those of $\overline{V}$ and the decay of $\overline{W}$ with r is faster than that of $\overline{V}$. The coefficient of discharge, the slip factor and the mechanical efficiency were calculated to be 0.88 and 0.58 and 19.5% respectively . The radial jet is inclined by about 7.5 ° to the horizontal. The results in the impeller stream of the mixture flow are in good agreement with those in the water flow reported by Yianneskis et al (1987).

The contours of axial mean velocity, figure 3.31, confirm the existence of ring vortices above and below the impeller similar to the results of sub-section 3.4.2.1. Above the impeller the wall jet accelerates up to Z=150 mm and then decelerates with velocities reducing to zero at Z=260 mm. Figure 3.32 shows the distributions of the tangential mean velocity above and below the impeller, with the positive velocities in the direction of the impeller rotation. The results show the two counter-rotating flow regions below the impeller like the previous geometry. Above the impeller, the $\overline{W}$ profiles are more uniform

and in the same direction as the impeller rotation except near the top corner of the vessel, near the free surface, where a counter rotating flow exists over an area of 21x40 mm.

The axial distributions of the three rms velocity components at the impeller stream, figure 3.33, are almost the same, indicating that the turbulence is nearly isotropic. The distribution of the turbulence kinetic energy around the impeller is shown in figure 3.34 (a) and (b) with higher levels in the impeller stream and an average value at the impeller tip, obtained by integrating the k profile, of 0.315 $(m/s)^2$ or 0.122 V_t^2. Figure 3.34 (c) shows that the profiles of $\overline{vw}$ at the impeller stream are almost symmetric about the centreline of the blade, with a peak at the centre of about 0.055 $(m/s)^2$ and decreases sharply on either side with sign changes near the top and bottom edges of the blade and a maximum negative $\overline{vw}$ value about 0.011 $(m/s)^2$. At r=68 mm the $\overline{vw}$ profile is more uniform with no change in sign. The average value of $\overline{vw}$ calculated at the impeller tip was 0.008 $(m/s)^2$ and the corresponding maximum and minimum turbulent shear stresses are 49 and 10 N/m^2.

The estimated rates of dissipation of the turbulence kinetic energy, figure 3.34 (d), show that there are large variations of ε at the impeller tip, with four distinct peaks corresponding to the axial locations where the $\overline{vw}$ levels are very small (shown by a dotted line), and that ε decays rapidly with r so that at r=68 mm the profile is more uniform than at the tip. An average value of ε, ε_{ave}=35 m^2/s^3 or 26 N^3D^2, was estimated using the same expression as in the previous sub-section and the average values of k, $\overline{vw}$ and shear strain rate, $e_{r\theta} \approx 31\ s^{-1}$, were obtained from the profiles at the impeller tip. An average value of ε can be also predicted using the expression $\varepsilon_o = 3.3(k_o)^{3/2}/\ r_o$ as suggested by Issa and Gosman (1981) and, for this impeller size, is ε_o=8.82 m^2/s^3 , i.e. about 75% less than the experimental value.

Figures 3.35 and 3.36 show the contours of axial and tangential rms velocities above and below the impeller and that w' is always higher than u' except from r=63 to 105 mm where they are of similar magnitude. The maximum and minimum values of u' and w' in the bulk flow are about 0.18 m/s or 0.11 V_t and the levels of u' above and below the impeller are almost the same, whereas w' levels are higher below the impeller.

CHAPTER III

3.4.2.3 Flow characteristics with the D=T/2 and C=T/3 configuration

The larger impeller, D = T/2, was used for the measurements described in this sub-section with the same clearance as in section 3.4.2.1. All measurements were taken in the plane of $\theta = 0°$ with N =125 rpm and Re = 45,000. The lower speed was made necessary because of entrainment of air through the free surface.

Figure 3.37 (a) shows the development of the radial and tangential mean velocities in the jet and that profiles become flatter with increasing radius. The inclination of the impeller radial jet is 5.9 °, about 1.5 times greater than that found for D=T/3 with the same clearance and Reynolds number; this increase is proportional to the increase in impeller size. Comparison of the radial and tangential mean velocities shows that the $\overline{W}$ profile is flatter than the radial profile at the impeller tip and that $\overline{W}$ is higher by about 10%. The decay of the tangential velocity with r is faster than that of the radial velocity. The radial velocity at the impeller tip is almost independent of baffle location, figure 3.37 (b), with near-uniform distributions of radial centreline velocities (both mean and rms) with θ (i.e. $\partial\overline{V}/\partial\theta \approx 0$).

Figure 3.38 shows the impeller stream characteristics. The centreline velocity (figure 3.38 (a)) reduces from 0.79 V_t at the impeller tip to 0.42 V_t at r = 125 mm . The spread of the impeller jet, figure 3.38 (b), is similar to that with D = T/3: it is nearly constant up to 10 mm from the impeller tip before increasing linearly from 0.5 h to 1.1 h at r = 125 mm. Figures 3.38 (c) and (d) quantify the pumping capacity of the impeller jet and show that the flow rate increases to a maximum of 8.7 kg/s at r = 112 mm before it starts to decrease. The maximum flow rate is 1.52 times the discharge flow at the tip; the total induced axial flow is about 34% of the discharge flow. The coefficient of discharge, the slip factor and the mechanical efficiency were calculated to be 0.87, 0.59 and 17.8 % respectively.

The axial mean velocity above and below the impeller is shown in figure 3.39 and the presence of the ring vortex below the impeller is evident. The width of the wall jet increases with distance from the impeller disc in accordence with the deceleration of the jet

and the peak velocity moves away from the wall with a maximum value of 0.46 V_t at z = 75 mm which reduces to 0.23 V_t at z = 20 mm. Just above and below the impeller (z = 80 and 115.5 mm) the axial profiles are nearly symmetrical and, from r = 0 up to 100 mm, the profiles are nearly uniform. Figures 3.40 (a) and (b) show the distribution of tangential velocity in profile and contour form, with positive value indicating the flow is in the direction of the impeller rotation. There are two counter-rotating flows below the impeller and close to the bottom of the vessel; one extends from r = 70 to 110 mm and to a height of about z = 60 mm and the second is at the corner of the vessel covering an area of 15 x 20 mm. These two counter-rotating flows can be seen more clearly in figure 3.40 (b). The contours of $\overline{V}$ also show a vortical motion in the direction of impeller rotation below the impeller around the axis, with its centre at the centre of the vessel,where the velocities are almost zero at all axial locations

The distributions of the axial, radial and tangential rms velocity fluctuations, figure 3.41(a), are similar to those for the D=T/3 impeller with intensities of about 0.35 V_t at the impeller tip. The three components of the rms velocities are of similar magnitude indicating that the turbulence is near-isotropic in the impeller stream. The centreline v' velocities, figure 3.41 (b), decay from 0.33 V_t at the tip to 0.24 V_t at r = 125 mm. The profiles of k at Z=80 and 115.5 mm, figure 3.42 (a), show a sharp increase in k at the top and bottom face of the impeller along the length of the blade; from the inner edge of the blade towards the axis the profiles are uniform. The k values decreases rapidly with distance from the blade in the axial direction and the maximum values at Z=80 and 115.5 mm are 0.057 $(m/s)^2$and 0.096 $(m/s)^2$ respectively. In the impeller stream and at its tip, figure 3.42 (b), the magnitude of k in the impeller stream is higher than outside by an order of magnitude with a maximum of 0.162 $(m/s)^2$. An average value of k at the impeller tip, of about 0.116 $(m/s)^2$ or 0.12 V_t^2, was obtained from the profile .

Figure 3.42 (c) and (d) show the distributions of $\overline{vw}$ around the impeller and that $\overline{vw}$ is very small from the vessel axis to the inner edge of the blade. From there towards the impeller tip, $\overline{vw}$ increases sharply and becomes near-uniform along the length of the

blade. In the impeller stream, figure 3.42 (d), the magnitude of $\overline{vw}$ is much higher than in figure 3.42(c) and the profiles are almost symmetric about the centreline of the blade, with a peak at the centre of about 0.082 $(m/s)^2$ or 0.088 V_t^2. The $\overline{vw}$ levels decrease sharply to a negative value of about 0.009 $(m/s)^2$ at 1/6 of the blade width on both sides and then increase again on both sides. The same behaviour can be seen at r = 82.5 mm but with the magnitudes considerably reduced. The rate of decay of $\overline{vw}$ with r in the impeller stream is faster than that of k. An average value of $\overline{vw}$ was found to be 0.014 $(m/s)^2$ or 0.015 V_t^2 from the profile at the impeller tip.

The estimated dissipation of turbulence kinetic energy values, figure 3.43, show a rapid increase from top and bottom edges of the impeller at its tip and then a decrease to a minimum at the centre of the blade. The value of ε tends to infinity, about $\pm$10 mm above and below the centre, shown by the dotted lines on the profile, because ε is proportional to $k^2/\overline{vw}$ and $\overline{vw}$ tends to zero there. The profile at Z=82.5 mm also shows that the dissipation profile tends to become flatter with two sharp peaks on either side of the centre. An average value of ε was estimated from the results using the same expression by taking average values of k, $\overline{vw}$ and $e_{r\theta}$ (19.5 s^{-1}), which is ε_{ave}=1.7 m^2/s^3 or 8.8 N^3D^2. As before, an average value of ε was calculated as suggested by Issa and Gosman (1981) as ε_o=1.3 m^2/s^3, i.e. 26% less than the experimental value.

The rms velocity profiles in the bulk of the flow and mainly in the lower vortex are presented in figures 3.44-3.46, together with the corresponding contours. They show that the profiles are near-uniform except in the vicinity of the impeller blade where they increase considerably due to the strong periodic nature of the flow around the impeller. The turbulence intensities below the impeller decrease with r up to r = 75 mm, and then remain constant up to r = 110 mm and start to increase towards the wall, with values in the region around the axis higher than those near the wall. The radial and tangential intensities are similar in magnitude and slightly higher than the axial levels. Figures 3.47 (a) and (b) show the distributions of turbulence kinetic energy and its contours below the impeller: the k levels decrease with r up to r = 100 mm and then increase towards the wall. In the

central region around the axis, k is higher than in the wall region with maxima at the centre of the vessel.

3.4.3 Parametric study

Detailed measurements were carried out to determine the influence of the impeller rotational speed, impeller size and clearance on the mean flow structure and to establish possible scaling rules. All the results were taken at $\theta=0^{\circ}$. The effects of the three parameters are presented and discussed in the three subsequent sub-sections.

3.4.3.1 Effect of impeller rotational speed

Measurements were obtained at rotational speeds of 50, 150 and 300 rpm corresponding to Reynolds numbers of 8,000, 24,000 and 48,000 respectively with the impeller of section 3.4.2. A less detailed investigation was carried out with the impeller of section 3.4.2.3 at speeds of 66.5 and 125 rpm, corresponding to Reynolds numbers of 24,000 and 45,000. The test with this impeller was carried out at lower speeds than with the T/3 impeller in order to avoid air entrainment from the free surface. All results were obtained in the $\theta= 0^{\circ}$ plane, primarily in the impeller stream and lower ring vortex.

D = C = T/3 impeller

Figure 3.48 (a) presents the distributions of radial mean velocity normalised with the tip velocity and confirms that the velocities in the impeller stream scale well with impeller rotational speed (or equivalently the impeller tip velocity). Small differences are evident with the 50 rpm profiles, especially away from the axis, in comparison to those obtained at 150 rpm and 300 rpm, which are nearly identical. This result is partly expected as there are laminar flow regions away from the impeller with the lowest speed. The radial mass flow, shown on figure 3.48 (b), increases with radial position up to r=105 mm where the jet impingement on the wall starts and then decreases. The results also show that the mass flow at each radial location increases linearly with rotational speed and the

proportionality factor increases with r up to r=105 and thereafter remains constant until r=120 mm. These results are in accord with those of Sacks and Rushton (1954), Cooper and Wolf (1968) and van der Molen and van Maanen (1978) who used the same type of impeller with speeds from 10 to 300 rpm.

The coefficient of discharge was calculated to be 0.72, 0.83 and 0.84 for speeds of 50, 150 and 300 rpm respectively. The values of K_d at 150 and 300 rpm are identical and, although there is a small difference with the lower speed, they are well within the range (0.75±0.15) recommended by Revill (1982). The results of figure 3.48 (c) show the variation of shearing rate, $\partial\overline{V}/\partial Z$, at the impeller tip as a function of impeller speed and that both the average and maximum shear rate are proportional to impeller speed. This finding is in agreement with the results reported by Oldshue (1983).

The effects of speed in the lower ring vortex and in the flow region just above the impeller are shown in figure 3.49. The structure of the ring vortex is unchanged, and the strength of the flowfield, in terms of the axial mean velocities, is proportional to speed. Small differences are evident again in the 50 rpm results. The power numbers, N_p, deduced from the torque measuremnts for speeds of 50, 150 and 300 rpm were 4.0, 4.3 and 4.7, respectively.

Figures 3.50 and 3.51 show the distributions of rms velocities in the impeller stream above and below the impeller and, when normalised by V_t, they are practically identical at all impeller speeds suggesting that the turbulence intensity in the impeller stream and in the bulk flow is independent of impeller rotational speed and scale well with the impeller tip velocity.

D = T/2; C=T/3 impeller

The results for this geometry were obtained at the tip of the impeller stream and below the impeller and are shown in figures 3.52 and 3.53. They again scale well with rotational speed everywhere in the vessel, and the coefficient of discharge was found to be 0.84 and 0.87 for speeds of 66.5 and 125 rpm. The difference is negligible considering

the errors associated with the integration of the profiles. Again, the impeller tip velocity is confirmed an appropriate and sufficient scaling factor to account for the effect of the rotational speed changes.

3.4.3.2 Effect of Impeller Size

The effect of impeller size on the impeller stream and below the impeller was investigated for D=T/4, T/3 and T/2 with corresponding Reynolds numbers of 36,000, 45,000 and 48,000. All the measurements were taken with C = T/3 at $\theta=0^{\circ}$ and the impellers were geometrically similar so that the ratios of D: d: h: L are the same in all cases (see figure 3.2). The thickness of the impeller disc and blades were kept the same in all three cases (3 mm). As the impeller size varies, it is more appropriate to characterise the results in terms of non-dimensional coordinates and, for this reason, the axial distance was normalised with half of the impeller width (h/2) with the origin at the centre of the impeller (i.e. at C=T/3) and the radial location, r, was normalized with the impeller radius (D/2). The axial and radial non-dimensional coordinates are presented in the graphs as $Z^*=Z/(h/2)$ and $R^*=r/(D/2)$.

Figure 3.54 (a) shows that the distributions of mean radial velocities at the impeller tip are independent of the impeller size when plotted at the corresponding R^* distances. These results are confirmed by the measurements for T/2 and T/3 impeller at different axial location in the impeller stream as shown in figure 3.54 (b). The characteristics of the impeller jet are shown in figure 3.55 and since the vessel diameter is the same in all cases and the radial location is normalised with respect to impeller radius, the position of the wall is therefore at R^*= 4.0, 3.0 and 2.0 for the T/4, T/3 and T/2 impellers respectively. Figure 3.55 (a) shows that the rate of radial centreline velocity decay is the same for all three sizes. Van der Molen and van Maanen (1978) suggested that the decay of the centreline velocity can be presented by the function;

$$\overline{V} / V_t = 0.85 \, (R^*)^{-7/6} \qquad (3.15)$$

which was the best fit to their data in the impeller stream, and this function is superimposed on the present results by a solid line. The agreement with present data is evident. The centreline rms velocities also decay in a similar manner (figure 3.55 (b)) for the T/3 and T/4 impeller, but the values for the T/2 impeller are higher by up to 10%.

The spread of the radial jet, $Z_{(1/2)}$, non-dimensionalised by the impeller width, is similar for all three impellers as shown in figure 3.55 (c) and the width of the normalised impeller jet is constant in the vicinity of the impeller tip up to $R^*=1.2$, and subsequently increases almost linearly. The straight line can be described by the equation

$$Z_{(1/2)} / h = 0.92\ R^* - 0.58 \qquad (3.16)$$

which is the best straight-line fit through the measured data.

The radial mass flow in the impeller stream is shown as a function of R^* in figure 3.55 (d) and has a similar increase in all three cases up to $R^*=1.5$, but thereafter the trends differ due to the difference in R^* for each impeller, i.e. $R^*=2$, 3 and 4 for T/2, T/3 and T/4 impellers respectively. The mass flow starts to decrease at $R^*=1.6$, 2.3 and 2.9 for T/2, T/3 and T/4 impeller respectively, and these values of R^* correspond to a radial location of r=112±5.0 mm which is similar for all impellers, suggesting that the location of impingement of the radial jet stream, i.e. the location where the axial velocities across the width of the impeller stream is zero or where there is no flow induced into the impeller stream, is independent of the impeller size. The maximum radial mass flows are 1.5, 1.66 and 2.2 Q_d for the T/2, T/3 and T/4 impellers respectively so that, the relative radial mass flow increases as the impeller size decreases, but this change is not in proportion to the impeller size.

The coefficients of discharge for the T/2, T/3 and T/4 impellers were calculated to be 0.87, 0.84 and 0.79 respectively which are similar and well within the range recommended by Revill (1982), k=0.75±0.15. Table 3.6 summarises the effects of impeller size on the impeller stream characteristics and indicates that the values of the

coefficient of discharge, mechanical efficiency and slip factor are independent of impeller size. However, the size of the impeller affectes the inclination of the impeller stream so that the inclinations are about 5.9, 4.0 and 2.0 degrees for T/2, T/3 and T/4 impellers respectively. The reason for this is the stronger recirculation in the lower ring vortex for the larger impellers which pushes the stream jet more upwards, as discussed below.

Table 3.6 Effect of impeller size at the impeller tip

D	C	N (rpm)	Re	N_p	K_d	η (%)	S
---	---	---	---	---	---	---	---
T/2	T/3	125	45,000	4.9	0.87	17.8	0.59
T/3	T/3	300	48,000	4.7	0.84	17.9	0.58
T/4	T/3	400	36,000	4.3	0.79	18.4	---

The effect of impeller size on the flow below and just above the impeller can be seen in figures 3.56, which shows that the axial mean velocities are the same from the tank centre up to r = 49 mm (the tip of the D = T/3 impeller). From that point onwards, the axial mean velocity of the bigger impeller size is higher everywhere, but the width of the wall jet remains unchanged for both impeller sizes. That is, the circulation for the larger impeller is faster than the smaller one and this can be seen much more clearly in figure 3.57 where the normalised velocity vector ($[\sqrt{(\overline{U}^2+\overline{V}^2)}] / V_t$) at $\theta = 0^\circ$ plane can be compared for both impeller sizes. The faster recirculation can be best judged by the longer vector length with the T/2 impeller, up to twice the length of those for D=T/3 impeller, below the impeller. The results also show that the centre of the lower ring vortex is at the same radial location of $r \approx 110$ mm for both sizes, but the axial location is moved downwards with the

larger impeller so that it is at Z≈63 mm for the T/3 impeller and at Z≈47 mm for T/2 impeller.

Comparison of tangential mean velocities below the impeller, figure 3.58, show that they are similar, but the area occupied by the counter-rotating flow is reduced by about 50% with larger impeller. The magnitude of the positive tangential velocity has been increased with the larger impeller especially in the region around the axis of the vessel where an increase of an order of magnitude can be observed. The three mean velocity components in the bulk flow below the impeller increased with impeller size at the same Reynolds number, but the increase is not in proportion to the change in impeller size.

The rms velocities in the impeller stream are shown in figure 3.59 and it is evident that the radial rms velocity profiles of all three sizes are identical at the impeller tip, figure 3.59 (a), and is confirmed at different radial location, figure 3.59 (b), for two sizes. Figure 3.59 (c) shows similarly that the axial rms velocity profiles are identical for both impellers at the tip of the impeller as are the turbulence kinetic energy profiles at the impeller tip of figure 3.60 (a). The average values of k at the tip along the width of the blade (i.e. $-1<Z^*<+1$) were calculated to be 0.139 V_t^2 and 0.145 V_t^2 for the T/2 and T/3 impellers. The results in the impeller stream suggest that the turbulence field is independent of impeller size when scaling factors of V_t, R^* and Z^* are used for normalising the measured velocities.

In the bulk of the flow, the rms velocities below the impeller are higher for the larger impeller as shown in figures 3.60 (b) and 3.61. The radial distribution of axial rms velocities above and below the impeller, figure 3.60 (b), show higher levels for the larger impeller. Close to the wall region and in the central region around the axis of the vessel, the increase in the u' levels with impeller size is up to 50%. The distributions of the turbulence kinetic energy of both impellers are compared in figure 3.61 and show that they are greater for the larger impeller, by about an order of magnitude, while the Reynolds numbers are the same. This increase is more evident around the axis of the vessel (i.e. from r=0 to 60 mm).

CHAPTER III

3.4.3.3 Effect of Impeller Clearance

To quantify the effect of clearance, measurements were obtained in the impeller stream with clearances of T/2, T/3 and T/4 and with the D=T/4 impeller, and more detailed measurements were made with the D=T/3 impeller at clearances of C=T/3 and T/4.

D = T/4 Impeller

Figures 3.62 and 3.63 show the distributions of mean and rms velocities in the impeller stream with different impeller clearances; the speed was 300 rpm with Re=36,000, and the measurements were in the $\theta = 0^\circ$ r-Z plane. It is evident that the clearance does not influence the magnitude of the velocity and this was checked by calculating Q_d at the impeller tip to obtain coefficients of discharge of 0.78, 0.79 and 0.78 for C = T/2, T/3 and T/4, which confirms that the clearance does not affect K_d. As C decreases, the impeller jet is directed increasingly upward until, at C = T/2, there is almost no inclination, but at C = T/3 and T/4 the impeller stream is at an angle of 2.9 and 4.6 ° to the horizontal respectively. Figure 3.63 shows the rms velocity at the impeller stream and confirms that the clearance of the impeller does not affect the turbulence levels in that region, except that the rms profiles are slightly shifted, as expected, since the velocity gradients are shifted due to the inclination of radial jet stream.

D = T/3 Impeller

The measurements presented below include some of the results of sub-section 3.4.2.1 and 3.4.2.2. As shown in figures 3.19 and 3.30 for C=T/3 and T/4 respectively, the corresponding radial jets are inclined by about 4.0 and 7.5 ° in the impeller stream. The inclination of the D=T/3 impeller is on average about 1.6 times higher than the T/4 impeller. The coefficient of discharge was calculated to be 0.88 and 0.84 for C=T/3 and T/4 clearances respectively and shows no dependence on impeller clearance, as in the case of the T/4 impeller discussed above. Table 3.7 summarises the effect of clearance on the characteristics of the impeller stream at the impeller tip, and shows that K_d, η and S are

independent of C in both cases.

Figures 3.64, 3.66 and 3.67 were already presented in sub-section 3.4.2.1 and 3.4..2.2 and are reproduced in this sub-section to facilitate comparisons between the C=T/3 and T/4 clearance configurations. Figure 3.64 presents comparisons of the contours of $\overline{W}$ mean velocity below the impeller and indicates that similar flow patterns exist with both clearances, but the area of the counter-rotating flow with T/4 clearance is smaller by about 50% than for T/3. For C=T/4 the counter-rotating flow occupies the region around $49 < r < 80$ mm with a maximum negative velocity of -0.035 m/s whereas for C=T/3 this range has been extended to $30 < r < 120$ mm with a maximum negative velocity of -0.07 m/s. The results also show that the magnitude of positive $\overline{W}$ velocities increases as the clearance is reduced, especially around the axis below the impeller where with the T/4 clearance there is a vortical motion stronger by an order of magnitude than the corresponding motion with the T/3 clearance. The overall effect of a reduction in the impeller clearance on the swirl motion below the impeller is the same as the effect of increasing the impeller size.

Table 3.7 Effect of impeller clearance at the impeller tip

D	C	N (rpm)	Re	N_p	K_d	η (%)	S
T/4	T/2	400	36,000	4.2	0.78	18.6	---
T/4	T/3	400	36,000	4.2	0.79	18.8	---
T/4	T/4	400	36,000	4.2	0.78	18.6	---
T/3	T/3	300	48,000	4.7	0.84	17.9	0.58
T/3	T/4	313	32,500	4.5	0.88	19.5	0.58

Comparison of k of the T/3 clearance with that of T/4 at the impeller tip, figure 3.65, indicates that they are of similar magnitude. The average values of k at the tip and

along the width of the blade (i.e. $-1 < Z^* < +1$) were 0.139 V_t^2 and 0.142 V_t^2 for T/3 and T/4 clearances respectively. Figures 3.66 and 3.67 allow comparison of w' and u' rms velocities above and below the impeller and show that w' is larger for C=T/4 below the impeller, figure 3.66, by about 23%, whereas in the axial direction the u' levels remain almost the same for both impeller clearances above and below the impeller.

The results presented in section 3.4 reflect some of the most important flow phenomena in stirred vessels. The flow patterns depicted in figure 3.14 and 3.15 present a typical description of flow development with the flow structure in the r-Z planes characterised by an annular jet stream emanated from the impeller and a system of two ring vortices, generated by the deflection of the jet stream on the wall, above and below the impeller. The spread of the radial jet stream is near-linear with near parabolic profiles, and this flow structure prevailed in other impeller geometries. In the r-θ planes, large counter-rotating flow regions exist, due to the presence of pressure gradients below the impeller which reduced in size with decrease in impeller clearance or increase in impeller size. There was also a helical vortex present behind each baffle rotating in a direction opposite to the impeller with a size comparable to the baffle width. Above the impeller the flow was mainly in the same direction as impeller rotation except at the top corner of the vessel where a small counter-rotating flow region was observed.

The turbulence results showed an overall decay away from the impeller with turbulence quantities near-isotropic in the impeller stream and anisotropic in most of the bulk flow. In the impeller stream from the tip to near the wall, the turbulence intensity was reduced by about 250% and the level of the turbulence in the bulk of the flow was generally lower by an order of magnitude than that in the impeller stream.

Comparison of the results with different impeller speeds showed that the flow scaled with speed everywhere in the vessel and the that the tip velocity was an approperiate scaling factor. The influences of impeller size and clearance, sub-sections 3.4.3.2 and 3.4.3.3, revealed that the mean and rms velocities were independent of impeller size when normalised with V_t and plotted against non-dimensional radial, R^*, and axial, Z^*,

directions. A reduction in impeller clearance resulted in large inclination of the jet stream, and that mean and rms velocities were affected by changing the impeller size and clearance in the bulk flow.

The single-phase mean and turbulence velocities are in agreement with most of the previous experimental results listed in table 1.1, especially with those that were made using laser-Doppler velocimetry such as those of Reed et al (1977), van der Molen and van Maanen (1978), van Doorn (1982) and Yianneskis (1987). The comparison of present results with those of Yianneskis et al (1987) showed that the agreement both in mean and turbulence flow field velocity results were within 3% and 10% (in k values) respectively. In the parametric study, it was shown that the effect of speeds on mean flow as well as turbulence were in good agreement with all previous work reviewed.

3.5 Two-phase flow results and discussion

The solid particle mean and rms velocity results for two-phase flows in the stirred vessel are presented in this section together with the corresponding single-phase results which are shown for comparison and include ensemble-averaged values measured over 360° of the impeller rotation. All the particle velocities have been normalised with the impeller tip velocity. The results are presented under two headings: the particle motion in dilute and in moderately dense suspensions respectively.

3.5.1 Particle motion in dilute suspensions

Measurements of particle mean and rms velocities in two-phase flow in a water-filled vessel were obtained with a particle concentration, C_v, of 0.02% by volume which was the maximum concentration for which velocity measurements could be made, as the signal quality and data rate deteriorated rapidly for higher concentrations. For C_v=0.03% it was not possible to make any measurements in the vessel. The flow conditions of the water two-phase experiments are summarised in table 3.1. Spherical

CHAPTER III

Diakon and lead-glass particles were used as the dispersed-phase with two different sizes for each so as to allow the determination of the effects of particle size and density ratio. The properties of the fluid and of the particles are given in table 3.2 (I). The flow configurations are listed as cases 1-5 in table 3.3. Cases 1-3 were with the standard configuration geometry and cases 4 and 5 with the D=T/2 and C=T/4 geometries.

D = C = T/3 Impeller

Particle mean and rms velocities for cases 1-3 are presented in figures 3.68 to 3.71 together with corresponding single-phase flow profiles. It is useful to define an apparent slip velocity as the particle velocity minus the fluid velocity in the absence of the particles denoted by the subscript s, i.e. $\overline{U}_s$, $\overline{V}_s$ and $\overline{W}_s$ are the apparent slip velocity in axial, radial and tangential components obtained as $\overline{U}_p$-$\overline{U}$, $\overline{V}_p$-$\overline{V}$ and $\overline{W}_p$- $\overline{W}$ respectively.

The profiles of $\overline{V}_p$ in the impeller stream are presented in figure 3.68 and show that the particle velocities are similar to those of the single-phase flow except near the plane of the impeller disc where the 725 μm diameter Diakon particles and the 232.5 μm diameter glass particles lag behind the fluid, with an apparent slip velocity, $\overline{V}_s$, of about 96 and 200 mm/s or 0.06 or 0.13 V_t. This lag around the peak of the jet is in agreement with the results presented in the previous chapter (see figure 2.31 (b) to (d)) around the peak value of the annular jet. The same trend was reported by Nouri et al (1984) in a flow around axisymmetric baffles in a horizontal pipe. In comparison to the calculated slip velocity,V_{gt}, of about 38 and 116 mm/s for Diakon and glass respectively, see table 3.2 (I), V_s is higher by about 200%. The 272 μm diameter Diakon particles appear to follow the flow with very small slip and at r=125 mm the particles follow the flow faithfully.

The profiles of the particle axial velocity component, figure 3.69 with that at Z=20 mm shown in larger scale, reveal small axial apparent slip velocity, $\overline{U}_s$, and that the particles lag behind the fluid in upflow regions due to gravity; as in the flow region in the wall jet above the impeller and around the axis below the impeller, and lead the fluid in downflow regions. The maximum $\overline{U}_s$ at Z=75.7 mm is 50 mm/s for glass particles and at

Z=20 mm it does not exceed 30 mm/s. The magnitudes of $\bar{U}_s$ in the near-axis region below the impeller are 15 mm/s on average for both Diakon particle sizes with no increase in $\bar{U}_s$ with particle size and 40 mm/s for glass particles. Above the impeller, only the glass particles show some some slip (of 15-30 mm/s), while the Diakon particles follow the flow.

An interesting flow feature can be observed by comparing the wall jet results at Z=75.5 mm with that at Z=20 mm; at the former axial location the particles lag behind the single-phase profile in downflow but they lead at Z=20 mm. The initial lag can be attributed to the particle inertia in that region where the impeller meets the wall and changes direction. Subsequently, the particles accelerate due to gravity and eventualy lead the fluid. However, the lag of particles in the wall jet at Z=120.3 mm (upflow) above the impeller is more pronounced than that at Z=75.7 mm due to gravity acting on the particles in an opposite direction to their motion.

In the impeller stream, figure 3.70, a reduction of the turbulence levels in comparison with the single-phase levels is evident and is more pronounced at the impeller tip (r=51.5 mm) and along the impeller width with a maximum reduction of 25% at the center of the blade for the heavier particles (lead-glass). The reduction of turbulence for the Diakon particles in the same region is about 13% and at r=125 mm the difference in particle and fluid turbulence levels is about 3%.

In the bulk of the flow, figure 3.71, the particle turbulence levels are similar to that of single-phase flow around the axis of the vessel (up to r=50 mm), both above and below the impeller, with a small reduction in turbulence of about 4% in the two-phase case. But the reduction in the wall jet region is more evident with levels lower by 7 and 15% for Diakon and glass particles.

D = T/2 and C = T/4 Impeller

Figures 3.72 - 3.74 present the particle mean and rms velocities for the cases 4 and 5 (see table 3.3) and show similar features to those of cases 1-3. The radial component

of the mean particle velocity at the impeller tip, figure 3.72 (a), indicate that the largest differences between single-phase flow and the solid-phase profiles are again found to be near the plane of the impeller disc where $\overline{V}_s$ is about 80 mm/s or 0.07 V_t for both the 232.5 and the 376.5 μm diameter glass particles. The apparent slip velocities in these case are smaller by about 46% and follow the fluid more faithfully than in the flow cases of 1-3 (0.13 V_t). The main reason for this large difference is the smaller single-phase velocity gradient, $\partial\overline{V}/\partial Z$, of the present cases (with a maximum of 80 s^{-1}).

The axial particles velocities, figure 3.73, show that the particles lag or lead the fluid in upflow and downflow situations respectively, and that $\overline{U}_s$ has a different sign in the near-axis and near-wall regions, as expected, and that $\overline{U}_s$ is larger in the case of the larger particles. $\overline{U}_s$ is about 25-80 mm/s, from the axis of the vessel up to r=110 mm and does not exceed 40 mm/s in the wall region. A similar effect, as in cases 1-3, of the particles initially lagging (Z=49.5 mm) and subsequently leading (Z=20 mm) the fluid can be observed in the wall jet region. As mentioned in section 3.3.1, data rate limitations prevented measurements above the impeller at Z=98 mm.

The turbulence results of case 4 and 5 are shown in figure 3.72 (b) and 3.74 in the impeller stream and in the bulk of the flow respectively and show that u'_p is smaller than u' by up to 23 % in the impeller stream, and the u'_p levels are similar for both sizes. In the bulk flow, figure 3.74, u'_p and u' are similar in the near-axis region, but u'_p is smaller than u' near the wall region.

3.5.2 Particle motion in moderately dense suspension

Detailed measurements of all three components of the particle mean and rms velocity were made for Diakon particles of 665 μm mean diameter for different volumetric particle concentrations. A mixture of oil of turpentine and 32.6% by volume of tetraline was used as working fluid. The refractive index of the fluid was the same as Diakon particles at a temperature of 28.5 °C. In this way, the maximum particle concentration at which velocity measurements could be made was 2.5 % in the mixture flow; i.e. 125

times more than when the particles were suspended in water (C_v=0.02%).

Flow visualisation was carried out to determine qualitatively the effects of the particle concentration and the impeller speed on sedimentation of the particles and sample photographs are shown in figurer 3.75 and 3.76. Photographs of the visualisation of the two-phase flow at particle volumetric concentrations (C_v) of 0.25, 0.75, 1.25 and 1.75% are shown in figure 3.75 and it can be seen that the particles are well suspended in the flow at C_v=0.25% with a concentration gradient evident along the height of the vessel and similar flow patterns for the four values. Figure 3.76 shows the effect of impeller rotational speed on the sedimentation of the particles. At 100 rpm, most of the particles are at the bottom of the vessel and the number of suspended particles increases with speed until, at 313 rpm, almost all of the particles are suspended in the flow. This speed is also close to the maximum operational speed, above which air was entrained into the flow through the free surface.

In order to quantify the concentration gradient along the height of the vessel, the number of particles crossing the measuring volume per second, $\dot{N}$, was counted in terms of the number of Doppler bursts at different axial locations from the bottom to the top of the vessel. The measurements were taken at a particle volumetric concentration C_v=0.5% and at a fixed radial location, r=20 mm because the variation of the particle velocity ($\overline{U}_p$) with height, Z, is small. In this way the local particle concentration (C_l) can be estimated as a measure of number of particles per unit volume as follows:

$$C_l = \dot{N} / (\overline{U}_p A_p) \qquad (3.17)$$

where A_P is the cross-sectional area of the particles. The maximum measured value was $C_{l,max}$=1.58x10^8 particles / m^3 at Z=16 mm which corresponds to a volumetric concentration of 2.5%; i.e. five times higher than C_v. The resulting distribution of the relative particle concentration, $C_l/C_{l,max}$, is presented in figure 3.77, and confirms the existence of the concentration gradient along the height of the vessel, as expected from the

flow visualisation results. Below the impeller, the gradient is very steep varying from 1.0-$C_{l,max}$ at Z=16 mm to 0.33 $C_{l,max}$ at Z=58 mm just below the impeller. Above the impeller the concentration and gradient are small, varying from 0.18 $C_{l,max}$ at Z=86 mm to 0.1-$C_{l,max}$ at Z=260 mm. The relative particle concentration of $C_l/C_{l,max}$= 0.20 corresponds to C_v=0.5% which is at an axial location of Z=83 mm, right above the upper face of the impeller blade. The present results suggest that the particle volumetric concentration of C_v=0.5% changes from 5.0 C_v at the bottom of the vessel to 0.5 C_v at the top. The radial concentration gradients were not measured because variations in the depth of the field would introduce errors, of unknown magnitude, which could not be reliably quantified in the transmitting and collecting side of the anemometer optics.

Particle mean and rms velocities are presented in figures 3.78 to 3.85 together with the single-phase flow profiles which are shown as dotted lines. Figure 3.78 shows the axial distributions of radial particle velocity profiles in the impeller stream for different particle concentrations and confirms that the particles lag behind the fluid everywhere along the width of the impeller and that the lag is again more pronounced near the plane of the impeller disc. This is in good agreement with findings of the previous section (3.5.1) for both Diakon and lead-glass particles suspended in a water filled vessel. The lag is more uniform along the width of the impeller at r=68 mm than at r=51 mm. The apparent slip velocity, $\overline{V}_s$, increases with C_v, i.e. the particle velocity decreases as C_v increases, so that at r=51 mm $\overline{V}_s$ increases from 20-100 mm/s to 50-120 mm/s for a change of C_v from 0.25% to 2.5% respectively, and at r=68 mm, for the same change in C_v, V_s increases from 40 mm/s to around 75 mm/s. The same conclusion can be reached when the present results are compared to those of the previous section where $\overline{V}_s$ at the impeller tip and near the plane of the impeller disc, was about 6% of V_t at C_V=0.02%. The corresponding value of $\overline{V}_s$ in the present case at C_V=2.5% is 7.5% of V_t. This effect is consistent with the two-phase pipe flow results presented in the previous chapter.

The effect of concentration on the axial and tangential particle velocities is shown in figure 3.79. The particles lead the fluid in the axial direction, figure 3.79 (a) , when the

flow is directed downwards and lag when the flow is upwards, as expected. As a result, the width of the wall jet increases below the impeller and decreases above it . The change in particle velocity with C_v is small, but decreases everywhere with increasing C_v. $\overline{U}_s$ decreases in downflow and increases in upflow. At Z=150 mm, in the near-axis region (downflow), $\overline{U}_s$ is about 25 mm/s at C_v=0.5% and decreases to almost zero at C_v=2.5%, and in the wall jet (upflow) $\overline{U}_s$=25 mm/s at C_v=0.5% and is increased to about 40 mm/s with C_v=2.5%. Similar results can be seen at Z=20 mm where $\overline{U}_s$ is about 35 mm/s in the upflow region and 25 mm/s in the wall jet. Figure 3.79 (b) shows that there is no variation in particle velocity with C_v at Z=20 mm in the tangential direction, and that the particles are not following the counter-rotating flow very faithfully . The width of the counter-rotating flow region at Z=20 mm is reduced from 35 mm in the single-phase flow to 22 mm for the solid-phase at this axial location, a reduction of 37%.

Figures 3.80 and 3.81 show that the particle concentration at each axial location is a maximum measured, i.e 2.5% above the impeller and in the impeller stream and 1.75% below the impeller. The axial particle velocities of figure 3.80 show that the apparent slip velocities are smaller in the downflow than in upflow regions due to the increase in concentration. The same effect as in previous section can be seen below the impeller where the particles lag in the wall jet (downflow) at Z=58.5 mm and lead at Z=20 mm for the same reason. In the tangential direction, figure 3.81, the particles follow the fluid faithfully except in the counter-rotating region below the impeller, where the particles resulted in a reduction of the width of this region at all axial locations and that, close to the axis of the vessel, the particles lag behind the fluid below the impeller and lead above it.

The axial distribution of radial particle turbulence intensity at the impeller stream is shown in figure 3.82 for different values of C_v and shows that the particle rms velocities are smaller than in the single-phase flow by about 15% at the impeller tip and 12% at r=68 mm, and that there is no change in the rms levels as C_v increases. Figure 3.83 shows radial distributions of the particle axial and tangential rms velocities for different values of C_v and at different Z-locations. Again there is no change in u'_p and w'_p levels with

increasing C_v and the levels of turbulence are similar to the single-phase levels except in the wall region where the particle rms velocities are smaller by about 5-10%. The results of the water flow experiments of the previous section showed that the turbulence levels of the Diakon particles in the impeller stream and in the bulk of the vessel close to the wall were lower than single-phase by about 13% and 7% respectively at C_v=0.02%, which are similar to the present findings at higher values of C_v.

The results suggest that the axial and radial particle mean velocities decrease with increasing particle concentration everywhere in the stirred vessel and this is in agreement with all previous investigations of two-phase pipe flows cited in the previous chapter, such as those of Birchenough and Mason (1976), Tsuji et al (1984) and with the results presented in the previous chapter. As a result the apparent slip velocity increases in upflows and decreases in downflows. However, the turbulence results in stirred vessel show that the turbulence levels remain unchanged as C_v increases.

The results also show that the particles lag behind the fluid in the impeller stream, especially around the peak of the jet stream and in the wall jet where the jet stream meets the wall. The former is in agreement with results presented in previous chapter in the annular jet and also with results reported by Nouri et al (1984) for an annular jet around a disc baffle in a horizontal pipe and Khezzar (1987) in unsteady flow behind a projectile in a gun barrel. Thus, the particles can not respond faithfully to the high velocity flow and also to sudden change in the flow direction due to the particle inertia and therefore lag behind the fluid.

The present mean and turbulence quantities have been used as boundary conditions for the prediction of the single and two-phase flows in stirred vessels by Looney et al (1985) and Politis (1988) in a parallel study. They solved the time-averaged Navier-Stokes equations for the liquid-phase and the dispersed-phase was treated as a continum with the initial velocity condition the same as for the liquid-phase. They also included terms for the particle drag effect and for the turbulence on the particle dispersion. The effects of the periodicity in and around the impeller were not considered since they

required a different methodology for these regions. Therefore, the experimental input data for the prediction of the flow should be made over the whole cycle of impeller revolution (i.e. 360 ° averaged) and not over a particlar part of the impeller rotation. The experimental data were fitted by polynomial curves to be used as initial boundary profiles around the impeller.

The present data have also been used for the validation and the assessment of the prediction results. The primary work of Looney et al (1985) showed that the comparison of their predictions, for both the single and two-phase flows, with present data were encouraging with good agreement qualitatively. Politis (1988) used finer grids and more detailed input data and showed that, in general, the agreement between the prediction results and the present experimental data was good. In single-phase flow, apart from some smearing of the velocity gradients the agreement was very good, but the predicted rms velocities were underestimated in comparison to the present experimental results and similar agreement can be observed for the two-phase flow case. The comparison of the relative motion, between the particles and the fluid, show favorable agreement.

3.6 Summary

The more important findings of this chapter are summarised below, for single and two-phase flows.

3.6.1 Single-phase flows

(1). The impeller stream emanated from the impeller tip and extended to the wall where it deflected into two thin axial jets along the wall. The impeller stream was inclined with two ring vortices generated above and below the impeller. There was a helical vortex in the wake of the baffle.

(2). The overall flow pattern was similar with different baffle positions and impeller sizes, but the impeller clearance affected the size of the main ring vortices and

changed the inclination of the impeller stream.

(3). With the D=T/3 andC=T/3 configuration, the main features of the flow are summarised below:

(a). The lower main ring vortex was more ordered and circular and smaller in size than the upper one with its centre at r=1.12D and Z=60 mm at θ=0 °. It moved radially towards the axis of the vessel with θ to a minimum distance from the axis of r=0.8 D at θ=45 ° and subsequently moved back toward the wall. In general, the overall flow pattern at different θ planes were similar, but the circulation was fastest at θ=45 °.

(b). The flow around the axis and along the wall of the vessel was predominantely axial, whereas, at the top and bottom of the vessel, it was predominantely radial. The flow in the vicinity of the impeller was symmetric to within 10%.

(c). There were large counter-rotating flow regions below the impeller especially close to the bottom of the vessel, but above the impeller the swirl motion, at θ=0 °, was mainly in the same direction as the impeller rotation with a small region of counter-rotating flow at the top corner near the free surface.

(d). The results around the baffle show that the tangential velocities reduce to zero in front of the baffle (up to 5 °) and there was a helical vortex behind each baffle with a size comparable to the baffle width. The width of the axial wall jet increased with θ to a maxima at θ=40 °, remained constant up to θ=56.25 ° before it decreased again. There was a double-peak axial jet behind the baffles due to intraction of the wall jet with the recirculation zone in the wake of the baffle.

(e). Maximum $\overline{U}$, $\overline{V}$ and $\overline{W}$ velocities were measured in the bulk of the flow as 0.35, 0.3 and 0.11V_t respectively with small shearing rates in all directions except $\partial\overline{U}/\partial r$ in the wall region and $\partial\overline{V}/\partial Z$ whose maximum values were 23 and 10 s^{-1} respectively. The corresponding maximum velocities in the impeller stream were 0.12, 0.75 and 0.8 V_t at the tip of the impeller with maximum shearing rates of 6.0, 150 and 120 s^{-1} for $\partial\overline{U}/\partial Z$, $\partial\overline{V}/\partial Z$ and $\partial\overline{W}/\partial Z$ respectively.

(f). The radial and tangential profiles, at the tip of the impeller showed an almost symmetric distribution about the plane of the impeller disc with a small inclination in jet stream of about 4 °. The results also showed that radial smmetry prevailed. The axial flow into the impeller came from below the impeller causing the inclination of the jet stream, and that the total induced flow was 1.7 times the discharge flow at the impeller tip.

(g). The spread of the radial jet stream was almost linear except in the vicinity of the impeller tip (up to R^*=1.2) where it remained almost constant. The coefficient of discharge, the slip factor and the mechanical efficiency of the impeller were 0.84, 0.58 and 18% respectively.

(h). Rms velocity measurements showed that the turbulence was near-isotropic in the impeller stream with a maximum value of about o.35 V_t for all three components at the impeller tip which reduced to o.15 V_t close to the wall.

(i). The turbulence kinetic energy level at the impeller tip was around 0.14 V_t^2 and almost constant along the width of the impeller blades. The Reynolds shear stresses were almost symmetric at the impeller tip along its blades with a maximum at the centre of the blade of 0.034 V_t^2.

(j). Three components of the tubulence intensities in the bulk of the flow were much smaller than those in the impeller stream with a minimum value, about 0.04 V_t around the centre of the ring vortices reaching a maximum of 0.1 V_t close to the wall and near the axis. The turbulence in the bulk flow was not isotropic except around the centre of the ring vortices. The k values in the bulk flow were smaller than in the impeller stream by an order of magnitude and the turbulence levels behind the baffles were higher than in front of it , with a maximum difference of about 30%.

(4). The mean and rms velocity components scaled with impeller speed everywhere in the vessel.

(5). For geometrically similar impellers, the mean and rms velocities in the impeller stream were independent of impeller size and the non-dimensionalised parameters R^* and Z^* together with V_t are appropriate scaling factors to account for the effects of

impeller changes in that region. The impeller size affected the inclination of the impeller stream so that the inclination was 5.9, 4.0 and 2.9 for T/2, T/3 and T/4 impellers respectively. In the bulk flow, the mean velocities increased by up to 200% with impeller size; i.e. the circulation for the T/2 impeller was faster than that of the T/3 impeller at the same Reynolds number. The counter-rotating flow region was reduced in size and magnitude by about 50% for an increase of the impeller size from T/3 to T/2.

(6). The turbulence in the bulk flow was strongly affected by impeller size so that the u' levels increased by about 50% with an increase in size from T/3 to T/2, and the turbulence kinetic energy levels for the T/2 impeller were higher by an order of magnitude than for the T/3 impeller.

(7). A decrease in impeller clearance from C=T/3 to T/2 resulted in a stronger swirl motion, below the impeller, in the same direction as impeller rotation by about 6 times, and the counter-rotating flow region became weaker and smaller in size by about 50%. This effect was the same as that of (5) above. In the impeller stream, the mean and rms velocities were similar except that the jet stream was inclined, so that, for the T/4 impeller at C=T/2, the inclination was almost zero increasing to 2.9 and 4.6 ° at C=T/3 and T/4 respectively, and for the T/3 impeller the inclination increased from 4.0 to 7.5 for a reduction in C from T/3 to T/4.

(8). The coefficient of discharge, the slip factor and the mechanical efficiency were independent of impeller size and clearance and the recommended values are 0.83±0.05, 0.58 and 18.5% respectively.

3.6.2 Two-phase flow

(1). The trends were similar for both water (C_v=0.02%) and mixture (up to C_v=2.5%) flows. A strong particle concentration gradient existed in the stirred vessel for all concentrations. For example, the local volumetric concentration at C_v=0.5% was about 5.0 C_v at bottom of the vessel and reduced to 0.5 C_v close to the free surface.

(2). In the impeller stream, the particles lagged behind the fluid and this lag was more pronounced near the plane of the impeller disc. The maximum lag in the water flow was 0.06 and 0.13 V_t for Diakon and glass particles respectively and in the mixture flow 0.075 V_t for Diakon at C_v=2.5%. The results also show that the lag reduced with radial position so that, in the mixture flow, $\overline{V}_s$ at the impeller tip (r=51 mm) was higher by about 35% than at r=68 mm.

(3). In the bulk of the flow, the axial particle velocities of the single-phase fluid velocity depended on the local flow direction and on the effects of particle settling and acceleration; in general, the particles led the fluid in downflow and lagged behind in upflow. The tangential velocity measurements showed that the width of the counter-rotating flow region was less than that in the single-phase by about 37% at C_V=1.75% and Z=20 mm.

(4). The particle turbulence levels were lower in the impeller stream than those of the single-phase levels by about 13 and 25 % for Diakon and glass particles in water flow (C_V=0.02%) respectively and 15% for Diakon particles in mixture flow (C_V=2.5%). In the bulk of the flow the levels of turbulence of both particles and fluid were similar around the axis, while the particle turbulence levels were smaller in the wall region by about 7% for Diakon particles in both the water and mixture flows and up to 15% for glass particles.

(5). The effects of particle size, material (density) and concentration are as follows:

(a). The radial apparent slip velocities in the impeller stream were similar and not dependent on particle size. In the bulk of the flow, the apparent slip velocity of the 376.5 μm diameter glass particles was greater by about 1.5 times than with the 232.5 μm particles, but the slip velocities of Diakon particles were similar for all sizes. The turbulence levels for all particle sizes were similar everywhere in the vessel.

(b). The results with glass and Diakon particles show that the apparent slip velocity was larger with the heavier particles so that they were 0.13 and 0.06 V_t respectively at C_v=0.02% and the corresponding values in the bulk of the flow were 0.026

and 0.01 V_t. The turbulence levels were reduced with the heavier particles by a factor of 2.

(c). The axial and radial particles mean velocities decreased with increasing particle concentration by up to 4% and 10% in the impeller stream and in the bulk of the flow respectively, for a change in C_v from 0.25 to 2.5 %. The apparent slip velocity increased in the upflow situation and decreased in the downflow situation with C_v. The turbulence results show that the turbulence levels were unaffected for C_v up to 2.5%.

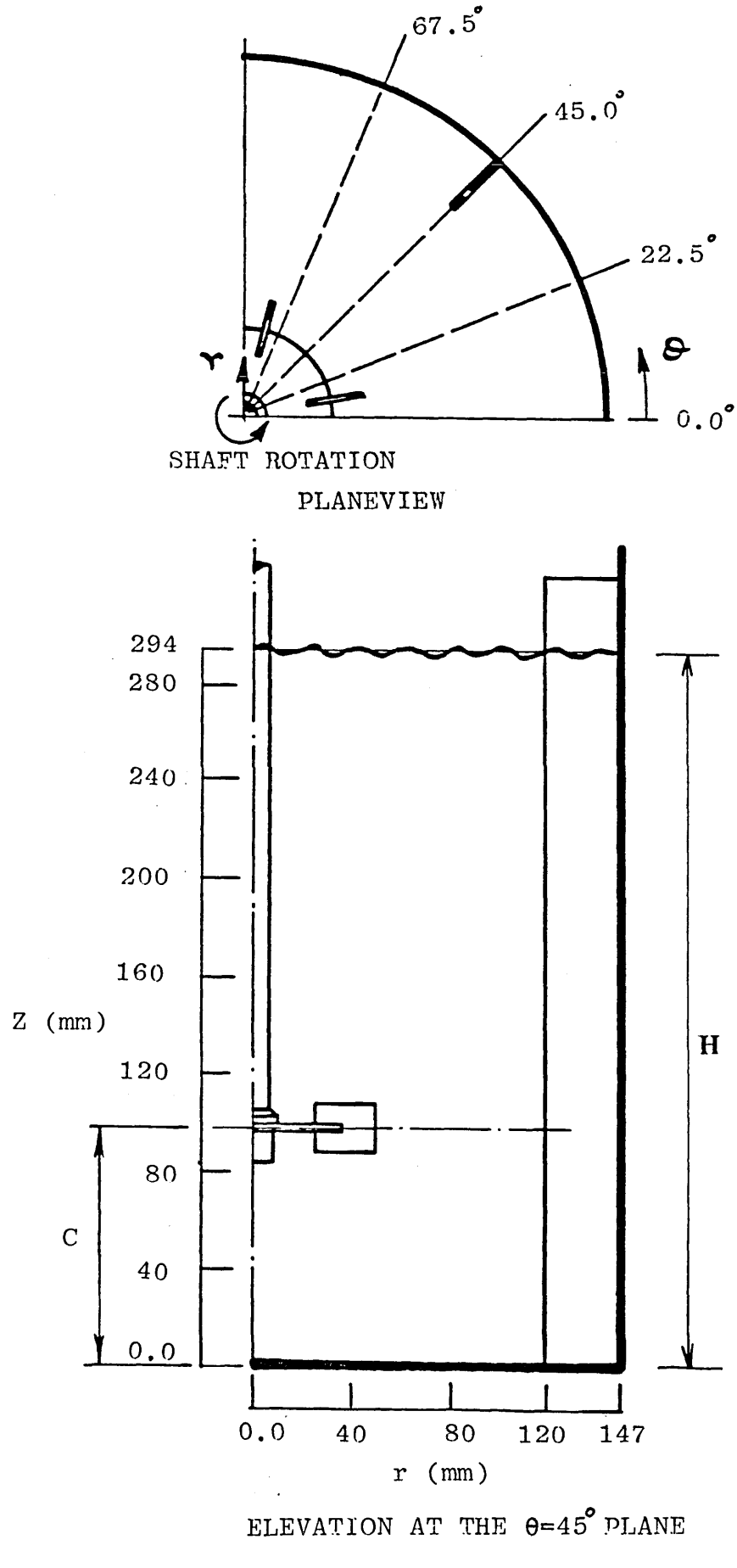

Fig 3.1 Flow configuration, dimensions and co-ordinate system.

IMPELLER	D	d	L	h
T/4	73.5	55.12	18.37	14.7
T/3	98.0	73.5	24.5	19.6
T/2	147	110.3	36.75	29.4

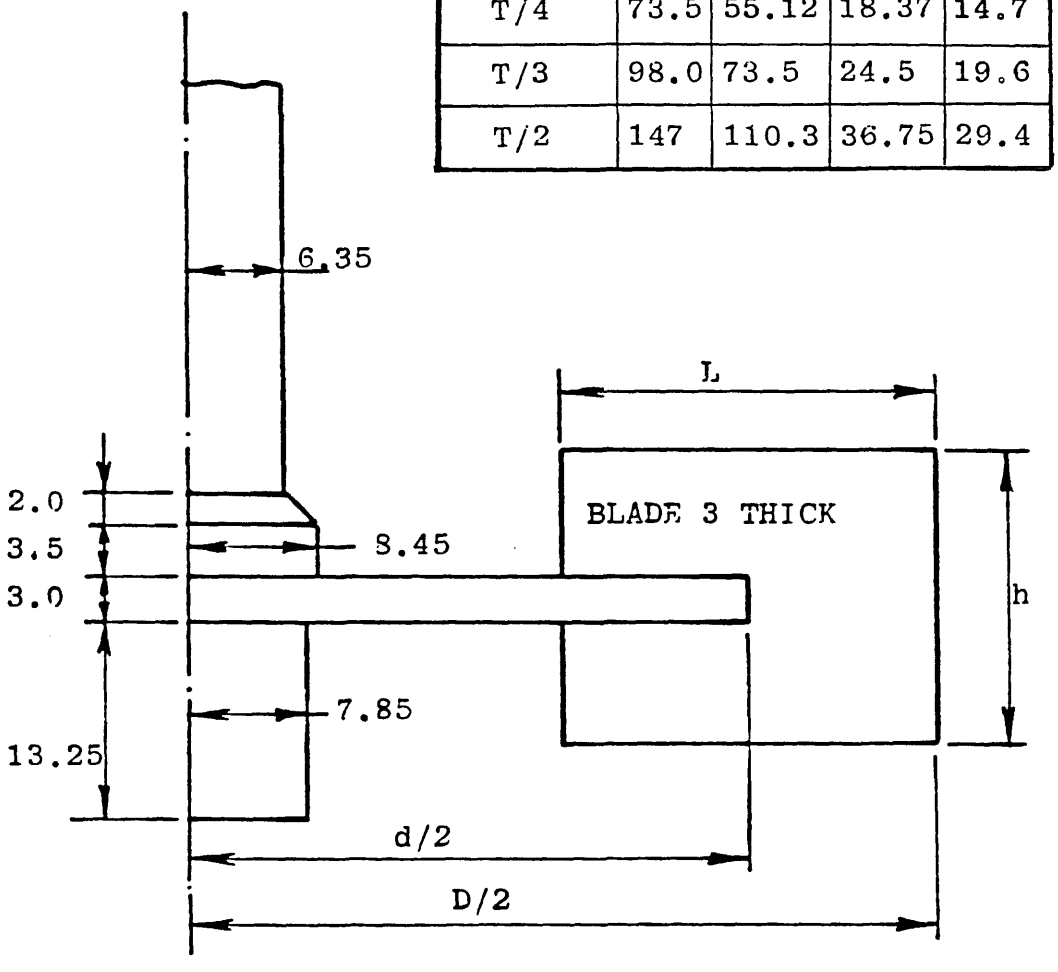

Fig 3.2 Impeller geometry.

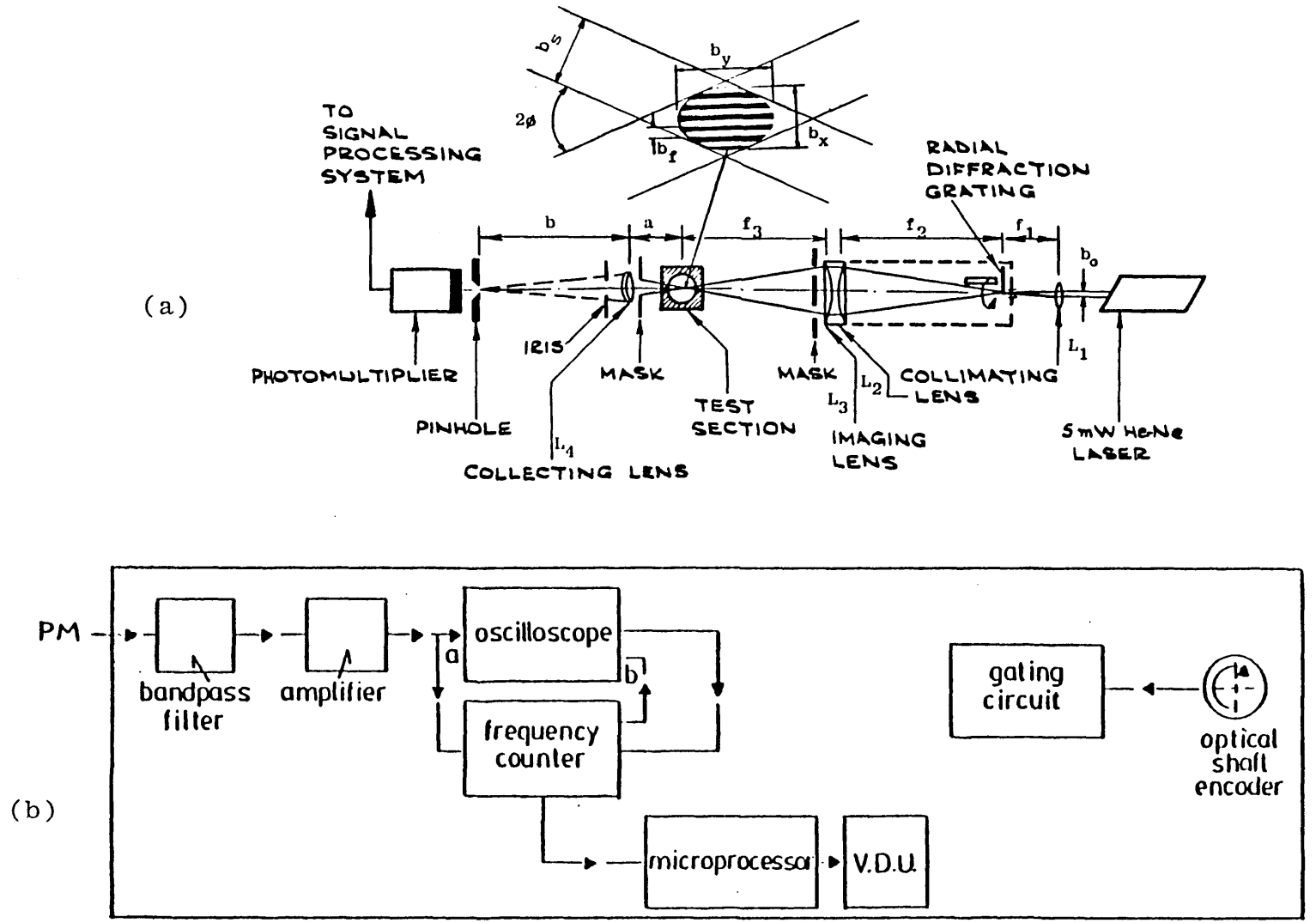

Fig 3.3 Laser-Doppler velocimetry: (a) optical system; (b) signal processing system.

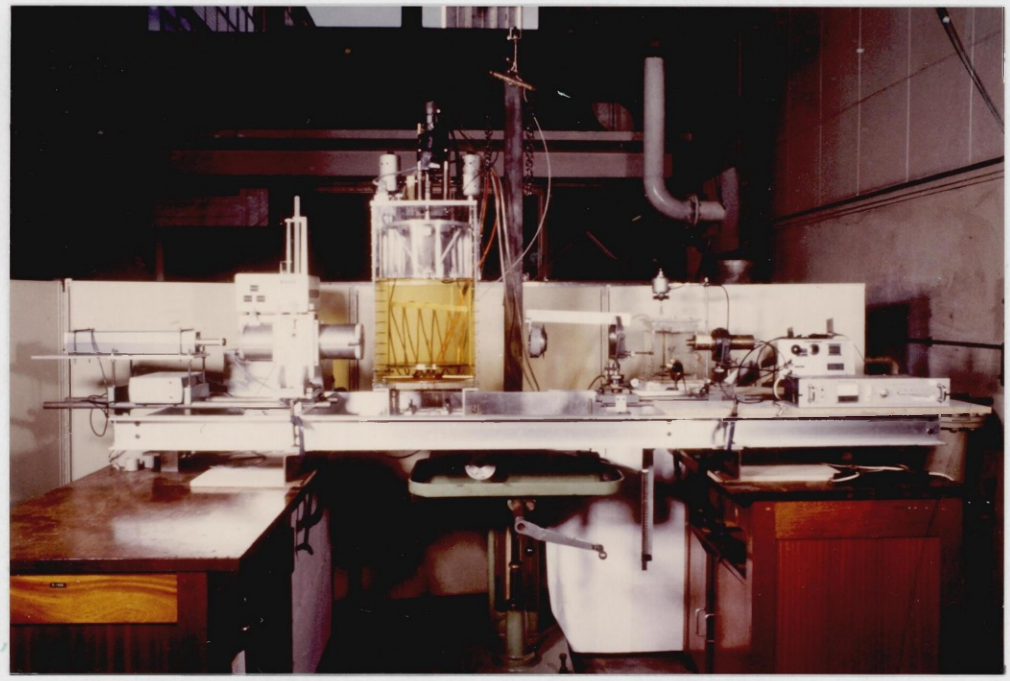

(a)

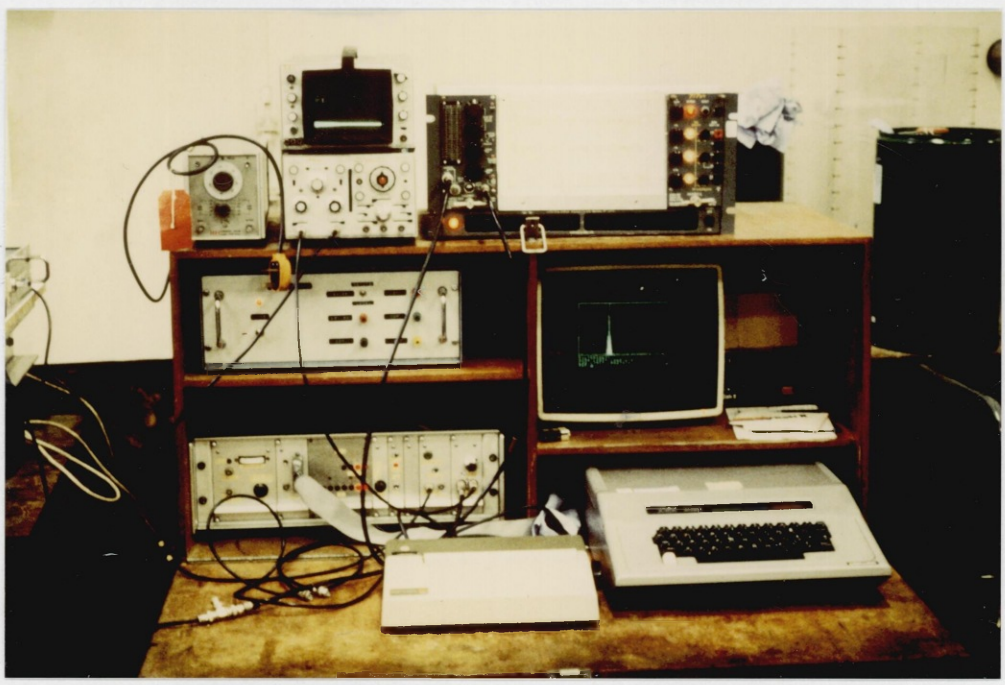

(b)

Fig 3.4 Photograph of laser-Doppler velocimeter: (a) optical system and stirred vessel and (b) signal processing system.

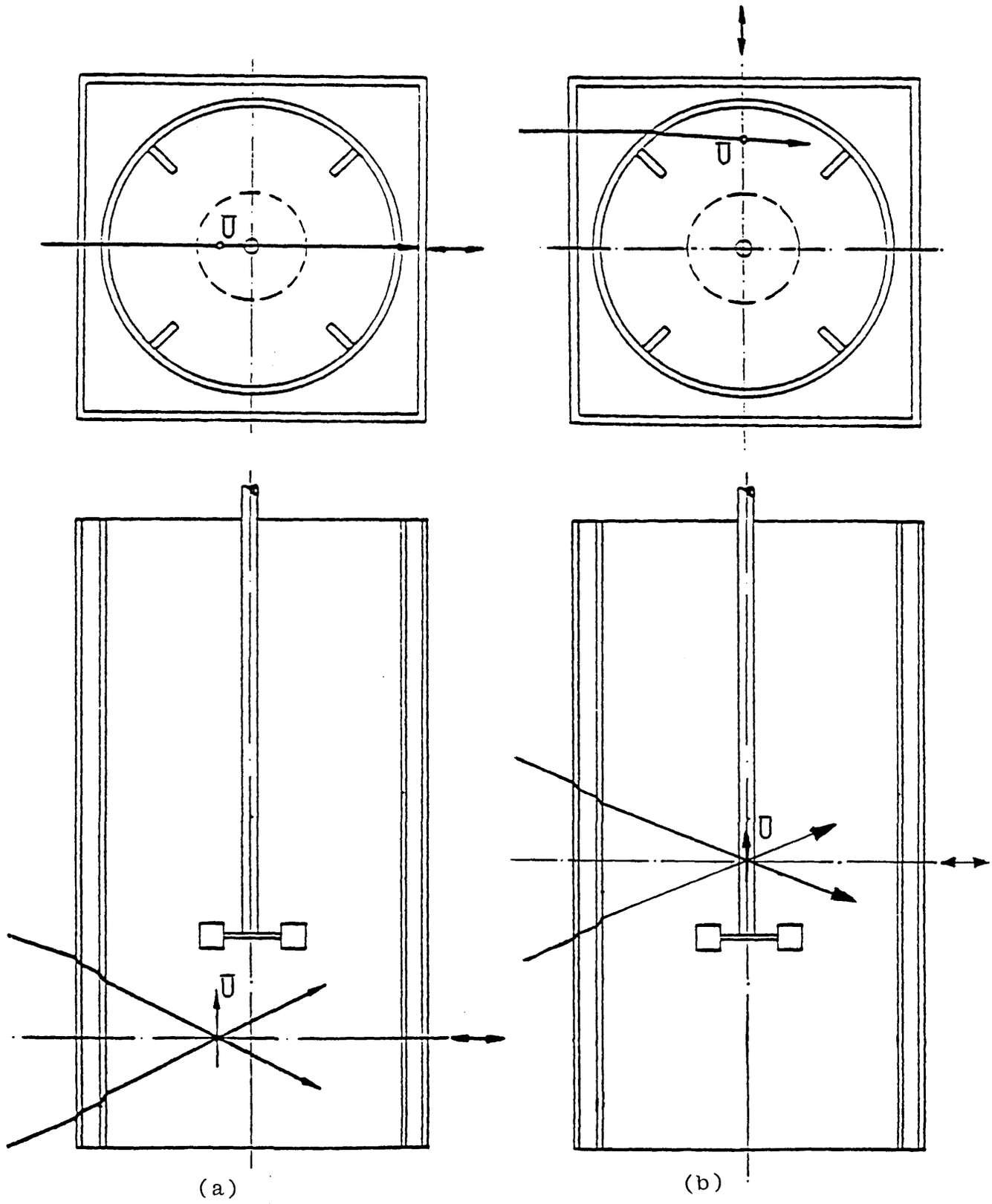

Fig 3.5 Beam orientation for axial component measurements: (a) below the impeller and (b) above the impeller.

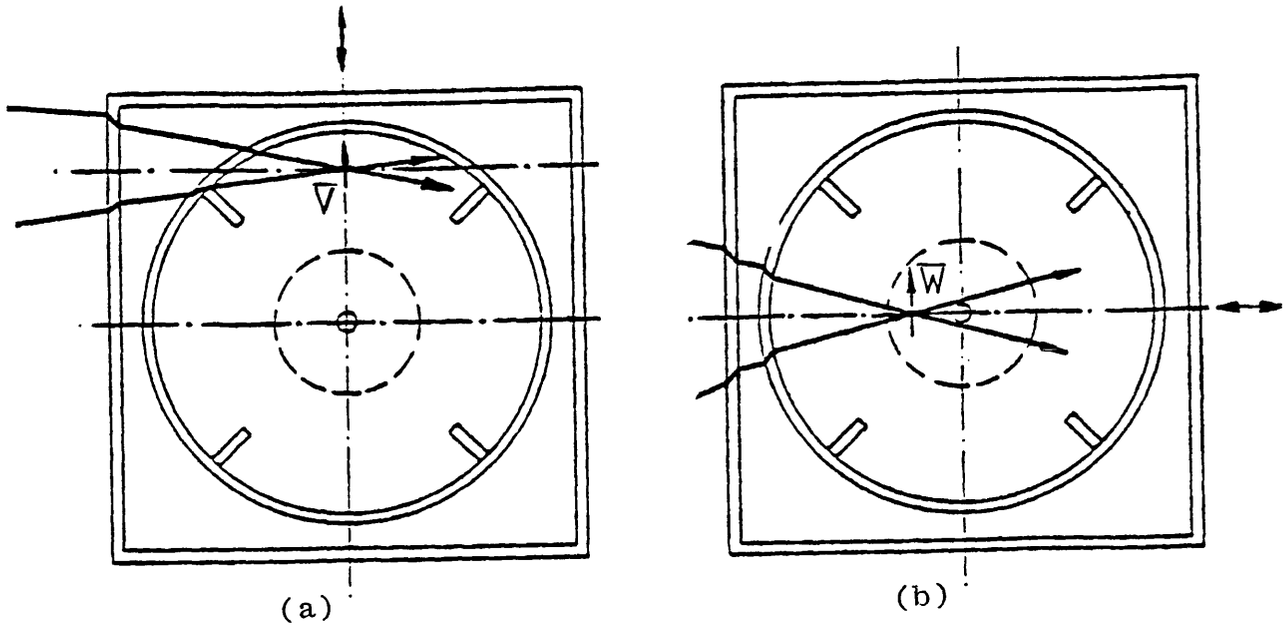

Fig 3.6 Beam orientation for the measurements of: (a) radial component everywhere in the vessel and (b) tangential component below the impeller.

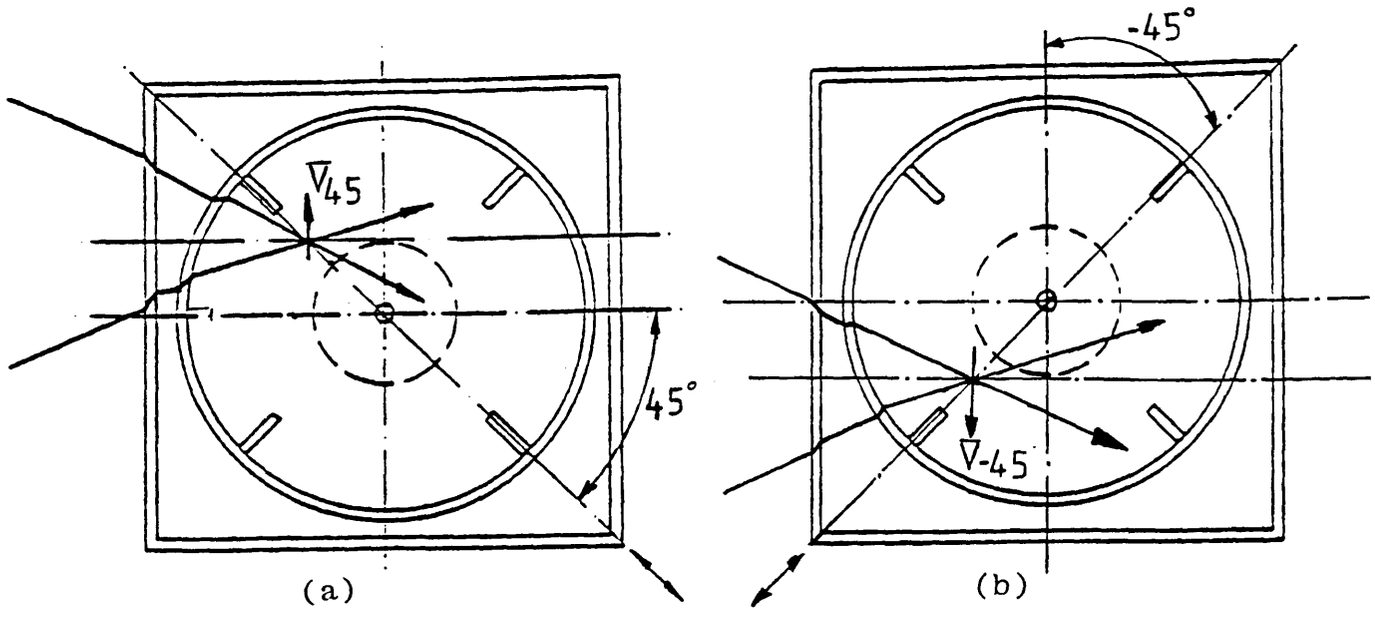

Fig 3.7 Beam orientation for tangential component measurements around and above the impeller.

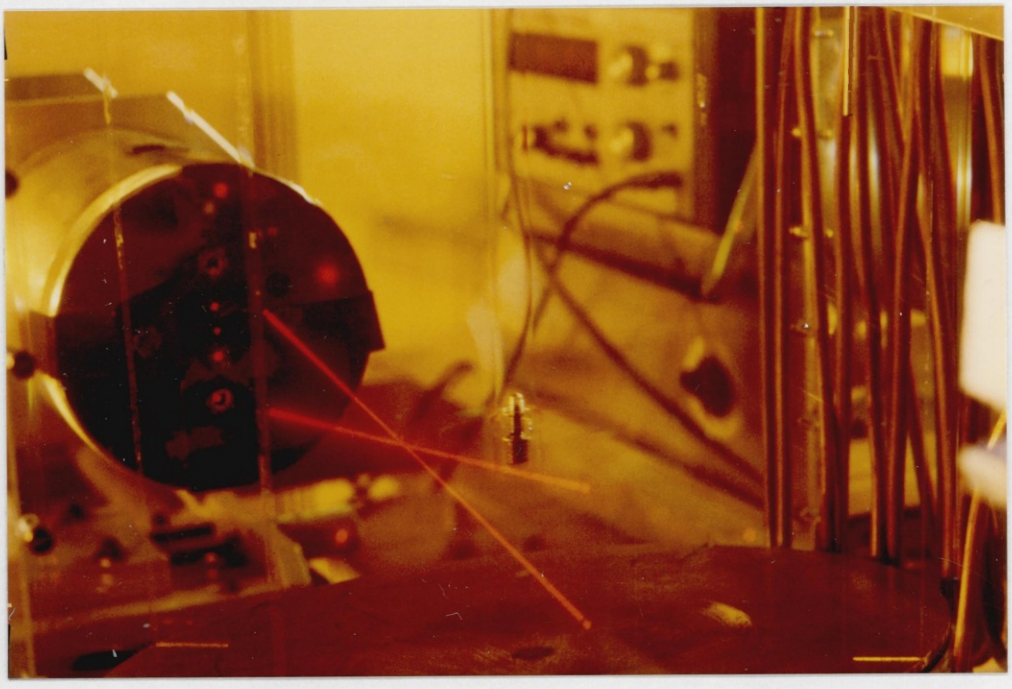

Fig 3.8 Photograph of laser beam through the tip of the impeller blades when the refractive index of the mixture was matched to that of the arcylic (Perspex) material.

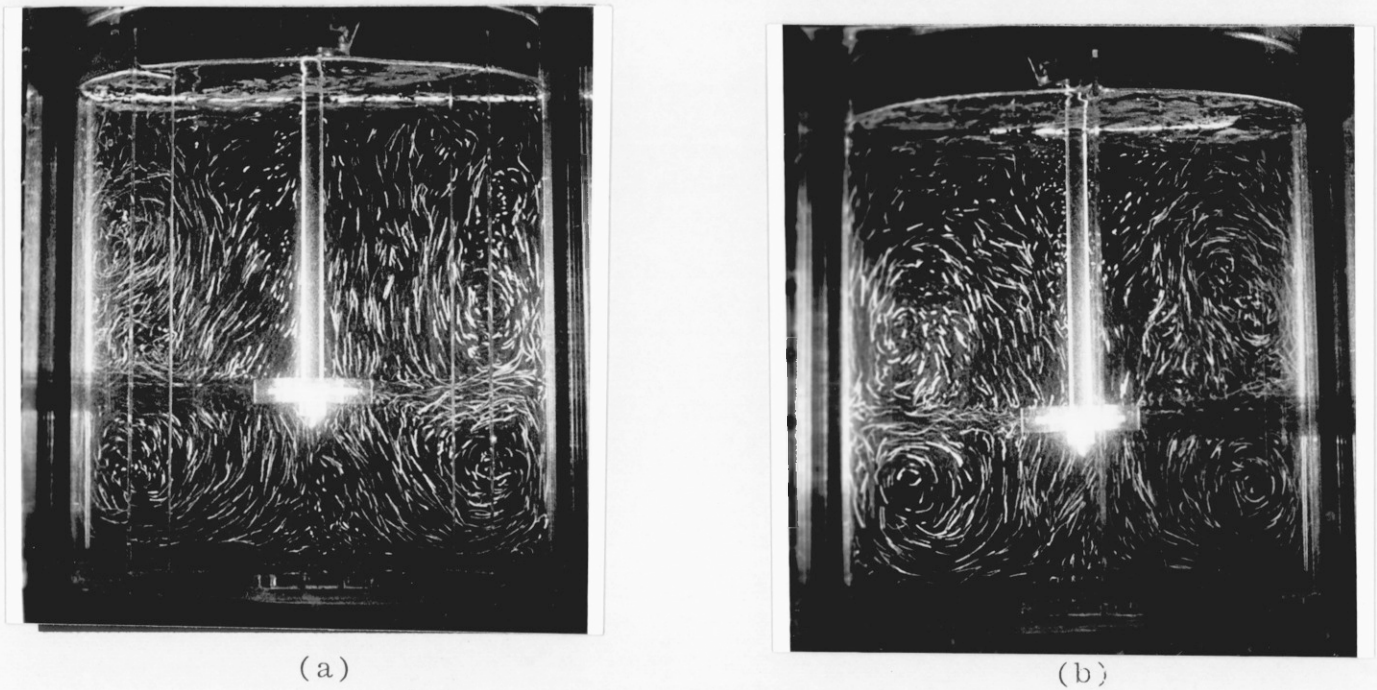

Fig 3.9 Photograph of the flow visualisation in r-Z plane for D=T/4, C=T/3 and N=300 rpm at: (a) θ=0.0 ° and (b) θ=42.5 °.

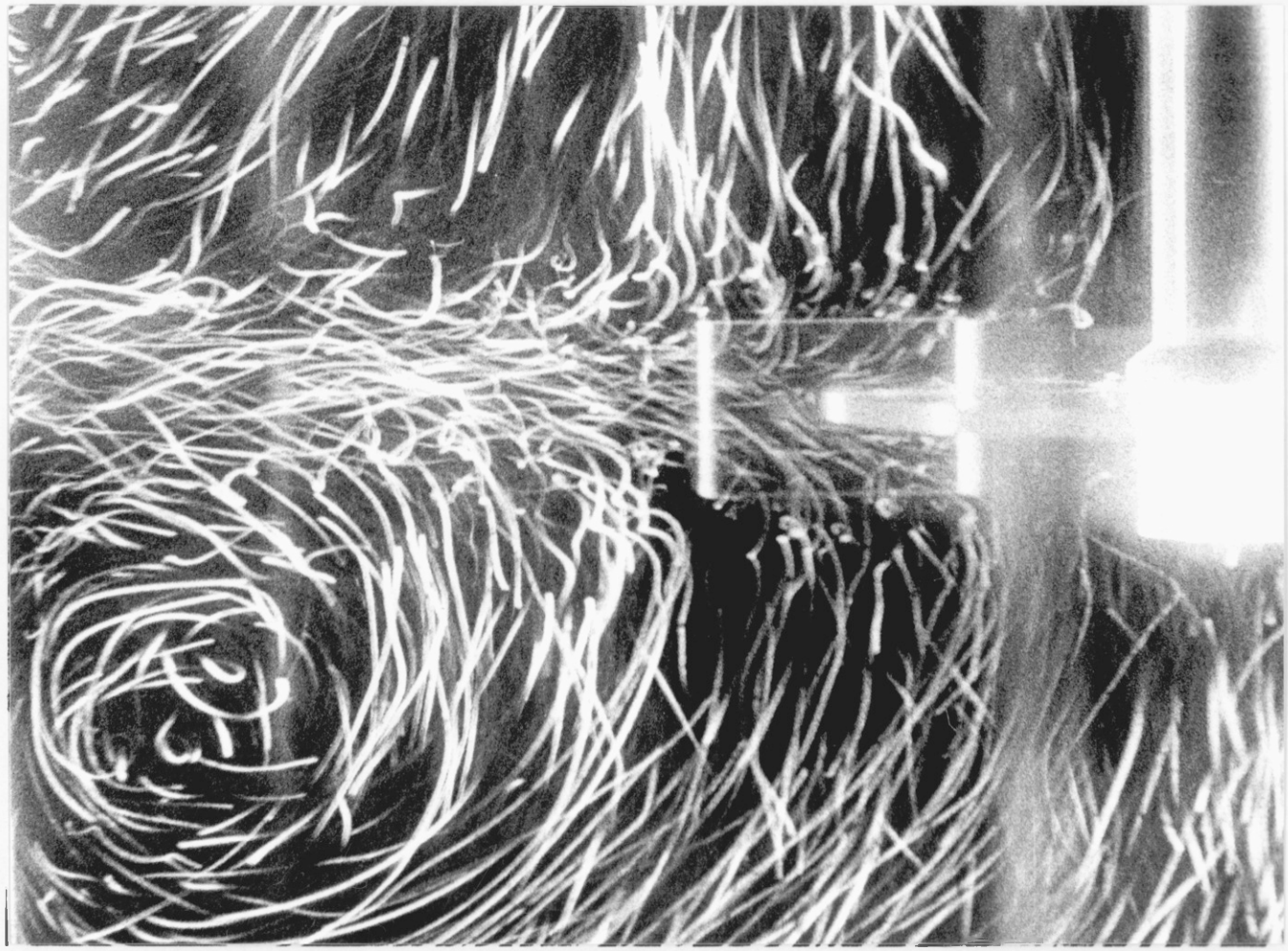

Fig 3.10 Close up photograph of the flow visualisation in the impeller stream and below the impeller in r-Z plane for D=C=T/3, N=100 rpm and θ=22.5 °.

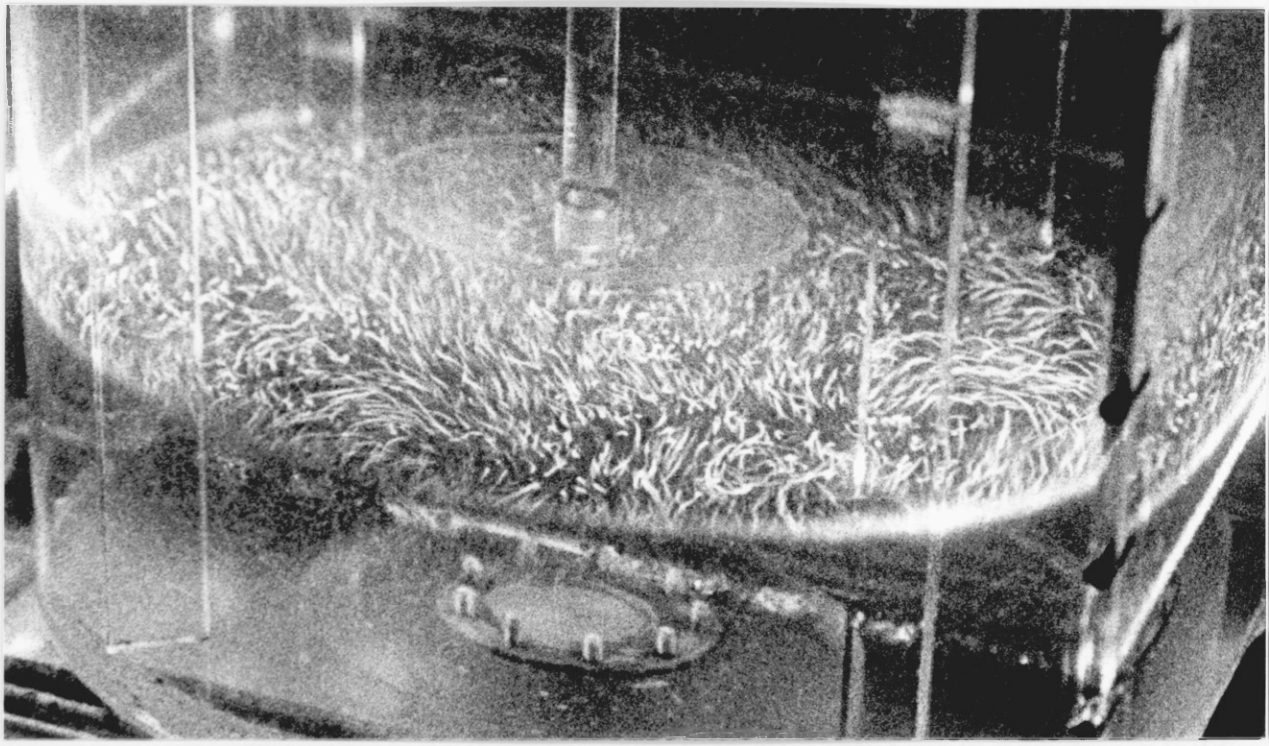

(a)

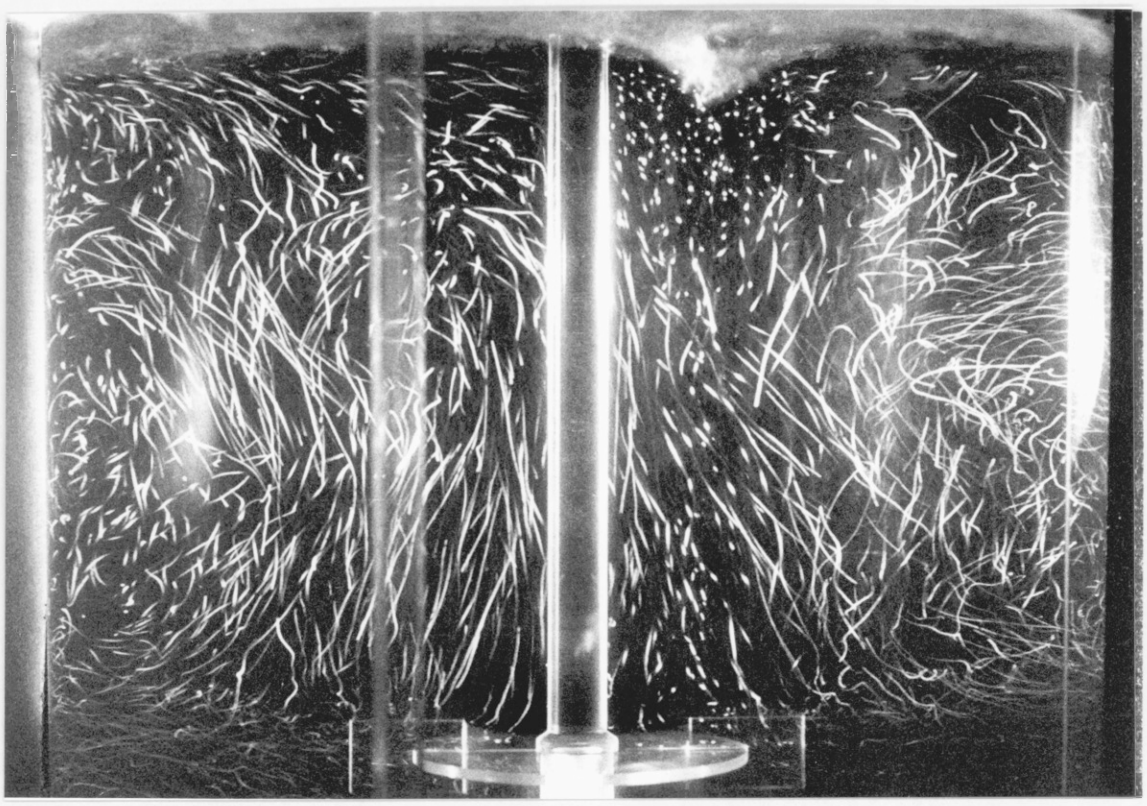

(b)

Fig 3.11 Photographs of the flow visualisation for D=C=T/3: (a) in r-θ plane at N=300 rpm and (b) in r-Z plane above the impeller at N=350 rpm and θ=22.5 °.

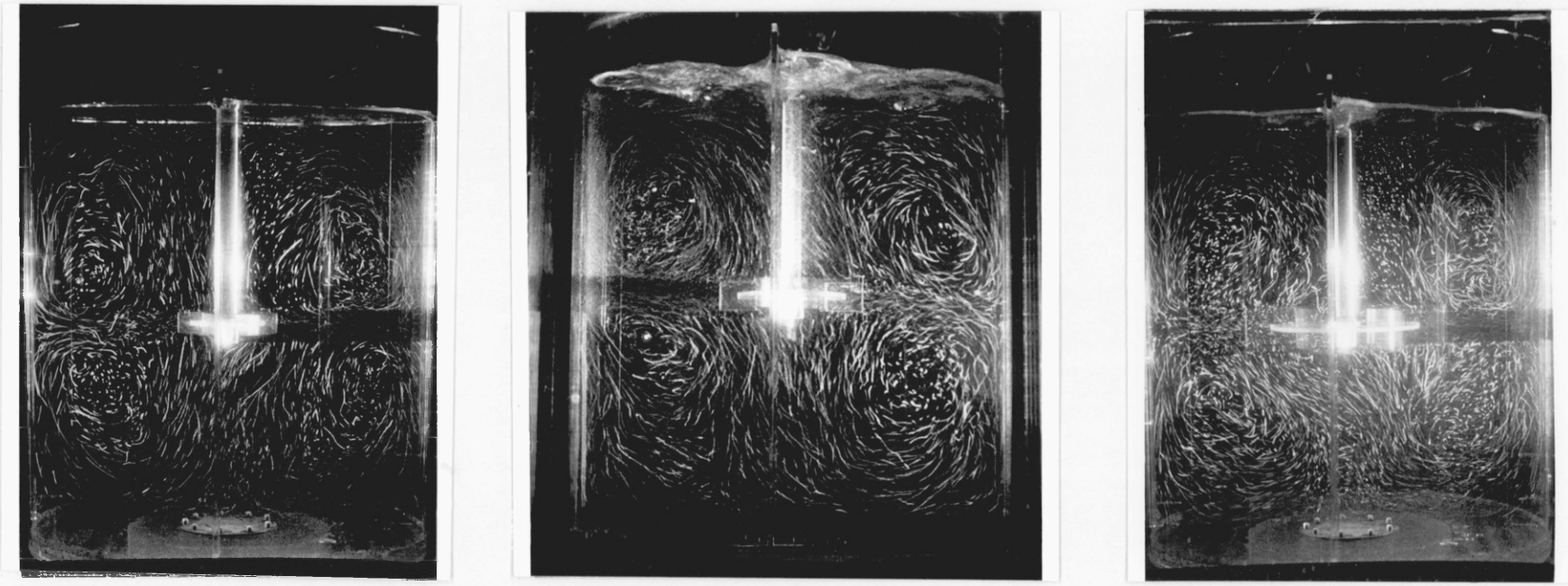

(a) (b) (c)

Fig 3.12 Photographs of flow visualisation in r-Z plane for C=T/3 and θ=42.5 ° for: (a) D=T/4 and N=300 rpm; (b) D=T/3 and N=300 rpm and (c) D=T/2 and N=100 rpm.

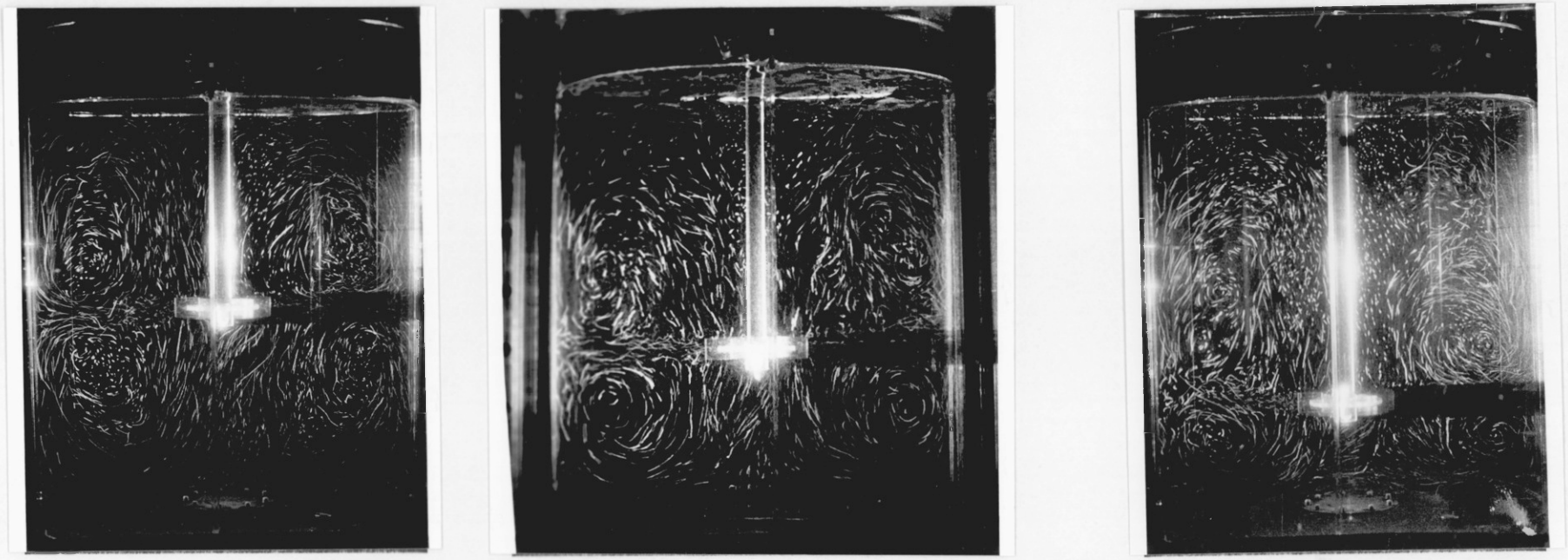

(a) (b) (c)

Fig 3.13 Photographs of flow visualisation in r-Z plane for D=T/4 and N=300 rpm for: (a) C=T/2; (b) C=T/3 and (c) C=T/4.

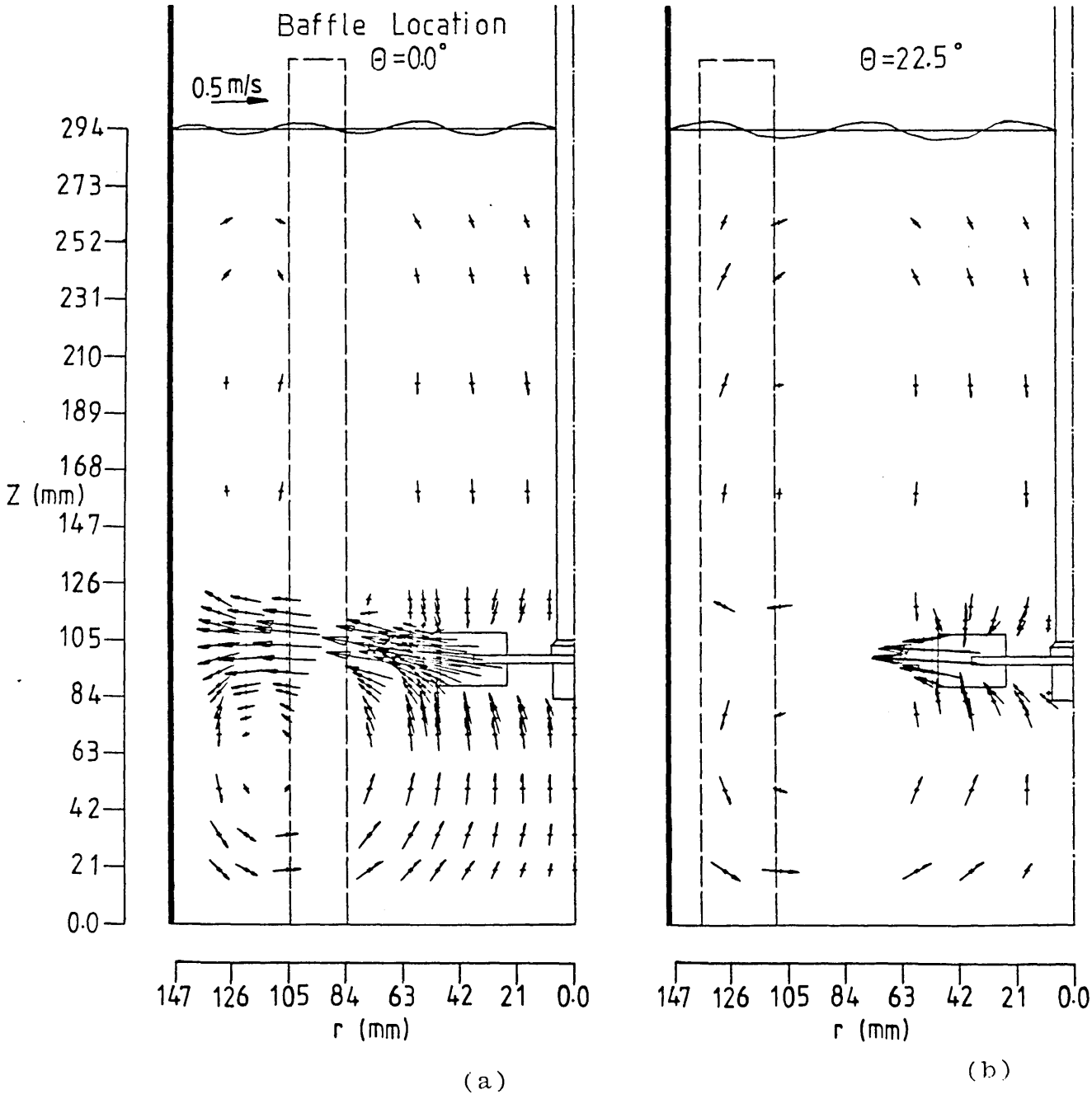

Fig 3.14 Mean velocity vector ($\sqrt{(\bar{U}^2+\bar{V}^2)}$) in r-Z planes for D=C=T/3 and N=300 rpm at: (a) θ=0.0 °; (b) θ=22.5 °; (c) θ=45 ° and (d) θ=67.5 °.

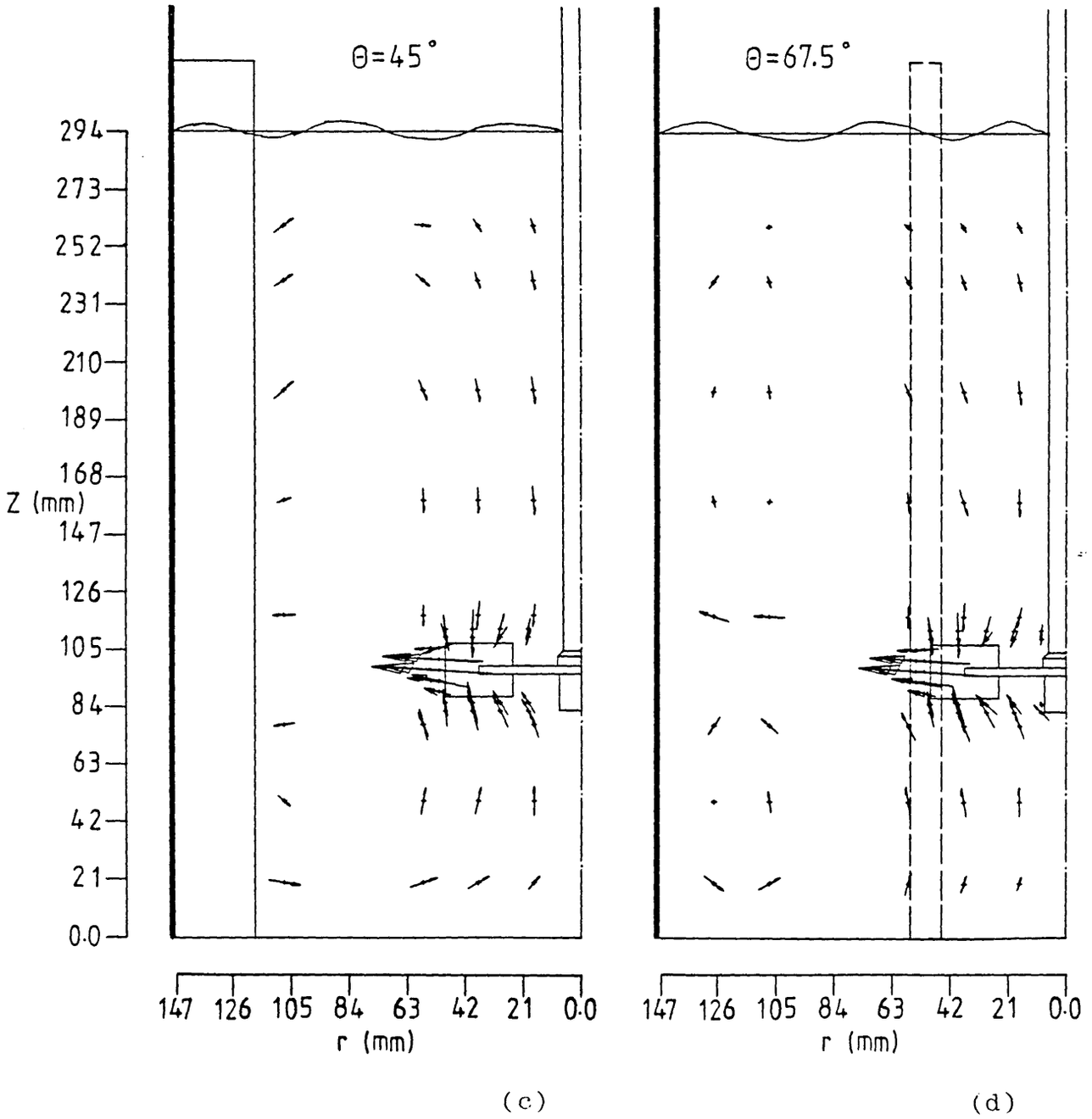

Fig 3.14 Continued.

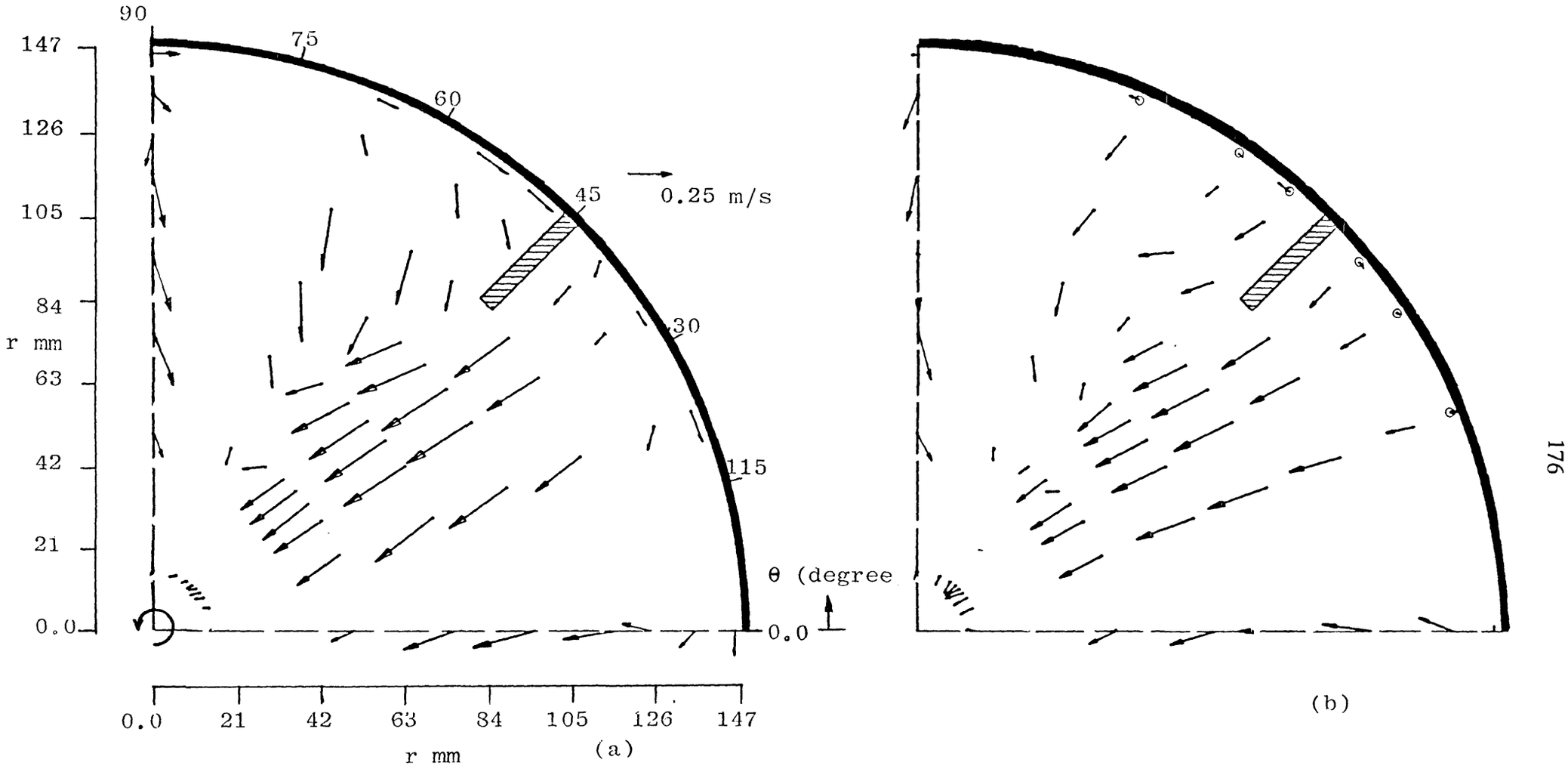

Fig 3.15 Mean velocity vector ($\sqrt{(\bar{V}^2+\bar{W}^2)}$) in r-θ planes for D=C=T/3 and N=300 rpm at: (a) Z=5 mm; (b) Z=20 mm; (c) Z=50 mm; (d) Z=70 mm and (e) Z=82.5 mm.

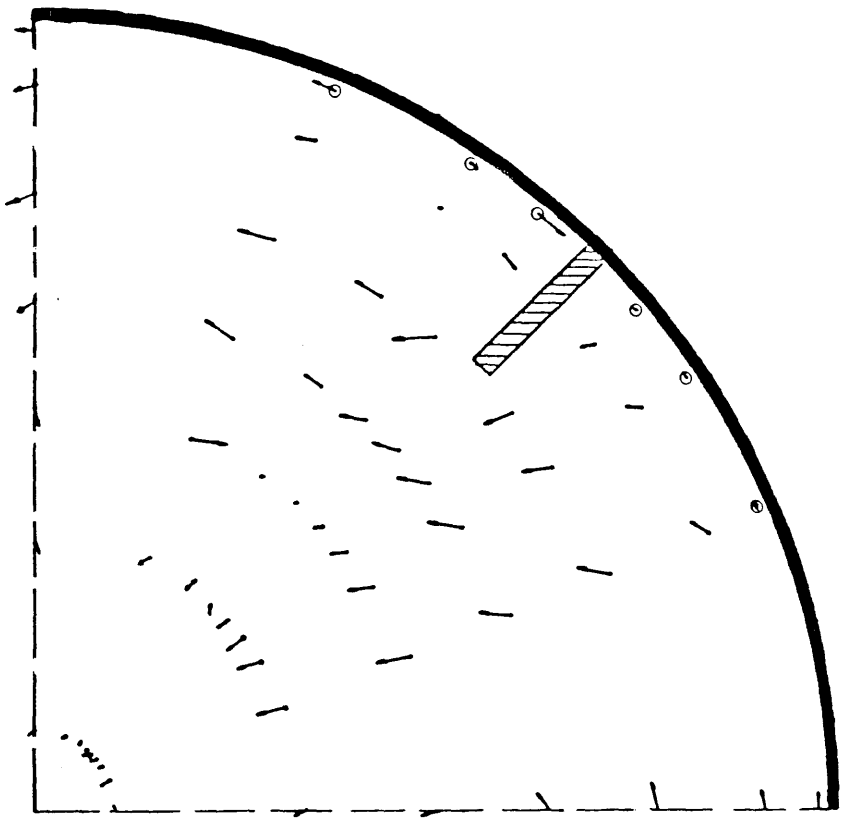

(c)

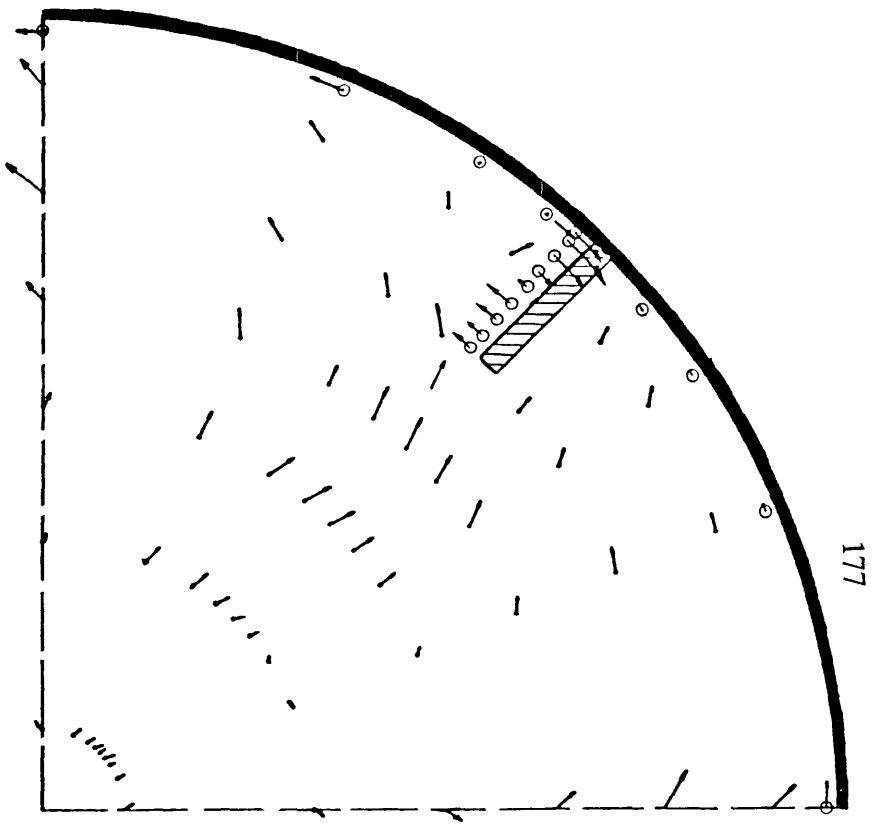

(d)

Fig 3.15 Continued.

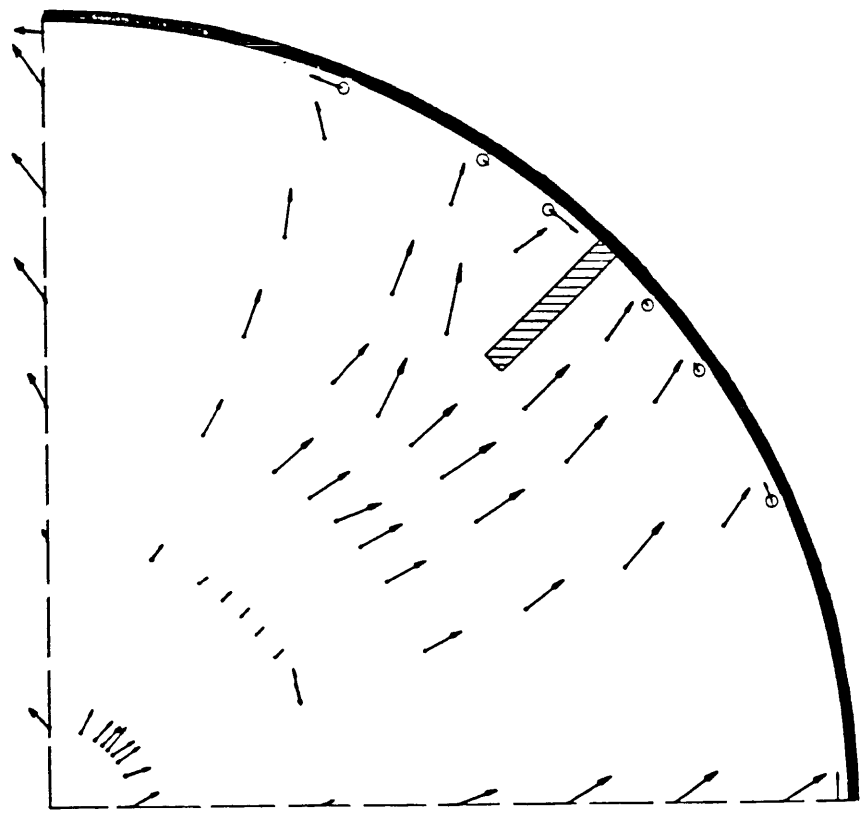

(e)

Fig 3.15 Continued.

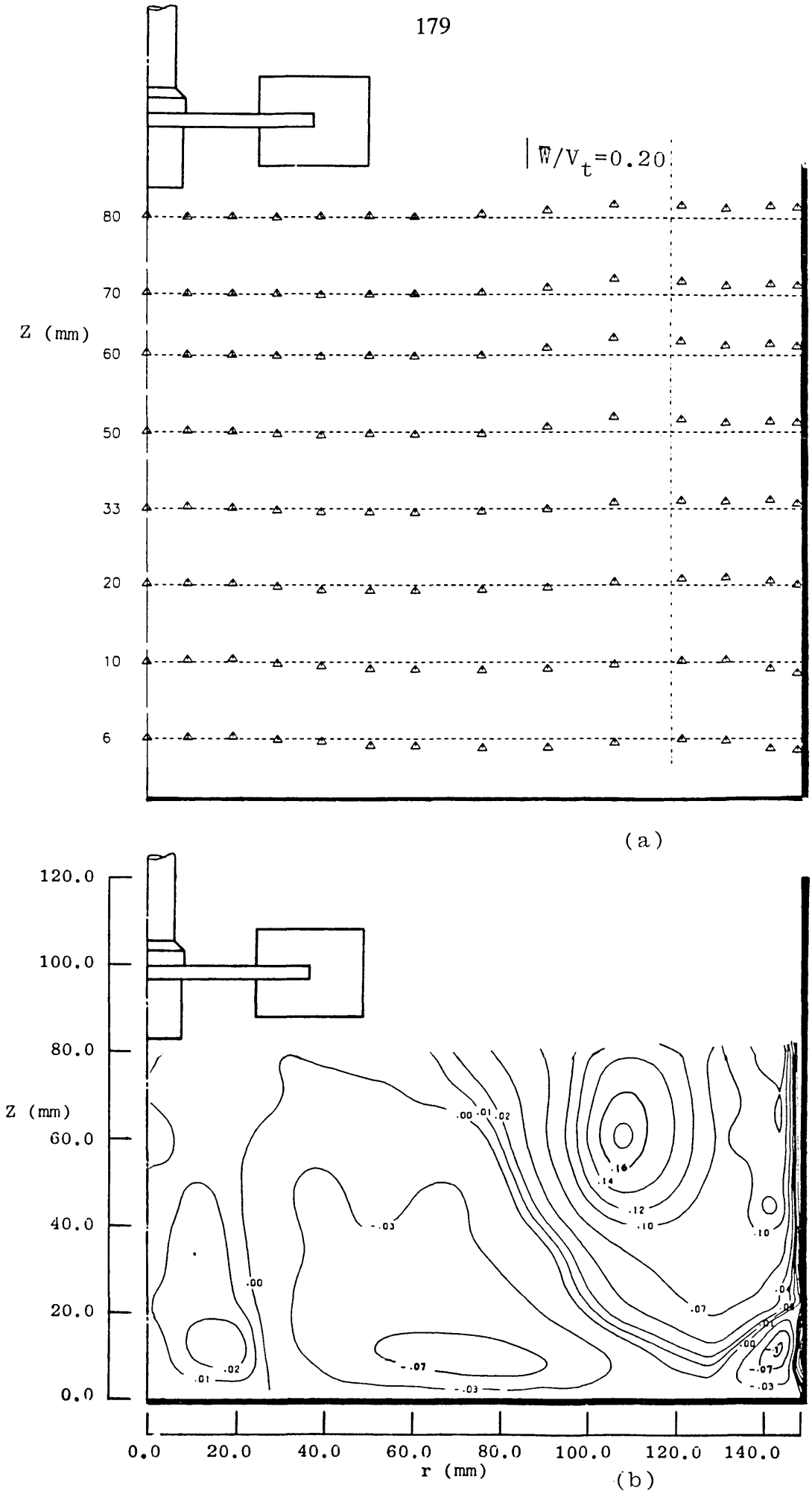

Fig 3.16 Tangential mean velocity below the impeller for D=C=T/3, N=300 rpm and θ=0.0 °: (a) radial profiles and (b) contours (values in m/s).

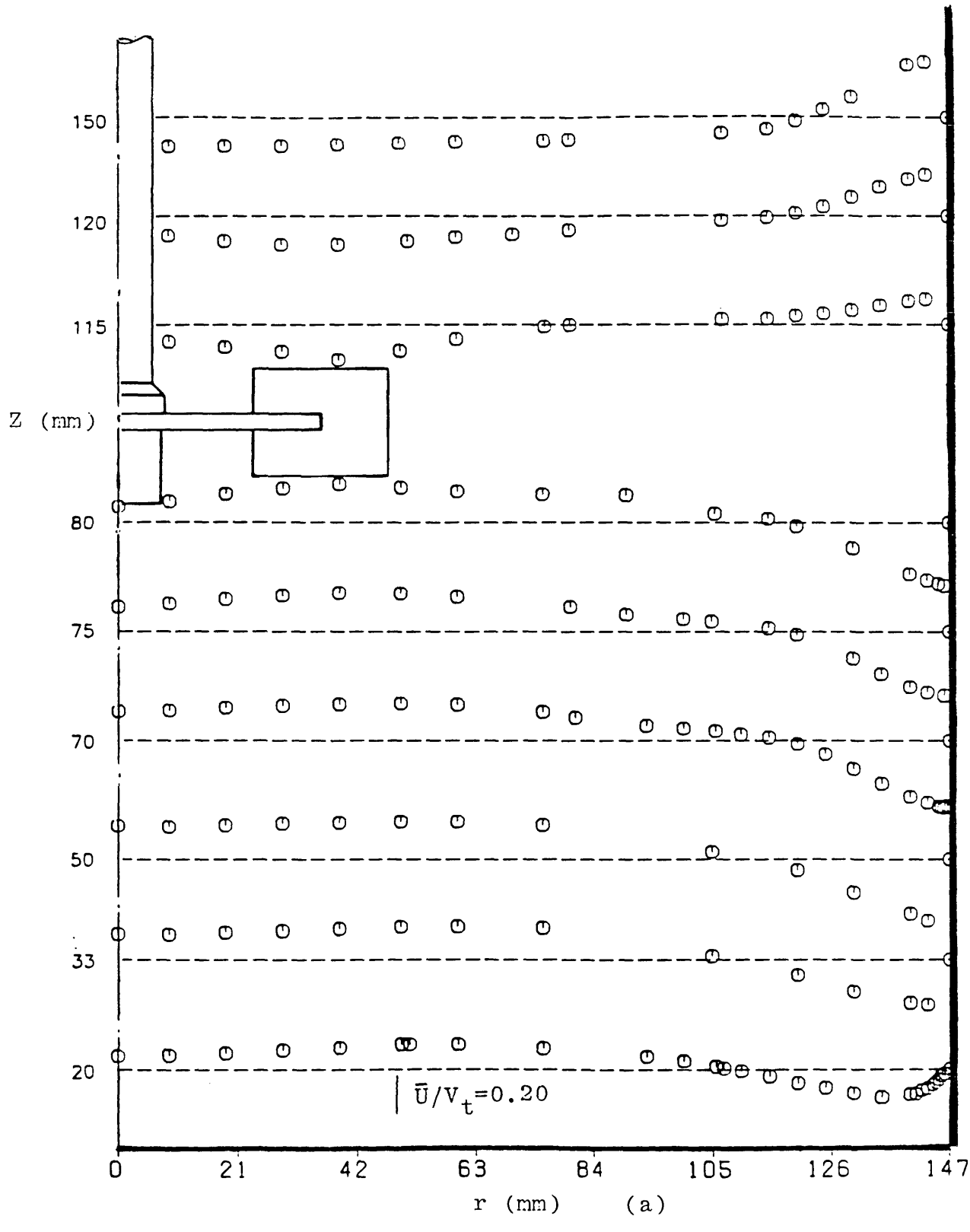

Fig 3.17 Axial mean velocity above and below the impeller for D=C=T/3 and N=300 rpm at: (a) θ=0.0 °; (b) θ=33.75 ° and (c) θ=56.25 °.

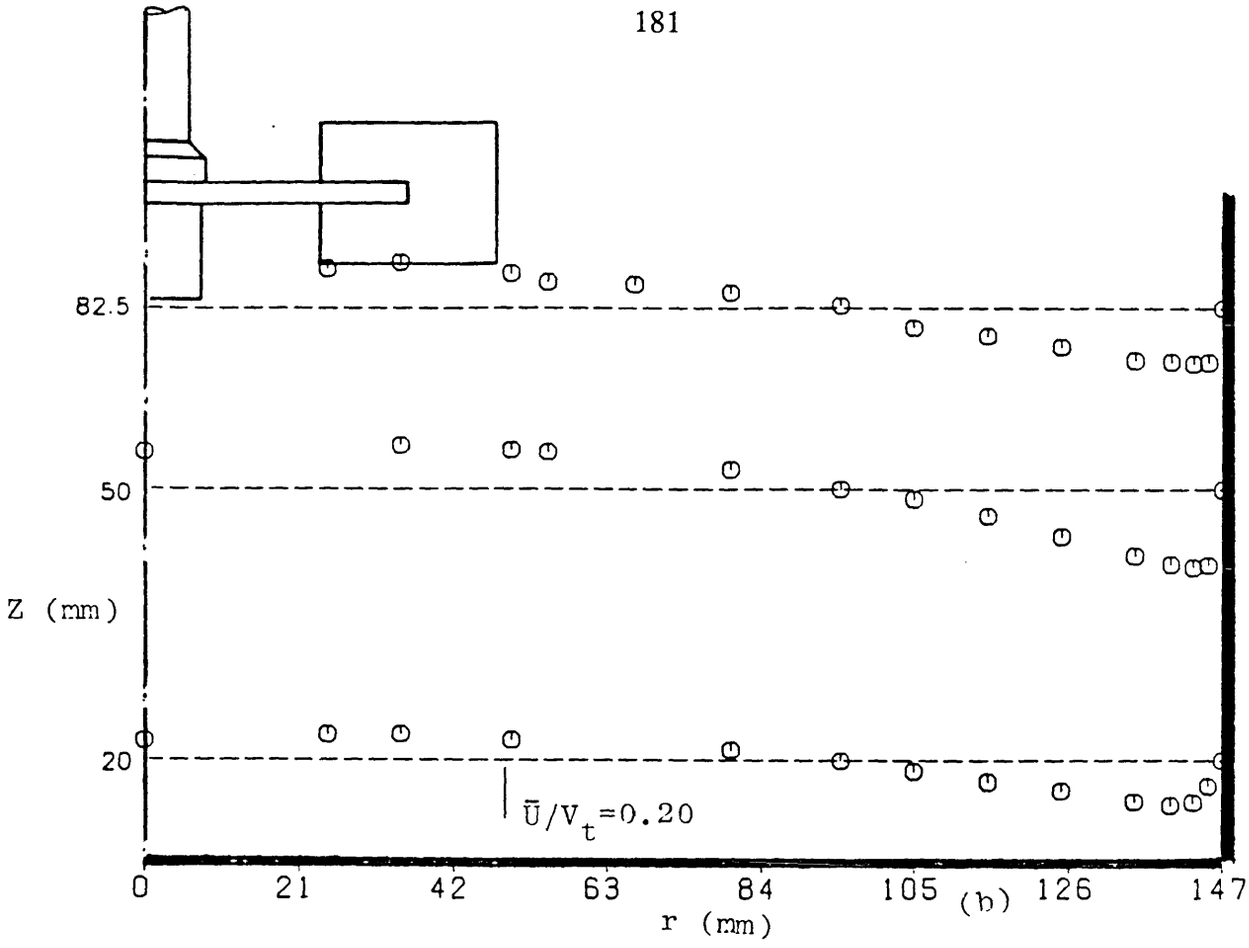

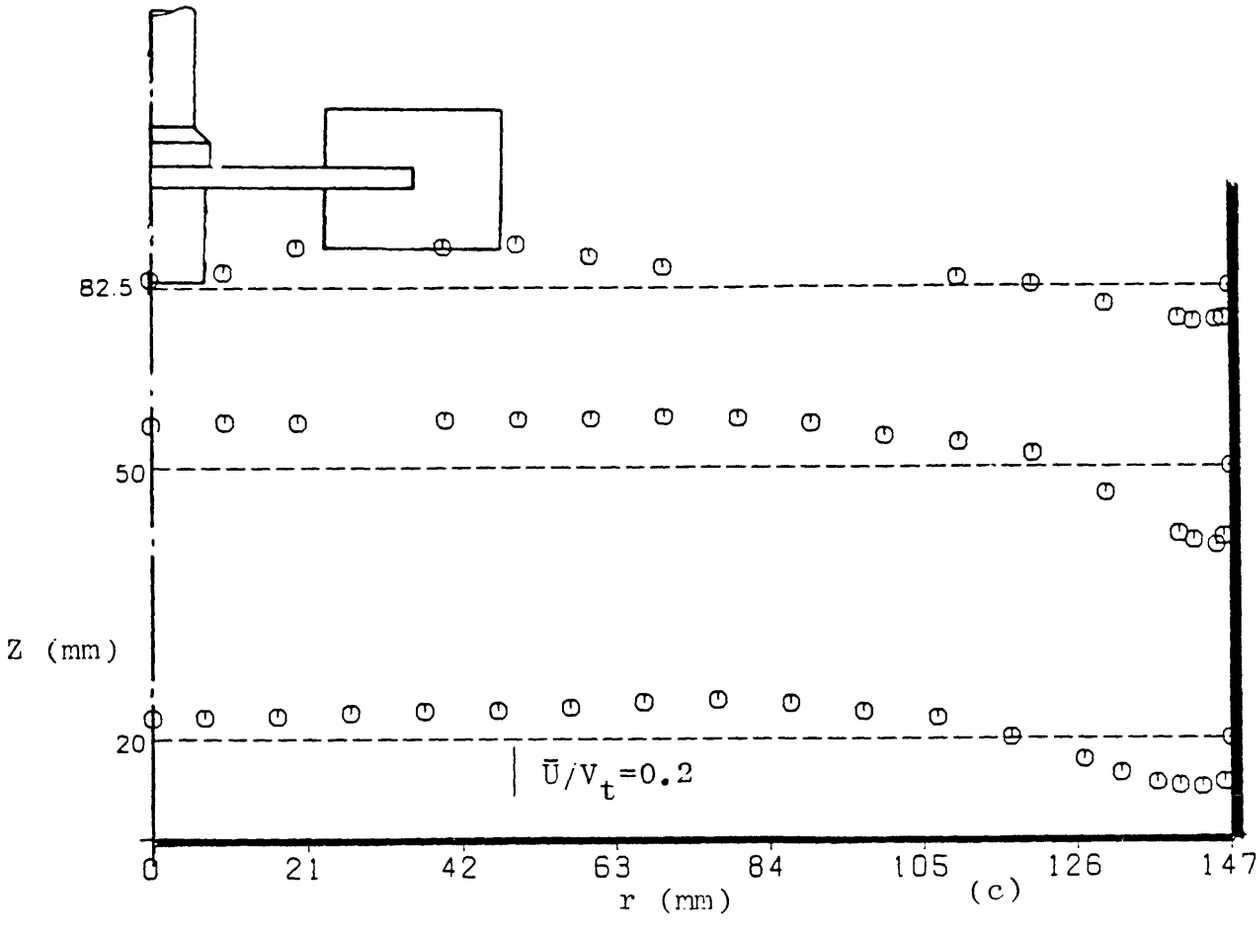

Fig 3.17 Continued.

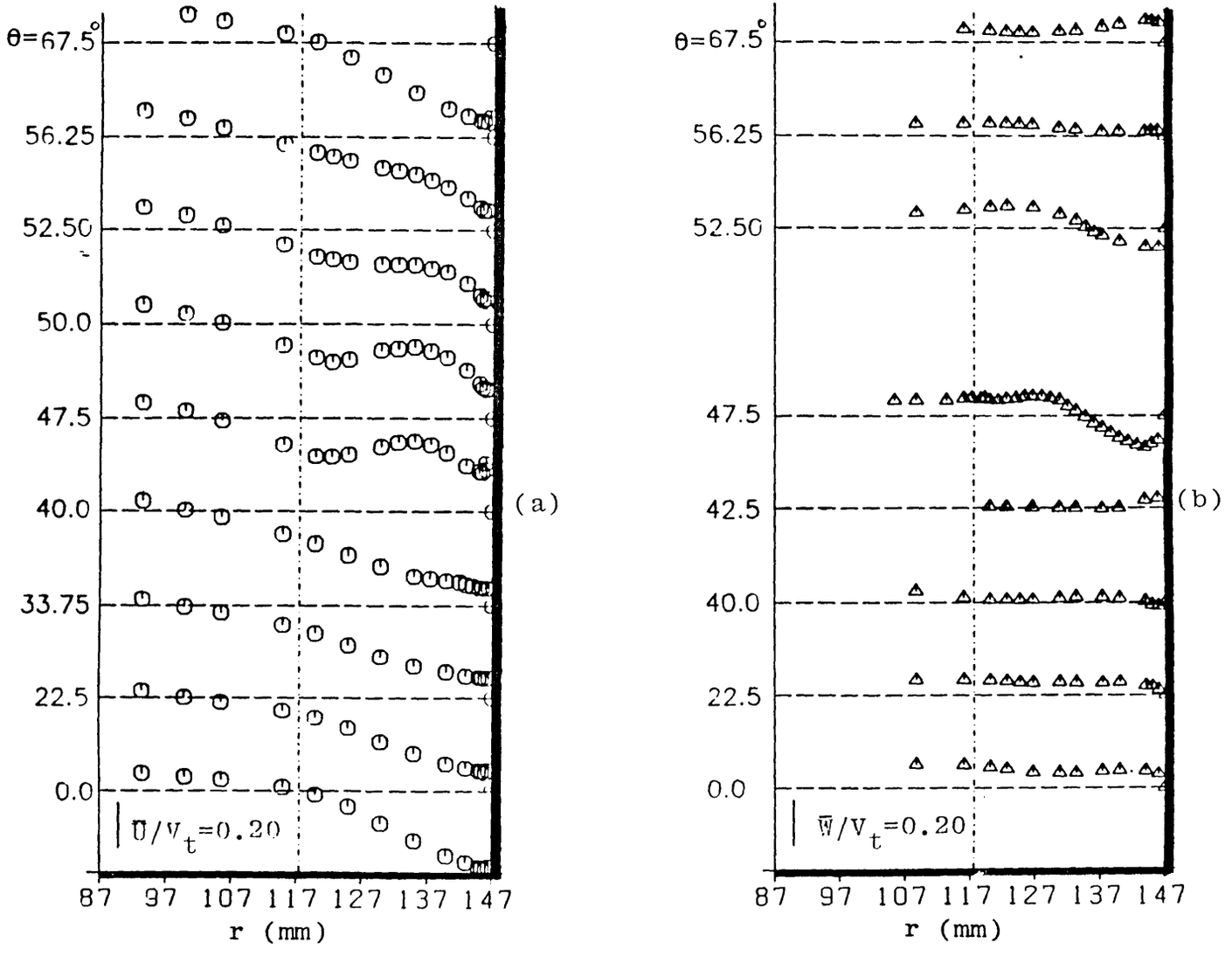

Fig 3.18 Radial mean velocity profiles around the baffle for D=C=T/3 and N=300 rpm at: (a) axial component and (b) tangential component.

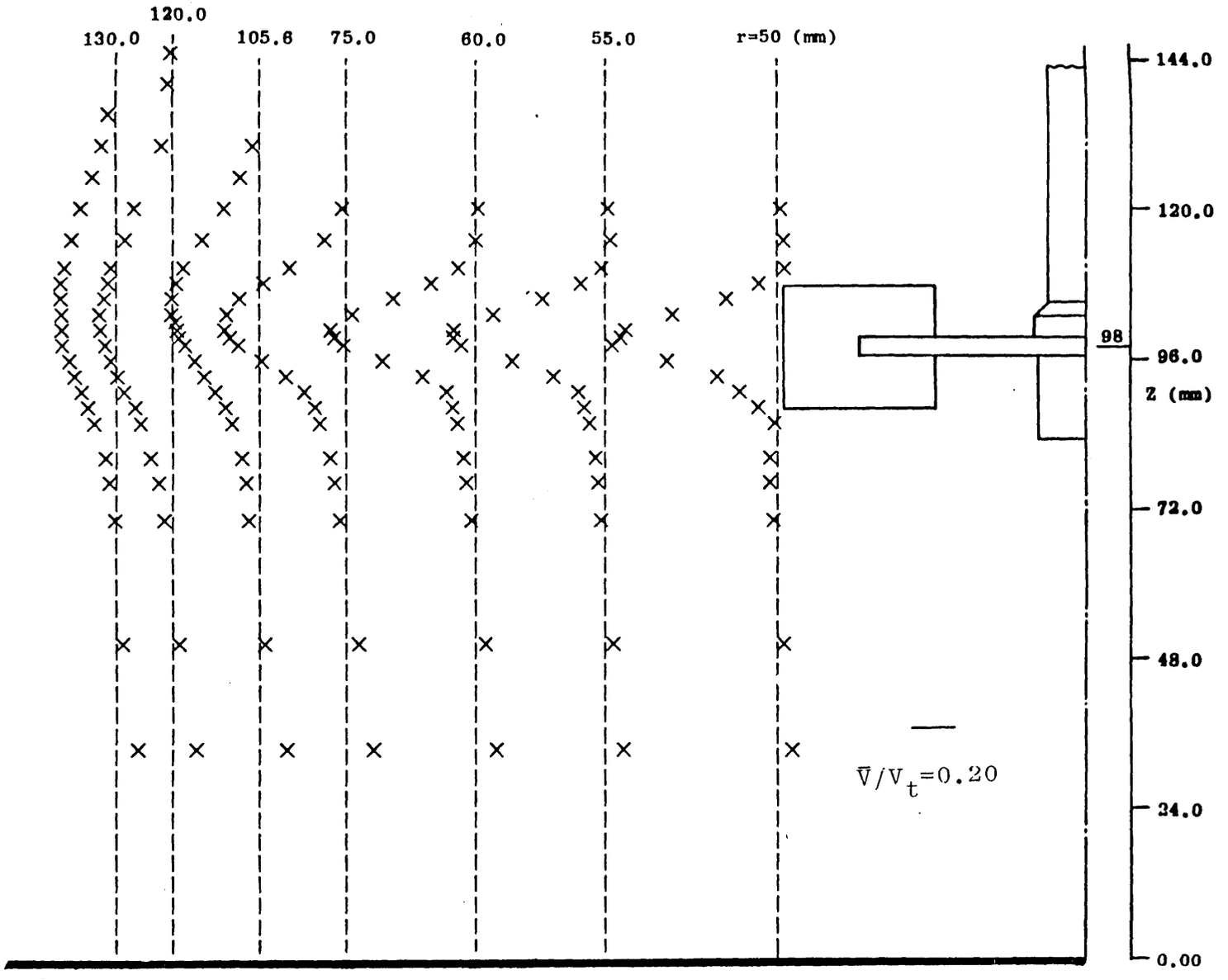

Fig 3.19 Radial mean velocity in the impeller stream for D=C=T/3, N=300 rpm and θ=0.0 °.

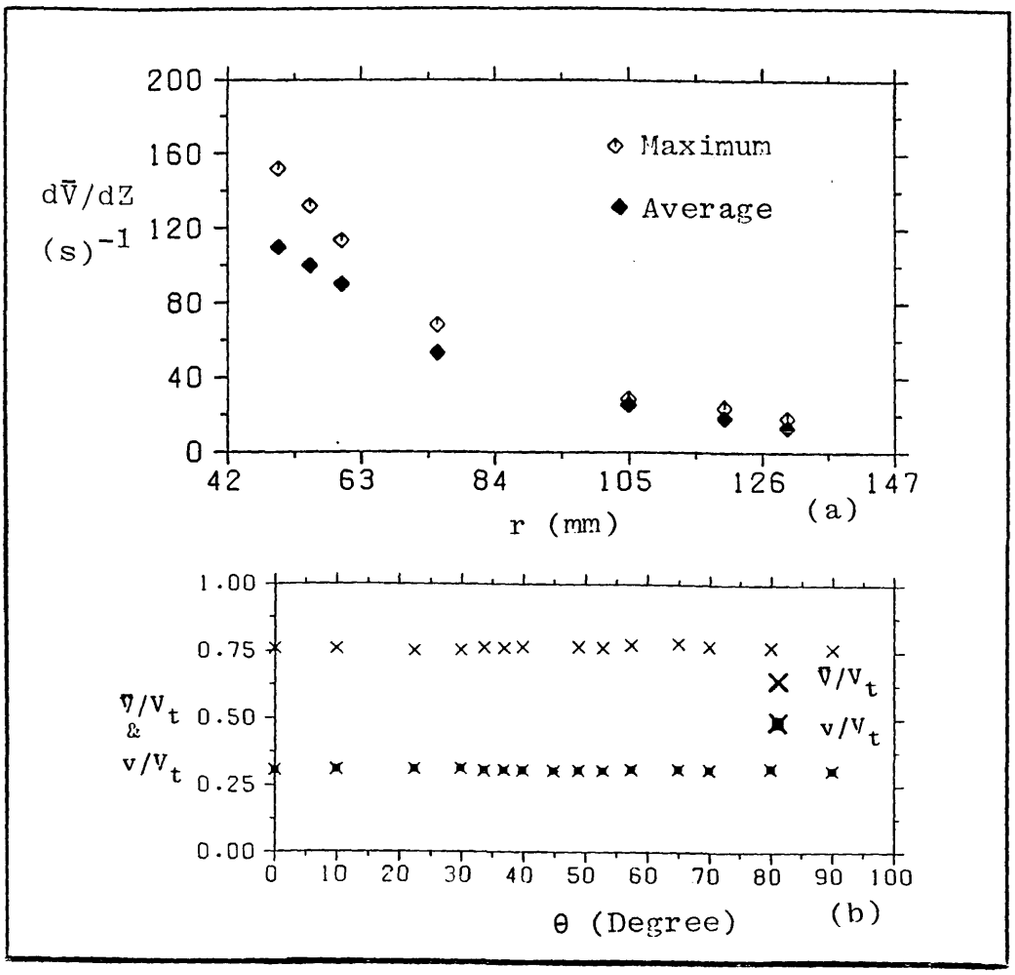

Fig 3.20 (a) Radial variation of axial shear rate and (b) the circumferential symmetry of radial mean and rms velocities. D= C = T/3, N=300 rpm and θ=0.0 °.

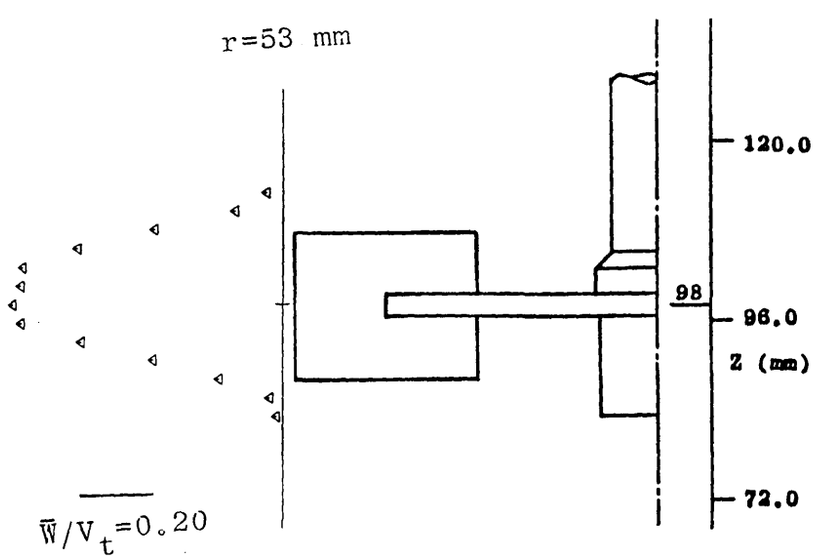

Fig 3.21 Tangential mean velocity at the impeller tip for D=C=T/3, N=300 rpm and θ=0.0 °.

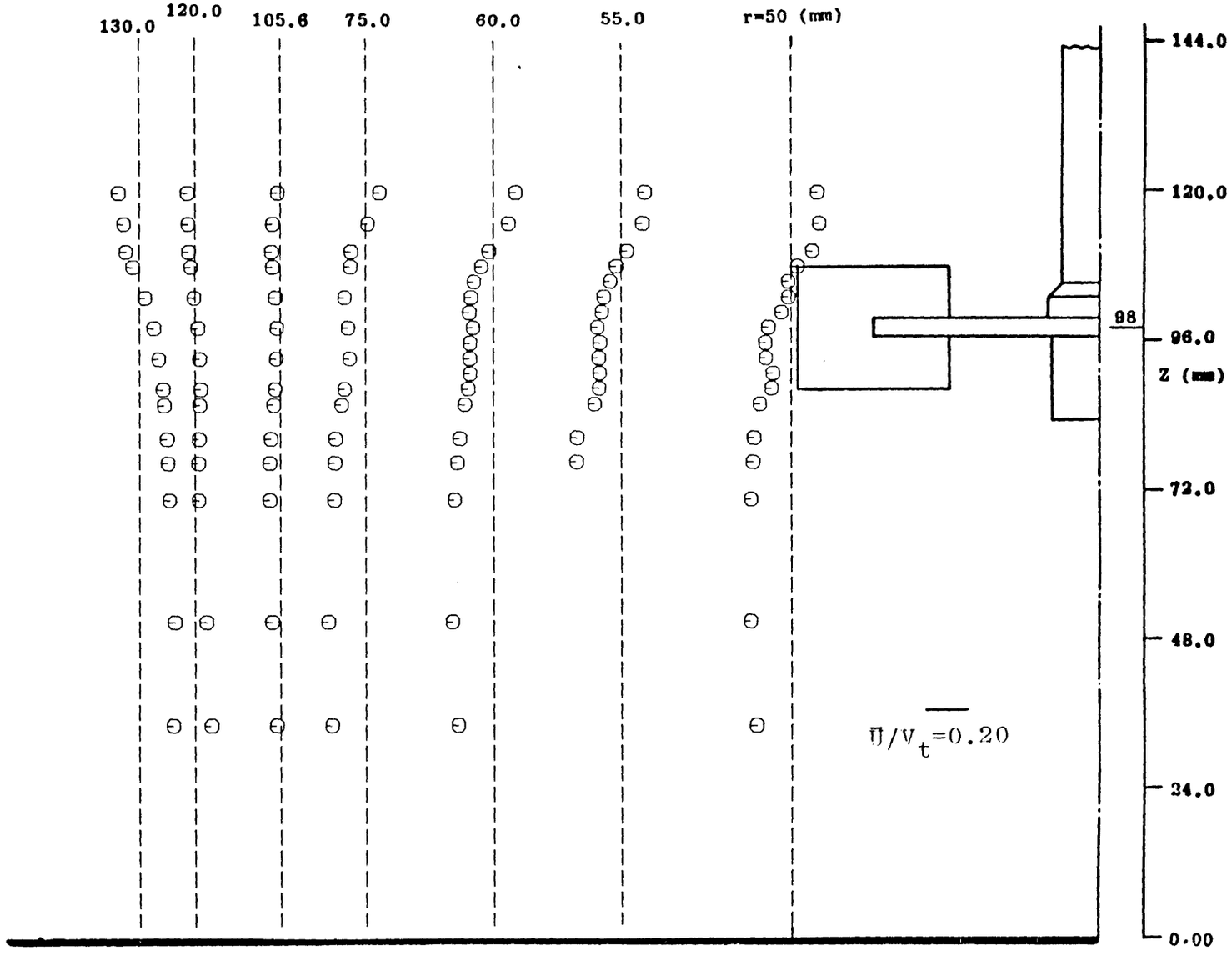

Fig 3.22 Axial mean velocity in the impeller stream for D=C=T/3, N=300 rpm and θ=0.0 °.

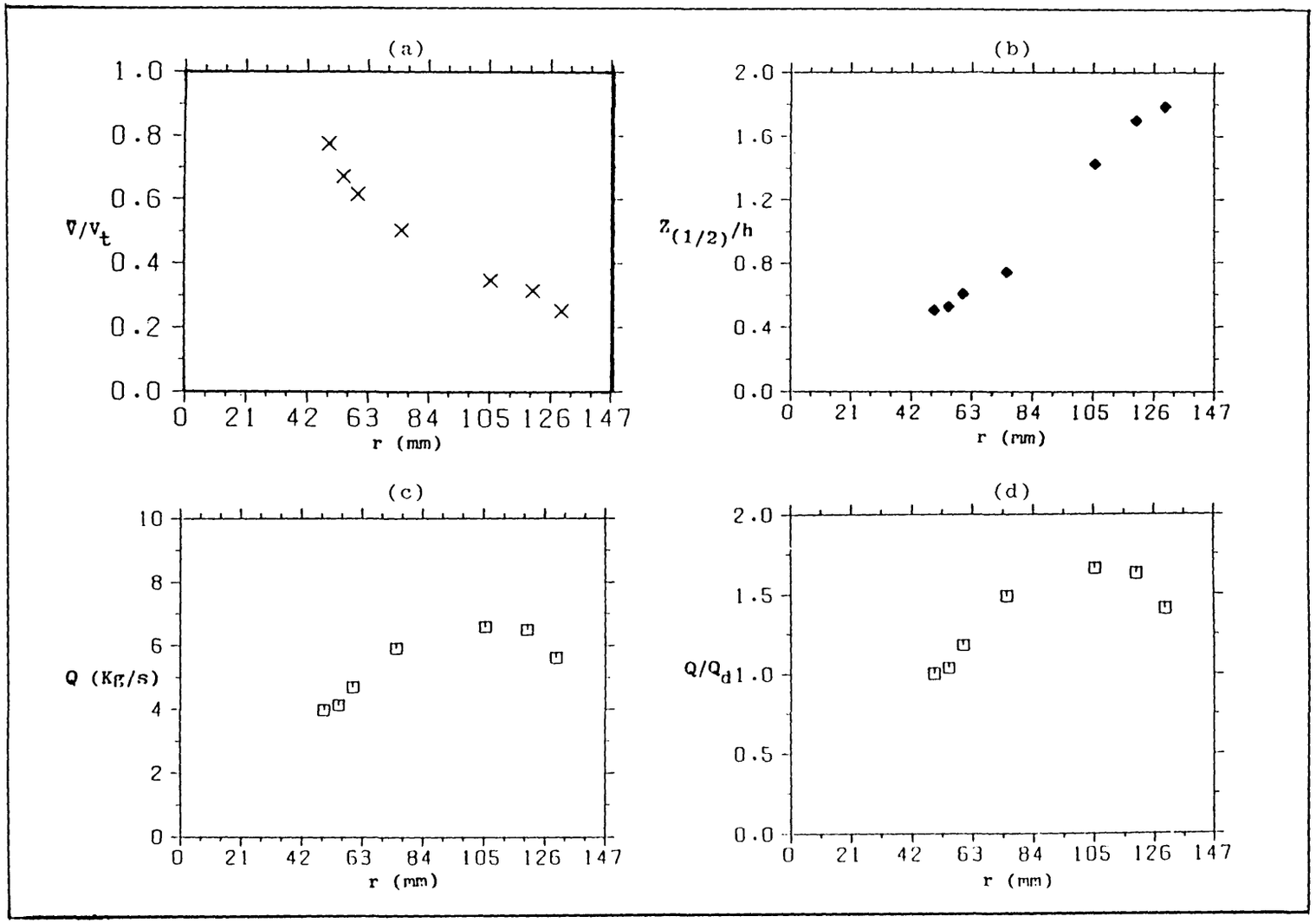

Fig 3.23 Characteristics of the radial impeller jet stream for D=C=T/3, N=300 rpm and θ=0.0 °: (a) centreline mean velocity decay; (b) spread of the jet stream; (c) radial mass flow and (d) pumping capacity.

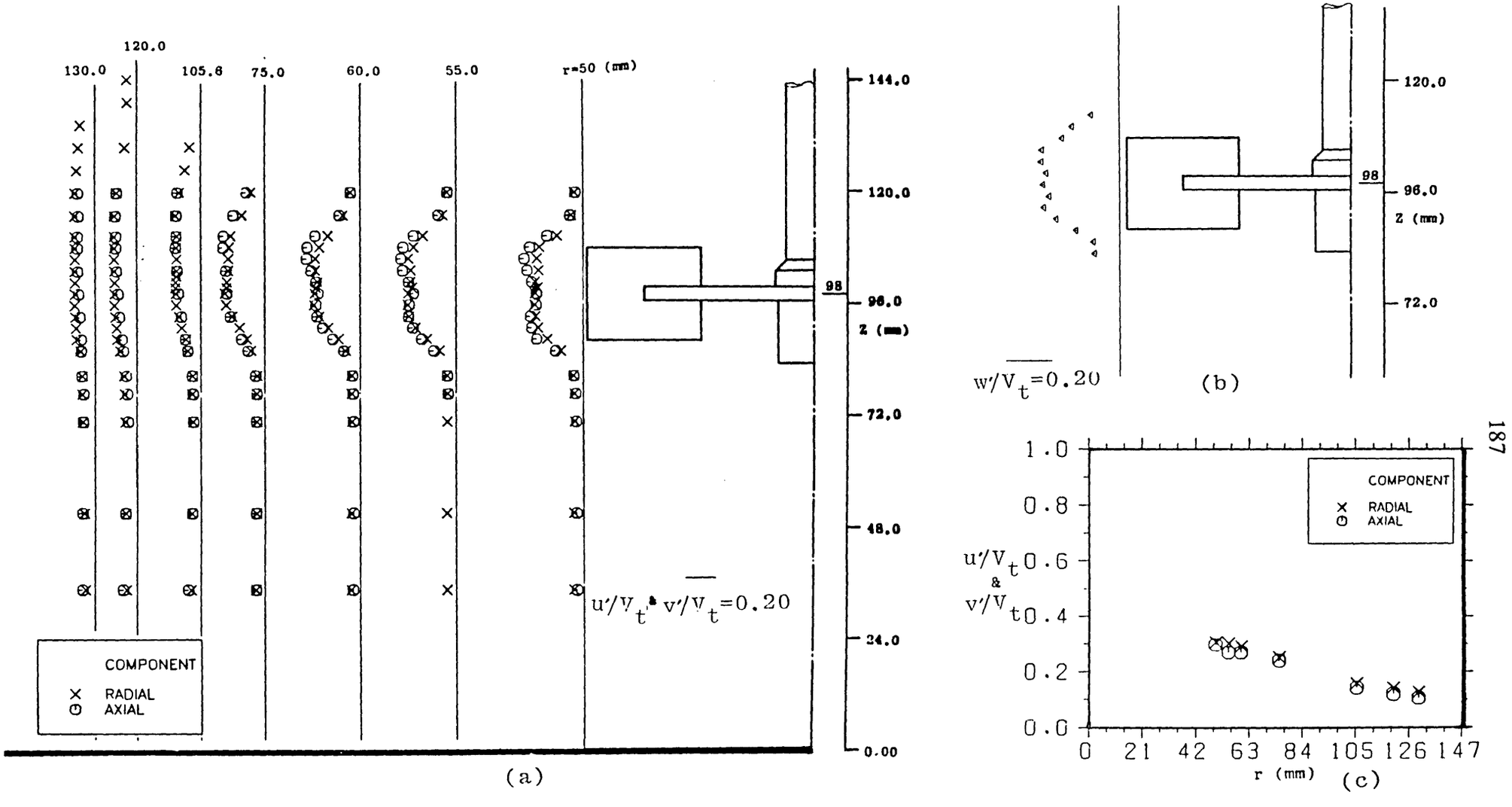

Fig 3.24 Rms velocity components in the impeller stream for D=C=T/3,N=300 rpm and θ=0.0 °: (a) u' and v' components; (b) w' component. and (c) centreline decay of u' and v'

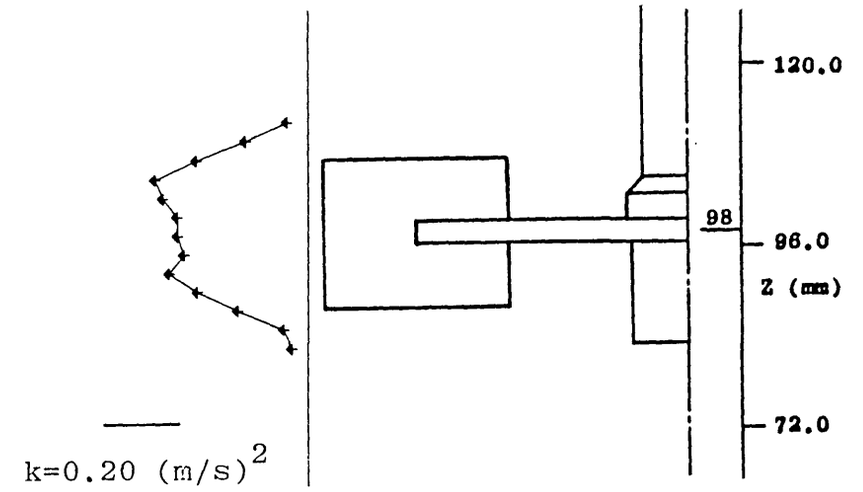

(a)

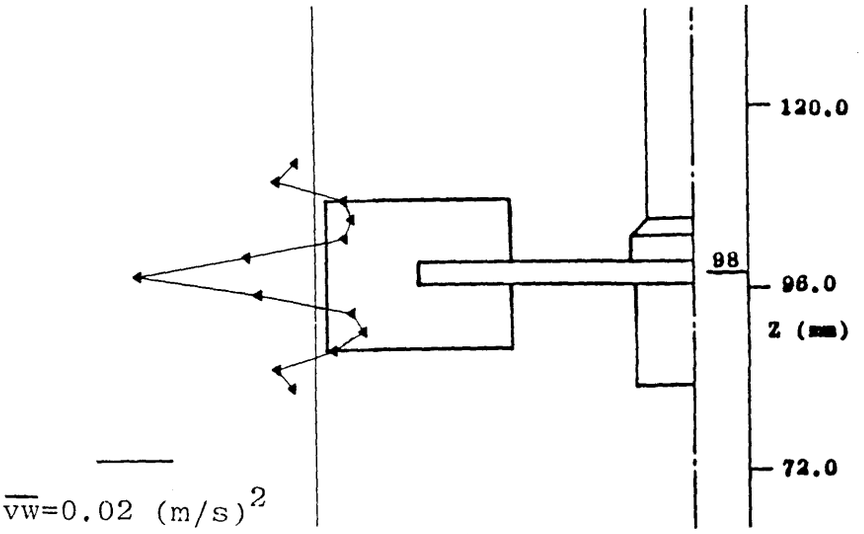

(b)

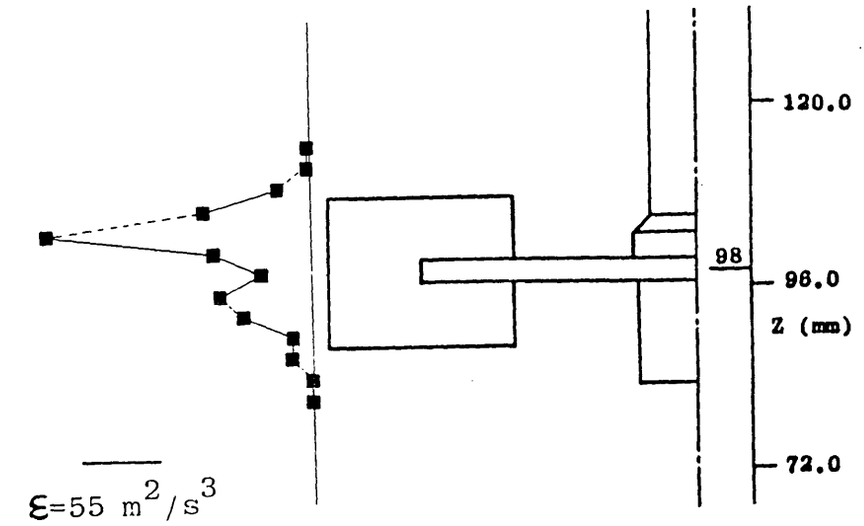

(c)

Fig 3.25 Turbulence quantities at the impeller tip for D=C=T/3, N=300 rpm and θ=0.0 °: (a) turbulence kinetic energy; (b) cross-correlation vw and (c) estimated rate of turbulence kinetic energy dissipation.

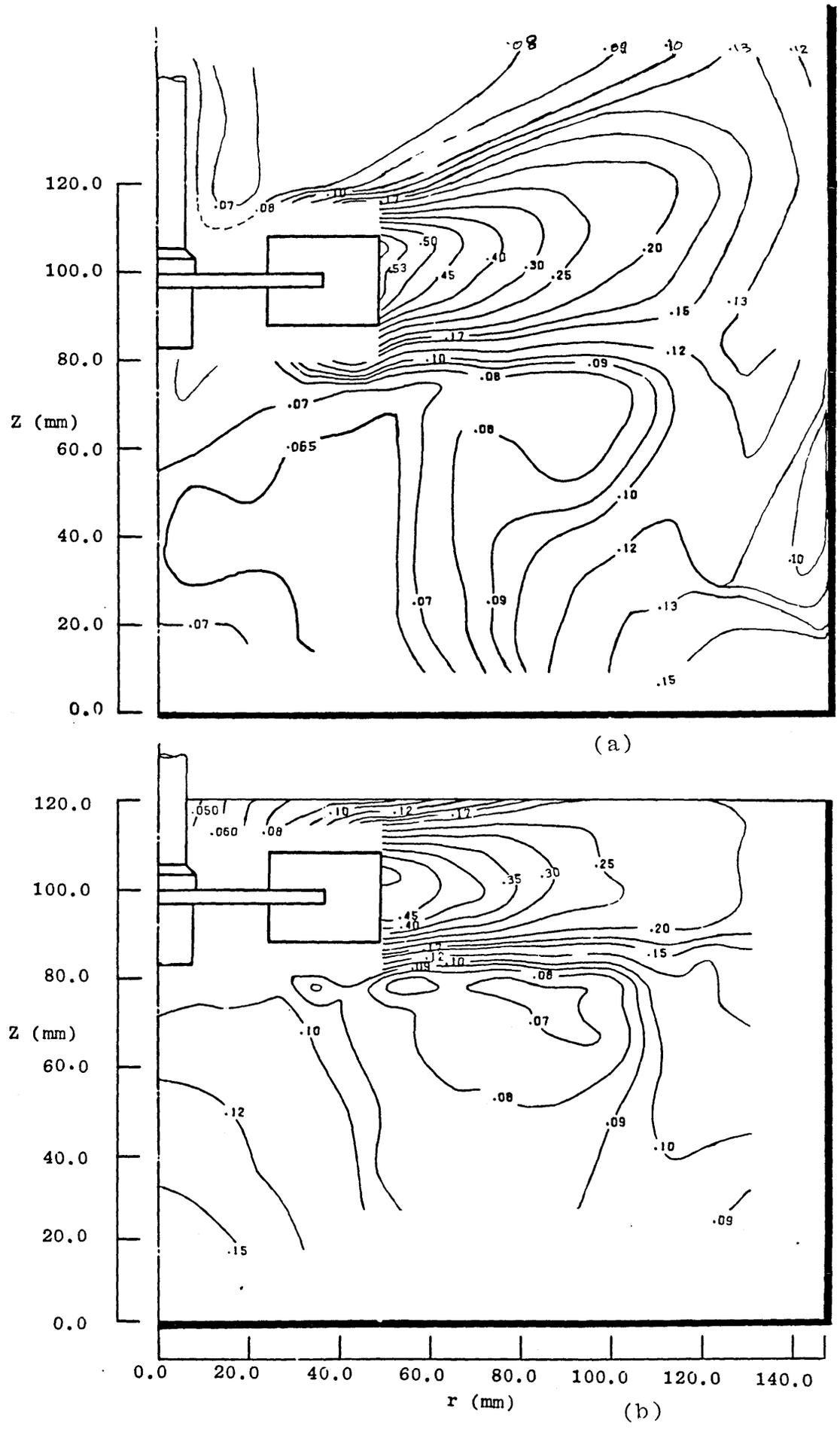

Fig 3.26 Contours of rms velocity above and below the impeller (values in m/s) for D=C=T/3, N=300 rpm and θ=0.0 °: (a) axial component and (b) radial component.

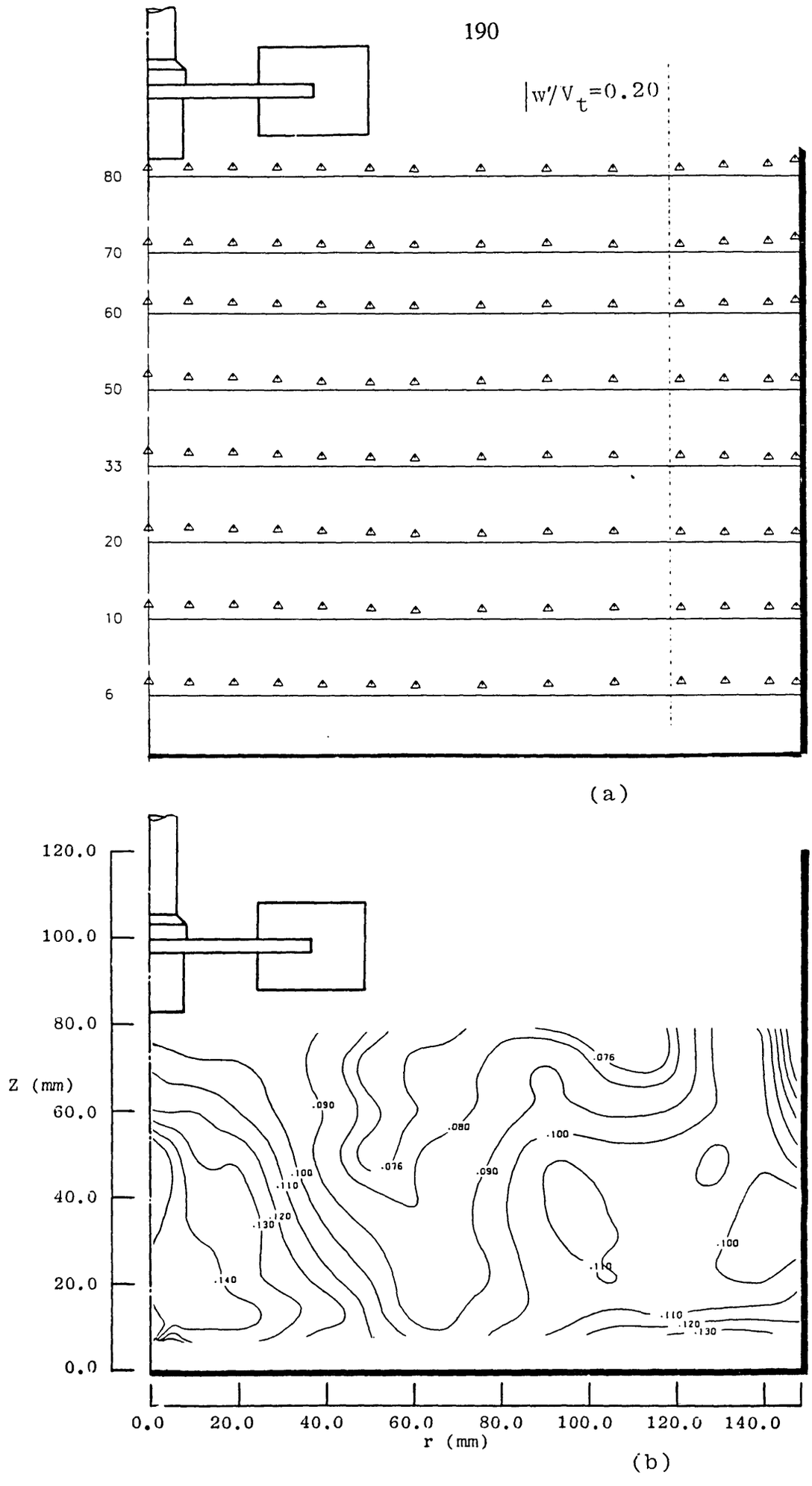

Fig 3.27 Tangential rms velocity below the impeller for D=C=T/3, N=300 rpm and θ=0.0 °: (a) radial profiles and (b) contours (values in m/s).

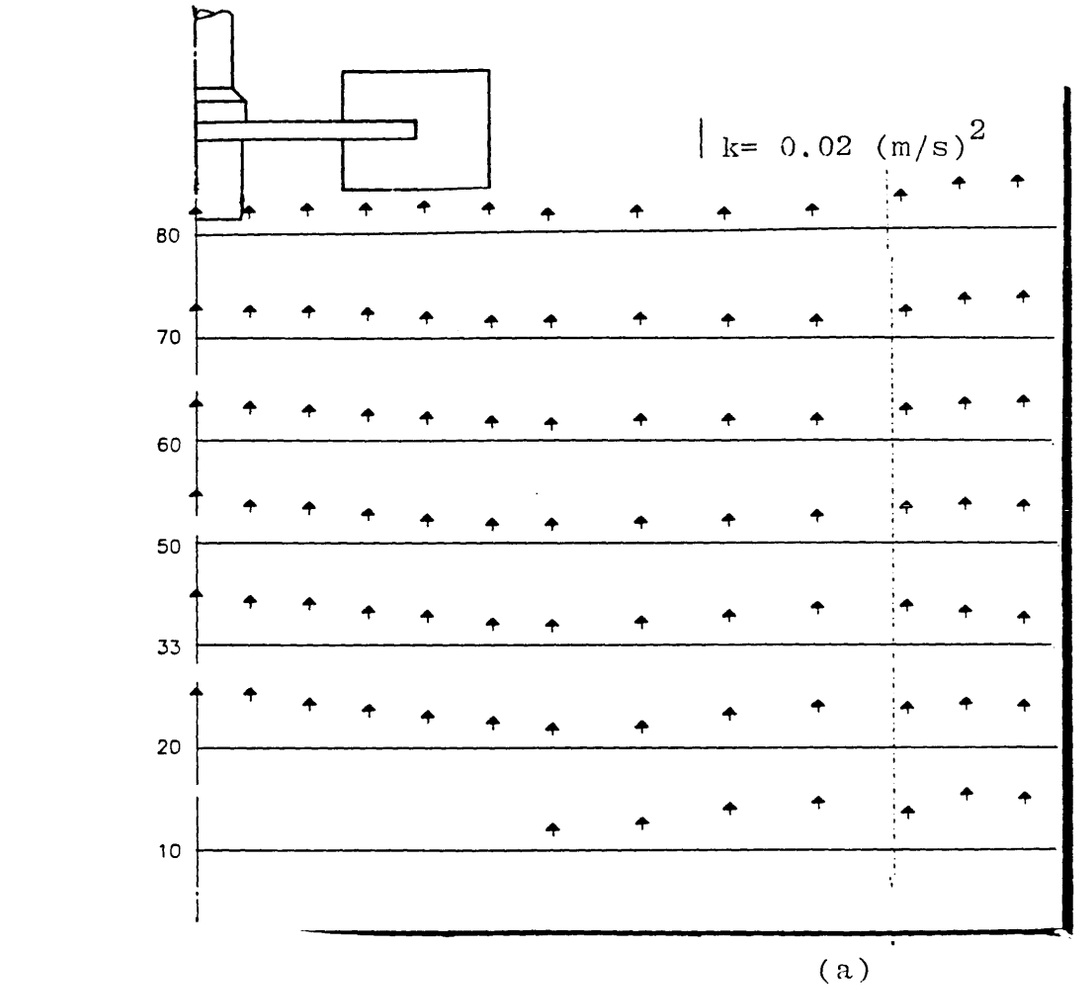

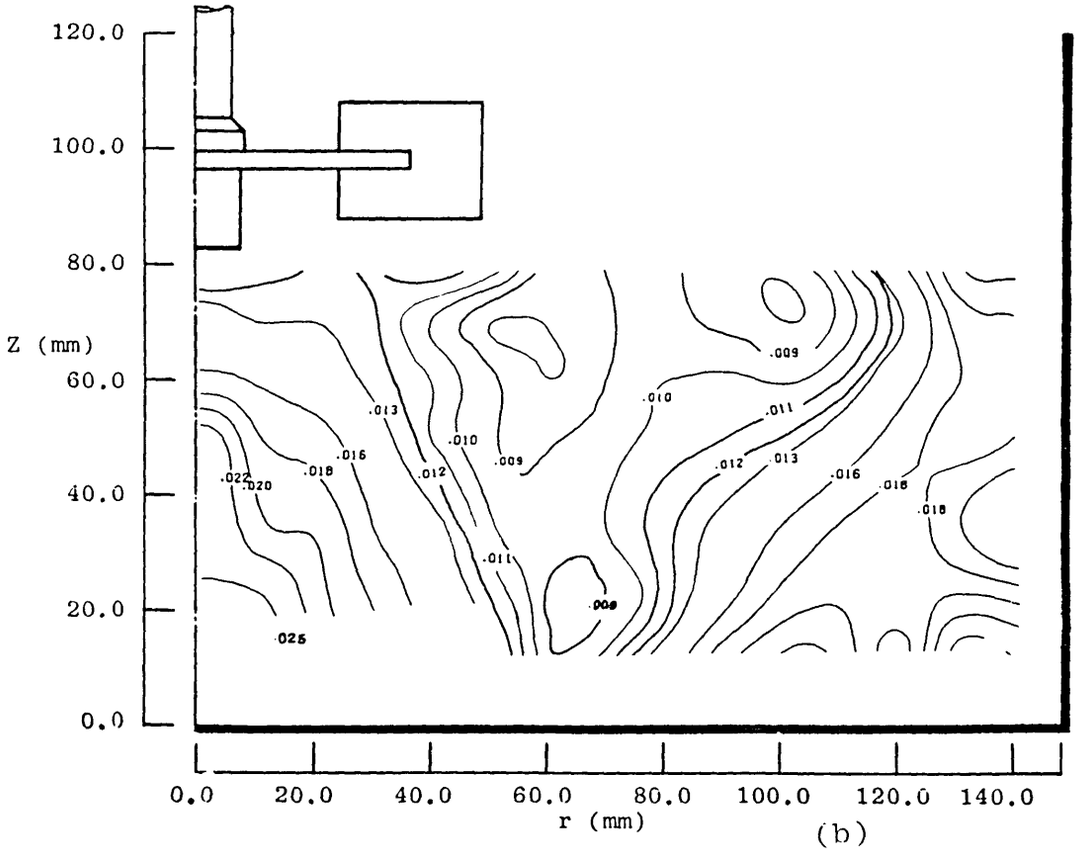

Fig 3.28 Turbulence kinetic energy below the impeller for D=C=T/3, N=300 rpm and θ=0.0 °: (a) radial profiles and (b) contours values in $(m/s)^2$.

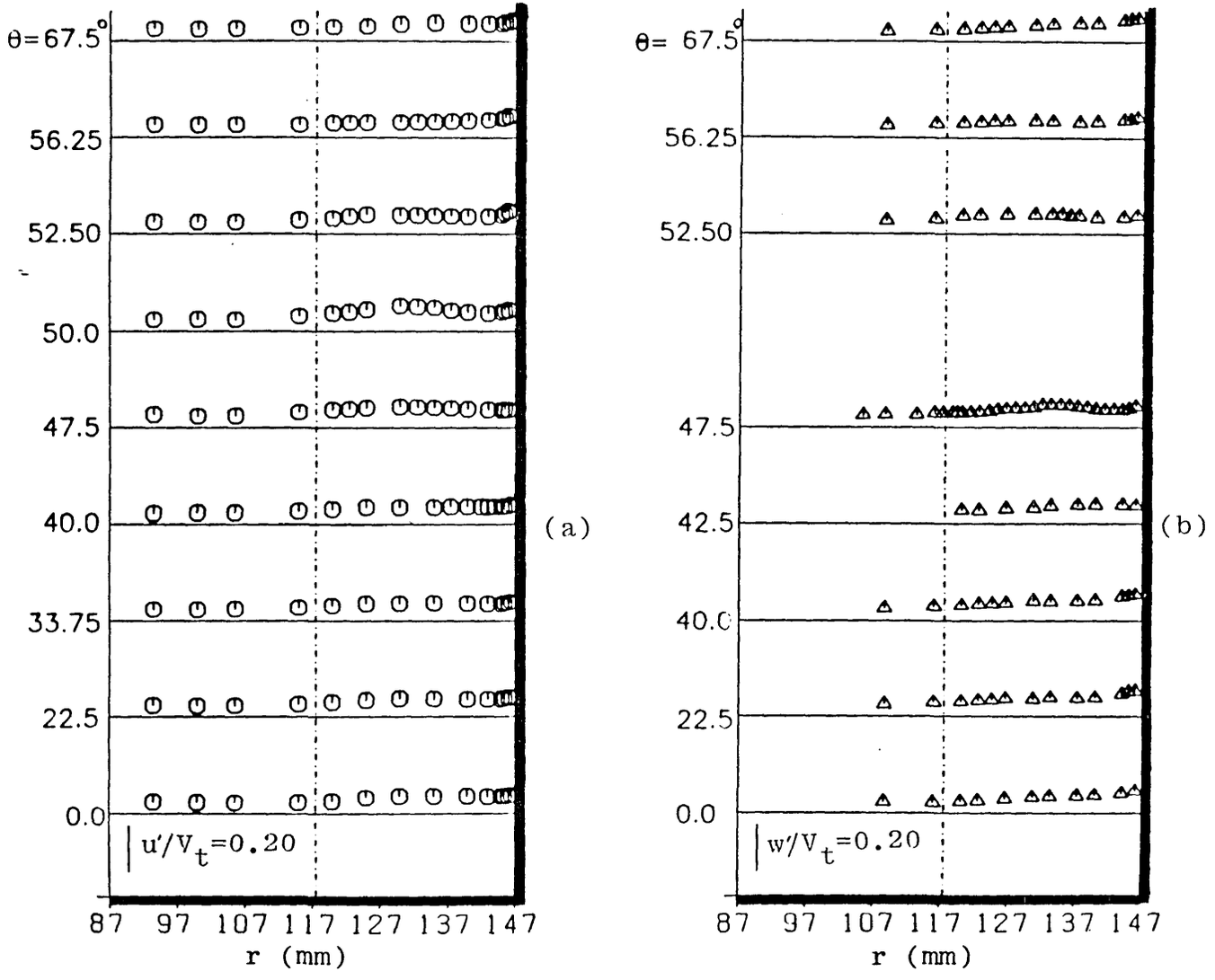

Fig 3.29 Rms velocity around the baffle for D=C=T/3, N=300 rpm and at Z=70 mm of: (a) axial component and (b) tangential component.

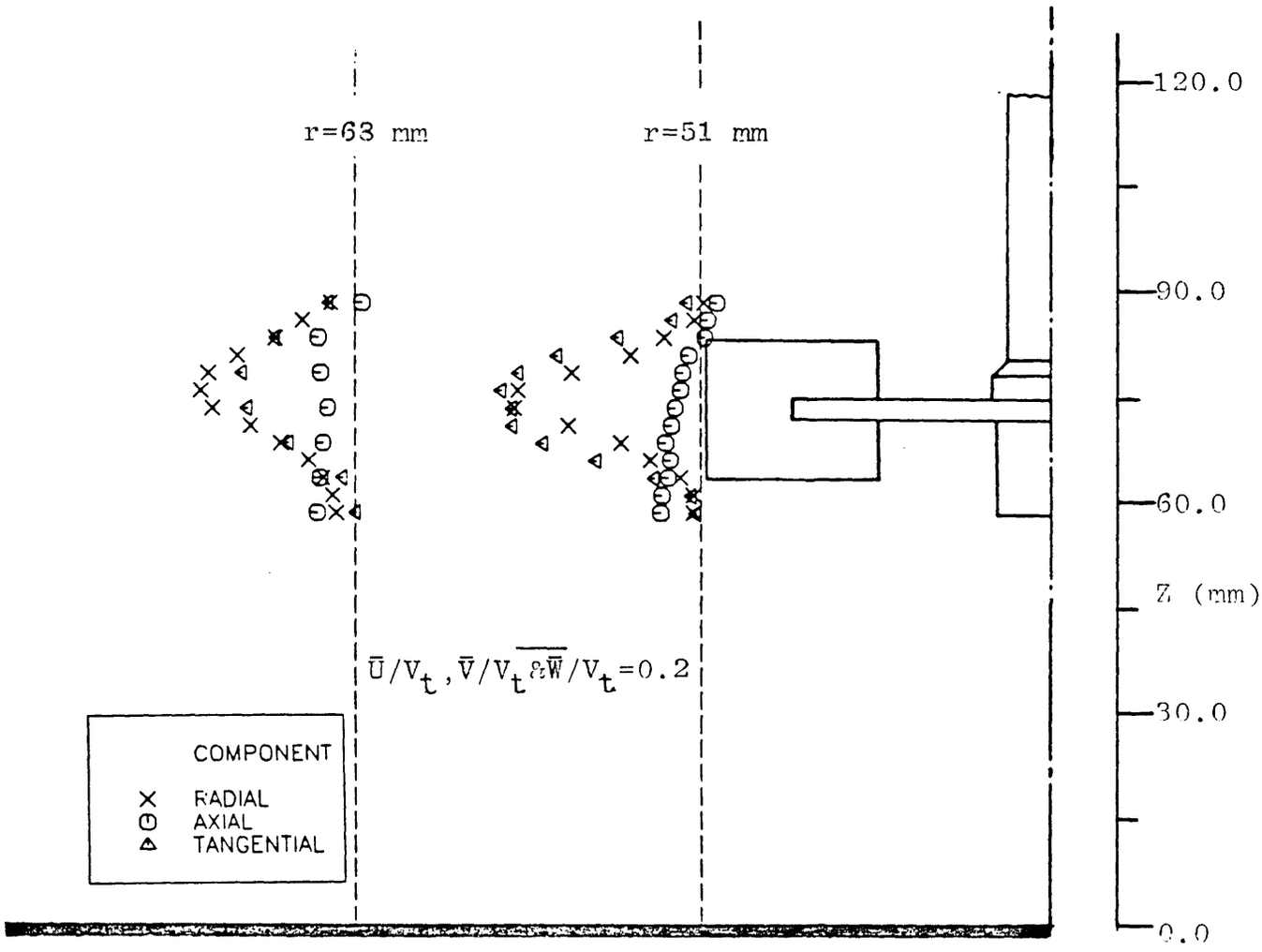

Fig 3.30 Axial, radial and tangential mean velocity components in the impeller stream for D=T/3, C=T/4, N=313 rpm and θ=0.0 °.

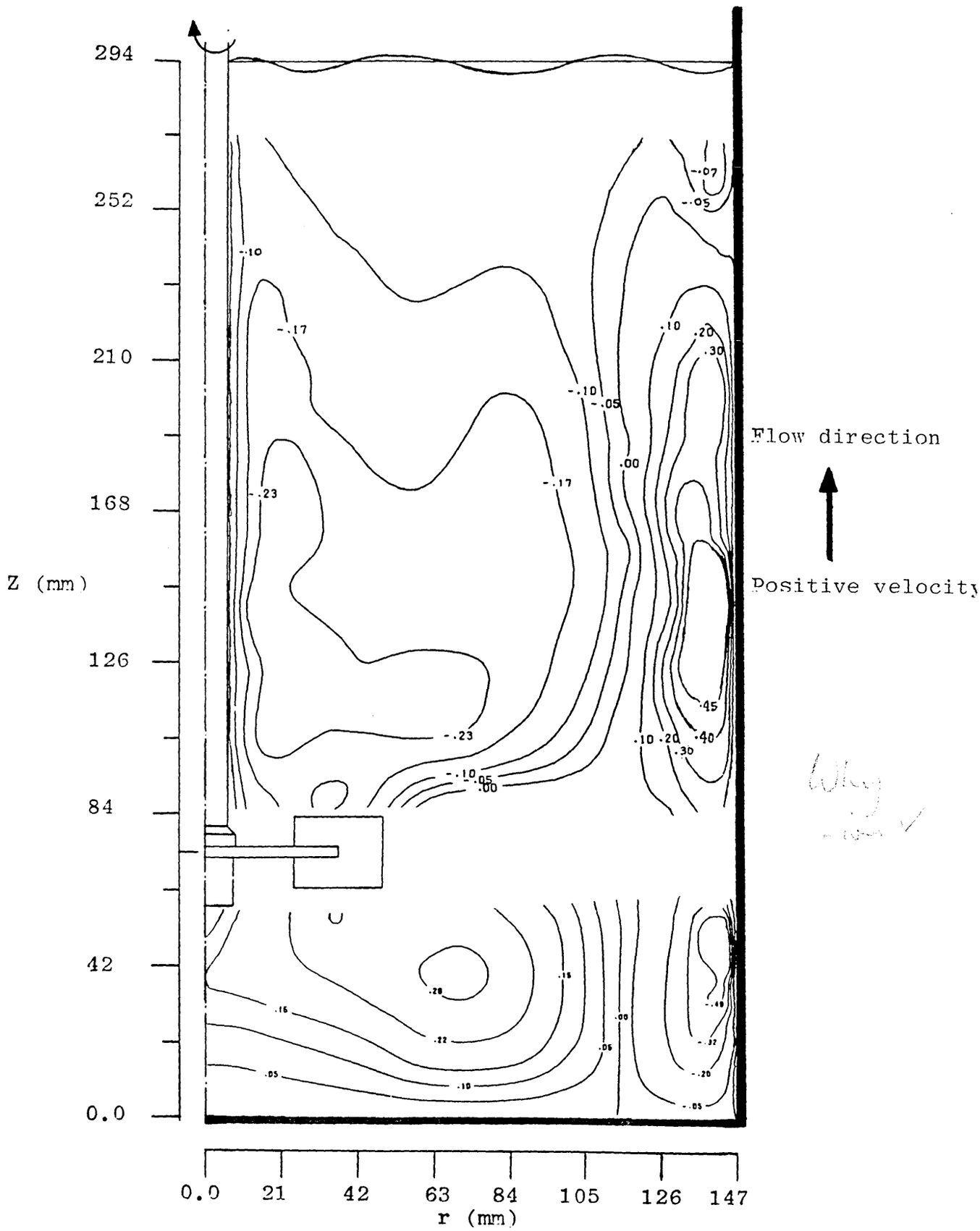

Fig 3.31 Contours of axial mean velocity above and below the impeller (values in m/s) for D=T/3, C=T/4, N=313 rpm and θ=0.0 °.

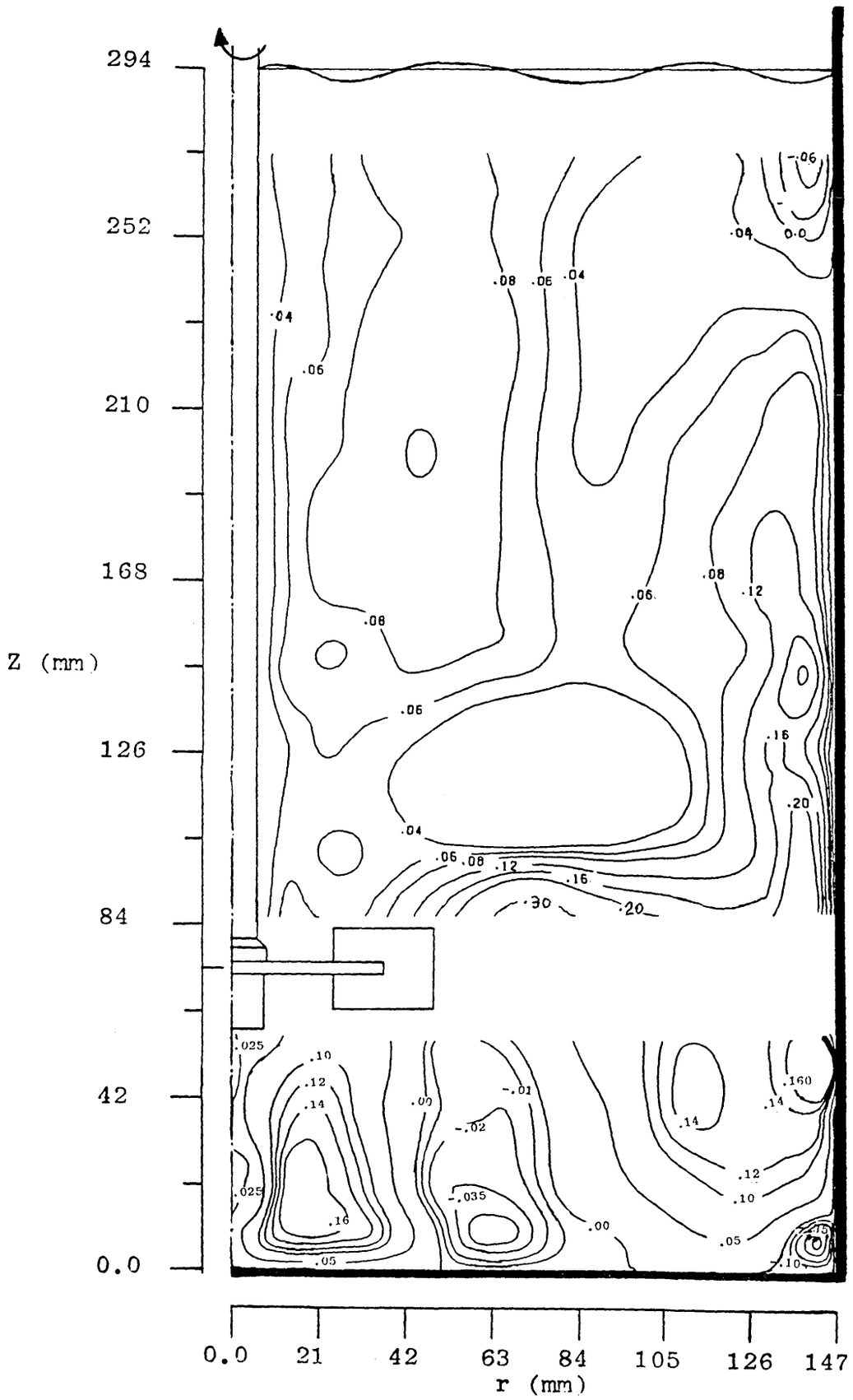

Fig 3.32 Contours of tangential mean velocity above and below the impeller (values in m/s) for D=T/3, C=T/4, N=313 rpm and θ=0.0 °.

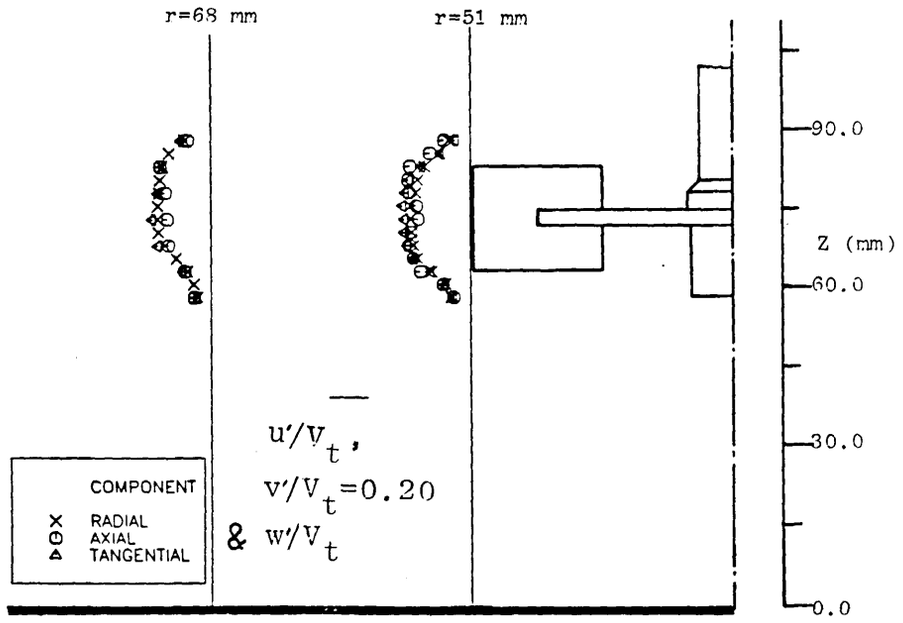

Fig 3.33 Axial, radial and tangential rms velocity components in the impeller stream for D=T/3, C=T/4, N=313 rpm and θ=0.0 °.

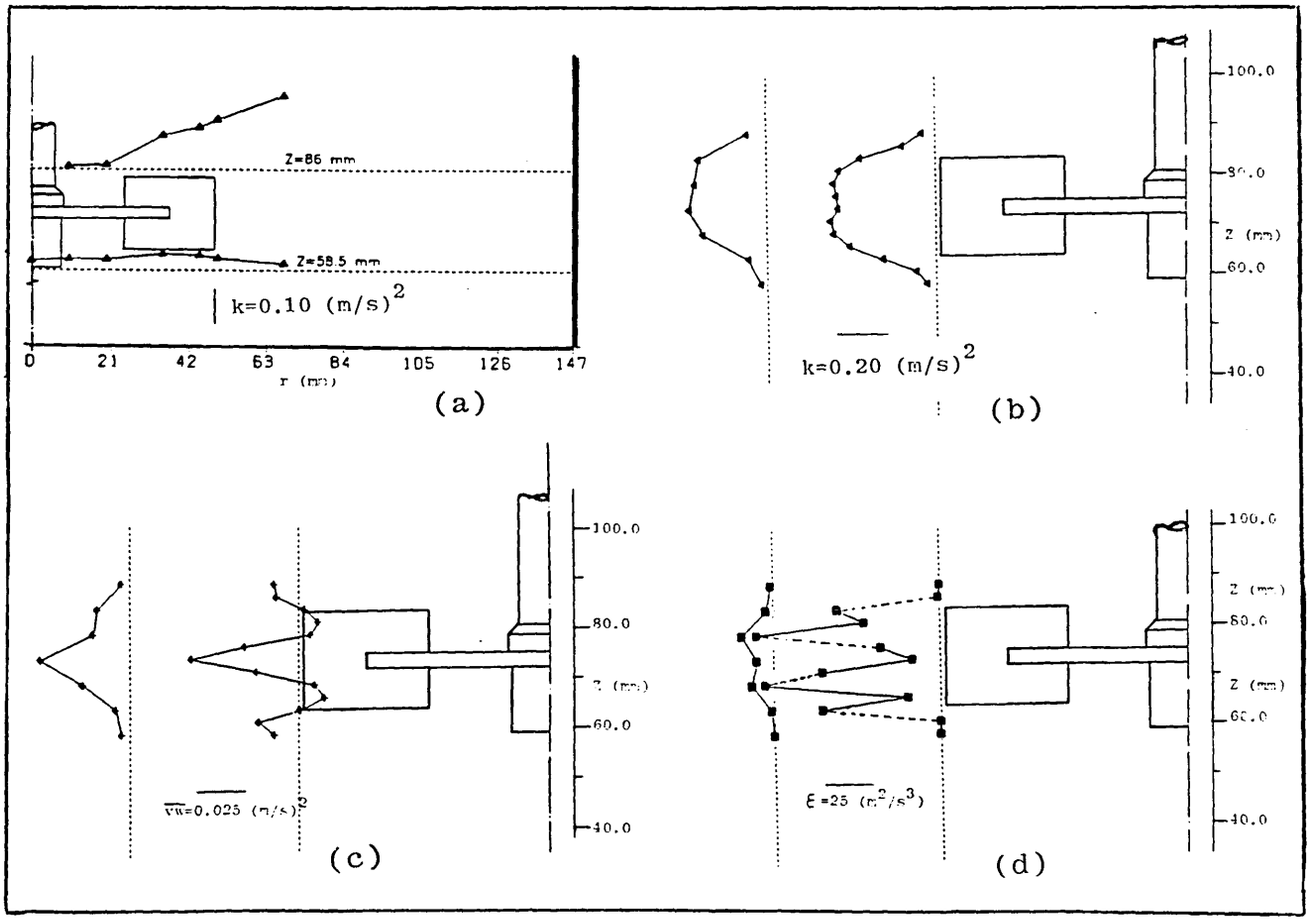

Fig 3.34 Turbulence quantities around the impeller for D=T/3, C=T/4, N=313 rpm and θ=0 °: (a) k above and below the impeller; (b) k in the impeller stream; (c) vw in the impeller stream; (d) dissipation of k at the impeller tip.

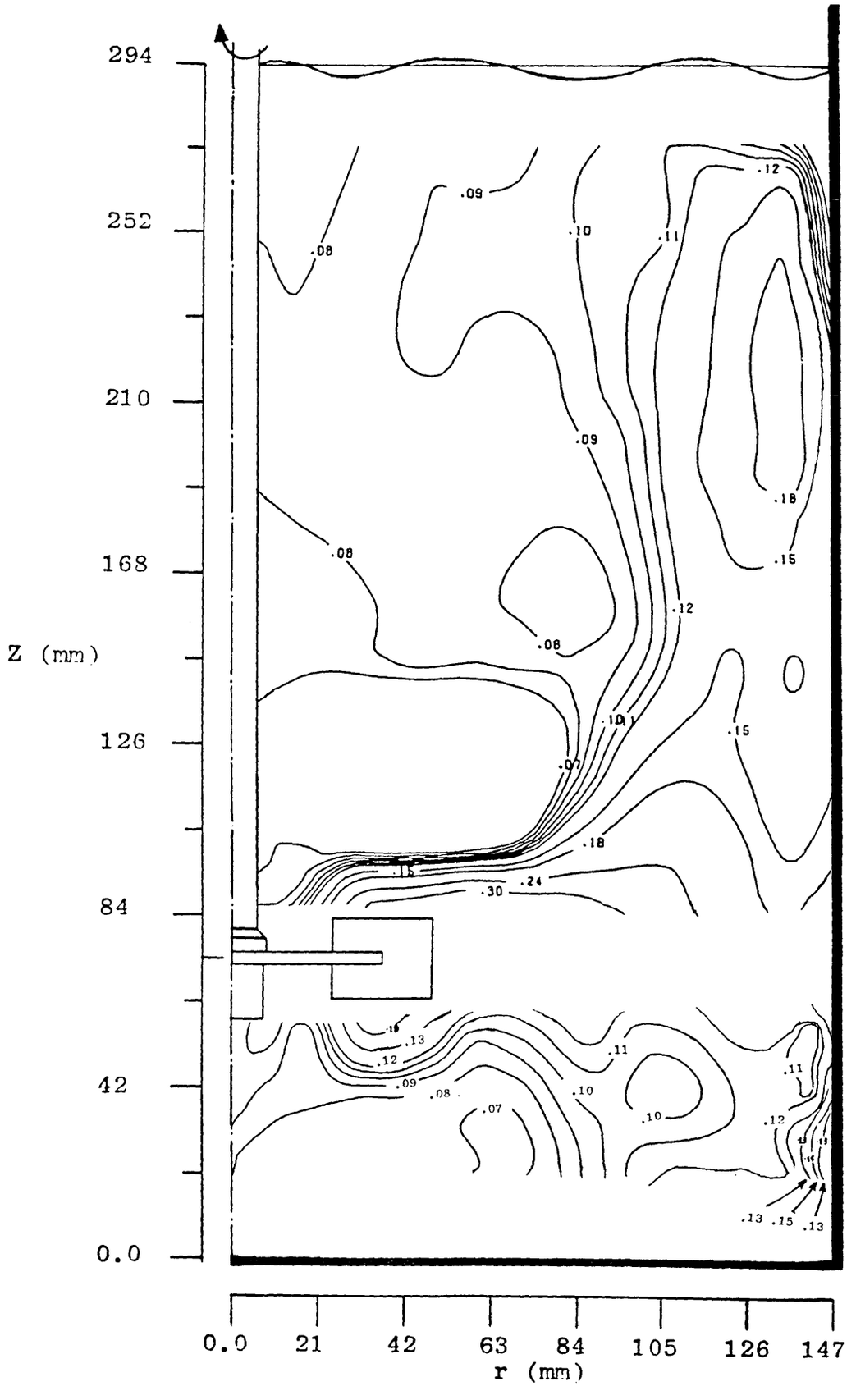

Fig 3.35 Contours of axial rms velocity above and below the impeller (values in m/s) for D=T/3, C=T/3, N=313 and θ=0.0 °.

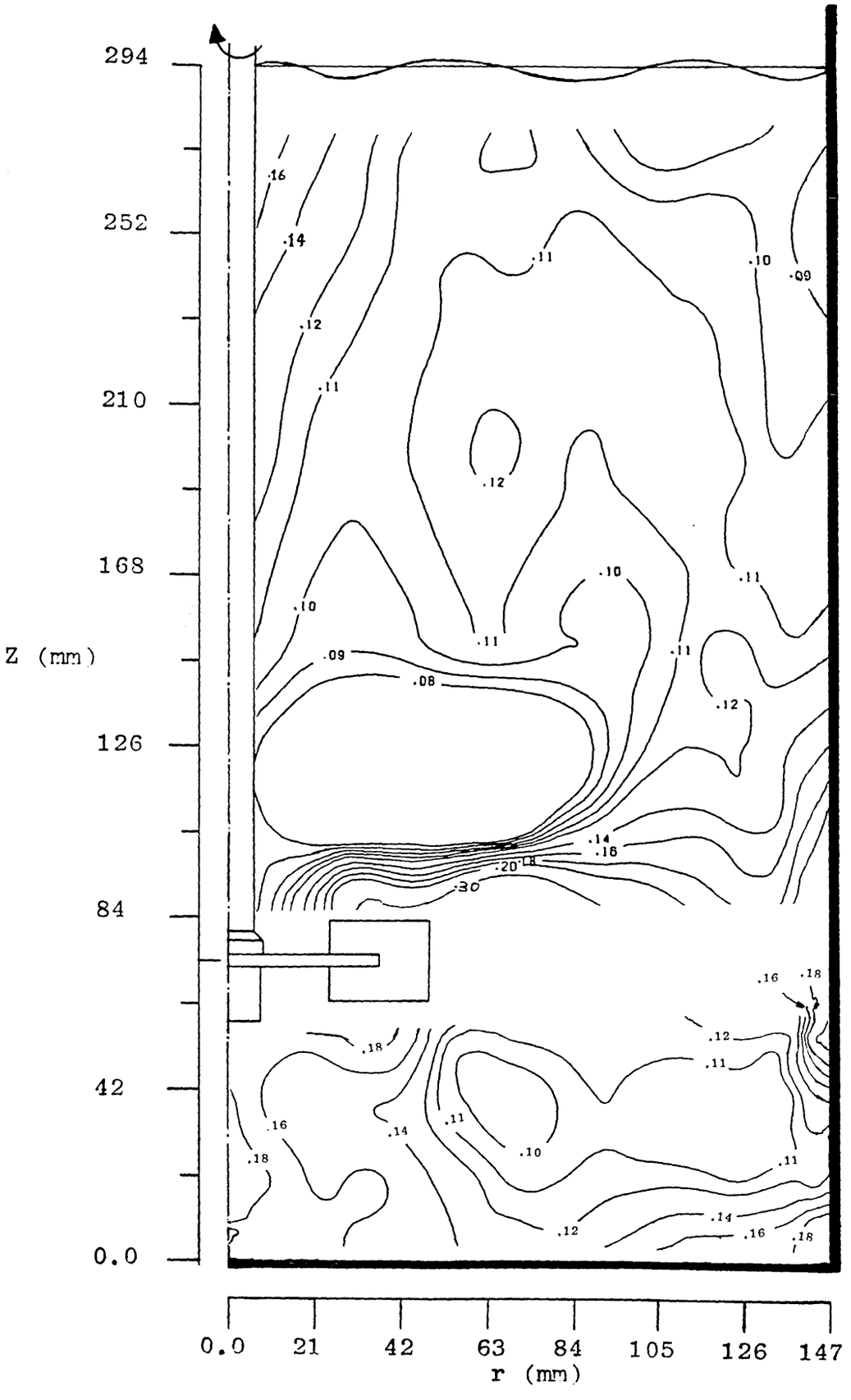

Fig 3.36 Contours of tangential rms velocity above and below the impeller (values in m/s) for D=T/3, C=T/4, N=313 rpm and θ=0.0 °.

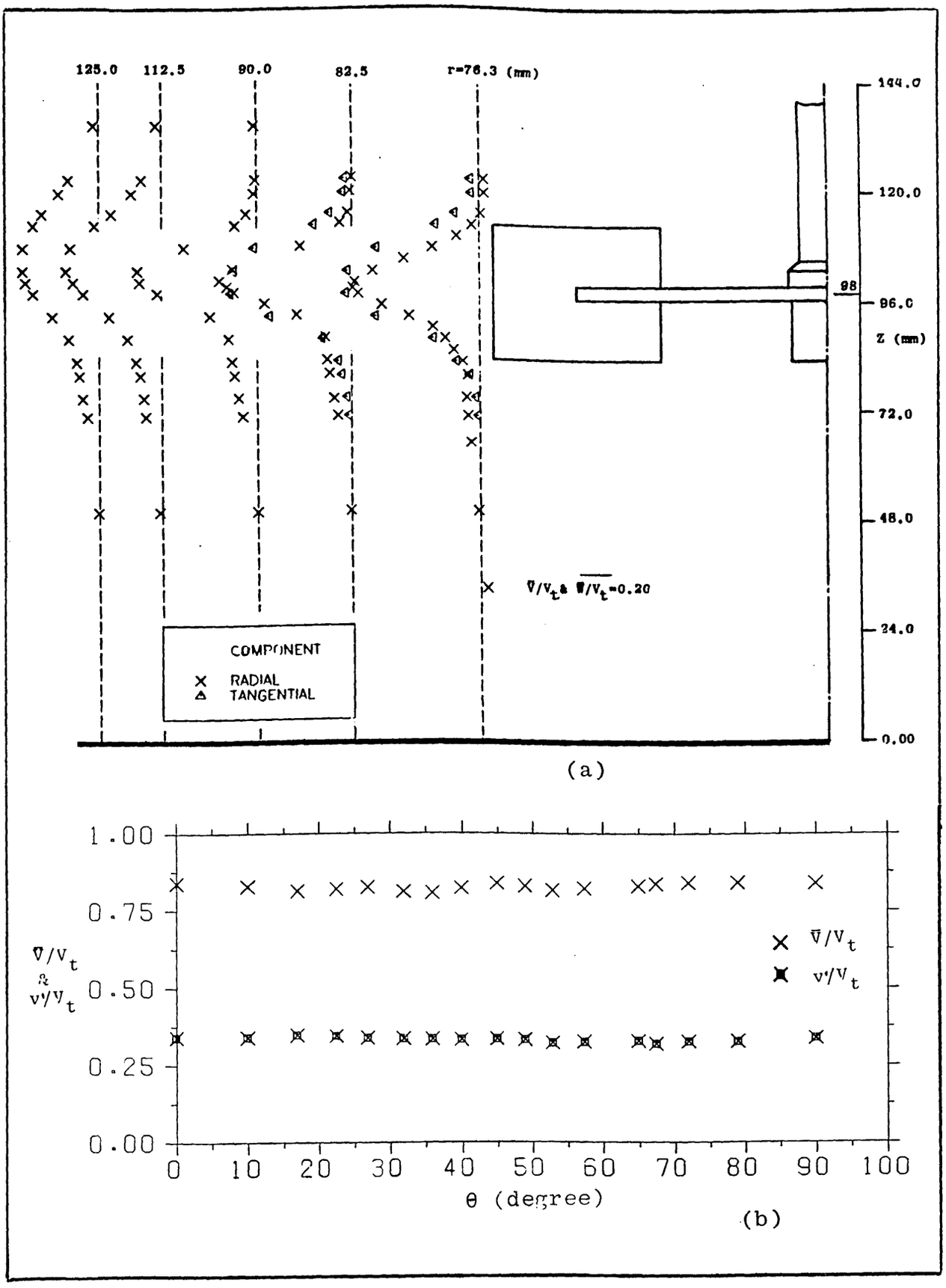

Fig 3.37 Mean velocity components for D=T/2, C=T/3, N=125 rpm and θ=0.0°: (a) radial and tangential components in impeller stream and (b) circumferential symmetry of radial mean and rms velocities.

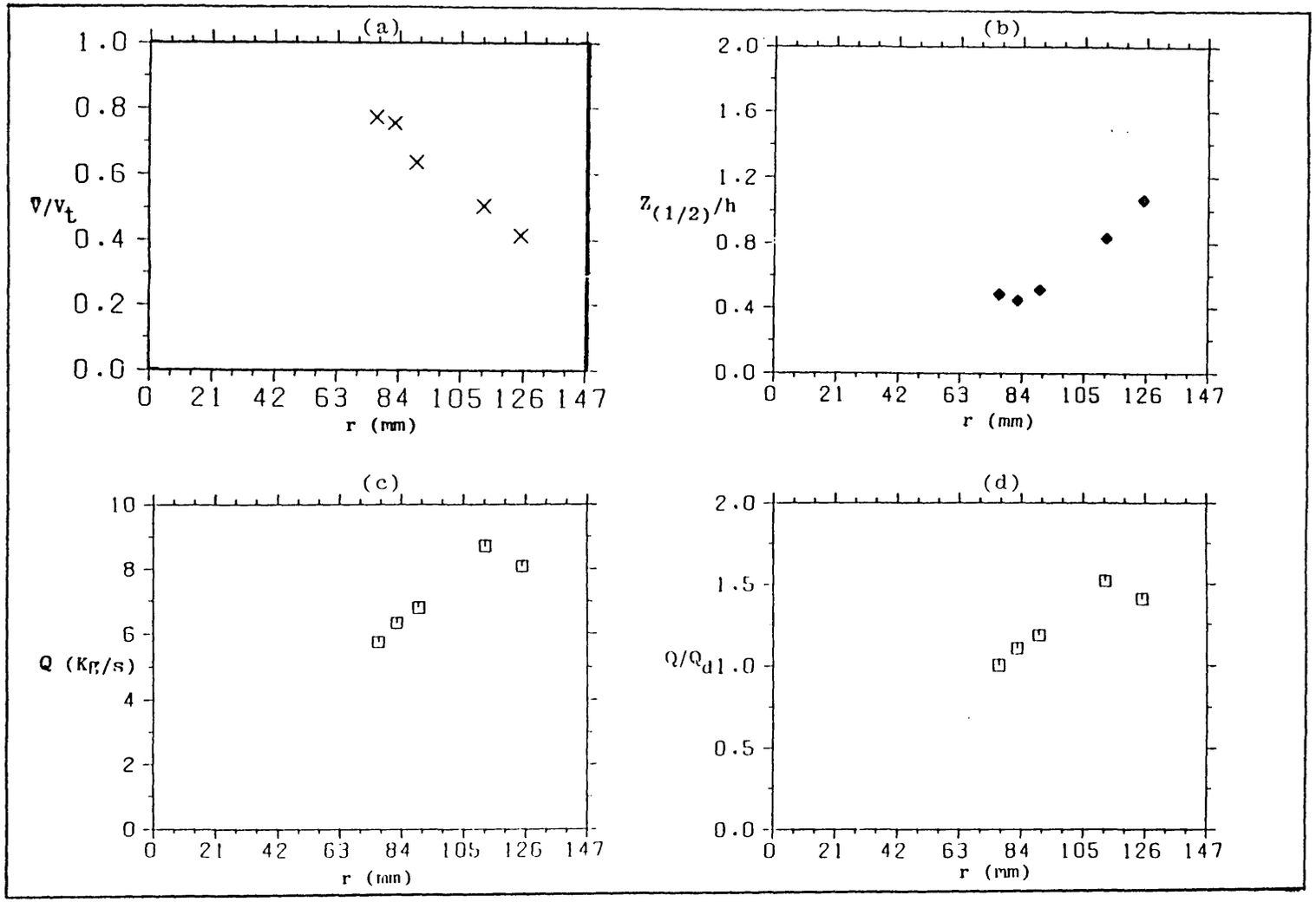

Fig 3.38 Characteristics of radial jet stream for D=T/2, C=T/3, N=125 rpm and θ=0.0 °: (a) centreline mean velocity decay; (b) spread of the jet stream; (c) Pumping capacity and (d) normalised pumping capacity.

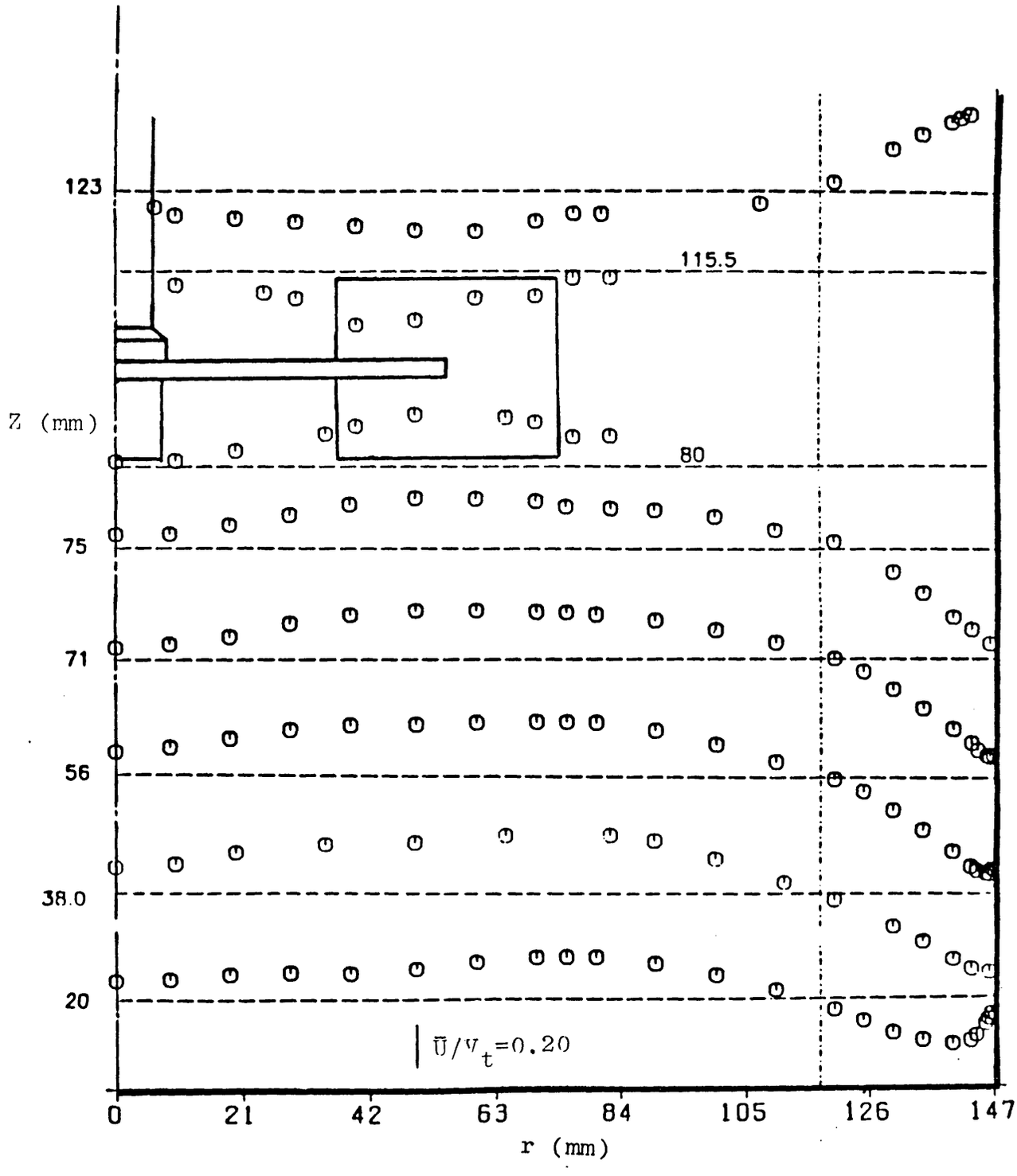

Fig 3.39 Axial mean velocity above and below the impeller for D=T/2, C=T/3, N=125 rpm and θ=0.0 °.

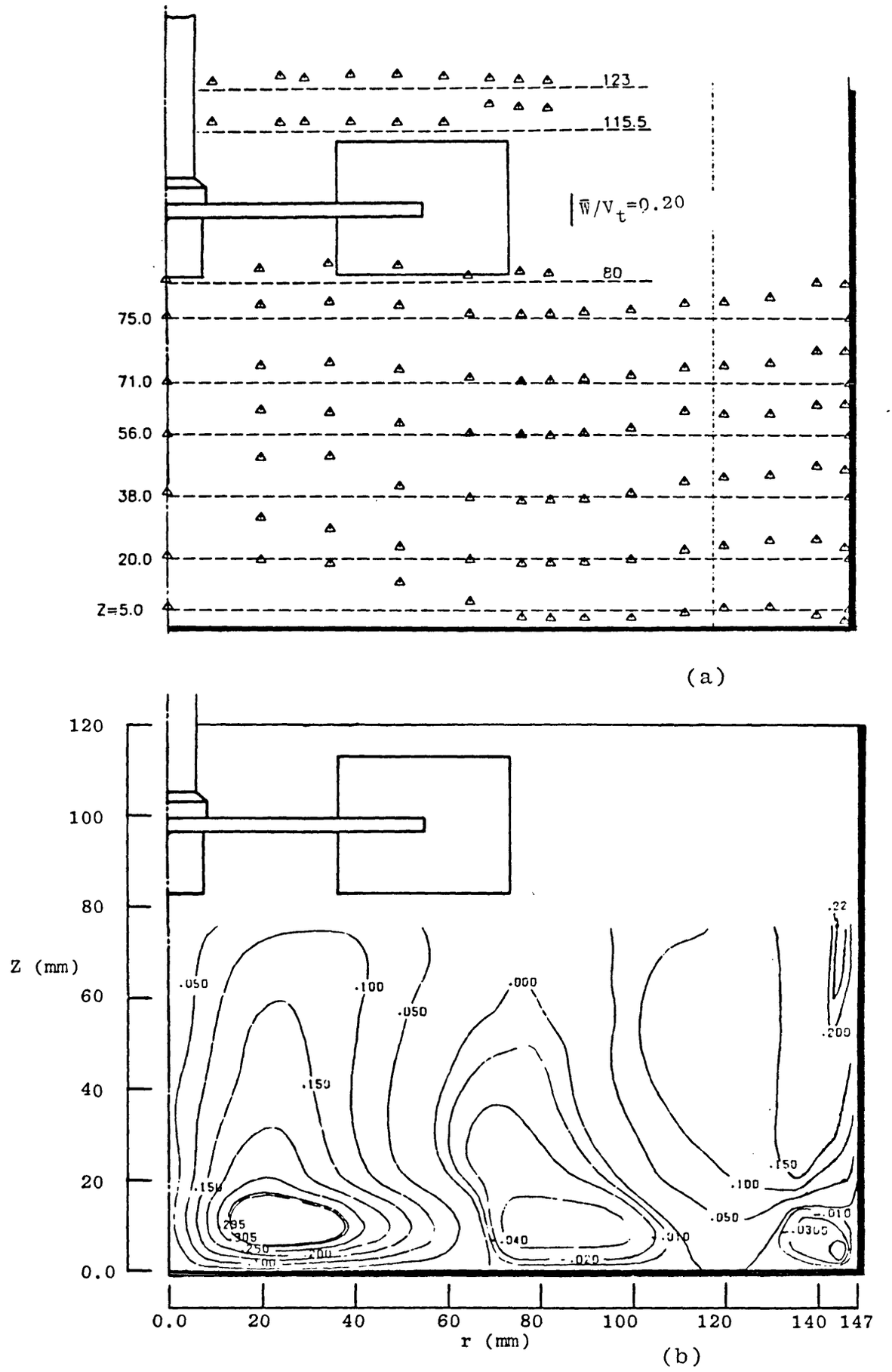

Fig 3.40 Tangential mean velocity above and below the impeller for D=T/2, C=T/3, N=125 rpm and θ=0.0 °: (a) radial profiles; (b) contours (values in m/s).

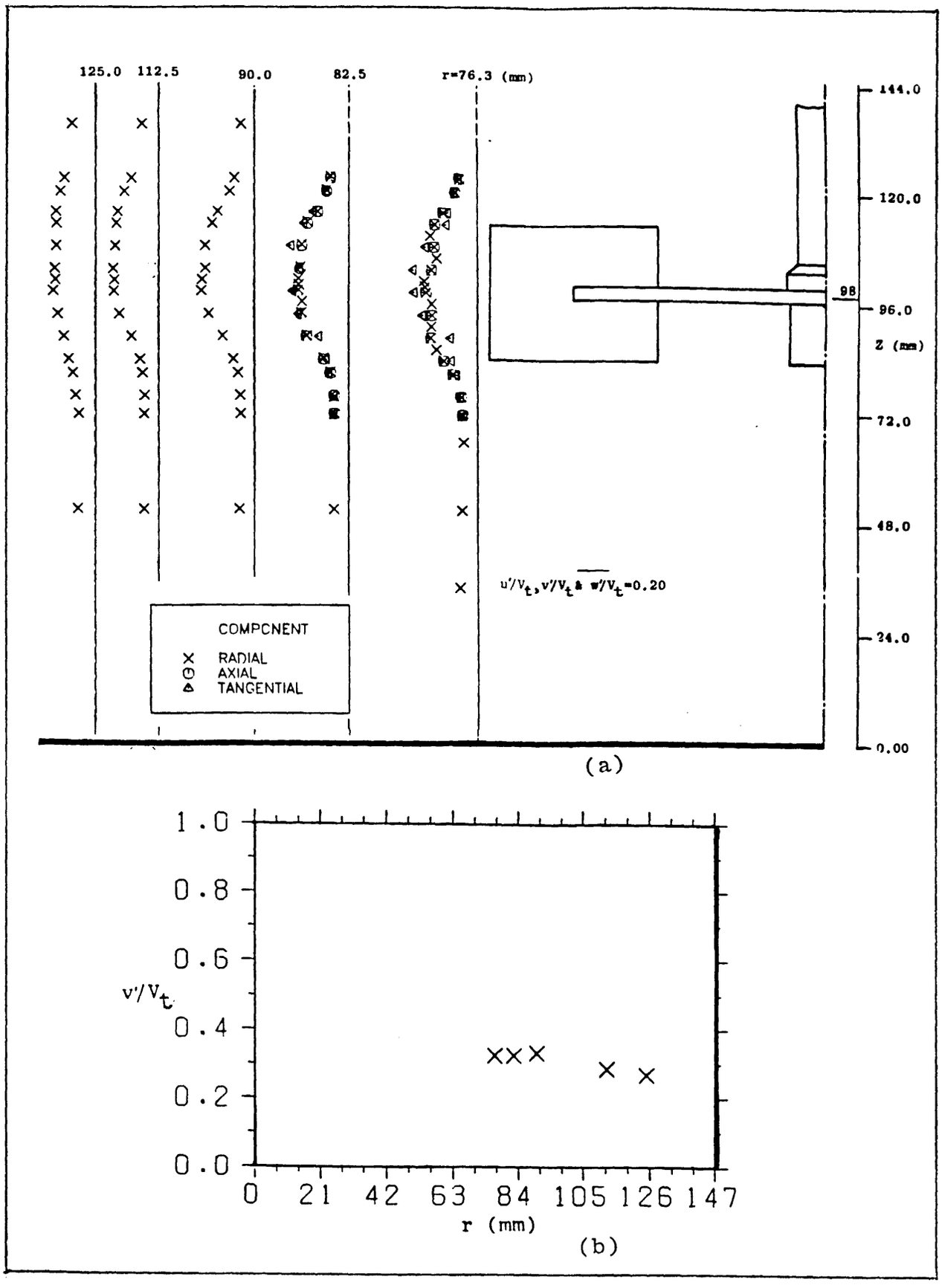

Fig 3.41 Rms velocity components in the impeller stream for D=T/2, C=T/3, N=125 rpm and θ=0.0 ° of: (a) axial, radial and tangential components and (b) centreline decay of u'.

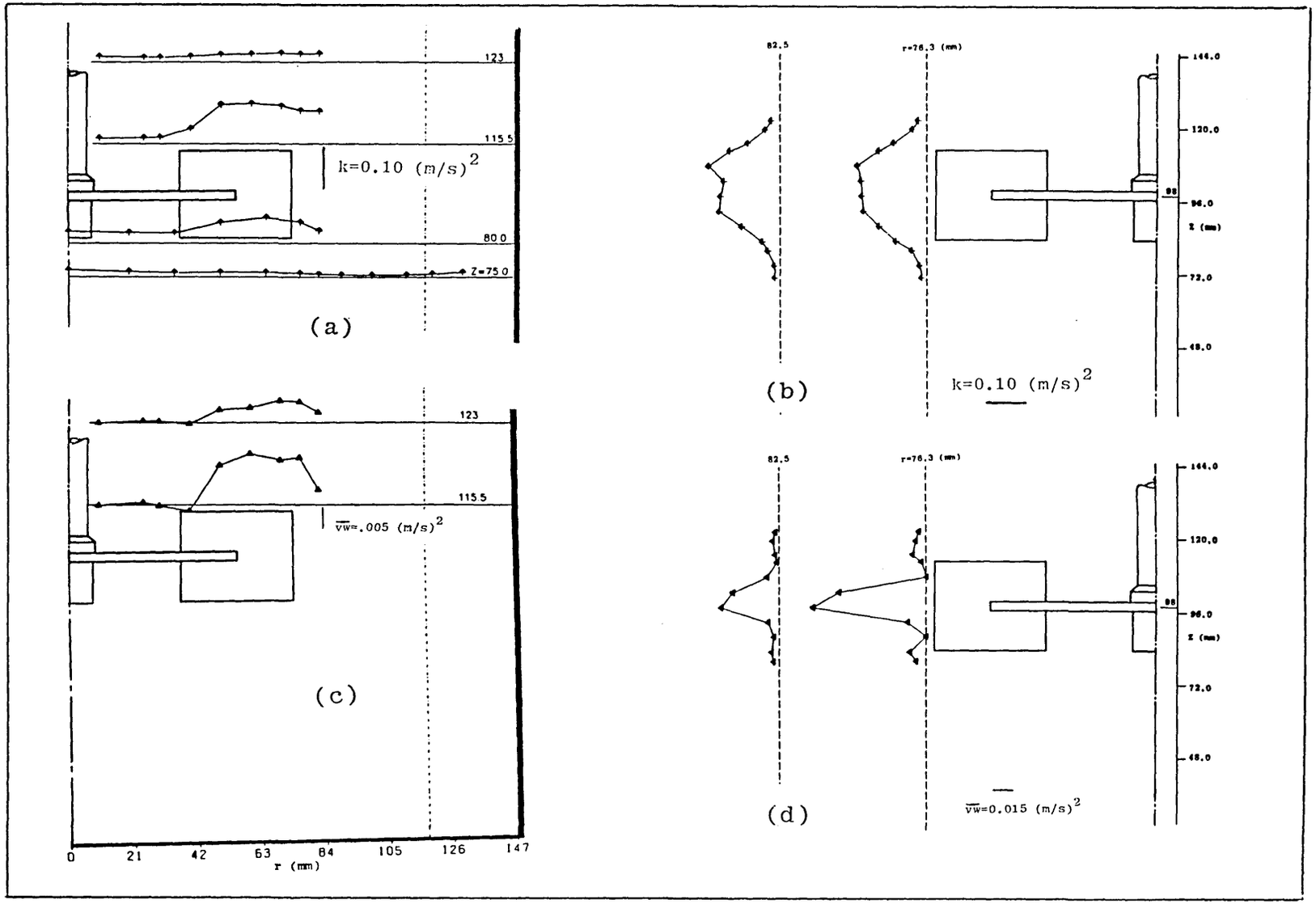

Fig 3.42 Turbulence quantities around the impeller for D=T/2, C=T/3, N=125 rpm and θ=0.0 °: (a) k above and below the impeller; (b) k in the impeller stream and (c) vw above the impeller; (d) vw in the impeller stream.

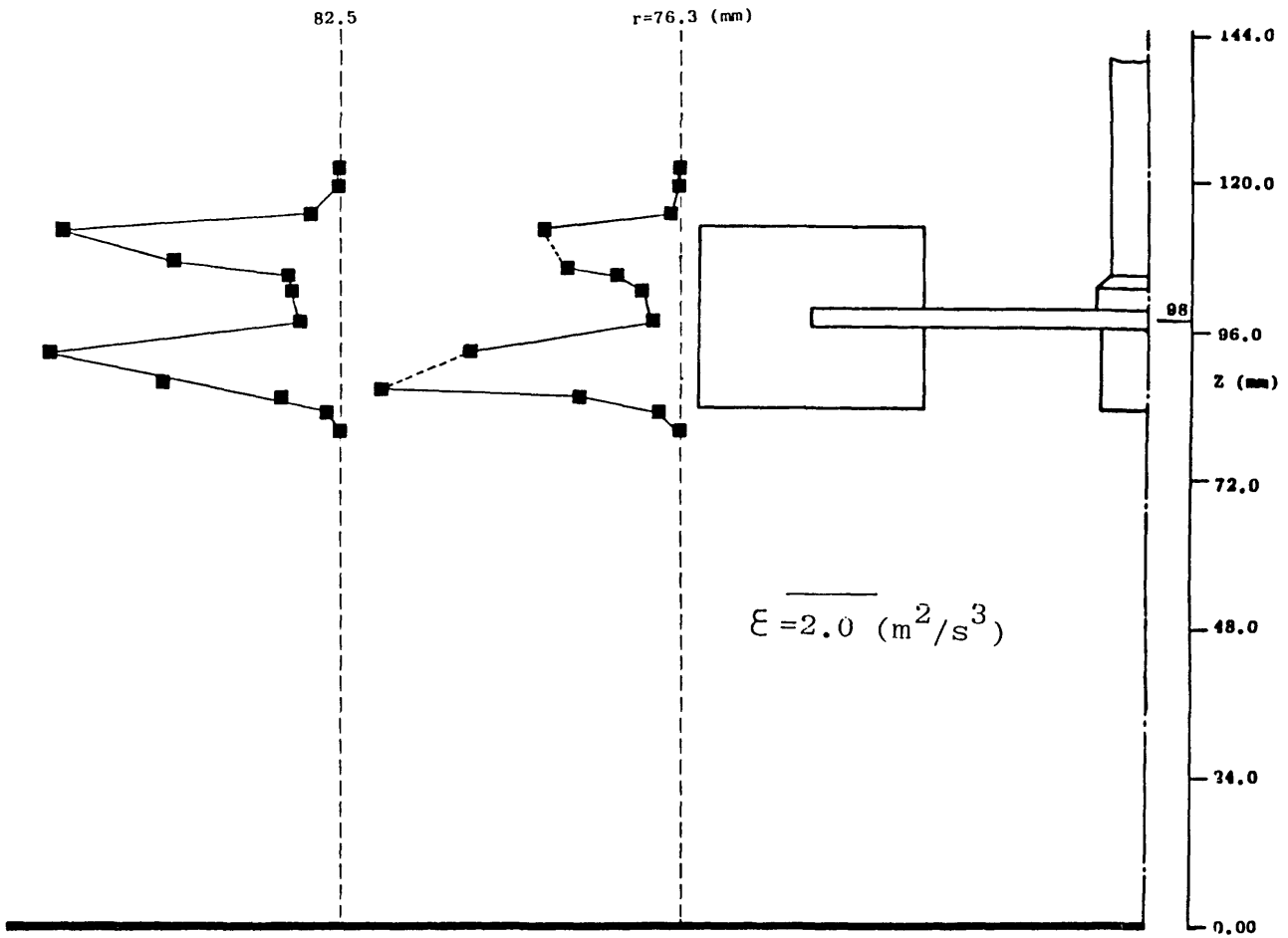

Fig 3.43 Profiles of the estimated rate of turbulence kinetic energy dissipation in the impeller stream for D=T/2, C=T/3, N=125 rpm and θ=0.0 °.

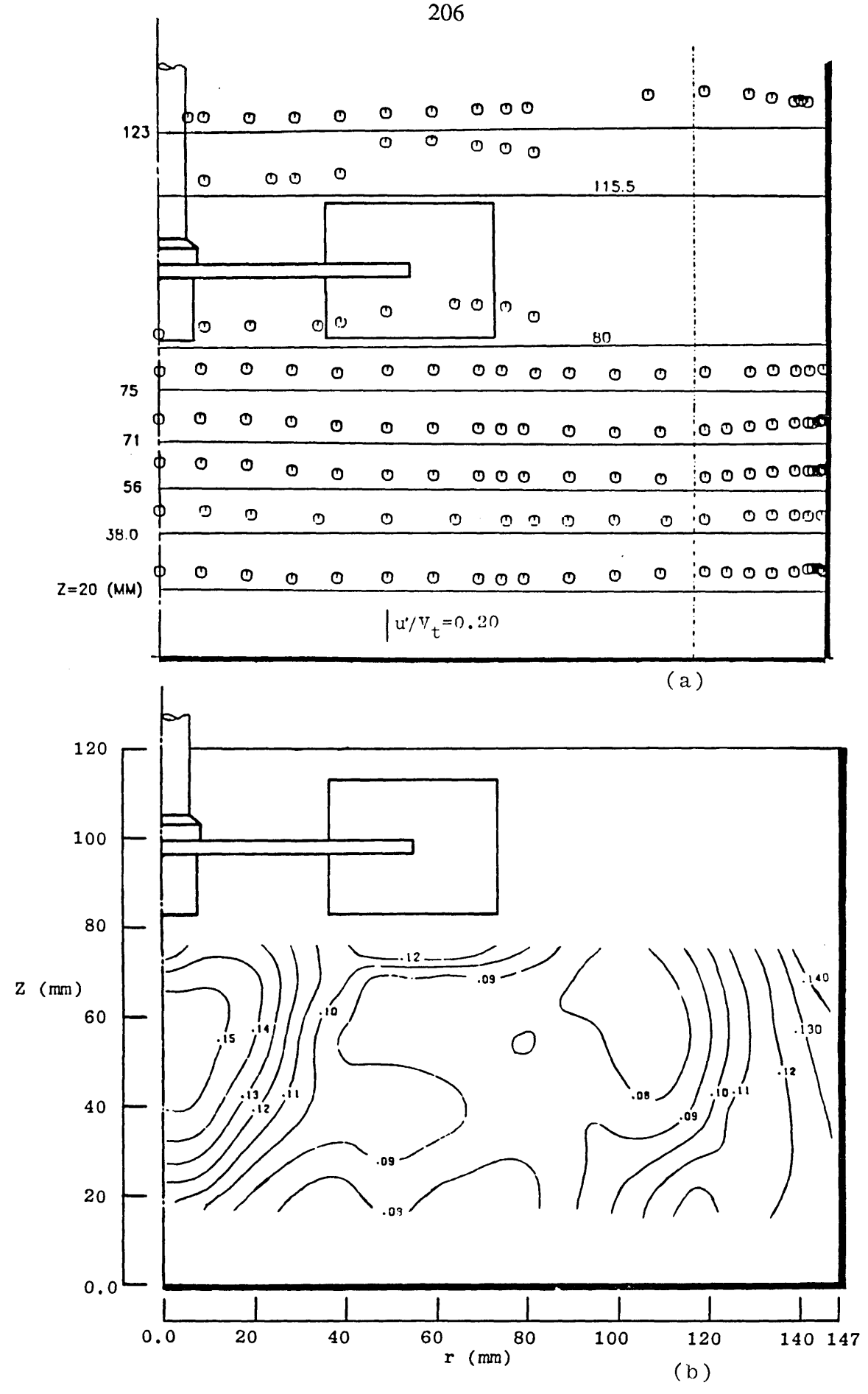

Fig 3.44 Axial rms velocity above and below the impeller for D=T/2, C=T/3, N=125 rpm and θ=0.0 °: (a) radial profiles and (b) contours (values in m/s).

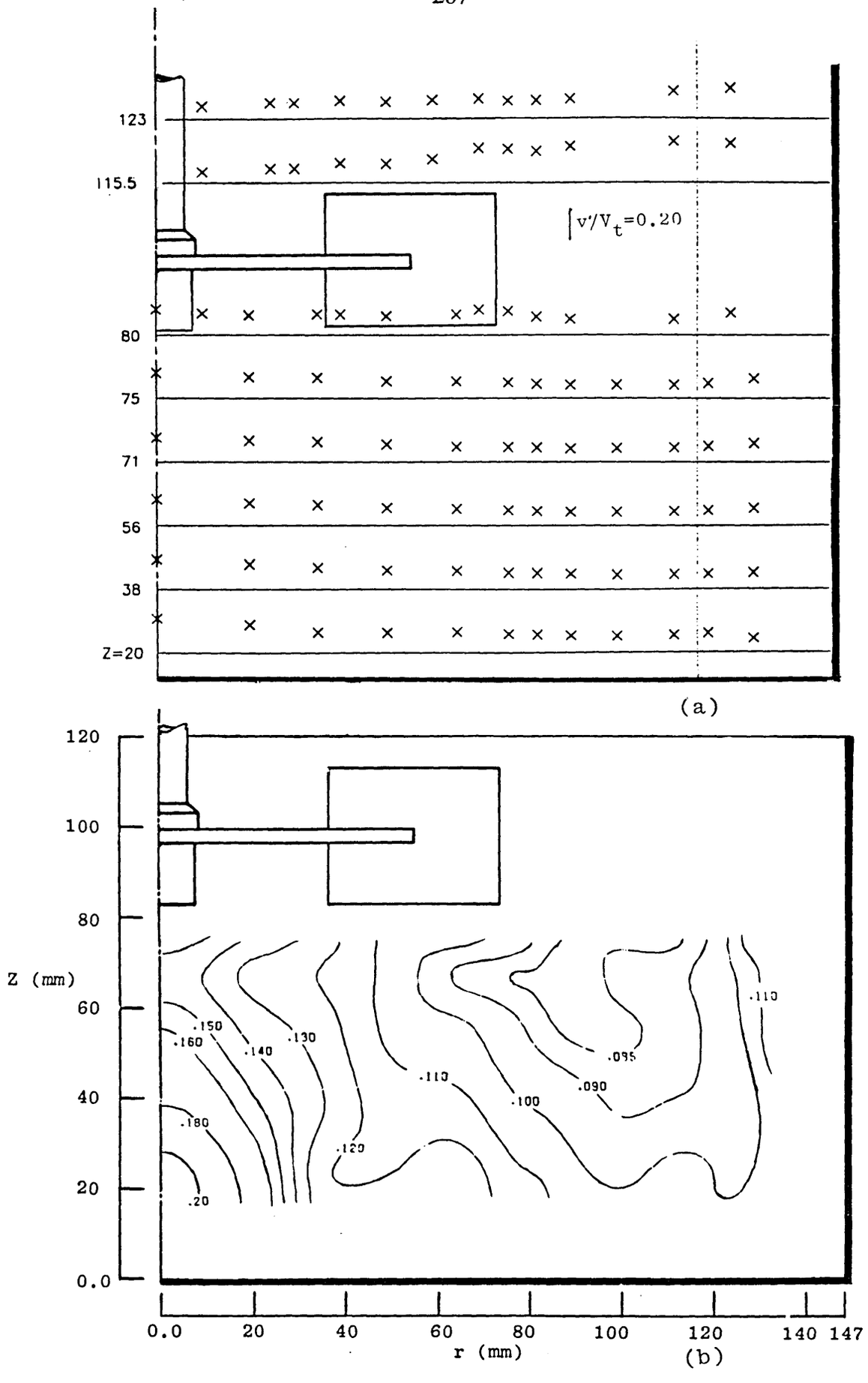

Fig 3.45 Radial rms velocity above and below the impeller for D=T/2, C=T/3, N=125 rpm and θ=0.0 °: (a) radial profiles and (b) contours (values in m/s).

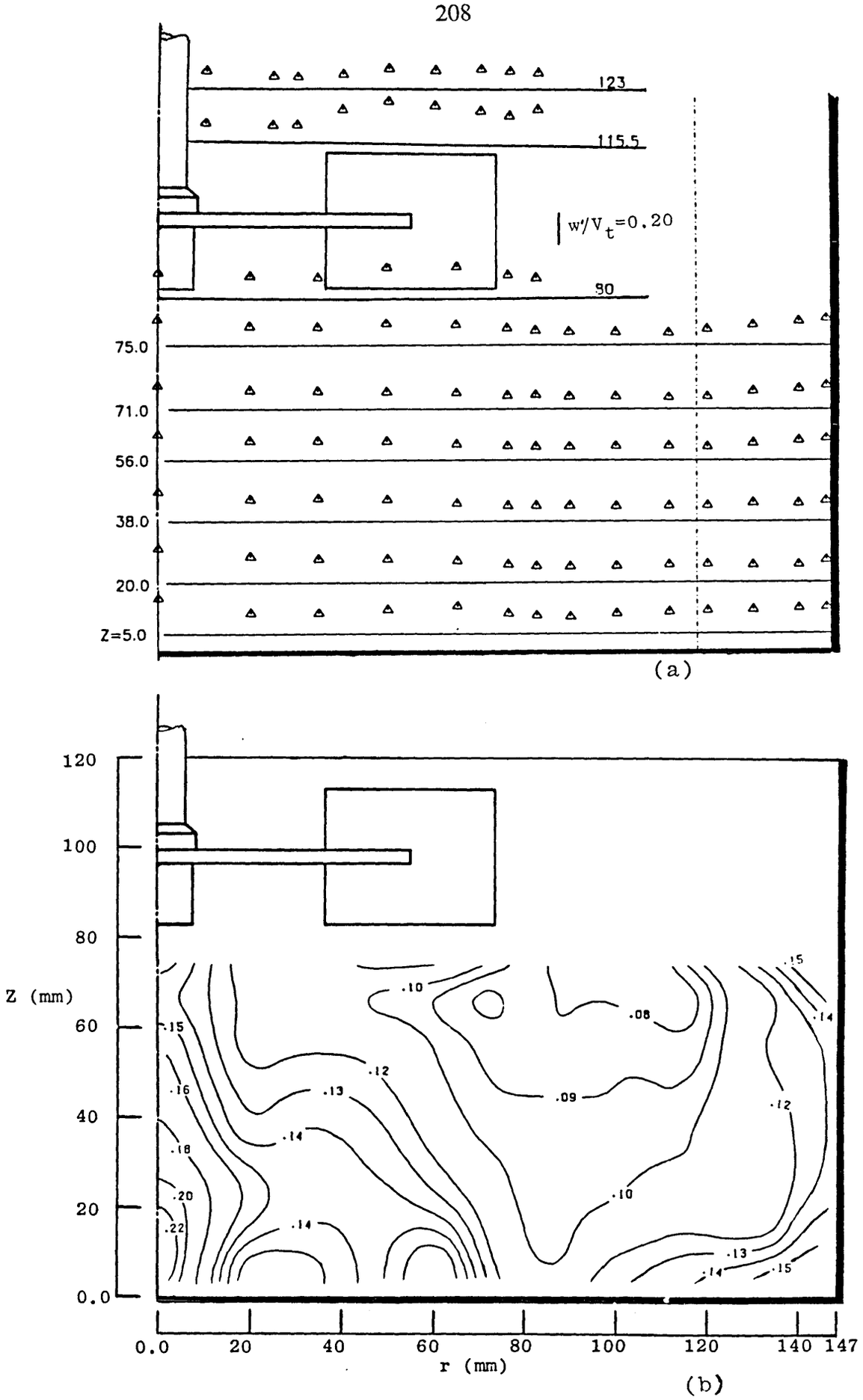

Fig 3.46 Tangential rms velocity above and below the impeller for D=T/2, C=T/3, N=125 rpm and θ=0.0 °: (a) radial profiles and (b) contours (values in m/s).

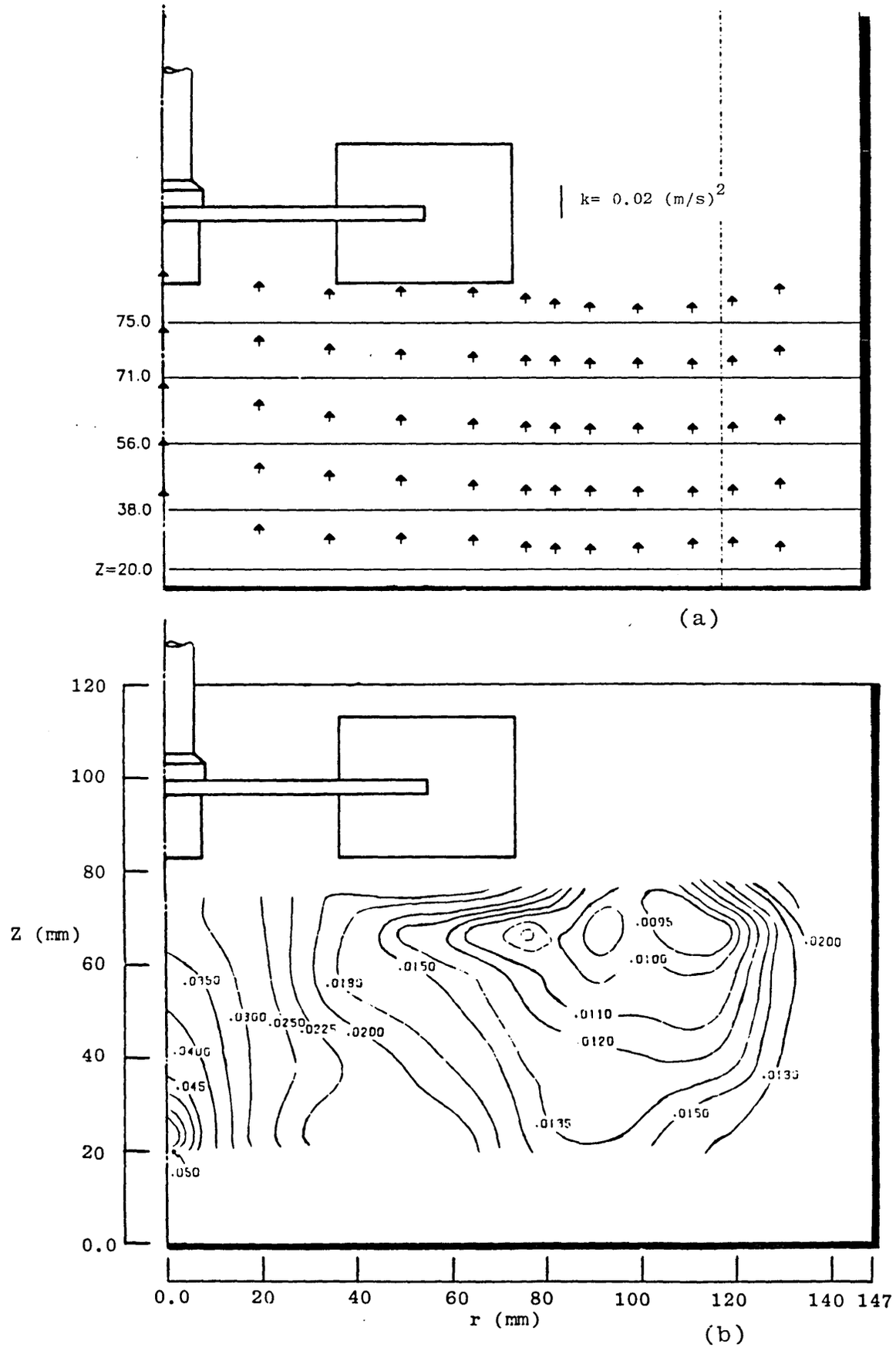

Fig 3.47 Turbulence kinetic energy below the impeller for D=T/2, C=T/3, N=125 rpm and θ=0.0 °: (a) radial profiles and (b) contours (values in $(m/s)^2$).

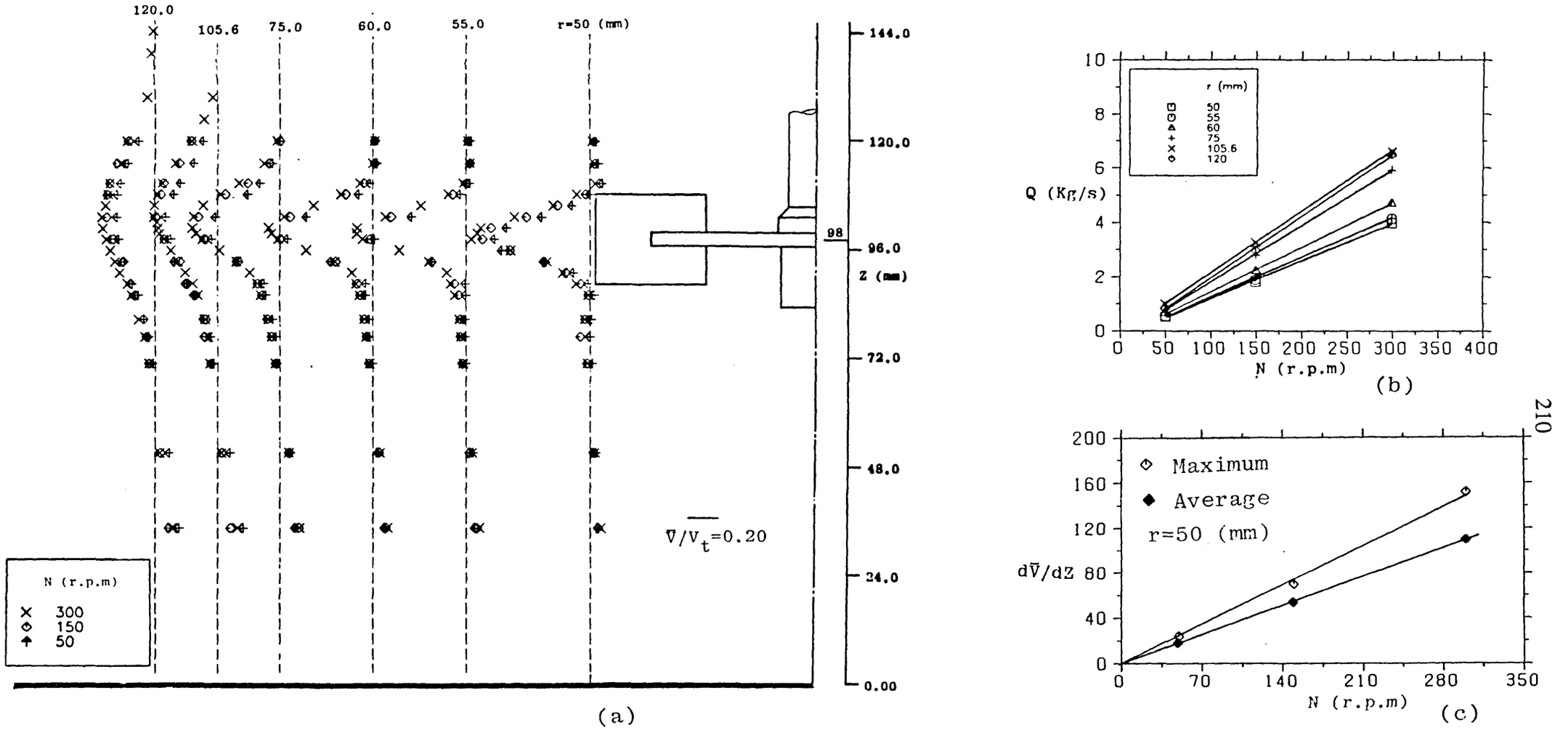

Fig 3.48 Effect of impeller rotational speed on the flow in the impeller stream for D=C=T/3 and θ=0.0 °: (a) radial mean velocities; (b) radial mass flow and (c) shear rate at the tip of the impeller.

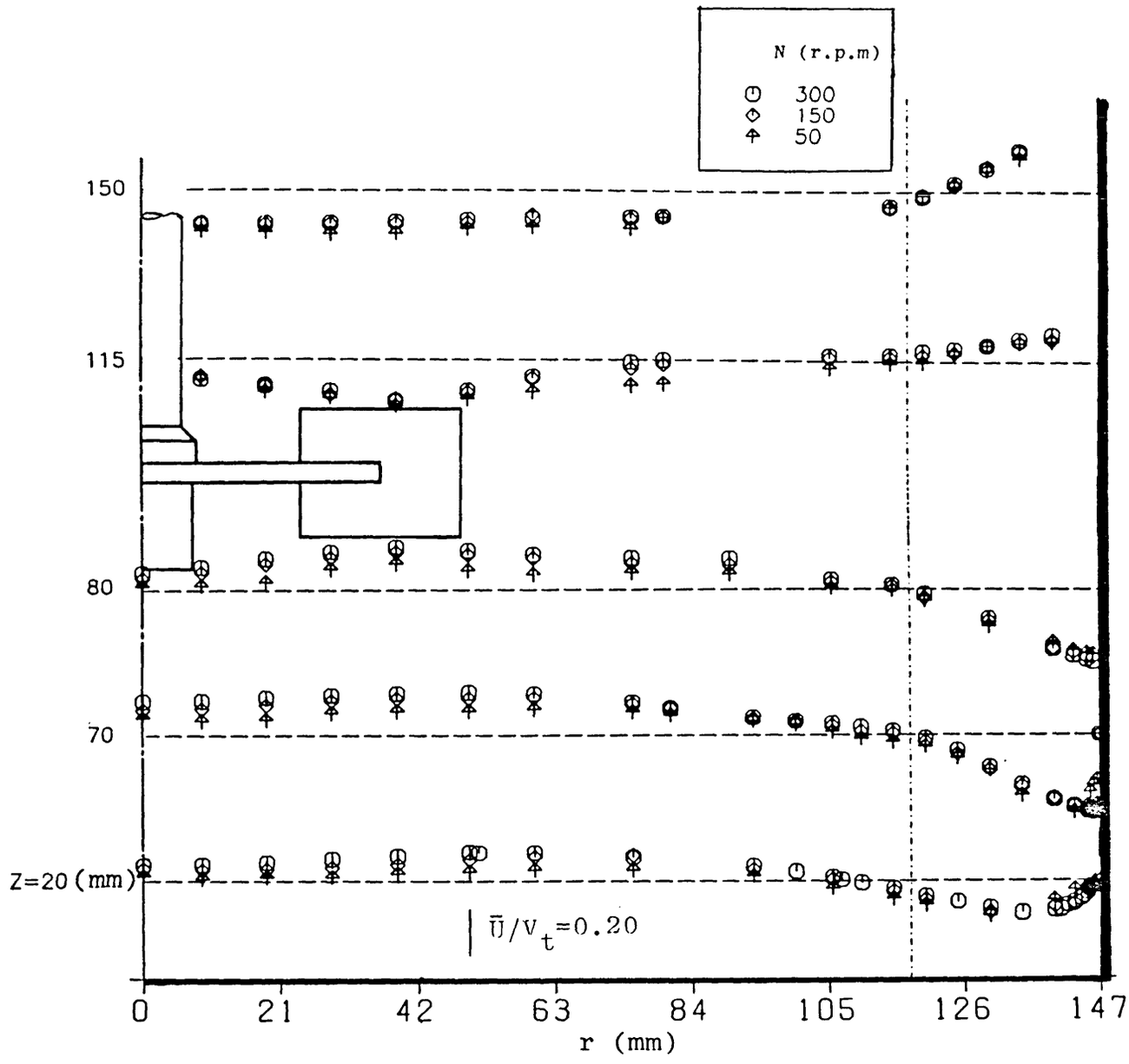

Fig 3.49 Effect of impeller rotational speed on axial flow above and below the impeller for D=C=T/3 and θ=0.0 °.

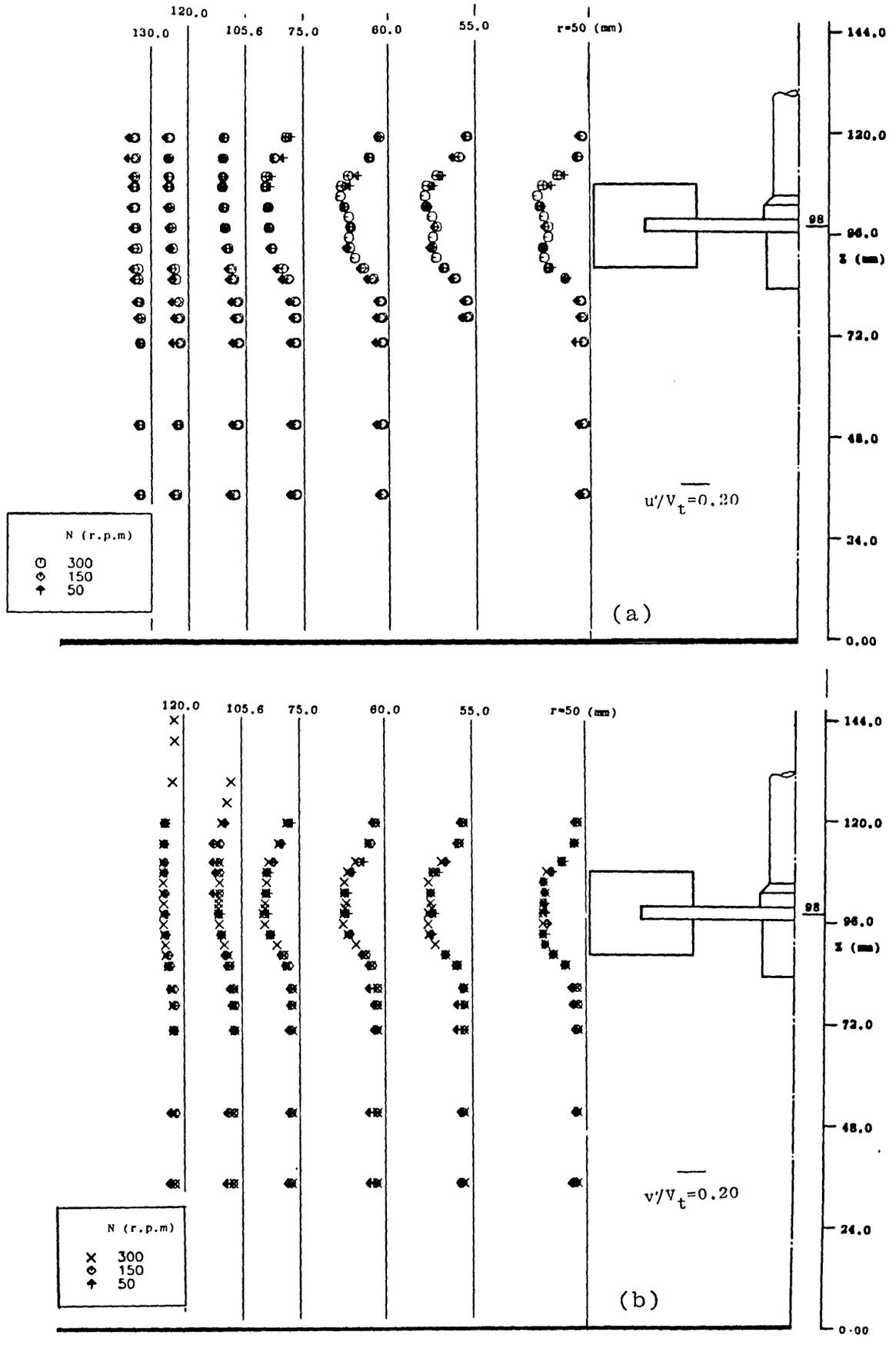

Fig 3.50 Effect of impeller rotational speed on rms velocities in the impeller stream for D=C=T/3 and θ=0.0 °: (a) u' component and (b) v' component.

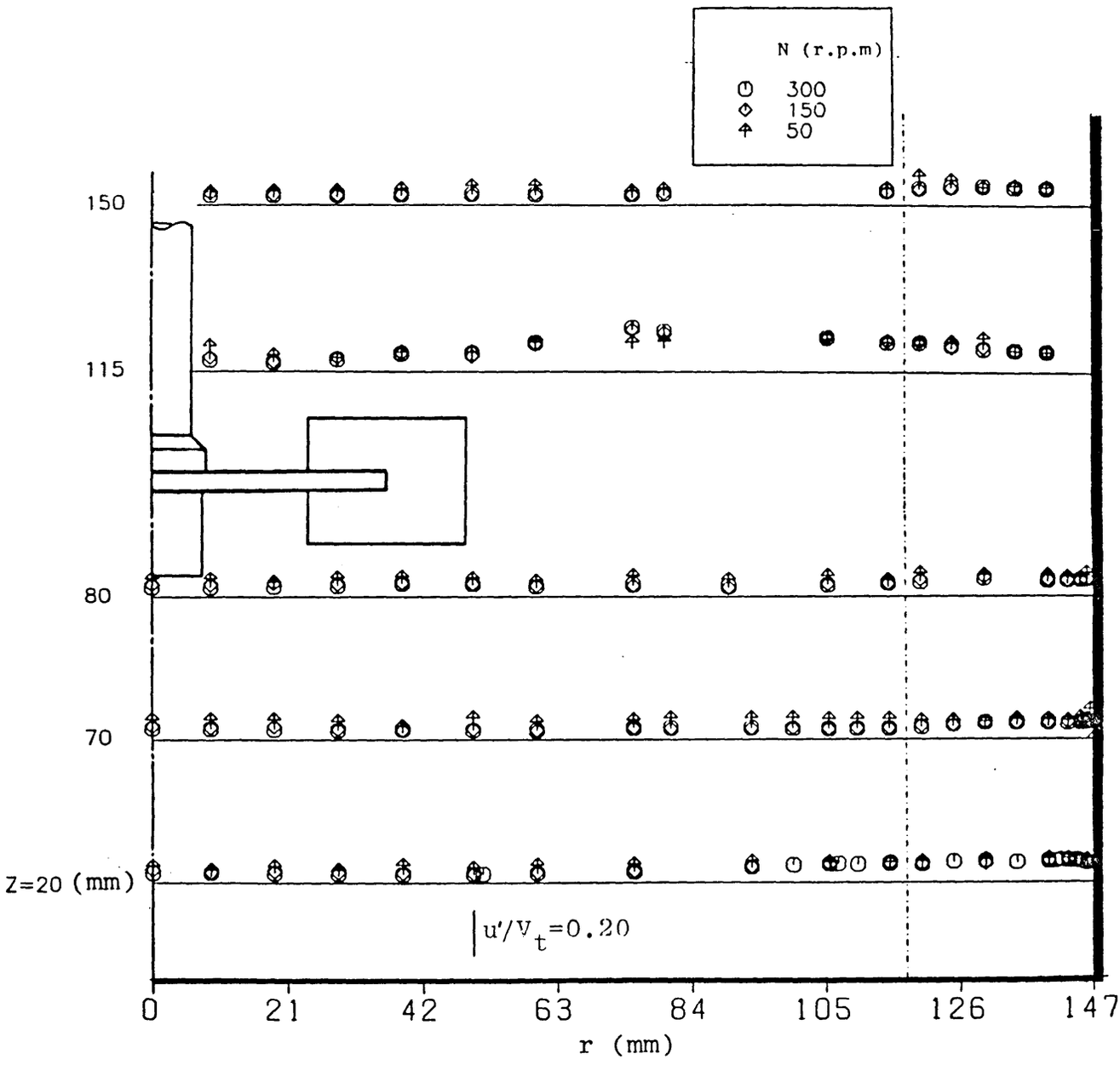

Fig 3.51 Effect of impeller rotational speed on axial rms velocities above and below the impeller for D=C=T/3 and θ=0.0 °.

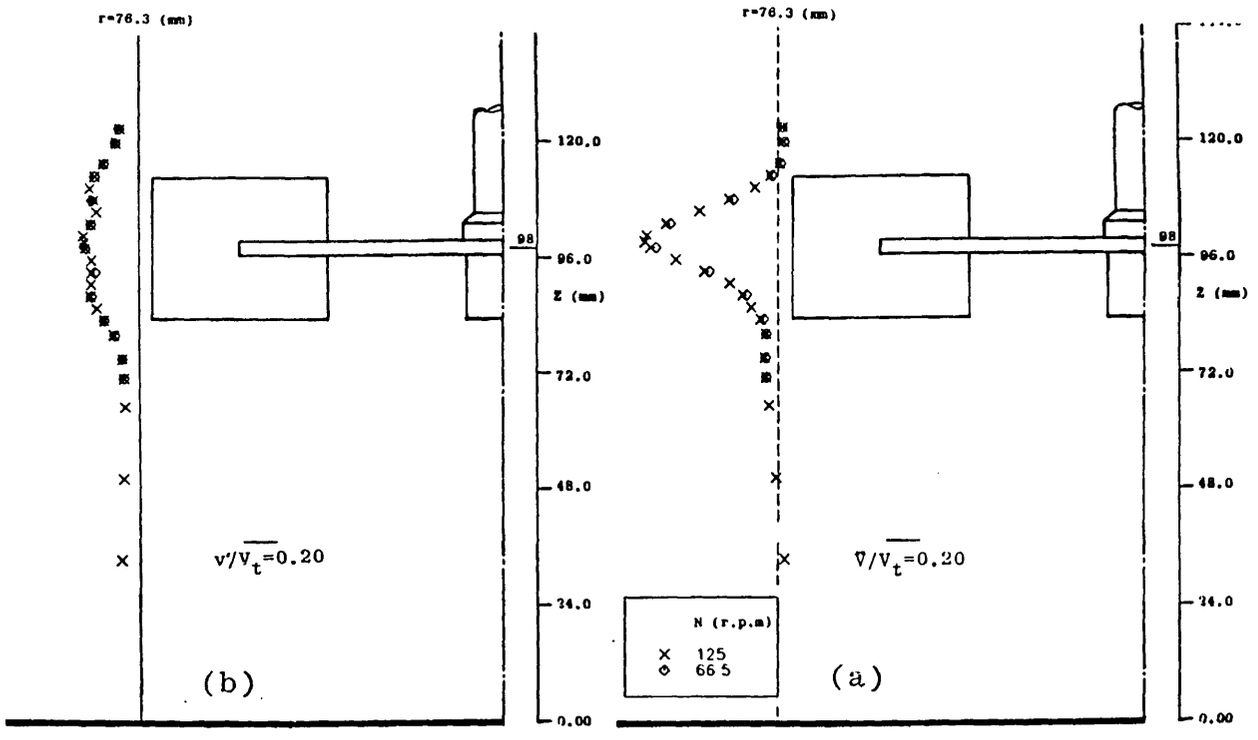

Fig 3.52 Effect of impeller rotational speed on the radial velocities at the impeller stream for D=T/2, C=T/3 and θ=0.0 °: (a) mean and(b) rms velocities.

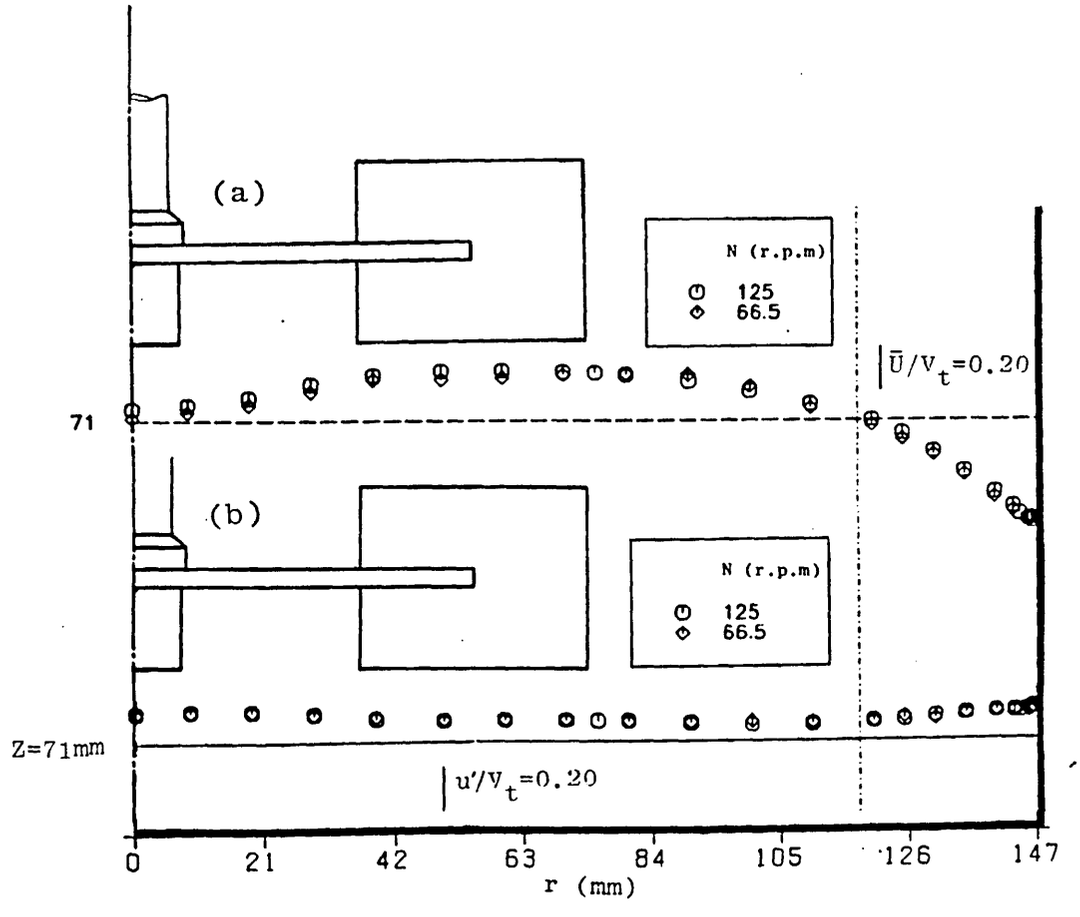

Fig 3.53 Effect of impeller rotational speed on the axial velocity above and below the impeller for D=T/2, C=T/3 and θ=0.0 °: (a) mean and (b) rms velocities.

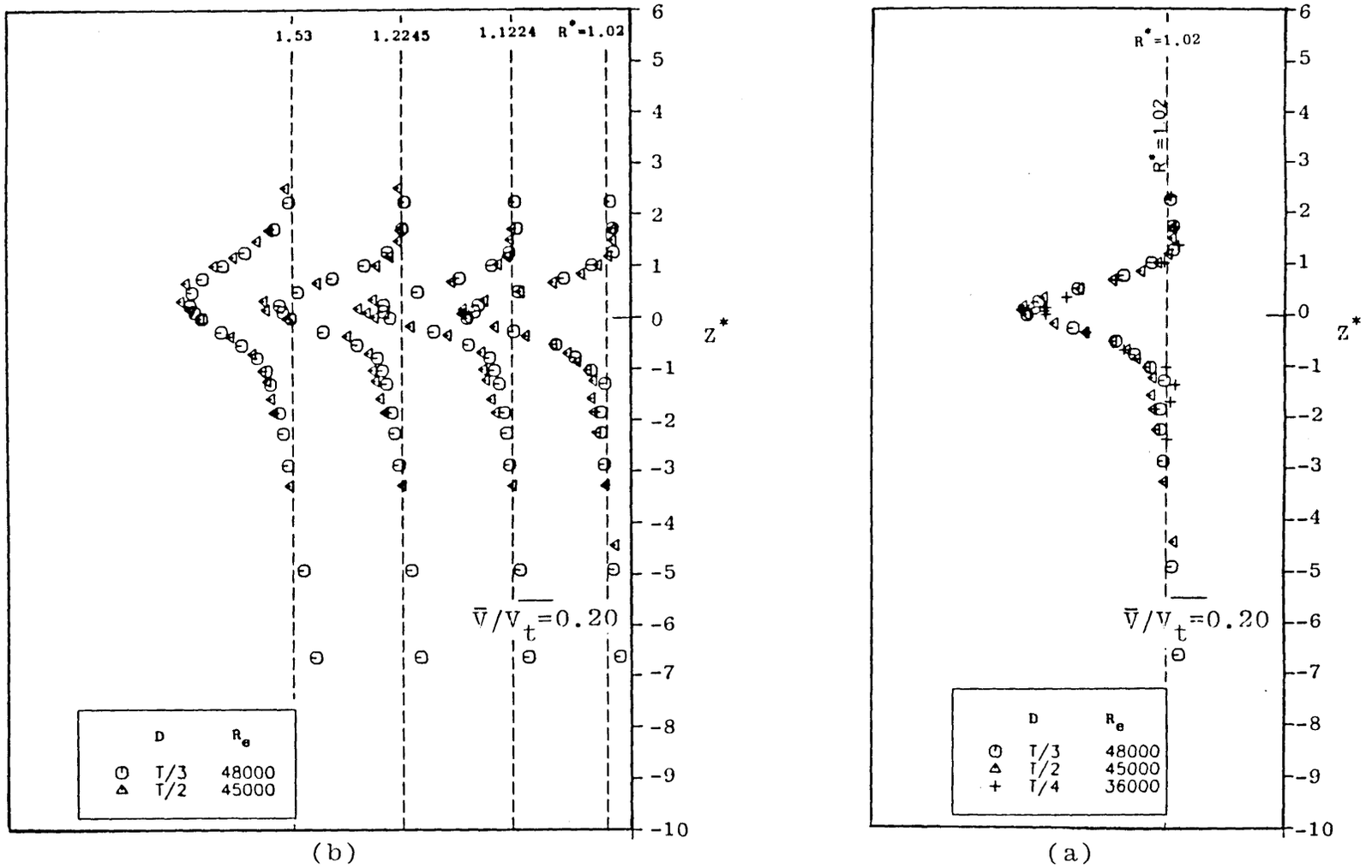

Fig 3.54 Effect of impeller size on the radial mean velocities in the impeller stream for C=T/3 and θ=0.0 °: (a) three impeller sizes and (b) two impeller sizes.

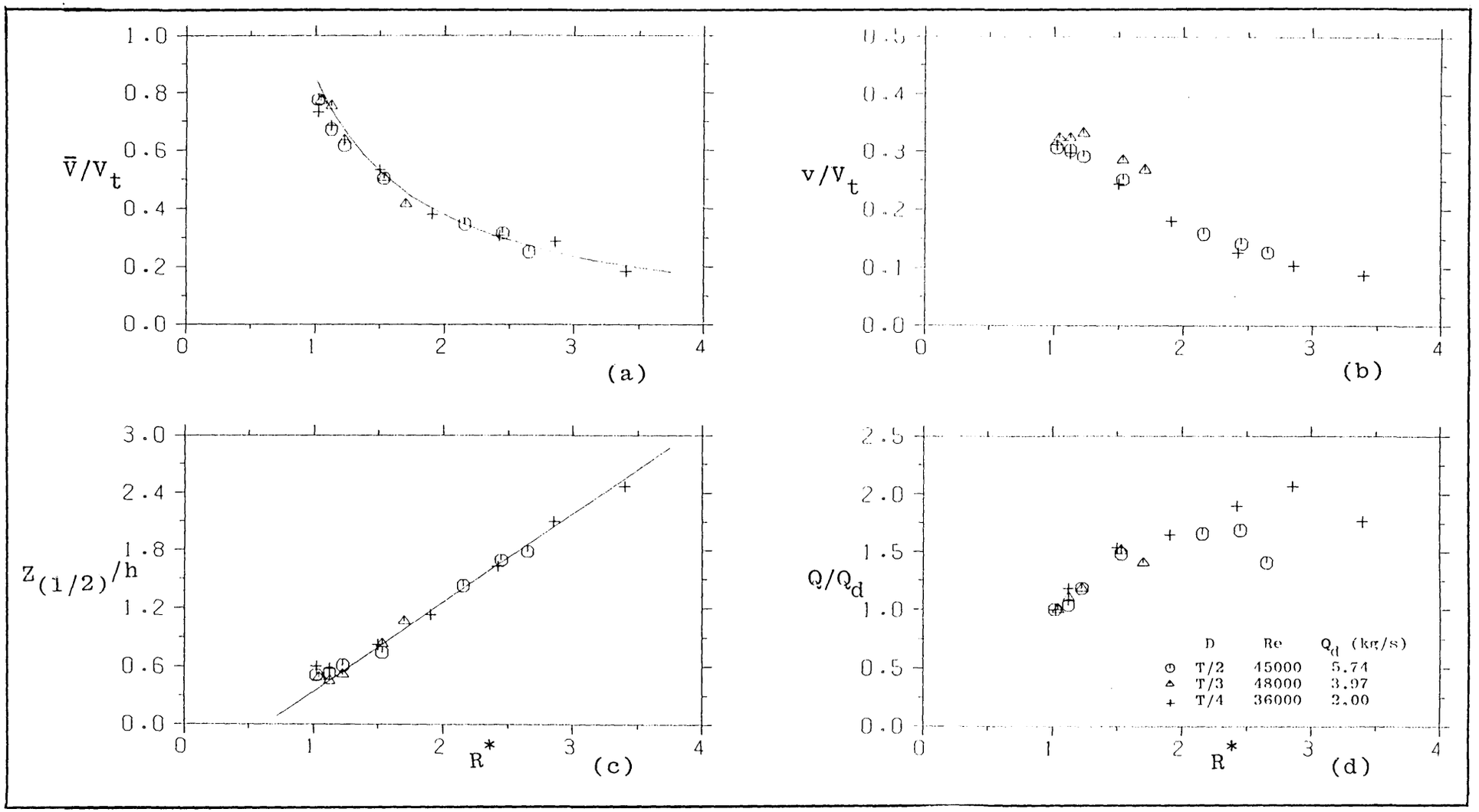

Fig 3.55 Effect of impeller size on the radial jet stream characteristics for C=T/3 and θ=0 °: (a) centreline mean velocity decay; (b)centreline rms velocity decay; (c) spread of the jet stream and (d) pumping capacity.

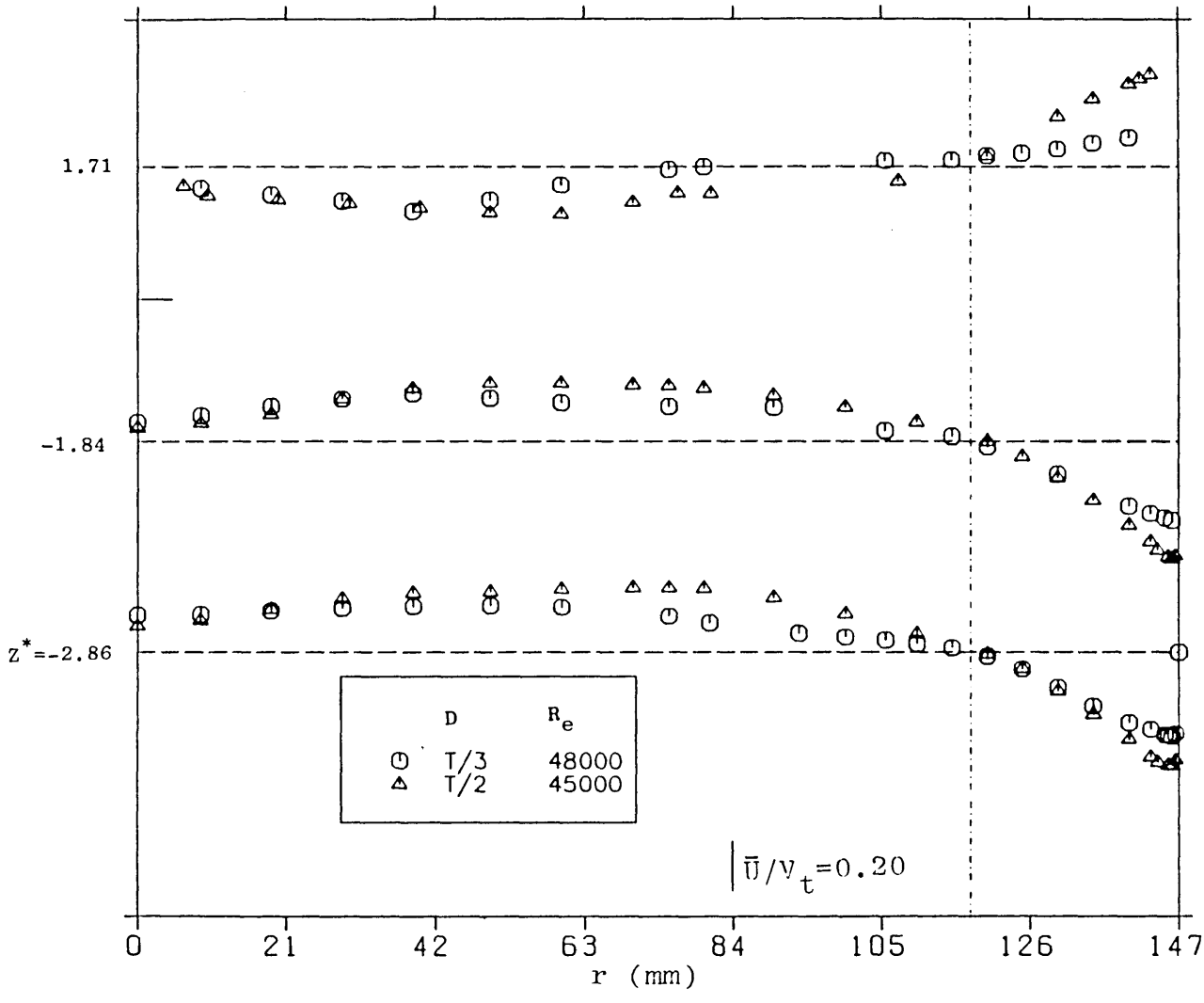

Fig 3.56 Effect of impeller size on axial mean velocity above and below the impeller for C=T/3 and θ=0.0 °.

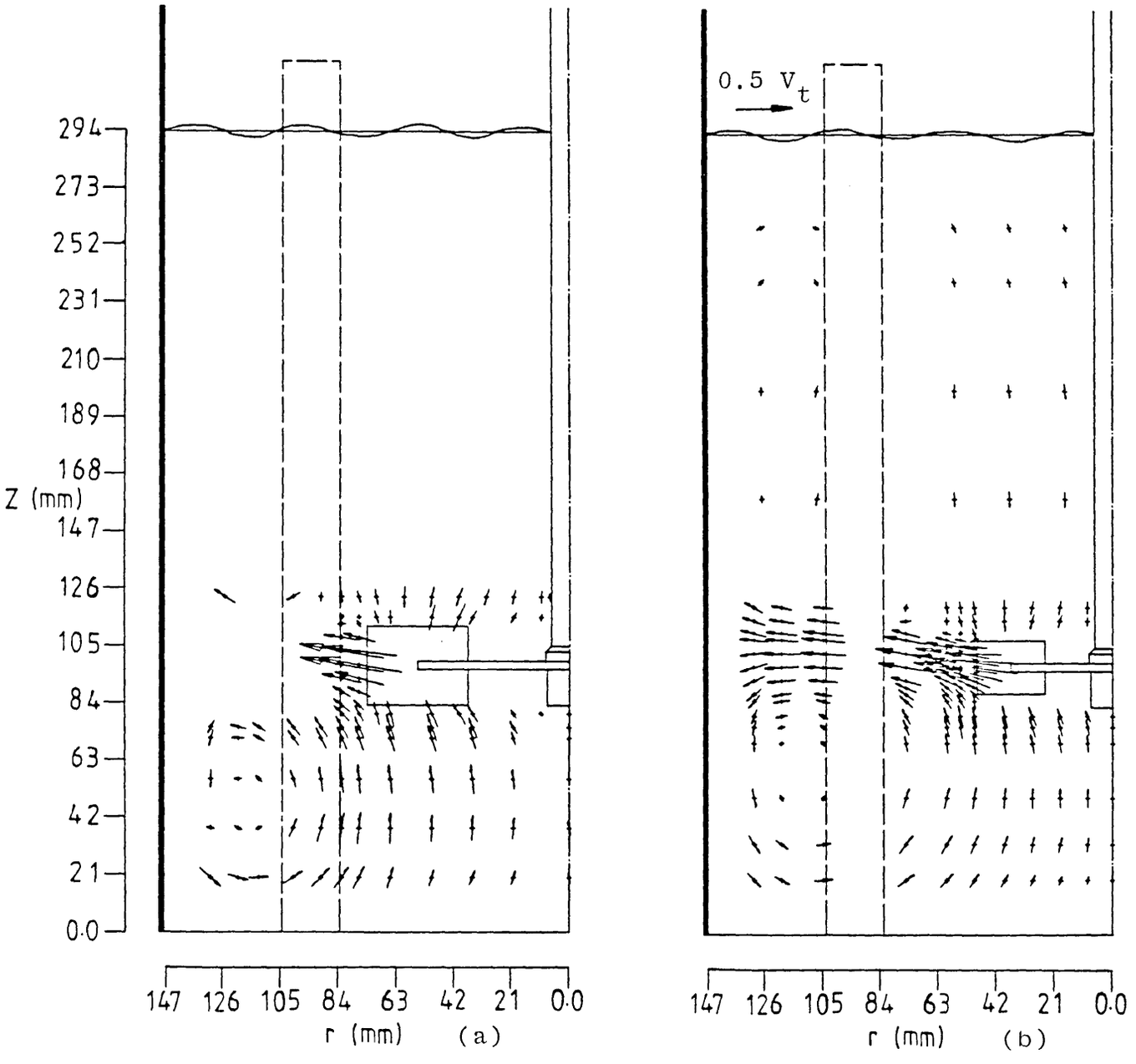

Fig 3.57 Effect of impeller size on the velocities in r-Z plane for C=T/3 and θ=0.0 °: (a) D=T/2 and Re=45,000 and (b) D=T/3 and Re=48,000.

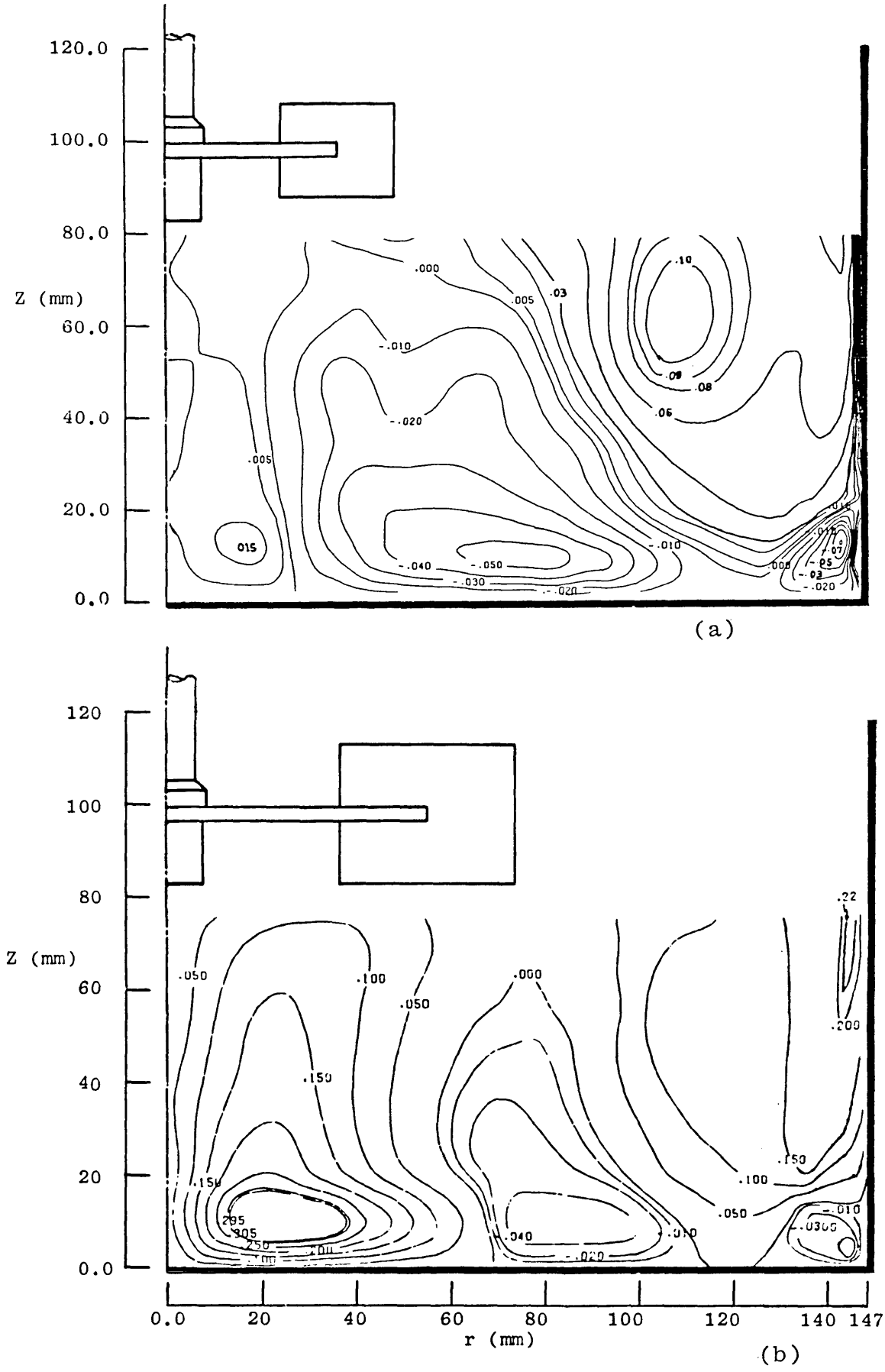

Fig 3.58 Effect of impeller size on tangential mean velocity below the impeller for C=T/3 and θ=0.0 °: (a) D=T/3 and Re=48,000 and (b) D=T/2 and Re=45,000.

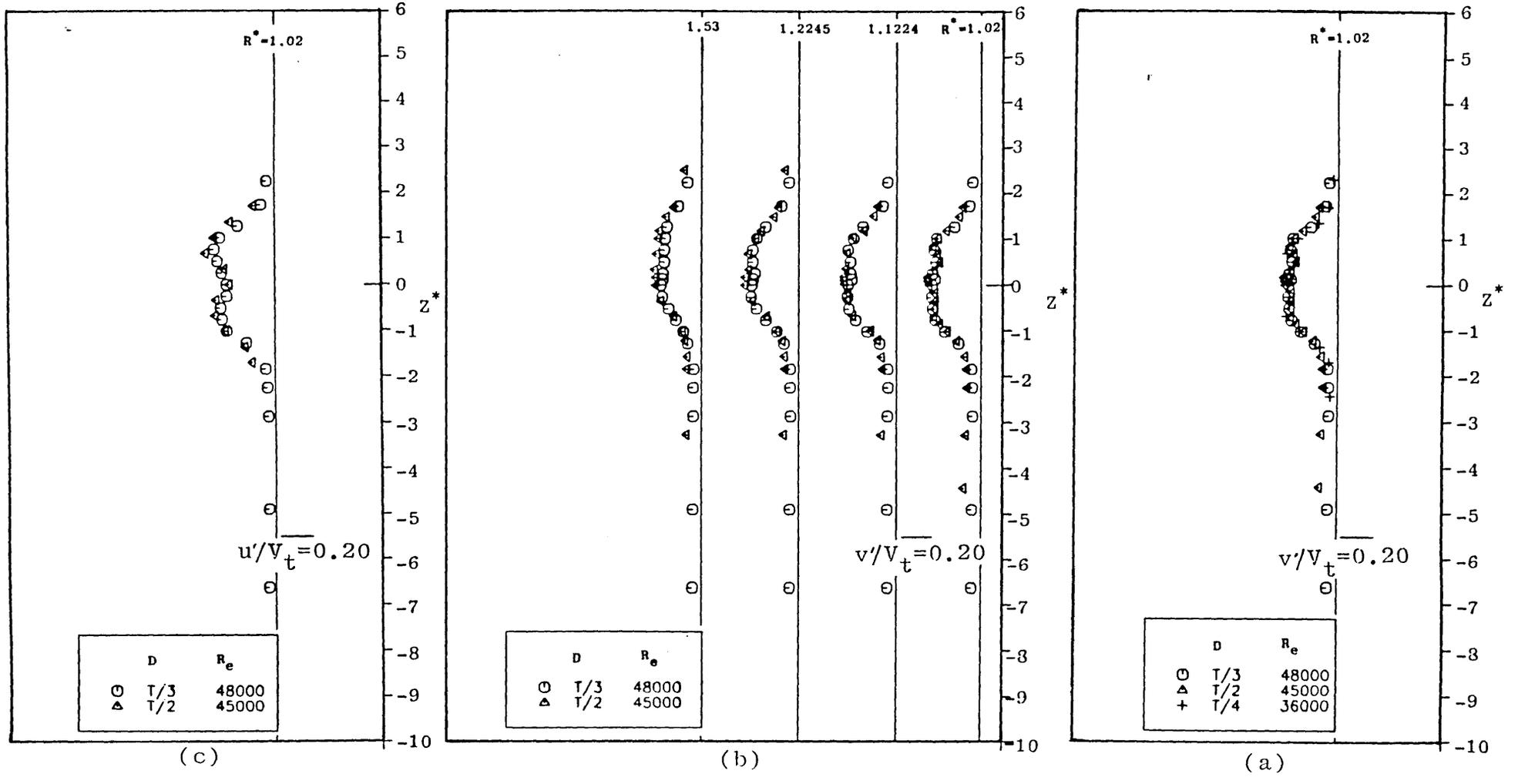

Fig 3.59 Effect of impeller size on the rms velocities in the impeller stream for C=T/3 and θ=0.0 °: (a) radial for three impeller sizes; (b) radial for two impeller sizes and (c) axial for two impeller sizes.

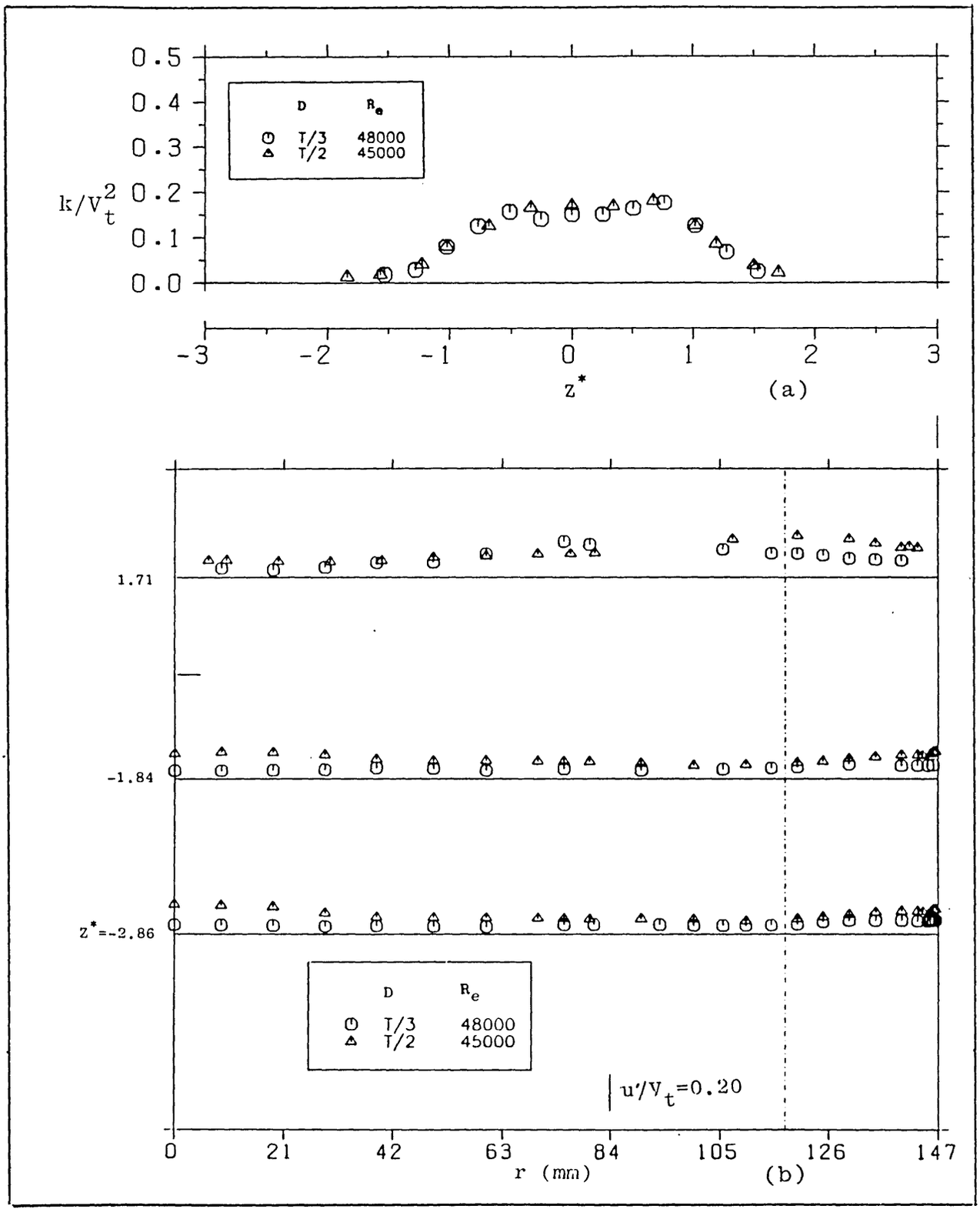

Fig 3.60 Effect of impeller size on: (a) k at the impeller tip and (b) axial rms velocities above and below the impeller; for C=T/3 and θ=0.0 °.

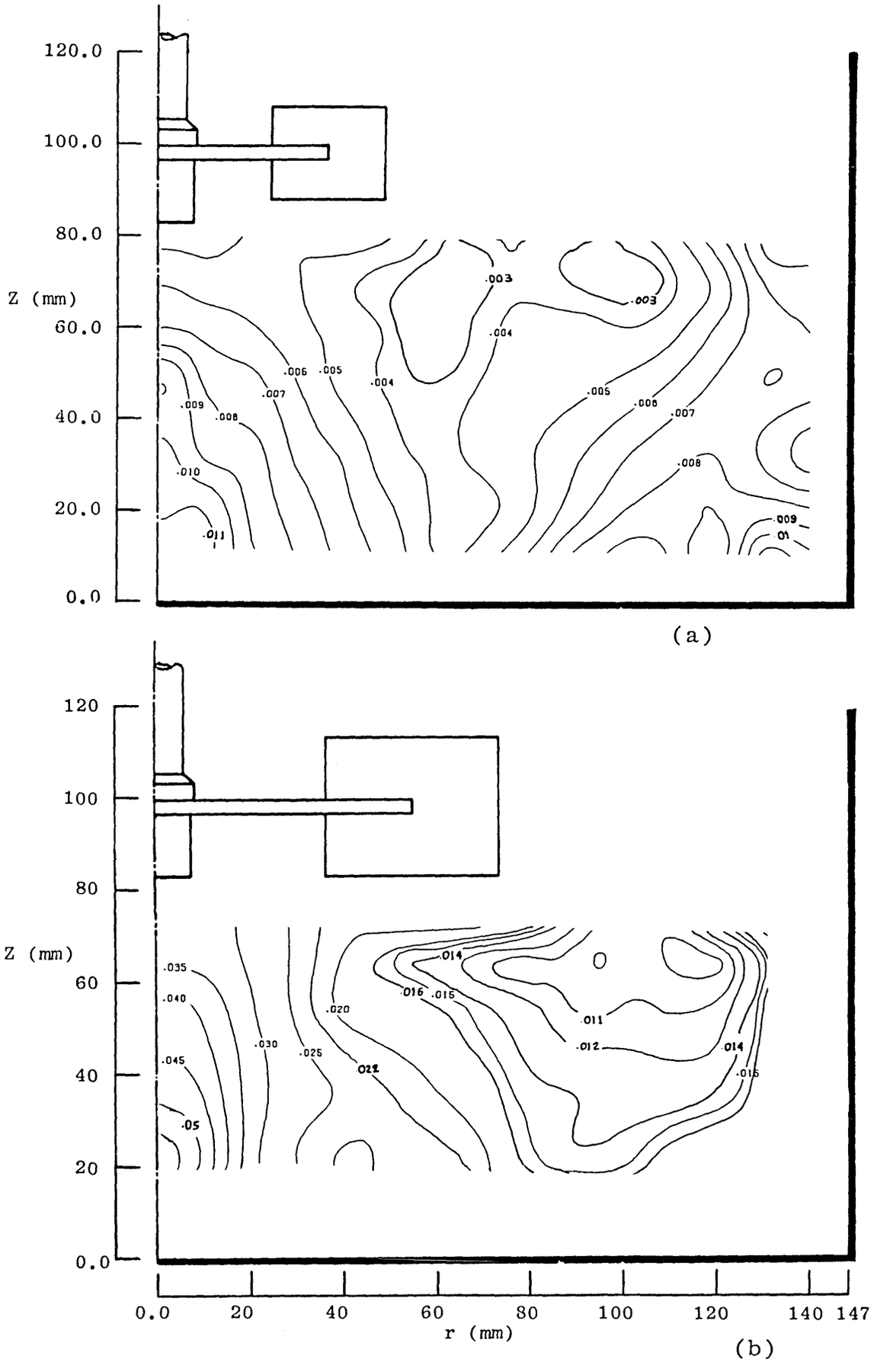

Fig 3.61 Effect of impeller size on the turbulence kinetic energy below the impeller for C=T/3 and θ=0.0 °: (a) D=T/3 and Re=48,000 and (b) D=T/2 and Re=45,000; (contour values shown are nomalised with V_t^2).

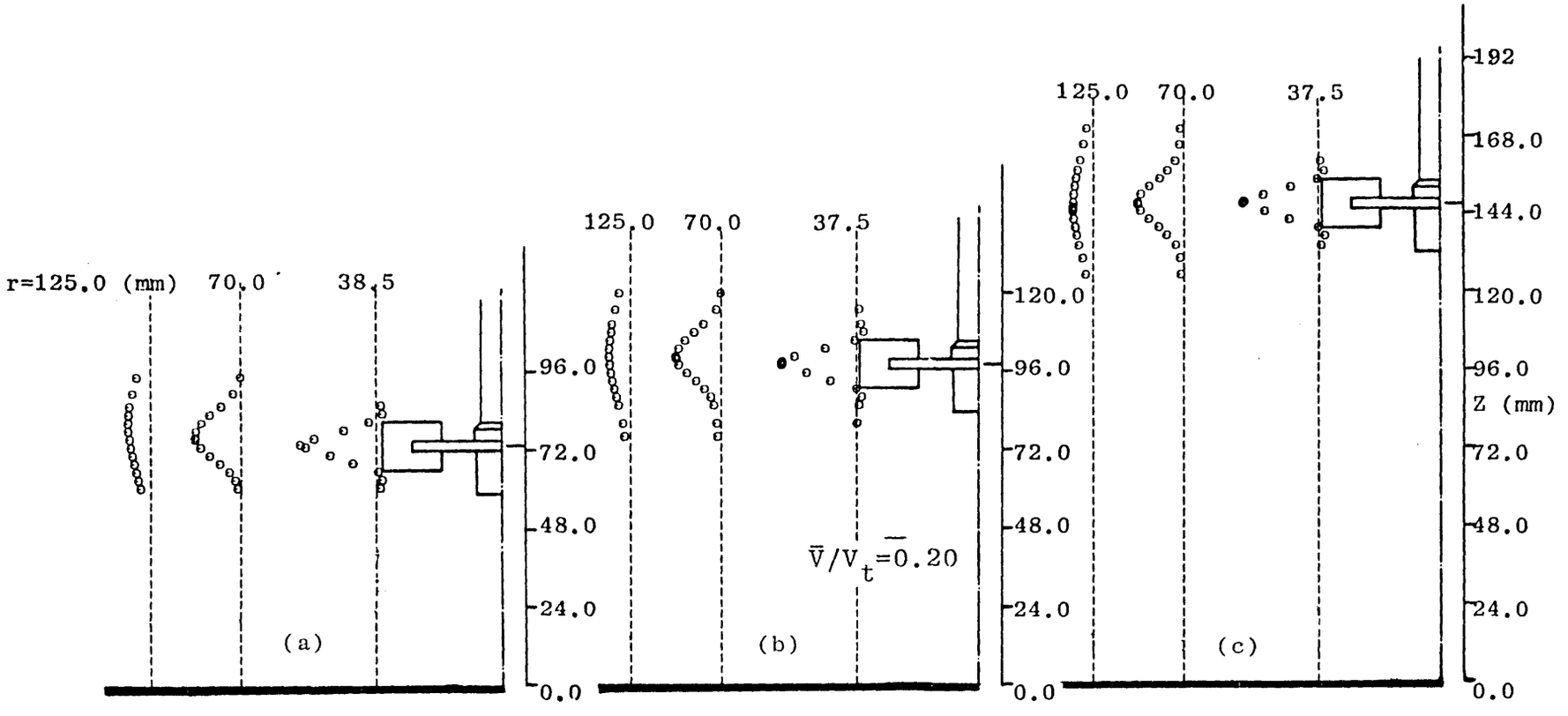

Fig 3.62 Effect of impeller clearance on radial mean velocities in the impeller stream for D=T/4 and θ=0.0 °: (a) C=T/4; (b) C=T/3 and (c) C=T/2.

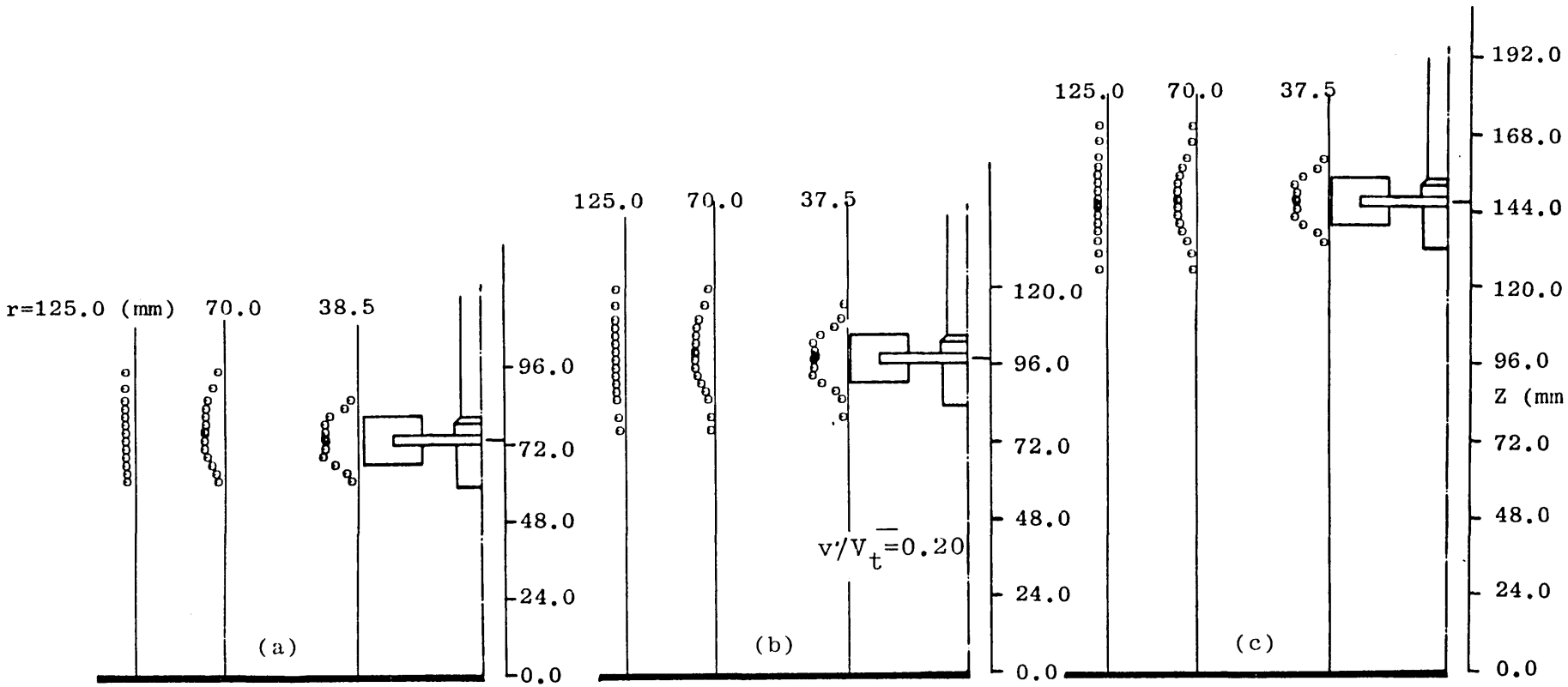

Fig 3.63 Effect of impeller clearance on radial rms velocities in the impeller stream for D=T/4 and θ=0.0 °: (a) C=T/4; (b) C=T/3 and (c) C=T/2.

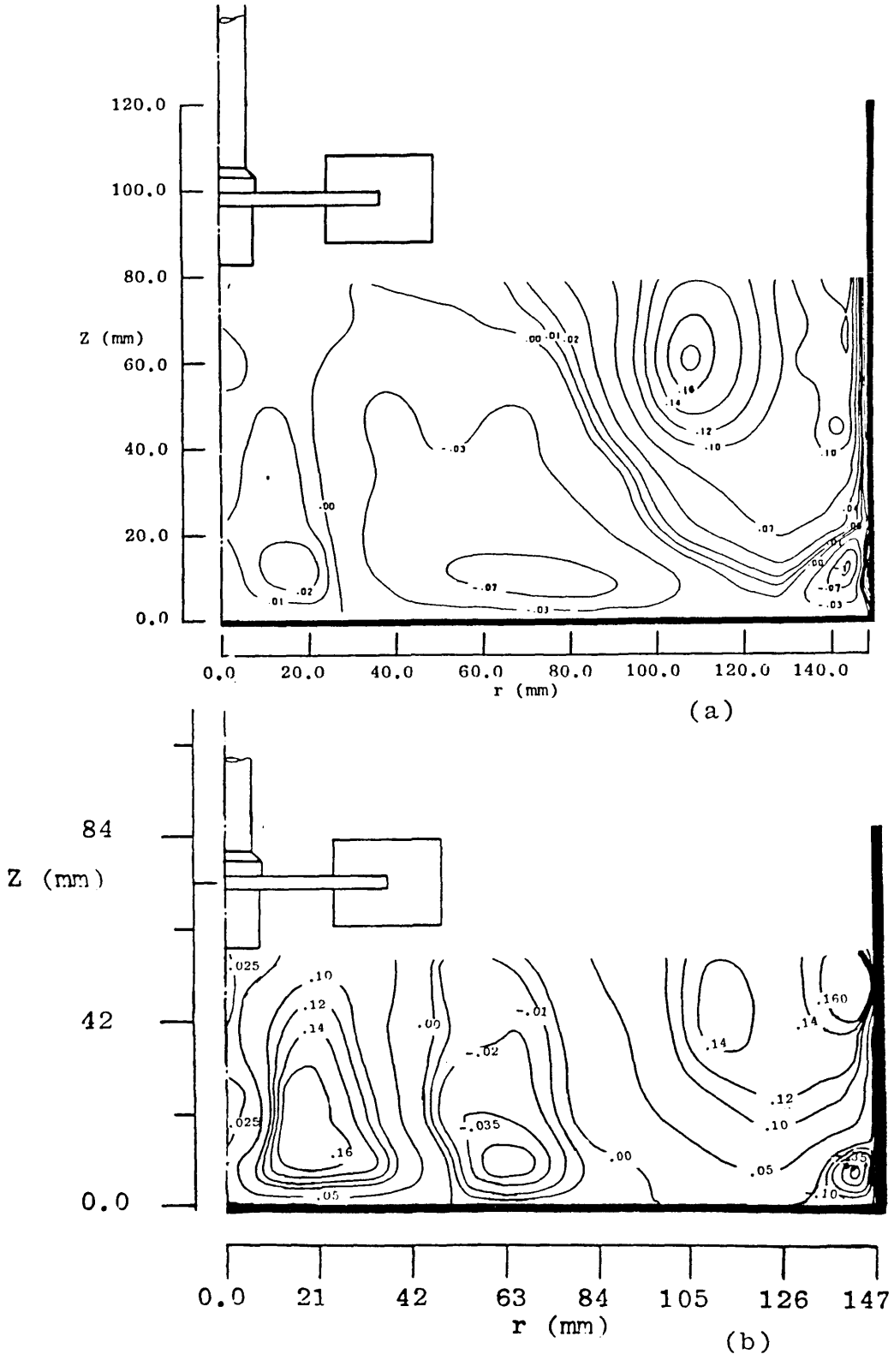

Fig 3.64 Effect of impeller clearance on the tangential mean velocity below the impeller for D=T/3 and θ=0 °: (a) C=T/3 and (b) C=T/4; (contour values shown was normalised with tip velocity).

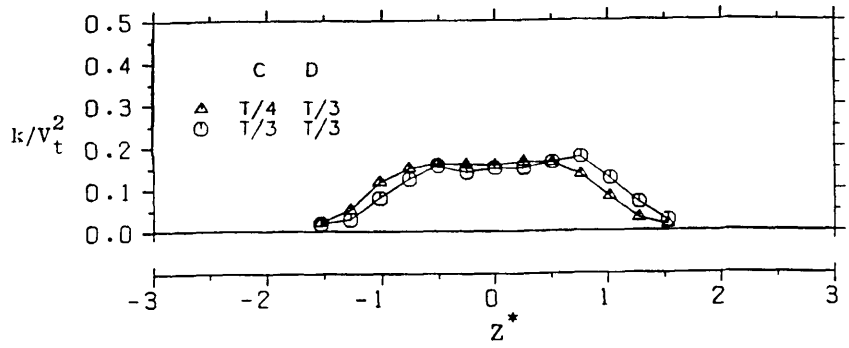

Fig 3.65 Effect of impeller clearance on the turbulence kinetic energy at the impeller tip for D=T/3 and θ=0.0 °; (contour values shown was normalised with V_t^2).

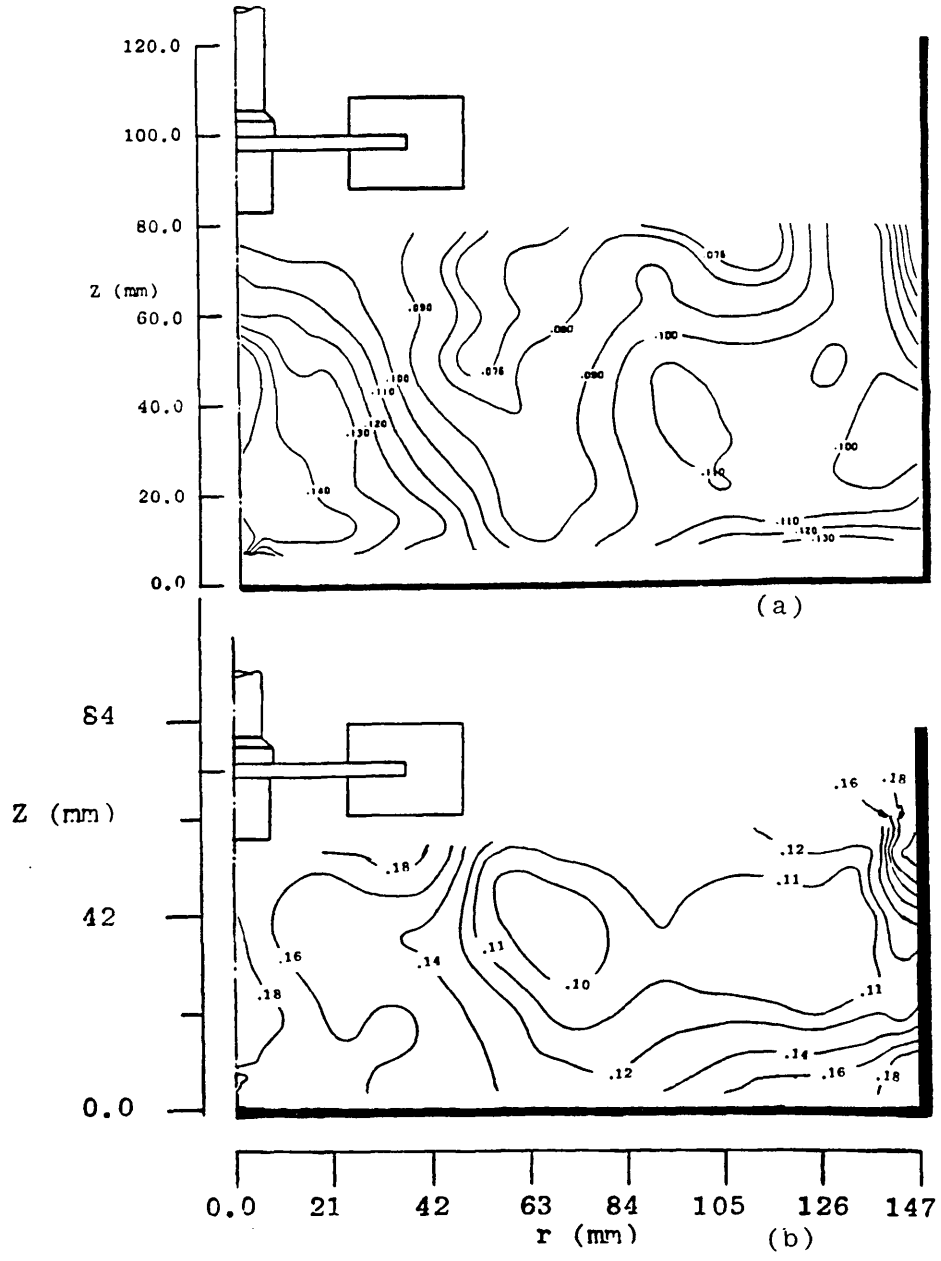

Fig 3.66 Effect of impeller clearance on the tangential rms velocities below the impeller for D=T/3 and θ=0.0 °: (a) C=T/3 and (b) C=T/4.

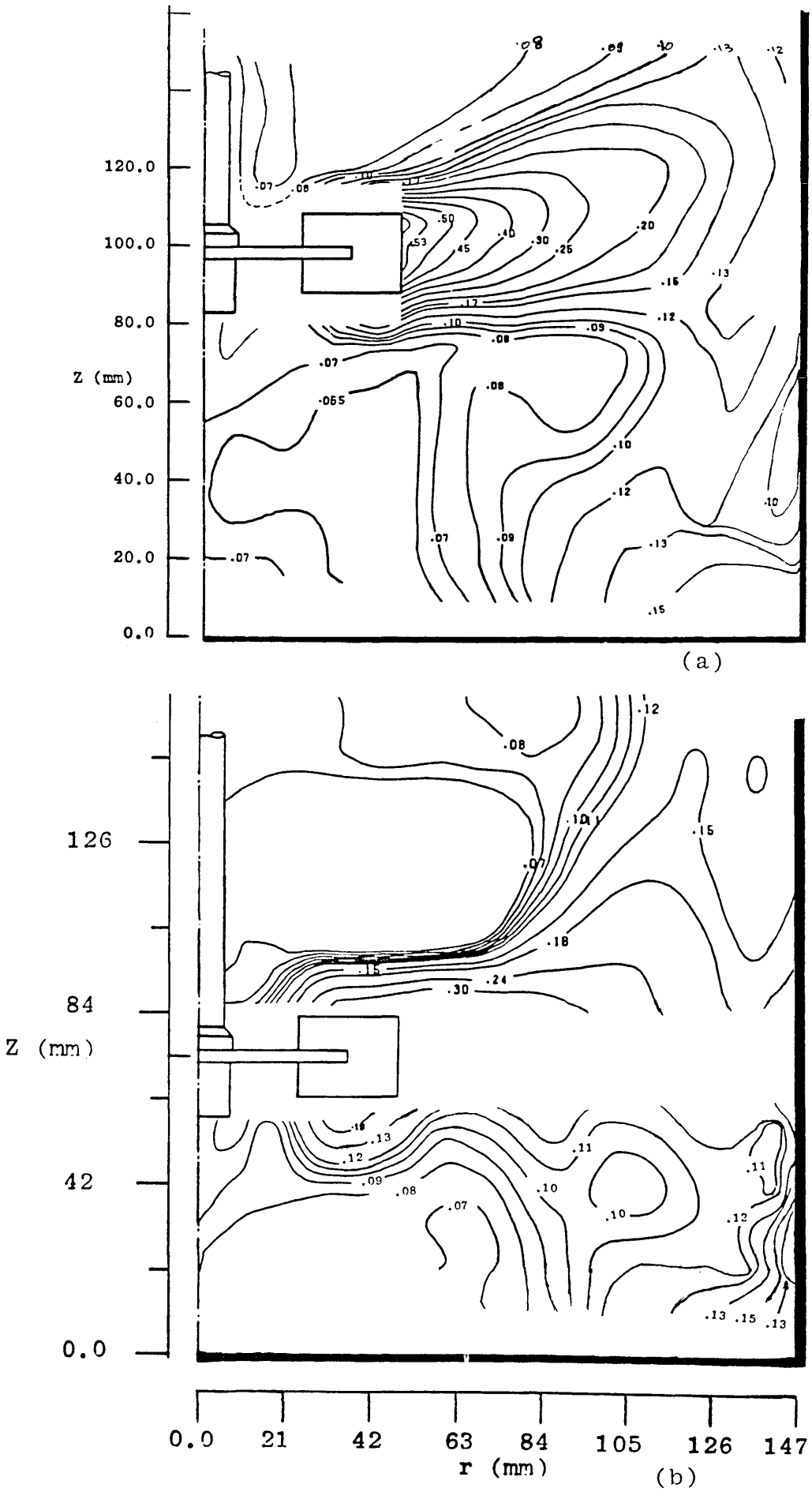

Fig 3.67 Effect of impeller clearance on axial rms velocities above and below the impeller for D=T/3 and θ=0.0°: (a) C=T/3 and (b) C=T/4.

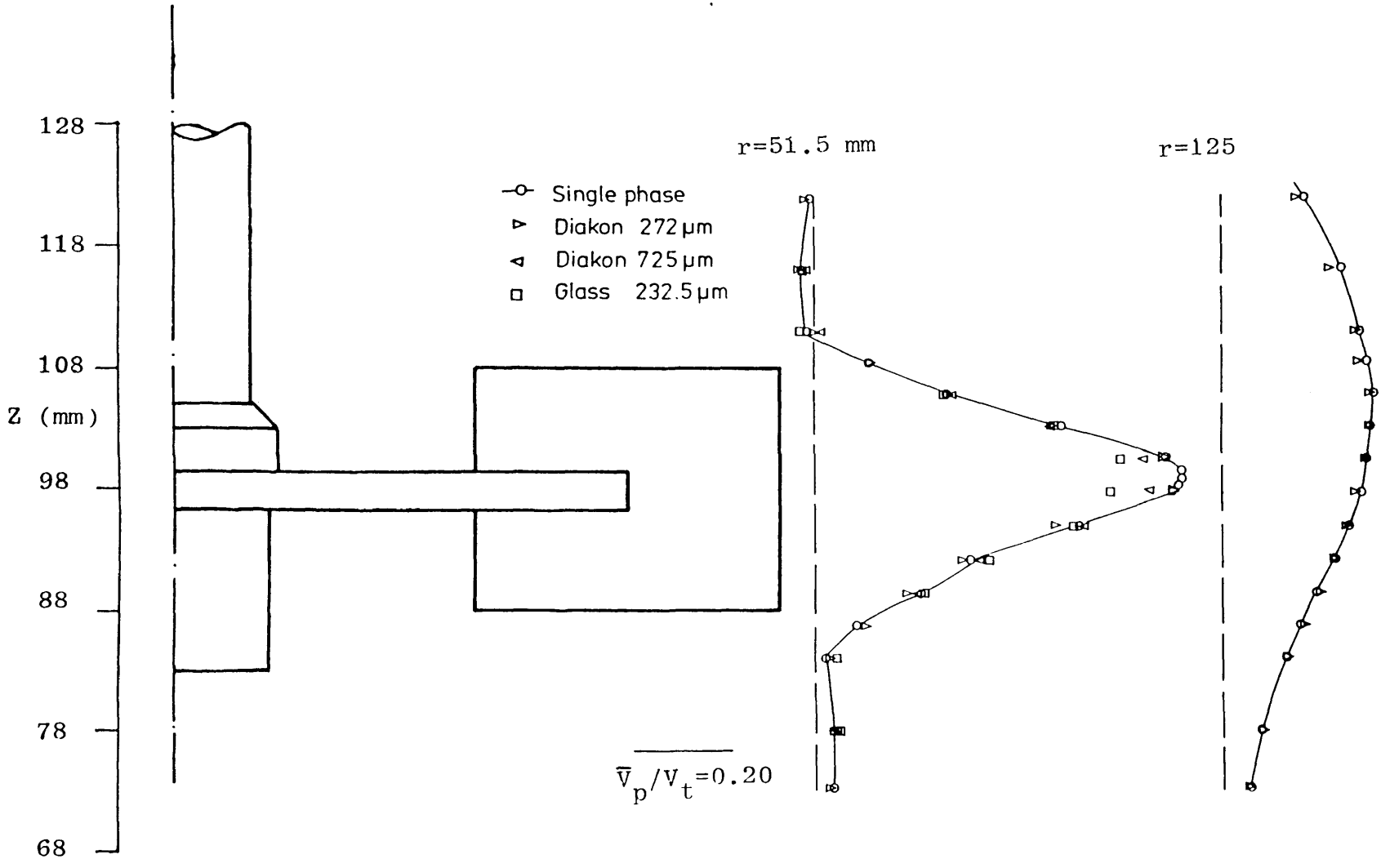

Fig 3.68 Particle radial mean velocities in the impeller stream for D=C=T/3, N=300 rpm and θ=0.0 °.

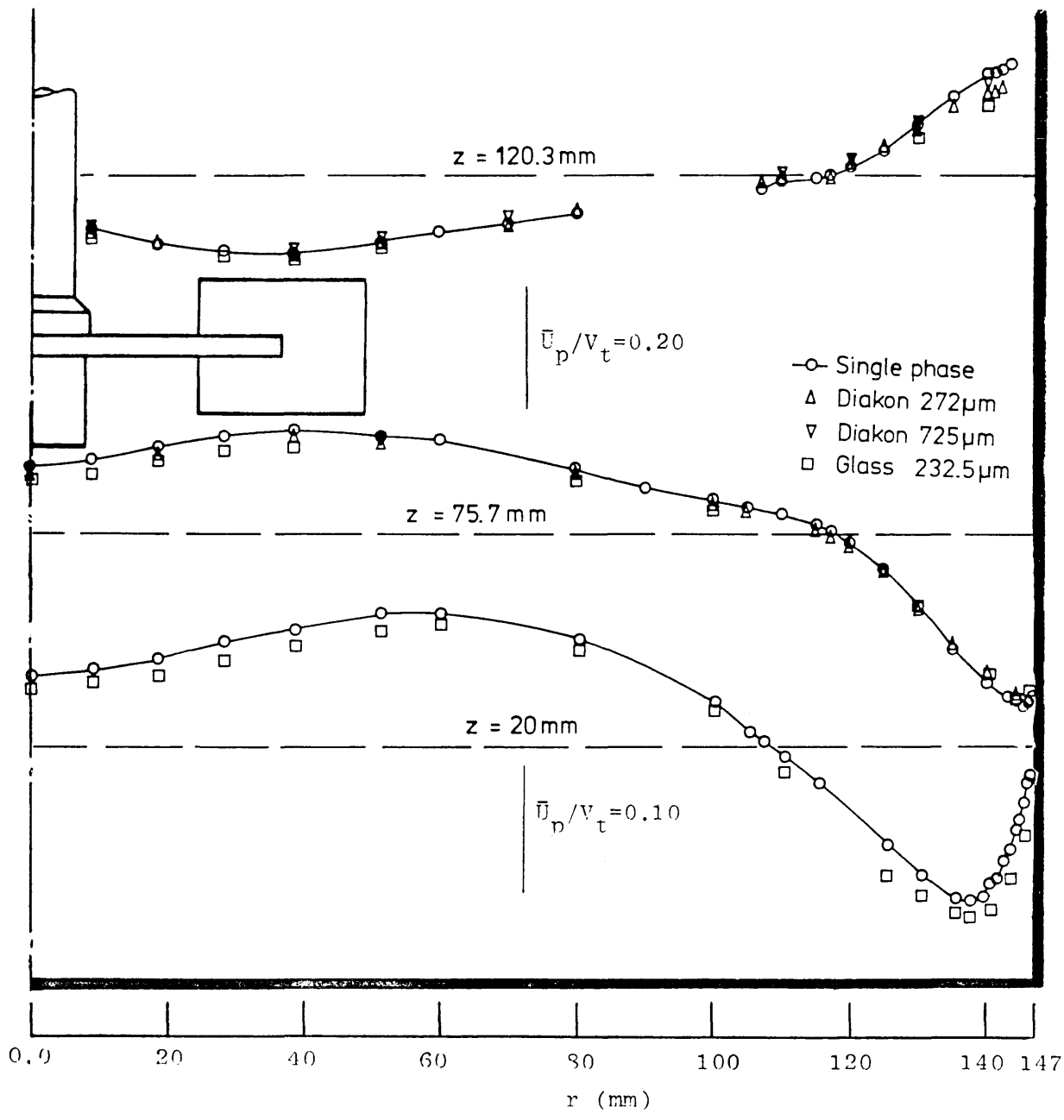

Fig 3.69 Particle axial mean velocities above and below the impeller for D=C=T/3, N=300 rpm and θ=0.0 °.

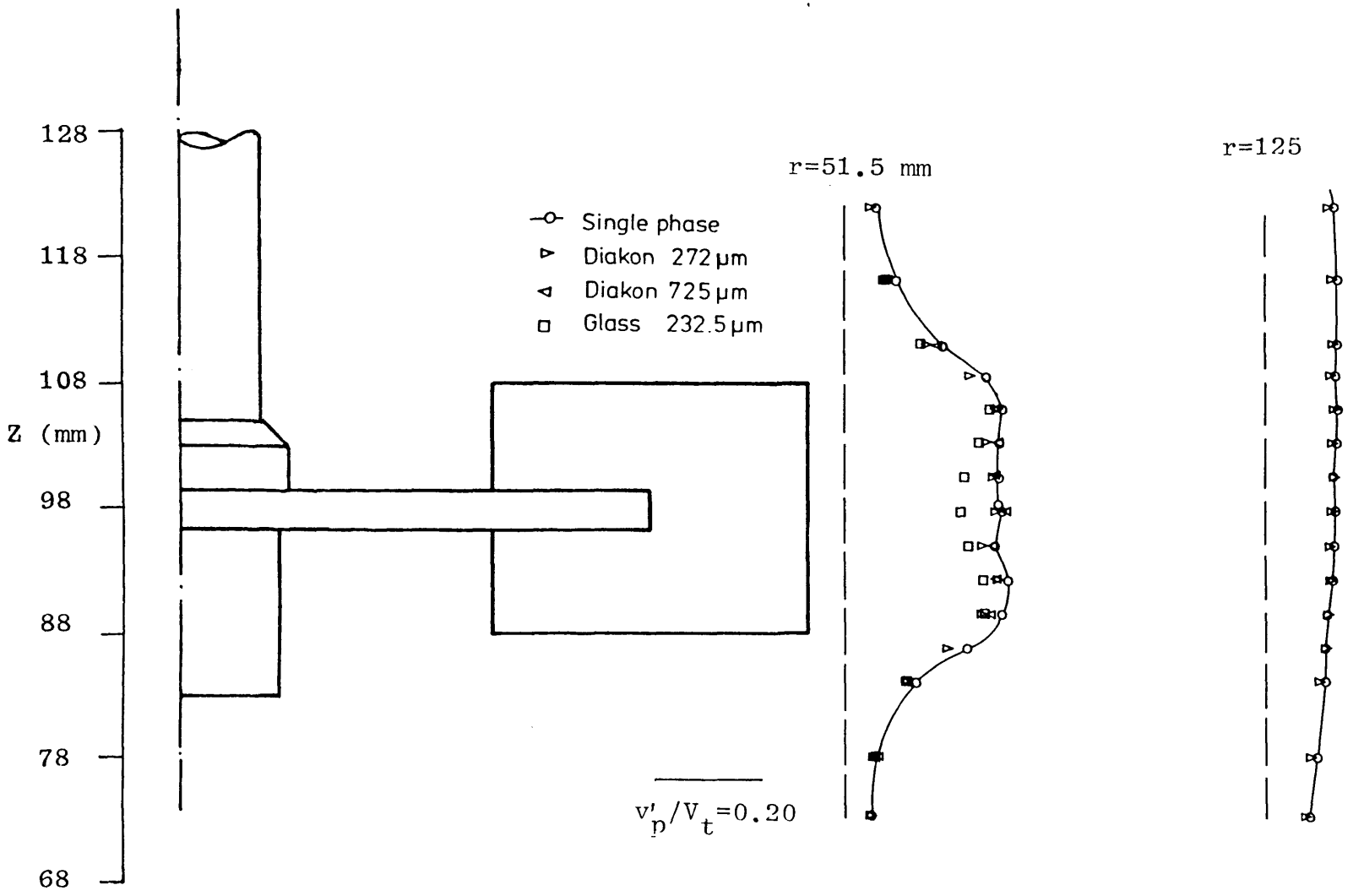

Fig 3.70 Particle radial rms velocities in the impeller stream for D=C=T/3, N=300 rpm and θ=0.0 °.

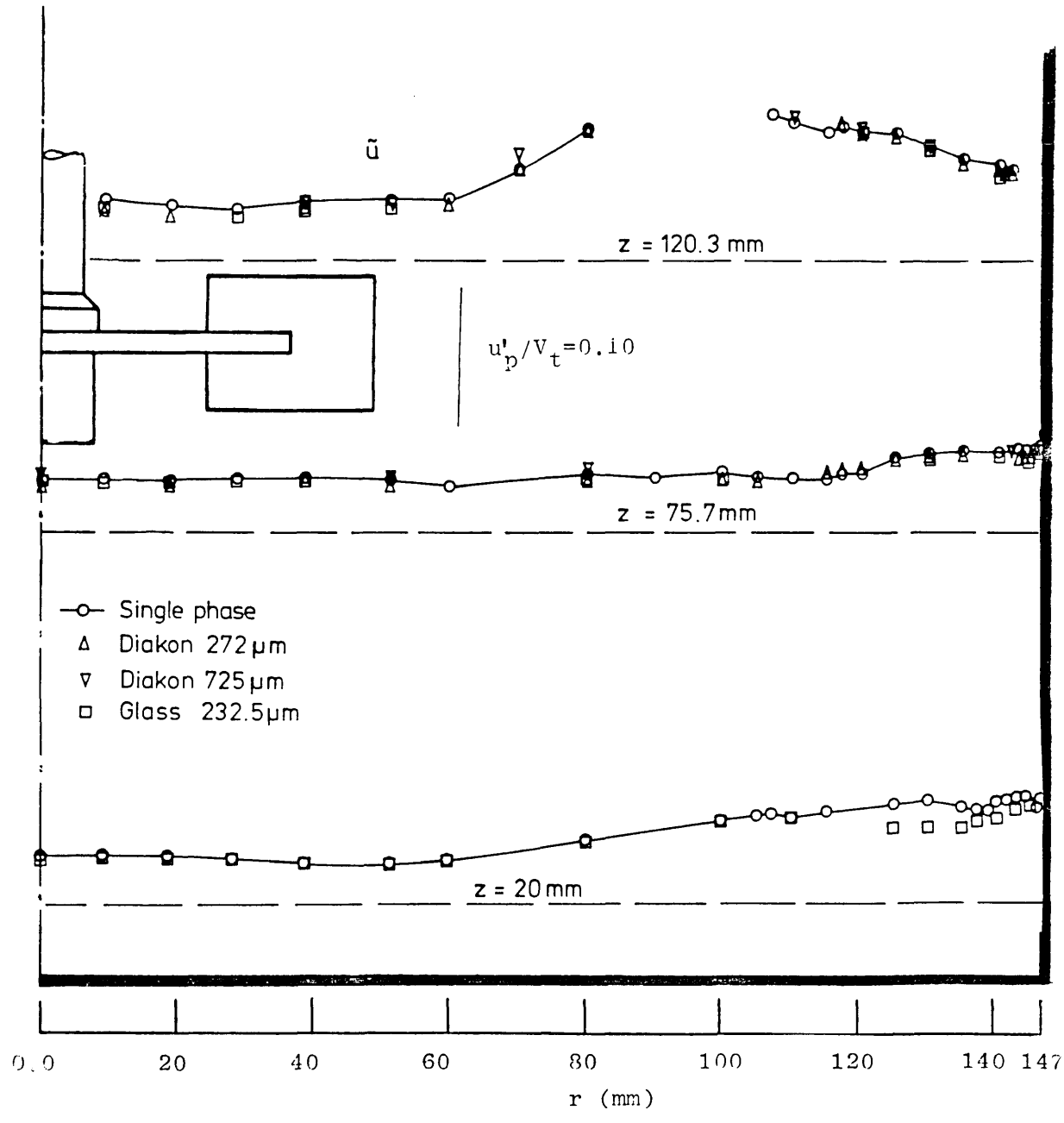

Fig 3.71 Particle axial rms velocities above and below the impeller for D=C=T/3, N=300 rpm and θ=0.0 °.

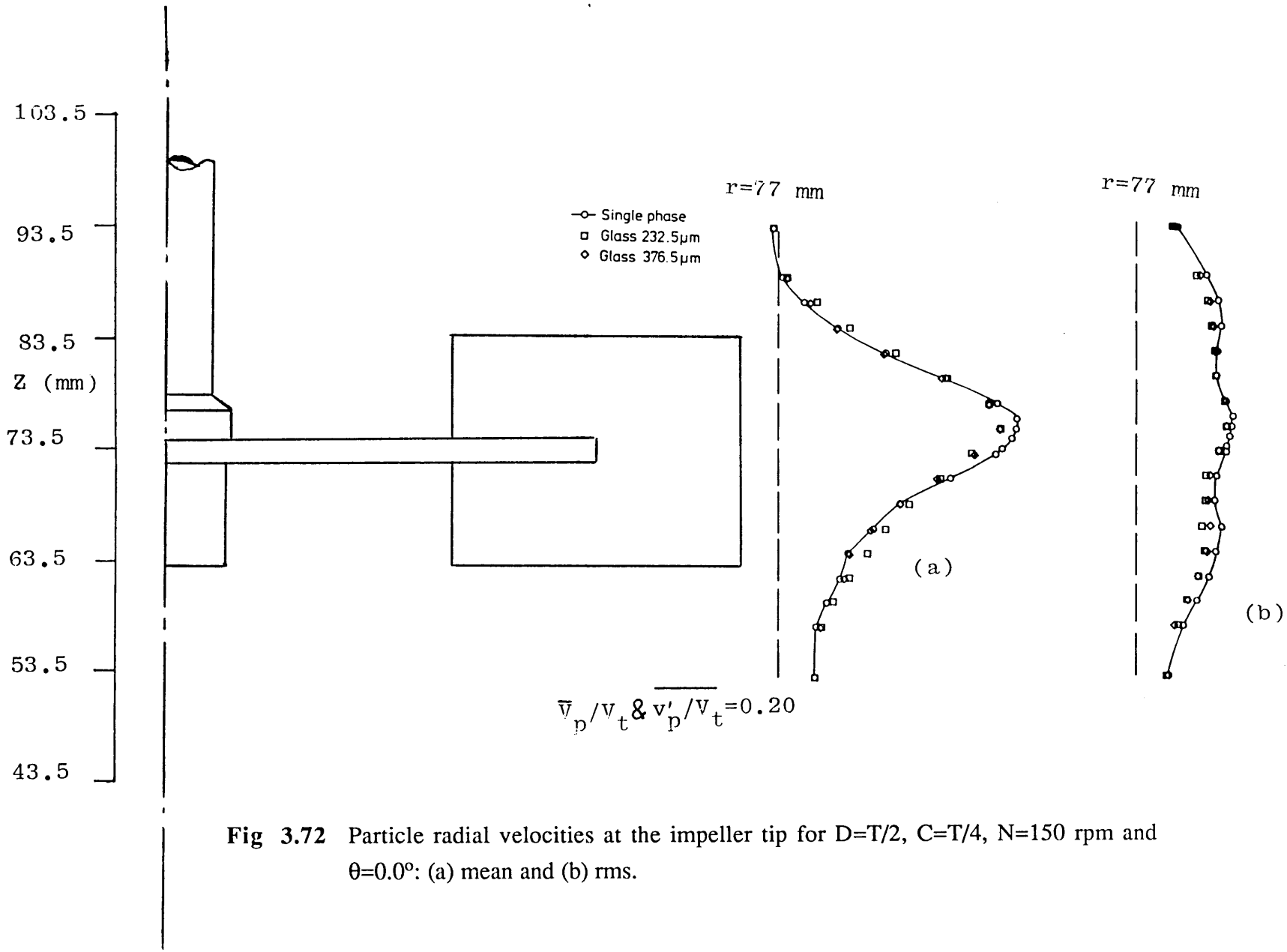

Fig 3.72 Particle radial velocities at the impeller tip for D=T/2, C=T/4, N=150 rpm and θ=0.0°: (a) mean and (b) rms.

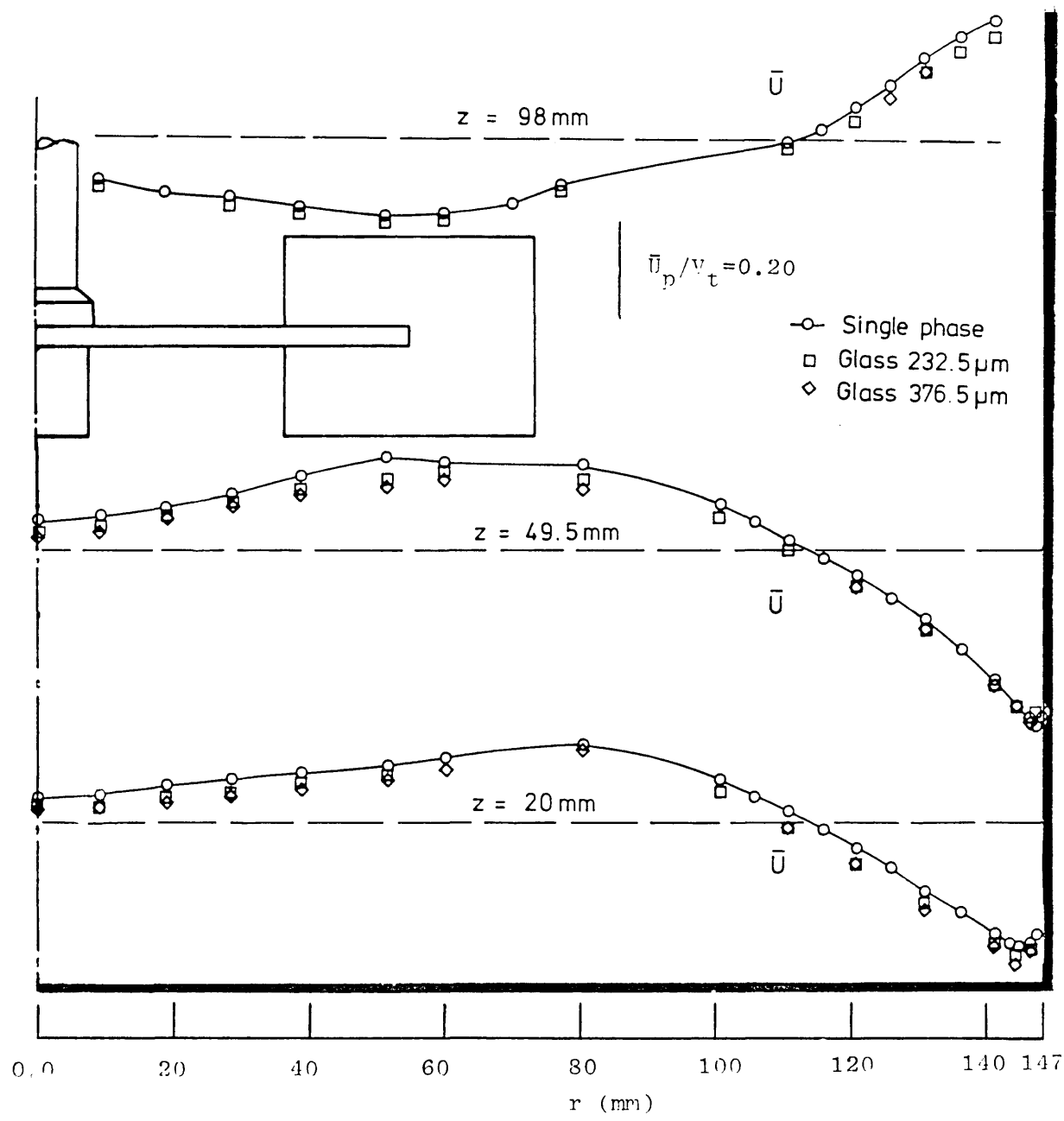

Fig 3.73 Particle axial mean velocities above and below the impeller for D=T/2, C=T/4, N=150 rpm and θ=0.0 °.

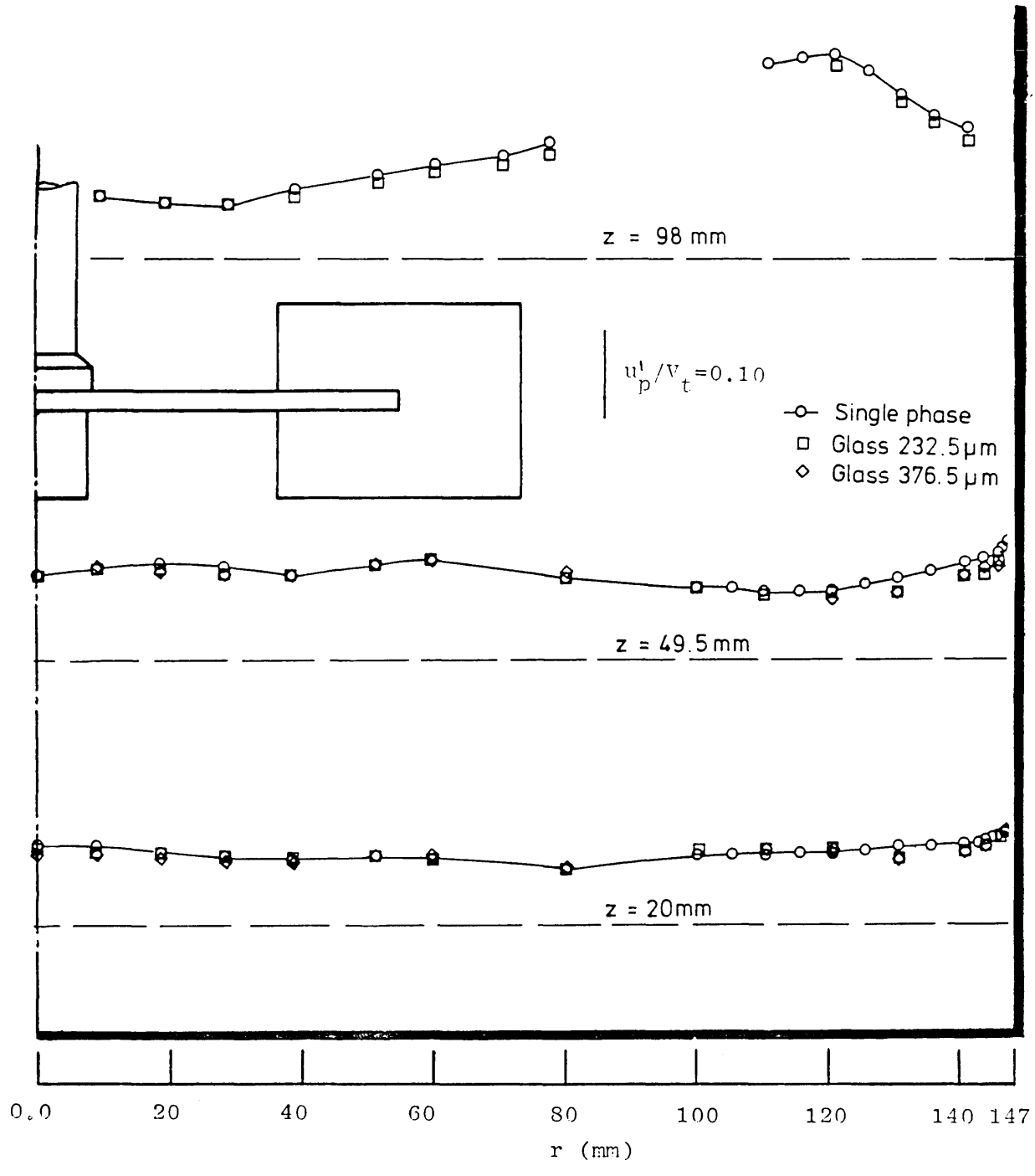

Fig 3.74 Particle axial rms velocities above and below the impeller for D=T/2, C=T/4, N=150 rpm and θ=0.0 °.

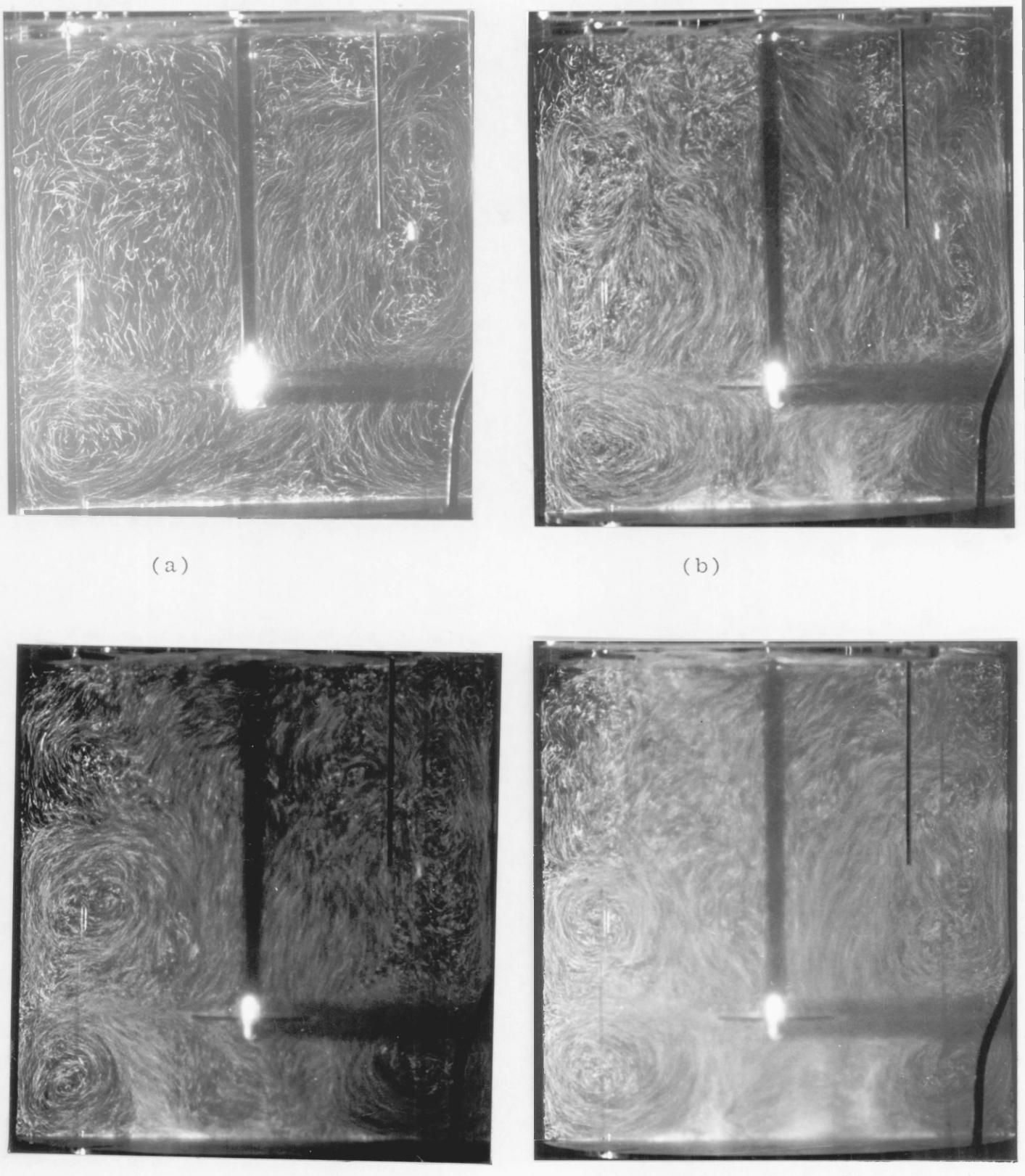

Fig 3.75 Photographs of two-phase flow visualisation in r-Z planes for D=T/3, C=T/4, N=313 rpm and θ=0.0 ° for different particle volumetric concentration; (a) C_v=0.25%; (b) C_v=0.75%; (c) C_v=1.25% and (d) C_v=1.75%.

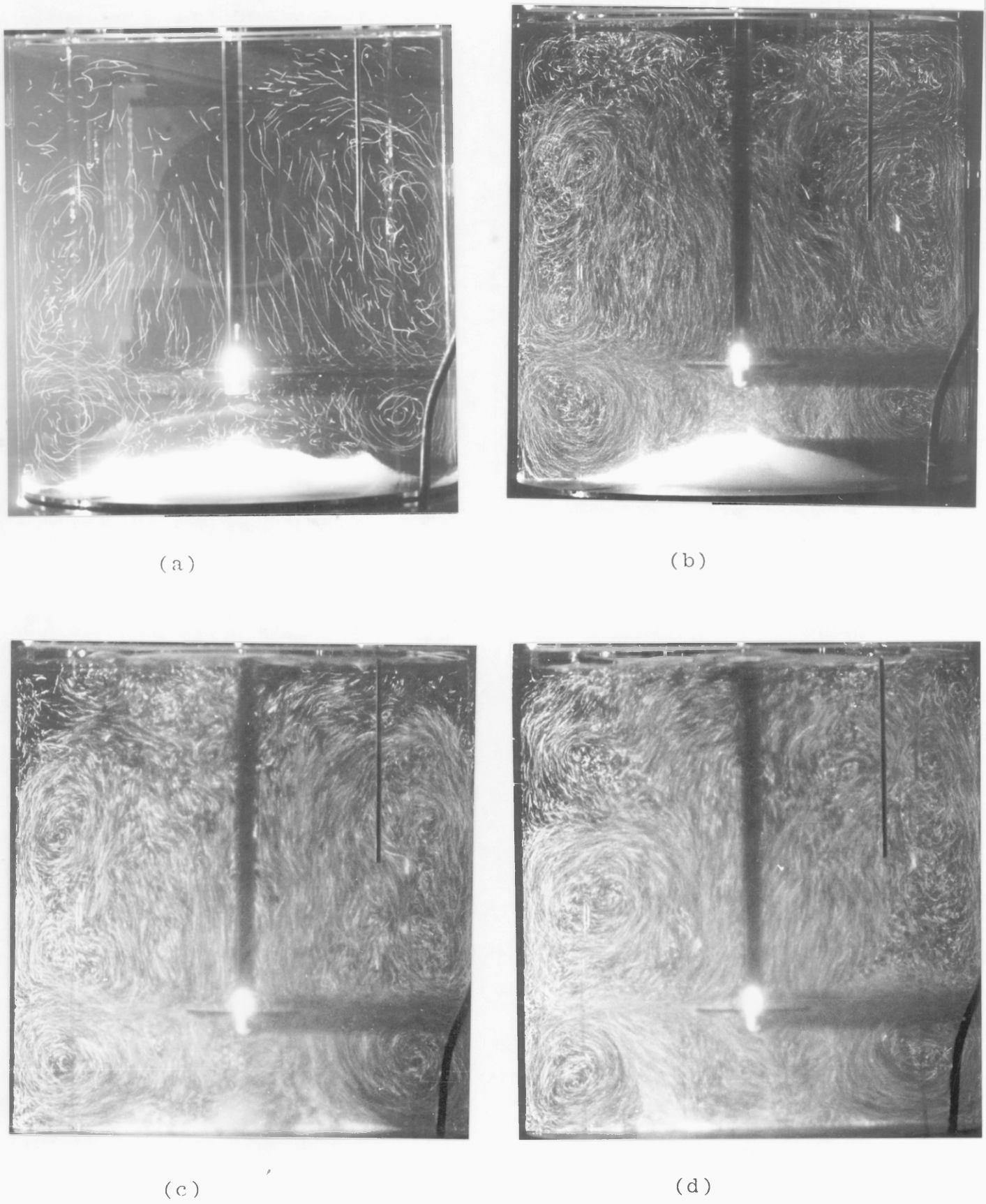

Fig 3.76 Photographs of two-phase flow visualisation in r-Z planes for D = T/3, C=T/4, C_v=1.25% and θ=0.0 ° at different impeller rotational speeds; (a) N=100 rpm; (b) N=180 rpm; (c) N=250 rpm and (d) N=313 rpm.

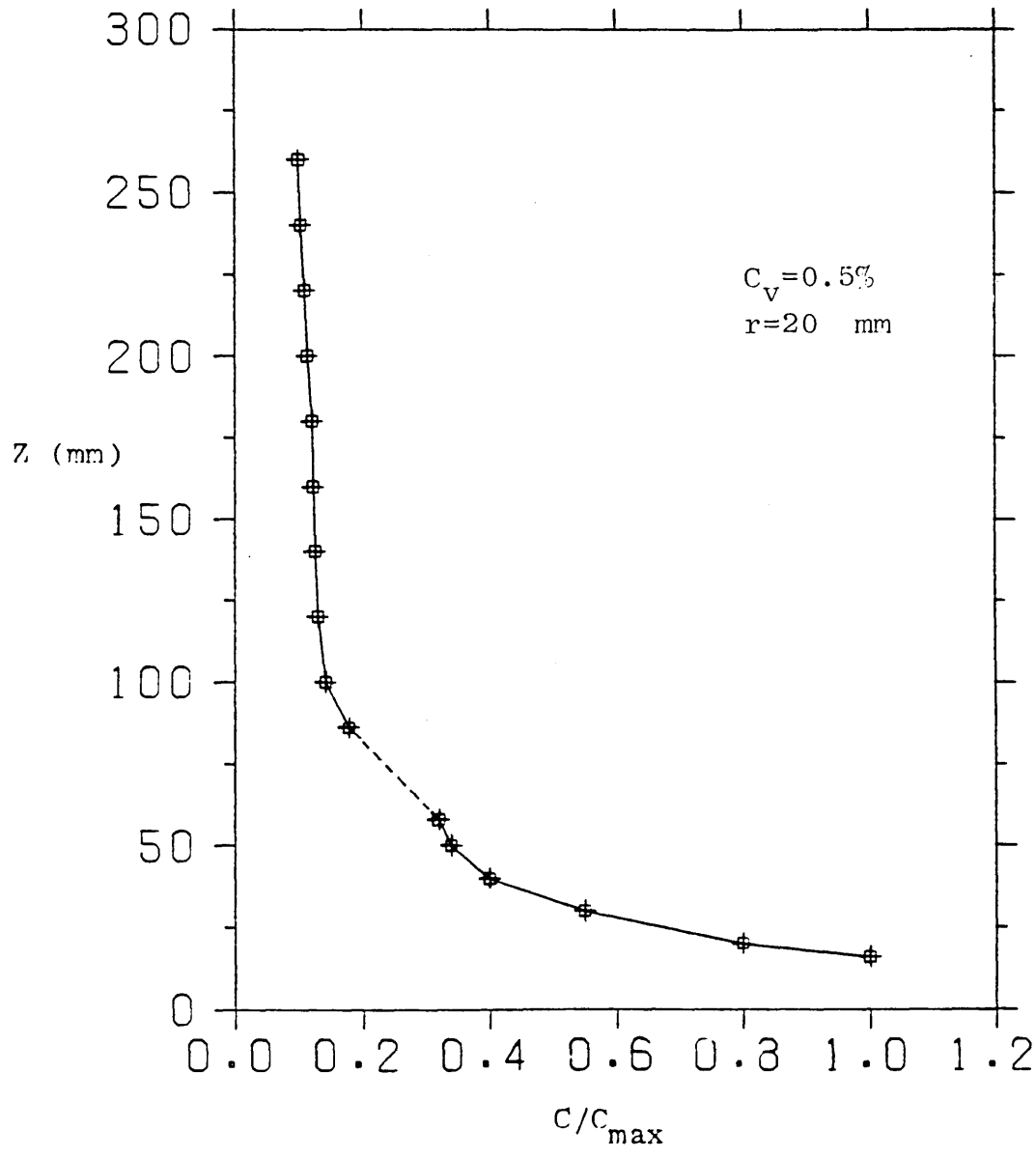

Fig 3.77 Variation of relative particle concentration along the height of the stirred vessel for D=T/3, C=T/4, N=313 rpm and θ=0.0 °.

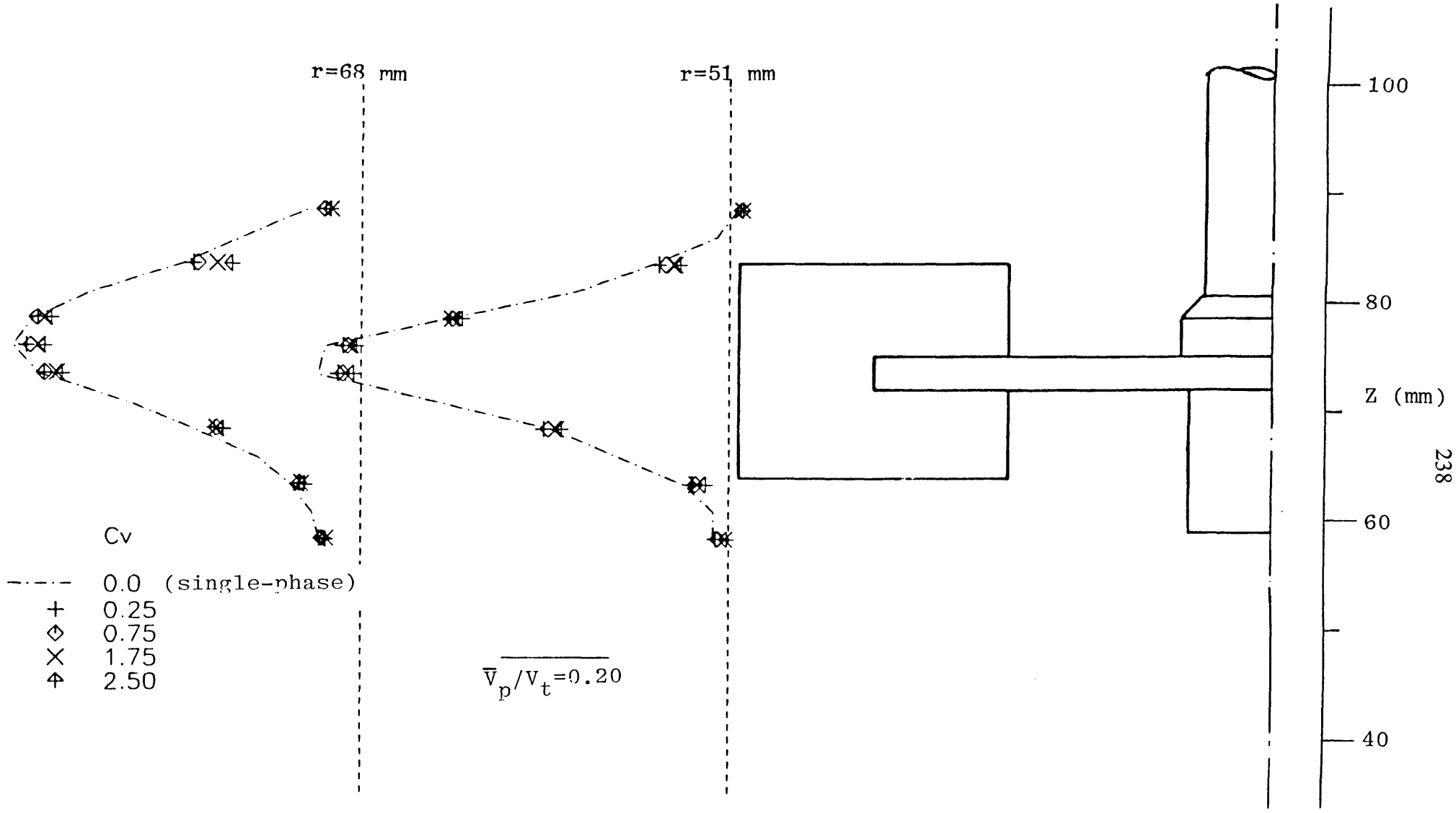

Fig 3.78 Particle radial mean velocities in the impeller stream for D=T/3, C=T/4, N=313 rpm and θ=0.0 ° for different C_v's.

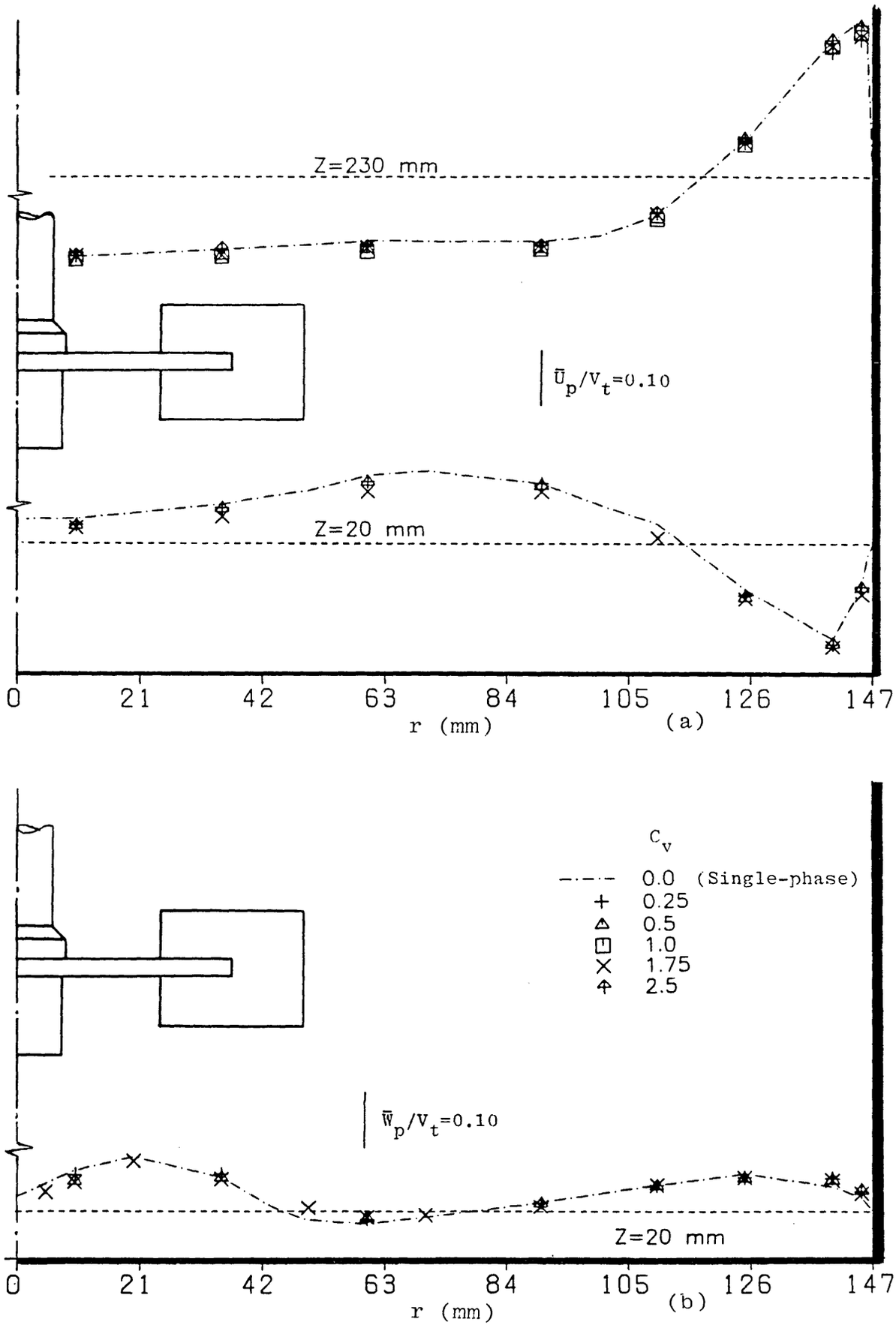

Fig 3.79 Particle mean velocities above and below the impeller for D=T/3, C=T/4, N=313 rpm and θ=0.0 ° for different C_v's: (a) axial component and (b) tangential component.

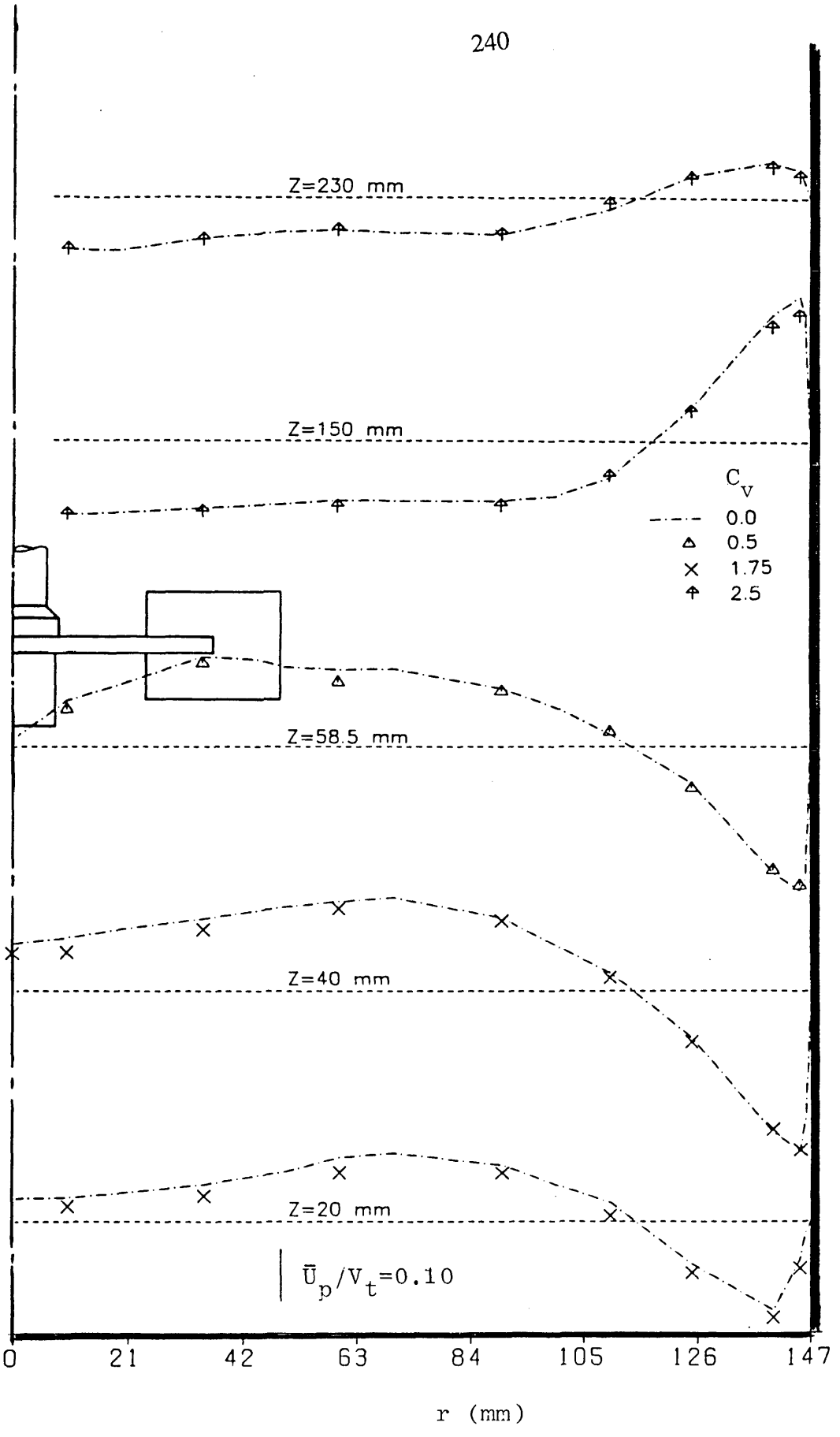

Fig 3.80 Particle axial mean velocities above and below the impeller for D=T/3, C=T/4, N=313 rpm and θ=0.0 °.

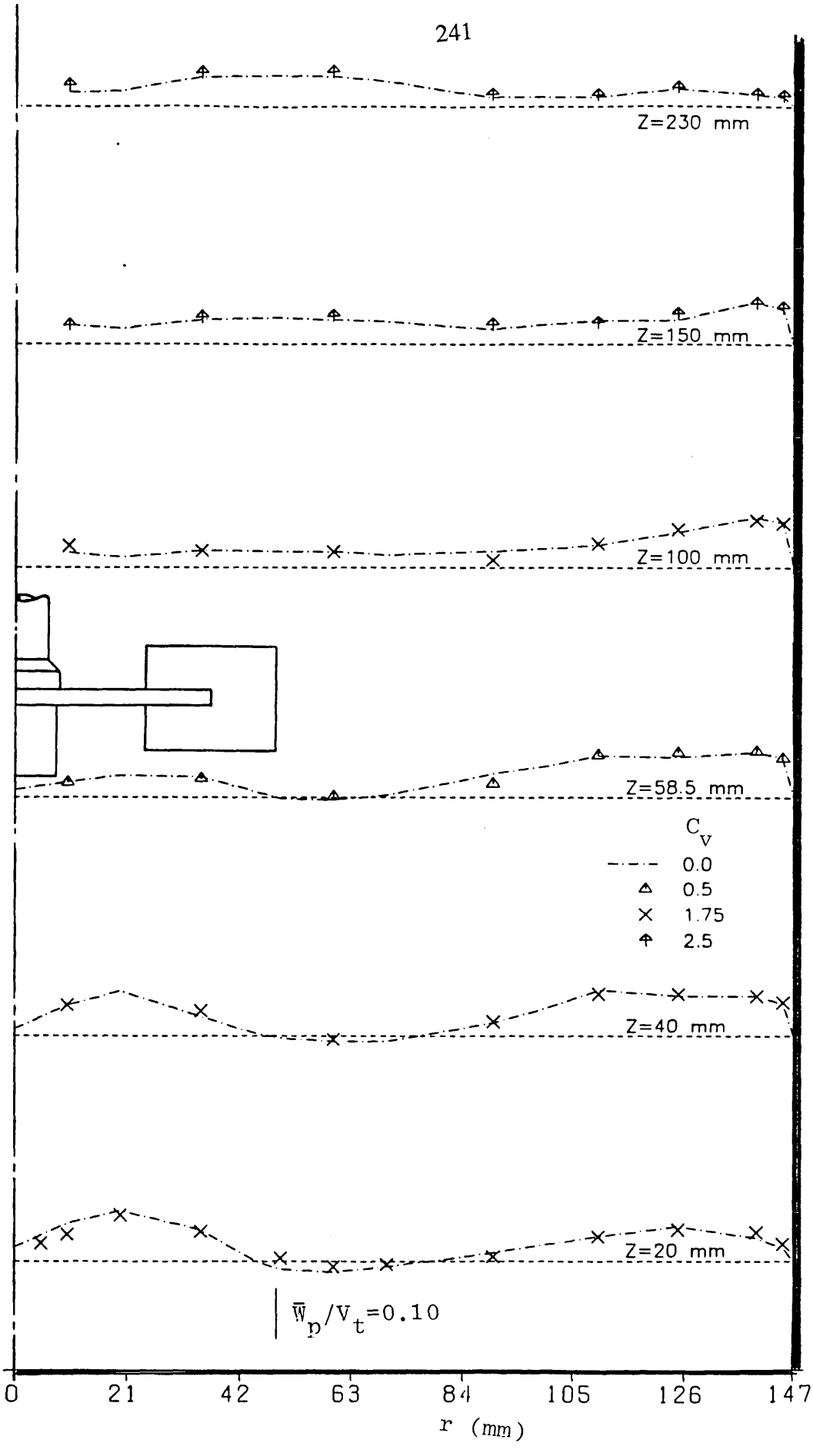

Fig 3.81 Particle tangential mean velocities above and below the impeller for D=T/3, C=T/4, N=313 rpm and θ=0.0 °.

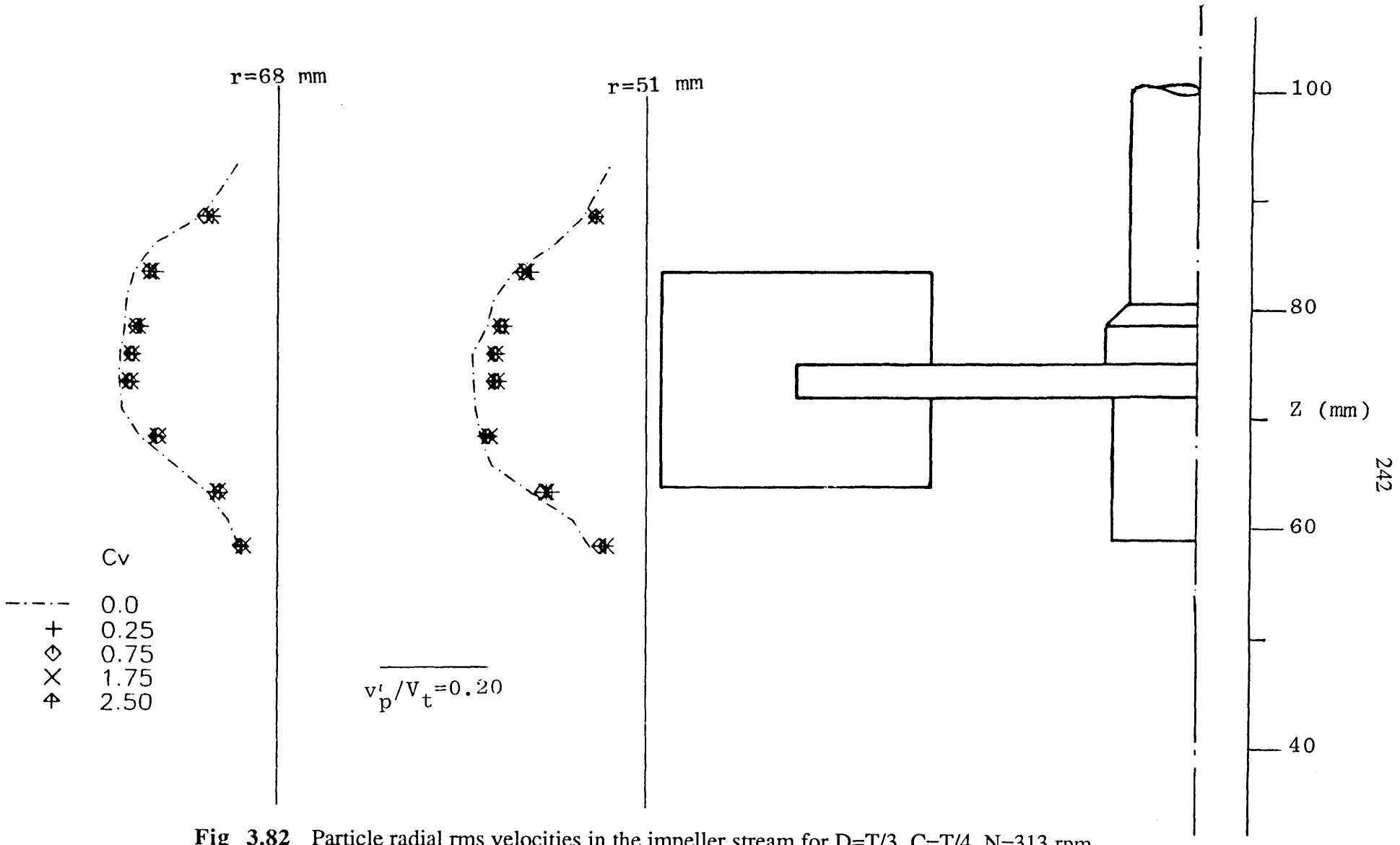

Fig 3.82 Particle radial rms velocities in the impeller stream for D=T/3, C=T/4, N=313 rpm and θ=0.0 ° for different C_v's.

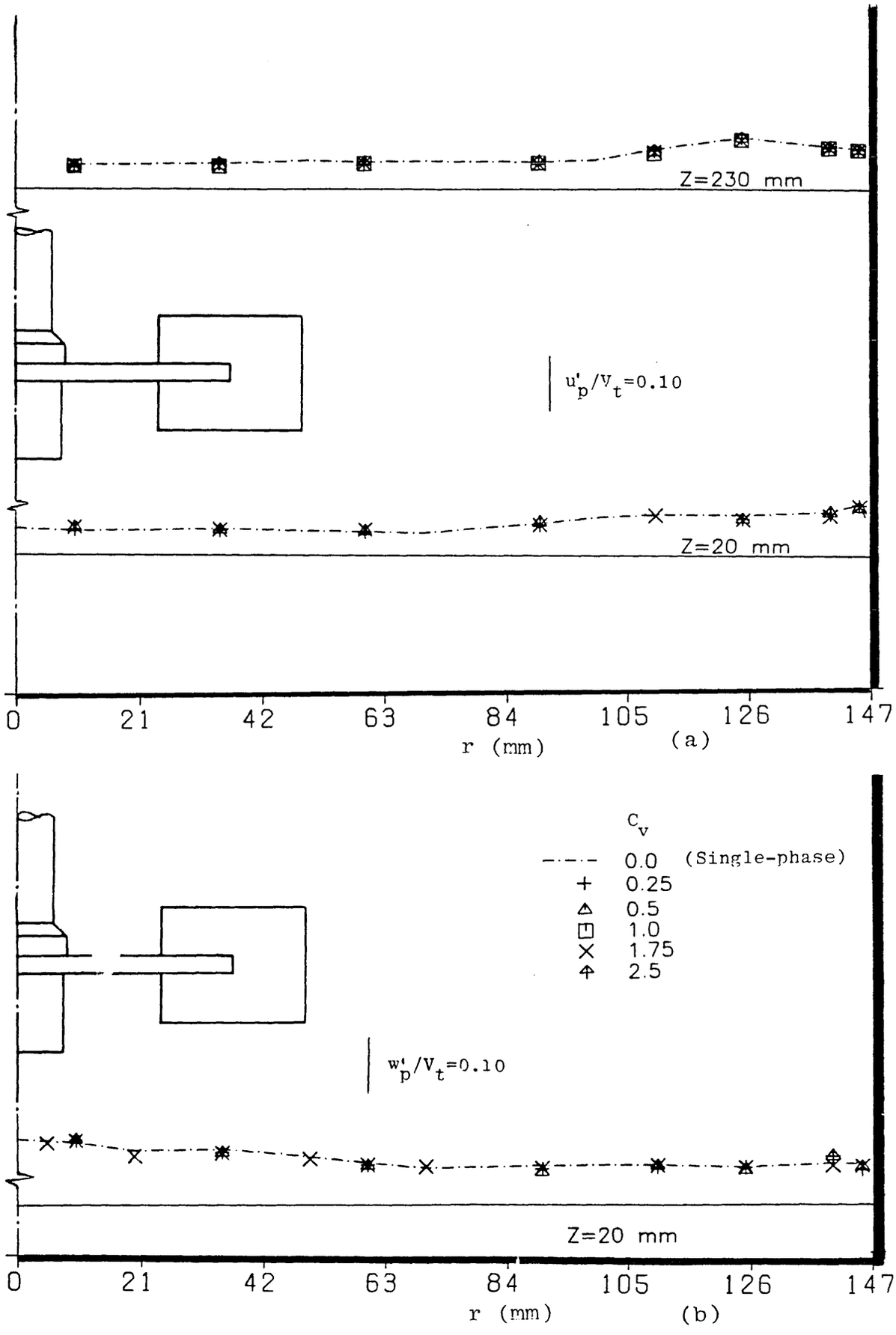

Fig 3.83 Particle rms velocities above and below the impeller for D=T/3, C=T/4, N=313 rpm and θ=0.0 ° at different C_v's: (a) axial component and (b) tangential component.

CHAPTER IV

CLOSURE

This chapter is divided into two sections. In the first, the main findings and achievements of the thesis are outlined in terms of knowledge of single and two-phase flow characteristics in circular ducts and stirred vessels. Areas in which further research is needed are identified in the second.

4.1 Achievements and conclusions

Measurements of the velocity characteristics of small and large particles, representing the liquid and solid-phase flows respectively, have been made by laser-Doppler velocimetry in fully-developed pipe flow and in the flow around an axisymmetric disc baffle with 50% area blockage. The mean velocities and the corresponding fluctuations were measured.

The velocities of the large particles were obtained, with particle volumetric concentrations of up to 0.75% when suspended in water and using an amplitude discrimination method. To allow penetration of the laser beams for particle velocity measurements at higher particle concentrations, a technique was developed in which the refractive index of the suspended particles was matched to that of the carrying fluid. Control of the fluid temperature to within ± 0.03 °C was required to apply the technique successfully. In the two-phase flow, the presence of gas-inclusions inside the particles limited the application of the method so that the measurement of particle velocities was achieved with a maximum concentration of particles of 14% in the pipe. A mixture of tetraline and oil of turpentine was used for this purpose and is recommended because of its low viscosity (close to water), of its refractive index which is close to that of the acrylic material and of its low toxic properties.

Two-phase flow results in the pipe and with the baffle showed that the solid-phase velocities decreased with increase in particle concentration, that the fluctuating velocities of the solid-phase were, in general, lower than those of the single-phase flow and were

reduced further with increase in particle concentration. In the fully-developed pipe flow, the solid-phase velocity profiles became more uniform as concentration increased and the solid-phase velocities decreased with increasing Reynolds number. Detailed solid-phase measurements around the disc baffle revealed that the solid-phase flow differed from the single-phase flow in the recirculation region due to particle's inertia, so that the length of the recirculation of the solid-phase flow was shorter than that in single-phase flow by 11% and 24% for particle concentrations of 4% and 8% respectively. For almost neutrally buoyant solid particles (Diakon) and within the measured range of particle concentration, up to 2% by volume, the solid-phase mean velocities of 310 μm and 665 μm were similar but the solid-phase fluctuating velocities of the larger particles were lower by up to 30%.

Similar measurements in single and two-phase flows have been made in baffled stirred reactors with the same methods as those used in the pipe flows. The maximum particle concentration at which the solid-phase velocity measurements could be made, was improved from the 0.02% limit encountered when particles were suspended in water to 2.5% when refractive-index-matching technique was implemented. Flow visualisation was conducted and provided useful qualitative information about the mean flow structure, such as the overall flow patterns in the vessel and the vortical and three-dimensional nature of the flow, and helped to identify flow regions of interest.

Detailed single-phase velocity measurements were presented and discussed in detail in chapter III and the most important flow features were as follows. The flow in a disc-turbine stirred vessel was highly vortical and three-dimensional and the main flow regions were the impeller jet stream emanating from the impeller tip and two ring vortices, one on either side of the impeller stream. The flow around the axis and along the wall of the vessel was predominantly in the axial direction, and was in the radial direction at the top and bottom of the vessel. The tangential velocities decayed rapidly with distance from the impeller and in the bulk of the flow they were smaller than those of the axial and radial components. There were large counter-rotating flow regions below the impeller due to the pressure gradients, whereas above the impeller the swirl motion was in the same direction

as the impeller rotation except for a small region between the wall and the free surface. In front of the baffle, the tangential velocities were reduced to almost zero while behind it a helical vortex existed with size comparable to the baffle width.

The turbulence quantities, measured over 360 ° of the impeller rotation, decayed with distance from the impeller. The turbulence in the impeller stream was near-isotropic and anisotropic in most of the bulk flow regions except around the centre of the lower ring vortex. Around the impeller the turbulence levels were high, about 0.35 of the impeller tip velocity, and reduced to 0.05 of the tip velocity in the bulk of the flow. The turbulence kinetic energy levels at the impeller tip were about 0.14 V_t^2 along the width of the impeller blade, and higher than the levels in the bulk of the flow by an order of magnitude.

Parametric studies were conducted and the results, in the impeller stream region, showed that the mean and rms velocities normalised by V_t were independent of impeller rotational speed. They were also found to be independent of impeller size when normalised by V_t and plotted against non-dimensional radial (R^*) and axial (Z^*) directions. A reduction in impeller clearance resulted in steeper inclination of the impeller jet stream. In the bulk flow, the axial and radial mean and rms velocities scaled with the impeller speed in the turbulent region, but an increase in impeller size from T/3 to T/2 resulted in recirculation velocities which were higher by about 200% in the lower ring vortex and in the overall turbulence levels higher by an order of magnitude in the same region. The swirl motion was stronger and the size of the counter-rotating flow regions smaller in the lower ring vortex when either the impeller size was increased or the impeller clearance was reduced.

In the two-phase flow in the stirred vessel, the results showed the presence of a strong particle concentration gradient along the height of the vessel and considerable particle settling was observed as the impeller speed was reduced. The mean velocity results showed that the particles lagged behind the fluid at the impeller stream, and in the bulk flow they either lagged or led the fluid depending on the local flow direction. In general, the particle velocities decreased with increasing the particle concentration and the particle

turbulence levels were lower by up to 15% than the corresponding single-phase levels. Both mean and rms particle velocities were affected by particle density so that the apparent slip velocity and the turbulence levels of relatively heavier glass particles were higher and lower than the Diakon ones respectively.

4.2 Suggestions for further work

The effects of impeller speed, size and clearance were considered in this investigation, and it could be interesting and useful to extend the research by reducing and increasing the size of the mixing vessel and of the impeller in order to quantify the mean and turbulent flow characteristics in the new size vessel under similar operating conditions. Comparison of the results obtained from these two similar geometrical models would allow conclusions about similarity, and help to establish scaling factors. Measurements of flow characteristics in stirred vessels with different types of gitators are also required to complement previously obtained power consumption and flow visualisation results and should include a pitched-blade impeller and a marine type propeller.

Ensemble-average measurements over, say, 1 ° interval of the impeller rotation in and around the impeller and especially between the impeller blades, would be a useful addition to the present data 360 ° averaged. Care would be required in regions between the blades of the impeller in water flow because of movement of the blades during the period of the measurement which introduces broadening effects on the mean and turbulence quantities measured (Popiolek et al, 1984) and thus corrections should be made like those suggested by Morse (1977) for "crank-angle" broadening. Applying refractive-index-matching with a mixture of tetraline and oil of turpentine is likely to remove this obstacle for the gated measurements. Comparison of gated and ungated results would establish the influence of the blade periodicity on the mean and turbulent flow characteristics and the results would be helpful in the development of calculation methods to include boundary conditions assigned on the surfaces of the blades.

The present single-phase experimental results in the stirred vessels do not include

CHAPTER IV

Reynolds stresses and triple-correlations which could be useful in identifying the detailed nature of the momentum transport and the corresponding turbulence energy balance. The measurement of these terms is likely to be limited to small regions of the stirred vessels with water because of the different refractive indices at the interface of the fluid and the curved solid boundary of the vessel and thus the use of the refractive-index-matching is recommended.

In two-phase flows, the velocity information about the liquid-phase in the presence of the suspended particles was not obtained for the present investigation. These velocities are likely to be of importance since they allow comparison with results of both the single-phase and the solid-phase. The presence of gas-inclusions inside the suspended particles made the measurement of liquid-phase velocities impossible and limited the velocity measurements of the solid-phase to a moderate level of particle suspension. Thus, further work is necessary to remove these gas-inclusions or to improve the process through which the particles are made so that the formation of these inclusions is prevented. Until such improvements are made, refractive-index-matching can be used to determine the particle motion and the effect of particle size, density and concentration of particle suspensions (liquid-solid) in flows of various geometries, which are encountered in engineering as a whole, at particle concentrations which are larger than those previously possible and certainly sufficiently large to ensure particle-particle interference.

The improvement of calculation of the flows in stirred vessels is restricted by the need for grid refinements which increase computer storage and time costs. The use of non-iterative (time-marching) techniques and improved algorithms in the numerical methods show promise in reducing these costs and thus permitting grid refinement and reduction of numerical errors. A further area of improvement would be to calculate the flow between successive blades, using fully three-dimensional turbulent flow methodology employing the k-ε model. This would facilitate the prediction of the periodic flow structure, and of the trailing vortices in particular, as part of the mean flow and also the predicted results can be used as the initial condition for the current numerical method used

by Bolour-Froshan (1986) and Looney et al (1985).

The above suggestions for further work, require a carefully co-ordinated programme of measurements and calculations in comparatively simple flow configurations so as to lay foundations for better understanding of turbulent single and two-phase flows relevent to engineering processes. This understanding would be useful where more complex flows are encountered, and this approach was the rationale behind the work of this thesis.

References

Adrian, R. J. (1983). Laser velocimetry in fluid mechanics measurements. Ed. R.J. Goldstein, Springer Verlag.

Aiba, S. (1958). Flow patterns of liquids in agitated vessels. A.I. Chem. Eng. Journal, vol. 4, p. 485.

Armstrong, S. G. and Ruszkowjki, S. (1986). Measurement and comparison of flow generated by different types of impeller in stirred tank. BHRA, Fluid Engineering Centre, Cranfield, Bedford, England.

Bachelor, G. K. (1953). The theory of homogeneous turbulence. Cambridge University Press, England.

Bicen, A. F. (1981). Refraction correction for LDA measurements in flows with curved optical boundaries. Fluid Section Report FS/81/17, Mech. Eng. Dept., Imperial College of Science and Technology, London.

Birchenough, A. and Mason, J. S. (1976). Local particle velocity measurements with a laser anemometer in an upward flowing gas-solid suspension. Powder Technology, Vol. 14, P. 139.

Bolour-Froushan, A. H. (1986). Prediction of single-phase turbulent flow in agitated mixing vessels. PhD Thesis, University of London, Imperial College of Science and Technology, London, England.

Boothroyd, R. G. (1967). Turbulence characteristics of the gaseous phase in duct flow of a suspension of fine particles. Trans. I. Chem. Eng., Vol. 45, P. 297.

Bower, R. H. (1965). An investigation of flow phenomena in stirred liquids. A.I.C.E.- I. Chem. E. Symp., series 10, p. 8.

Choi, Y. D. and Chung, M. K. (1983). Analysis of turbulent gas-solid suspension flow in a pipe. Proc. ASME Conf., Paper 83-FE-6, Houston, USA.

Cooper, R. G. and Wolf, D. (1968). Velocity profiles and pumping capacities for turbine type impeller. Canadian J. Chemical Engineering, vol. 46, p. 94.

References

Costes, J. and Couderc, J. P. (1982). Pumping capacity and turbulence intensity in baffled stirred tanks; influence of the size of the pilot unit. 4th Euro. Conference on Mixing, Vol. 1, Noordwijkerhout, Netherlands, Paper B2, P. 25.

Cox, R. G. and Mason, S. G. (1971). Suspended particles in fluid flow through tubes. Ann. Rev. Fluid Mech., Vol. 3, P. 291.

Cutter, L. A. (1966). Flow and turbulence in a stirred tank. A.I. Chemical Engineering Journal, vol. 12, p. 35.

Dimotakis, P. (1976). Signal scattering particle laser Doppler measurements of Turbulent. Application of Non - Intrusive Instrumentation in Fluid Flow Research, Paper 10, AGARD Conf. No. 193.

Drain, L. E. (1980). The laser Doppler Technique. Jhon Wiley, Chichester.

Dürao, D. F .G. and Whitelaw, J. H. (1978). Relationship between velocity and signal quantity in laser Doppler anemometry. J. Physics. Eng. Sci. Instrum., Vol. 12, P. 47.

Dürao, D. F. G., Laker, J. and Whitelaw, J. H. (1980). Bias effect in laser Doppler anemometry. J. Physics. E: Sci. Instrum., Vol. 13, P. 442.

Durst, F. (1982). Review - Combined measurements of particle velocities, size distributions, and concentrations. Trans. of the ASME., Vol. 104, p. 284.

Durst, F. and Zare, M. (1975). Laser Doppler measurements in two- phase flows. Proc. of the LDA - Symp., University of Denmark, Copenhagen.

Durst, F., Melling, A. and Whitelaw, J. H. (1976). Principles and practice of laser Doppler anemometry. Academic press, London.

Durst, F., Keck, T. and Kleine, R. (1979). Turbulence quantities and Reynolds stress in pipe flow of polymer solutions measured. 6th Symp. on Turbulence in Liquid, Chem. Eng. Dept., University of Missouri-Rolla.

References

Durst, F., Milojevic, D. and Schonung. B. (1984). Eulerian and Lagrangian predictions of particulate two-phase flows: a numerical study. Appl. Math. Modelling, Vol. 8, P. 101.

Edwards, R. V. and Dybbs, A. (1984). An index matched flow system for measurement of flow in complex geometries. Proc. 2nd Int. Symp. on Application of Laser Anemometry to Fluid Mech., Lisbon.

Einav, S. and Lee, S. L. (1973). Particles migration in laminar boundary layer flow. Int. J. of Multiphase Flow, Vol. 1, P. 73.

Elphick, I. G., Martin, W. W. and Currie, I. G. (1982). Application of LDA to high Reynolds number cross flow. Proc. 2nd Int. Symp. on Application of Laser Anemometry to Fluid Mech., Lisbon.

Farmer, W. M. (1972). Measurement of particle size, number density, and velocity using laser interferometer. Applied Optics, Vol. 11, No. 11, P. 2603.

Founti, M. A. and Laker, J. R. (1981). Performance characteristics of a new frequency counter interfaced to a microprocessor data acquisition and processing system. Fluid Section Report FS/81/36, Mech. Eng. Dept., Imperial College of Science and Technology, London.

George, W. K. and Lumley, J. L. (1977). The laser Doppler velocimetry and its application to measurement of turbulence. J. Fluid Mech., Vol. 60, p. 321.

Gosman, A. D., Khalil, E. E. and Whitelaw, J. H. (1979). The calculation of two-dimensional turbulent recirculating flow. Proc. 2th Symp. Turb. Shear Flow.

Günkel, A. A. and Weber, M. E. (1975). Flow phenomena in stirred tank, part I- the impeller stream; part II - The bulk of the tank. A. I. Chem. Eng. J., vol. 21, P. 931.

Hardalupas, Y. (1986). Phase-Doppler anemometry for simultaneous particle size and velocity measurements. Fluid Section Report FS/86/14, Mech. Eng. Dept., Imperial College of Science and Technology, London.

Harvey, P. S. (1980). Turbulent flow in an agitated vessel. PhD. Thesis, University of Bath, U.K.

References

Harvey, P. S. and Greaves, M. (1982). Turbulence flow in an agitated vessel. Part I - a predictive model; Part II - numerical solution and model predictions. Trans. I. Chemical Engineering, vol. 60, p. 195.

Heitor, M. V., Laker, J. R., Taylor, A. M. K. P. and Vafidis, C. (1984). Instruction manual for the FS "Model 2" Doppler frequency counter. Fluid Section Report FS/84/10, Mech. Eng. Dept., Imperial College of Science and Technology, London.

Hetsroni, G. and Sokolov, M. (1971). Distribution of mass, velocity and intensity of turbulence in a two-phase turbulent jet. J. Appl. Mech., June 1971, P. 315.

Hiroaka, S., Yamada, I. and Mizoguchi, K. (1978). Numerical analysis of flow behaviour of highly viscous fluid in agitated vessel. J. Chem. Engg. Japan, Vol. 11, P. 484.

Hodkinson, J. R. and Greenleaves, I. (1963). Computations of light-scattering and extinction by spheres according to diffraction and geometrical optics, and some comparison with Mie theory. J. opt. Soc. American. Vol. 53, p. 577.

Holland, F. A. and Chapman, F. S. (1966). Liquid mixing and processing in stirred tankes. Reinhold Publishing Corporation, N. Y.

Horvay, M. and Leuckel, W. (1984). LDA measurement of liquid swirl flow in converging swirl chamber with tangential inlets. Proc. 2nd. Int. Symp. on Application of LDA to Fluid Mech., Lisbon.

Issa, R. I. (1983). Solution of implicitly discretization of the effect of streamline curvature on turbulence. Physics of Fluids, vol. 18, p. 624.

Issa, R. I. and Gosman, A. D. (1981). The computational of 3-D turbulence two-phase flow in mixer vessels. Proc. Second Int. Conference in Numerical Methods in Laminar Turbulent Flow, July 1981, Italy.

Ito, S., Ogawa, K. and Yoshida, N. (1975). Turbulence in the impeller stream in a stirred vessel. J. Chemical Eng. of Japan Vol. 8, No. 3, P. 206.

Kay, B. H. and Boardman, R. P. (1962). Cluster formation in dilute suspensions. Proc. of Symp. on Interaction between Fluid and Particles, I. Chem. Eng., London, UK.

References

Kay, J. M. and Nedderman, R. M. (1985). Fluid mechanics and transfer process. Cambridge press, Cambridge, UK.

Keller, D. B. A. (1985). To determine the velocity distribution around an impeller in a stirred tank using laser anemometry. Int. Conf. on Laser Anemometry - Advances and Application. No. 2, Manchester, UK.

Khezzar, L. (1987). Experiments with steady and unsteady confined turbulent flows. PhD Thesis, University of London, Imperial College of Science and Technology, London, England.

Kliafas, Y., Taylor, A. M. K. P. and Whitelaw, J. H. (1985). The influence of depth of field on particle sizing by LDA. Fluid Section Report FS/85/30, Mech. Eng. Dept., Imperial College of Science and Technology, London.

Kramer, T. J. and Depew, C. A. (1972) Analysis of mean flow characteristics of gas-solids suspensions. Trans. of the ASME, J. of Basic Engineering, P.731.

Laufer, J. (1954). The structure of turbulence in fully developed pipe flow. National Bureau of Standards, Report 1174, Washington, D.C, USA.

Laufhütte, H.D. and Mersmann, A. B. (1985). Dissipation of power in stirred vessels. 5th Euro. Conference on Mixing, Wurzburg, West Germany, Paper 33, P. 331.

Lee, S. L. (1985). Particle drag in turbulent two-phase suspension flow. 2nd. Workshop on Two-Phase Flow Predictions, Erlangen, West Germany.

Lee, S. L. and Durst, F. (1982). On the motion of particles in turbulent flows. Int. J. Multiphase Flow, Vol. 8, p. 125.

Looney, M. K., Issa, R. I. Gosman, A. D. and Politis, S. (1985). Modelling of the turbulent flow solid/liquid suspension in stirred vessels. Proc. 5th Int. Conf. on Mathematical Modelling, University C. Berkeley.

Lumley, J. L. (1978). Two-phase and non-Newtonian flows in turbulence. (ed. P. Bradshaw), Springer Topics in Applied Physics, Vol. 12, P. 289.

References

Maude, A. D. (1960). The viscosity of suspension of spheres. J. Fluid Mech.Vol. 7, P. 230.

Mclaughlin, D. K. and Tiederman, W. G. (1973). Biasing correction for individual realisation of laser anemometer measurement in turbulent flow. The Physics of Fluids, Vol. 16, P. 2082.

Melling, A. (1975). Investigation of flow in non - circular ducts and other configuration by LDA. PhD Thesis, University of London, Imperial College of Science and Technology, London, England.

Melling, A. and Whitelaw, J. H. (1976). Turbulent flow in a rectangular duct. J. Fluid Mech., Vol. 78, P. 289.

Modarress, D., Wuerer, J. and Elgobashi, S. (1982). An experimental study of a turbulent round two-phase jet. AIAA Paper 82 - 0964.

Modarress, D., Tan, H. and Elgobashi, S. (1983). Two-component LDA measurement in a two-phase turbulent jet. AIAA Paper 83 - 0052.

Morse, A. P. (1977). The effect of crank-angle broadening on laser-Doppler measurements in reciprocating engines. Imperial College, Mech. Eng. Dept., Report FS/77/18.

Mujumdar, A. S., Huang, B., Wolf, D., Weber, M. E. and Douglas, W. J. M. (1970). Turbulence parameters in a stirred tank. Canadian Journal of Chemical Engineering, vol. 48, p. 475.

Nagata, S. (1975). Mixing - principles and applications. John Wiley and Sons, London.

Nienow, A. W. and Wisdon, D. J. (1974). Flow over disc turbine blades. Chemical Engineering Science, vol. 29, p. 1994.

Nishikawa, M., Okamoto, Y., Hashimoto, K. and Nagata, S. (1976). Turbulence energy spectra in baffled mixing vessels. Journal of Chemical Engineering of Japan, vol. 9, p. 489.

References

Nouri, J. M., Whitelaw, J. H., and Yianneskis, M. (1984). The flow of dilute suspension of particles around axisymmetric baffles. Fluid Section Report FS/84/18, Mech. Eng. Dept., Imperial College of Science and Technology, London.

Okuda, S. and Choi, W. S. (1978) Gas-particle mixture flow in various types of convergent-divergent nozzle. J. of Chemical Eng. of Japan, Vol. 11, No. 6, p. 432.

Oldshue, J. Y. (1983). Fluid mixing technology. McGraw - Hill Publications Co., New York.

Owen, P. R (1969). Pneumatic transport. J. Fluid Mech., Vol. 39, P. 407.

Patterson, G. K. and Wu, H. (1985) Distribution of turbulence energy dissipation rates in mixers. 5th Euro. Conference on Mixing, Wurzburg, West Germany, Paper 35, P. 355.

Placek, J. and Tavlarides, L. L. (1985). Turbulent flow in stirred tankes. A.I.Ch.E. Journal Vol. 31, No. 7, P. 1113.

Plion, P. Costes, J. and Couderc, J. P. (1985). Study by laser Doppler anemometry of the flow induced by a propeller in a stirred tank - influence of baffles. 5th Euro. Conference on Mixing, Wurzburg, West Germany, Paper 34, P. 341.

Politis, S. (1988). Three-dimensional prediction of solid/liquid flows in stirred vessels.. PhD Thesis In Preparation, University of London, Imperial College of Science and Technology, London, England.

Popiolek, Z., Whitelaw, J. H. and Yianneskis, M. (1984). Unsteady flow over disk turbine blades. 2nd Int. Symp. on Applications of Laser Anemometry to Fluid Mech., Lisbon.

Pourahmadi, F. and Humphrey, J. A. C. (1983). Modelling solid-fluid turbulent flows with application to predicting erosive wear. Physico. Chemical Hydrodynamics, Vol. 4, P. 191.

Reed, N. B., Princz, M. and Hartland, S. (1977). Laser-Doppler measurements of turbulence in a standard stirred tank. Second European Conference on Mixing, Cambridge.

References

Revill, B. K. (1982). Pumping capacity of disc turbine agitators. A literature review. Fourth European Conference on Mixing, Noordwijkerhout, Netherlands.

Robinson, D. M. and Chu, W. P. (1975). Diffraction analysis of Doppler signal characteristics for a cross beam laser Doppler velocimetry. Applied Optics, Vol. 14, No. 9, P. 2177.

Sachs, J. P. and Rushton, J. H. (1954). Discharge flow from turbine type mixing impeller. Chemical Engineering Progress, vol. 51, p. 599.

Schlichting, H. (1955). Boundary layer theory. Pergamon press limited, London, UK.

Shih, T. H. and Lumley, J. L. (1986). Second - order modelling of particle dispersion in a turbulent flow. J. Fluid Mech., Vol. 163, P. 349.

Shuen, J. S., Solomon, A. S. P., Zhang, Q-F. and Faeth, G. M. (1985). Structure of particle-laden jets: measurements and predictions. AIAA Journal, Vol. 23, No. 3, P. 396.

Shuen, J. S., Solomon, A. S. P. and Faeth, G. M. (1986). Droplet-turbulence interaction in a diffusion flame. AIAA Journal, Vol. 24, No. 1, P. 101.

Snyder, W. H. and Lumley, J. L. (1971). Some measurements of particle velocity autocorrelation function in a turbulent flow. J. Fluid Mech., Vol. 48, P. 41.

Soo, S. L. (1967). Fluid dynamics of multiphase systems. Blaisdell Publishing C0., Waltham, Mass.

Soo, S. L., Trezet, G. J., Dimick, R. C. and Hohnstreiter, G. F. (1964). Concentration and mass flow distribution in a gas-solid suspension. Ind. Eng. Chem. Fundamentals, Vol. 3, P. 98.

Stümke, A. and Umhauer, H. (1978). Local particle velocity distributions in Two-phase flows measured by laser-Doppler velocimetry. Proc. of the Dynamic Flow Conf. p. 417.

References

Sweeney, E. T. and Patrick, M. A. (1977) The numerical predictions of flow patterns around perpendicular stirrer blades for non-Newtonian power law fluids. 2nd. Euro. Conf. on mixing, paper A4.

Tabrizi, B. S. (1988). Three-dimensional Diesel spray predictions in combustion chamber flows. PhD Thesis In Preparation, University of London, Imperial College of Science and Technology, London, England.

Taylor, A. M. K. P. (1981). Confined isothermal and combusting flows behind axisymmetric baffles. PhD Thesis, University of London, Imperial College of Science and Technology, London, England.

Taylor, A. M. K. P. and Whitelaw, J. H. (1984). Velocity characteristics in the turbulent near wakes of confined axisymmetric bluff bodies. J. Fluid Mech. Vol. 139, P. 391.

Theofanous, T. G. and Sullivan, J. (1982) Turbulence in two-phase dispersed flows. J. Fluid Mech., Vol. 116, P. 343.

Tridimas, Y. D., Hobson, C. A., Wooley, N. H. and Lalor, M. J. (1982). Measurement of the velocities of the two phases in a flowing gas solid suspension using LDA. Proc. 1st Symp. on Application of Laser Anemometry to Fluid Mechanics, Lisbon.

Tsuji, Y. and Morikawa, Y. (1982). LDA measurements of an air-solid two-phase flow in a horizontal pipe. J. Fluid Mech., Vol. 120, P. 385.

Tsuji, Y., Morikawa, Y. and Shiomi, H. (1984). LDA measurements of an air-solid two-phase flow in a vertical pipe. J. Fluid Mech., Vol. 139, P. 417.

Tsuji, Y., Morikawa, Y. and Mizuno, O. (1985). Experimental measurement of Magnus force on a rotating sphere at low Reynolds number. Trans. ASME., Vol. 107, P. 484.

Uhl, V. W. and Gray, J. B. (1966). Mixing: theory and application. Volume 1, Academic Press.

Vafidis, C. (1985). Aerodynamics of reciprocating engines. PhD Thesis, University of London, Imperial College of Science and Technology, London, England.

References

Van de Hulst, H. C. (1957). Light scattering by small particles. Dover Publications New York.

Van der Molen, K. and van Maanen, H. R. E. (1978). Laser-Doppler measurements of the turbulent flow in stirred vessel to establish scaling rules. Chemical Engineering Science, vol. 33, p. 1161.

Van Doorn, M. (1982). The impeller flow in a stirred tank. University of Missouri - Rolla, report 820115.

Van't Riet, K. and Smith, J. M. (1973). The behaviour of gas liquid mixture near Rushton turbine blades. Chemical Engineering Science, vol. 28, p. 1031.

Van't Riet, K. and Smith, J. M. (1975). The trailing vortex system produced by Rushton turbine agitators. Chemical Engineering Science, vol. 30, p. 1093.

Watkins, A. P., Gosman, A. D. and Tabrizi, B. S. (1986). Calculation of three dimensional spray motion in engines. SAE, Technical paper, series 860468.

Weetman, R. J. and Salzman, R. N. (1982). Effect of side flow on mixing impeller. DISA Information, No. 27.

Wells, M. R. and Stock, D. E. (1983). The effects of crossing trajectories on the dispersion of the particles in turbulent flow. J. Fluid Mech., Vol. 136, p. 31.

Yanta, W. J. (1973). Turbulence measurements with a laser Doppler velocimeter. Naval Ordonance Laboratory, Report NOLTR 73 - 94, White Oak, Silver Spring, CA, USA.

Yianneskis, M. and Whitelaw, J. H. (1984). Velocity characteristics of pipe and jet flows with high particle concentration. Proc. Int. Symp. on Liquid-Solid Flow and Erosion Wear in Industrial Equipment, ASME Fluids Eng. Conf.

Yianneskis, M., Tindal, M. J. and Paul, G. R. (1986) The application of laser anemometry to the study of flows inside diesel engine inlet ports. 3rd Int. Symp. on Appl. of Laser Anemometry to Fluid Mech., Lisbon.

References

Yianneskis, M., Popiolek, Z. and Whitelaw, J. H. (1987). An experimental study of the steady and unsteady flow characteristics of stirred reactors. J. Fluid Mech., Vol. 175. P. 537.

Zisselmar, R. and Molerus, O. (1978). Investigation of solid-liquid pipe flow with regard to turbulence modification. Int. Symp. on Momentum, Heat and Mass Transfer in Two-Phase Energy and Chamical System, Dubrovnik, West Germany.

Errata

J.M. NOURI Ph.D. Thesis

Page	Line	Incorrect	Correct
iv	4	dipersed	dispersed
18	22	present	presented
47	11	of rod	of the rod
54	8	cetain	certain
68	24	reciculation	recirculation
107	11	charactrising	characterising
108	10	peliminary	preliminary
111	4	setted	settled
111	22	cocentration	concentration
125	24	aroundthe	around the
132	13	proportioal	proportional
147	22	about 250%	a factor of 2.5
158	3	smmetry	symmetry